

Integrated Experimental and Theoretical Studies of Saccharide Structure

Thomas Ethan Klepach

Publication Date

22-07-2008

License

This work is made available under a All Rights Reserved license and should only be used in accordance with that license.

Citation for this work (American Psychological Association 7th edition)

Klepach, T. E. (2008). *Integrated Experimental and Theoretical Studies of Saccharide Structure* (Version 1). University of Notre Dame. <https://doi.org/10.7274/v405s754q1d>

This work was downloaded from CurateND, the University of Notre Dame's institutional repository.

For more information about this work, to report or an issue, or to preserve and share your original work, please contact the CurateND team for assistance at curate@nd.edu.

INTEGRATED EXPERIMENTAL AND THEORETICAL STUDIES OF
SACCHARIDE STRUCTURE

VOLUME I

A Dissertation

Submitted to the Graduate School
of the University of Notre Dame
in Partial Fulfillment of the Requirements

for the Degree of

Doctor of Philosophy

by

Thomas E. Klepach

Anthony S. Serianni, Director

Graduate Program in Chemistry and Biochemistry

Notre Dame, Indiana

July 2008

© Copyright 2008

Thomas E. Klepach

INTEGRATED EXPERIMENTAL AND THEORETICAL STUDIES OF SACCHARIDE STRUCTURE

Abstract

by

Thomas E. Klepach

Broadly speaking the objective of this dissertation is the investigation of carbohydrate structure through an integrated theoretical and experimental approach. In addition to being the most evolutionary ancient class of biopolymer, carbohydrates have the highest potential for structural diversity. This structural diversity is manifest both in terms of primary sequence, and in a very high potential for conformational flexibility due to the high concentration of geometrically mobile dihedrals present in saccharides. The structural biology of saccharides is further complicated by a dearth of robust experimental and theoretical techniques.

A large component of this work involved developing experimental and theoretical tools for the conformational analysis of carbohydrates, specifically parameterizing the conformational dependence of NMR spin-spin couplings for the interpretation of experimental couplings in structural terms. On the experimental side measurement of ^{13}C -based spin-spin couplings necessitated the development of technologies for strategic

isotopic enrichment. The couplings measured in these compounds are interpreted using theoretically derived relationships between molecular conformation and coupling magnitude. These Karplus relationships are based upon quantum mechanical density functional theory (DFT) calculations of spin-spin couplings on energetically optimized model compounds in which a particular geometric feature such as a dihedral is varied. The structural interpretations of these couplings takes the form of populational distributions about the relevant molecular dihedrals. This is applied in a modular fashion to various molecular fragments of biologically significant monosaccharides.

The natural bonding orbital (NBO) method is used to dissect spin-spin coupling mechanisms based upon discrete through space and through bond orbital interactions.

Lastly, an *x*-ray crystal structure of methyl-allolactoside is presented with a complete structural analysis including a discussion of ring-puckering behaviour.

The battery of experimental and theoretical techniques presented in this dissertation set the ground work for application to a broad spectrum of biological investigations involving carbohydrate structure and function.

Dedicated to my father,
Garron L. Klepach, M.D.

ND Class of '63

πατερ παντοκρατερ

“Pater pantokrater...”

CONTENTS

Volume I

Figures	ix
Tables	xxiv
Schemes	xxviii
Preface	xxxii
Acknowledgments	xxxvii
Chapter 1: Introduction.....	1
1.1. Background.....	1
1.1.1. Carbohydrate Chemistry	1
1.1.2. Experimental and Theoretical Methods.....	10
1.2. Dissertation Outline	12
1.2.1. Conceptual Research Approach	12
1.2.2. Research Objectives	17
1.3. References	22
Chapter 2: ¹³ C-Labeled <i>N</i> -Acetyl-neuraminic Acid in Aqueous Solution: Detection and Quantification of Acyclic Keto, Keto Hydrate and Enol Forms by ¹³ C NMR	26
2.1. Abstract	26
2.2. Introduction	27
2.3. Experimental.....	29
2.3.1. ¹³ C-Labeled Sialic acids.	29
2.3.2. Preparation of Unlabeled Sialic Acid.	29
2.3.3. Preparation of 2- <i>O</i> -Methyl-β-D-N-Acetylneuraminic acid (2).	30
2.3.4. NMR Spectroscopy.	31
2.4. Calculations	32
2.4.1. Selection and Geometric Optimization of Model Compounds.	32

2.4.2. Theoretical Calculations of ^{13}C - ^1H and ^{13}C - ^{13}C Spin-Coupling Constants.	33
2.5. Results and Discussion.....	33
2.5.1. Cyclic pyranose and acyclic keto forms of 1	33
2.5.2. Acyclic hydrate form of 1	34
2.5.3. Acyclic enol forms of 1	39
2.5.4. pK_a Values of tautomers of 1	46
2.5.5. Exchange Rates Between Tautomers of 1	48
2.5.6. Solvent Deuterium exchange in 1	48
2.6. Conclusions	50
2.7. Acknowledgements.....	53
2.8. Supporting Information.....	54
2.9. References	62
Chapter 3: ^{13}C - ^1H and ^{13}C - ^{13}C NMR <i>J</i> -Couplings in ^{13}C -Labeled <i>N</i> -Acetyl-neuraminic Acid: Correlations with Molecular Structure.....	65
3.1. Abstract	65
3.2. Introduction	66
3.3. Experimental Methods	70
3.3.1. ^{13}C -Labeled <i>N</i> -Acetyl-neuraminic Acid (2 ¹ , 2 ² and 2 ³).	70
3.3.2. NMR Spectroscopy.	70
3.4. Computational Methods.....	71
3.5. Results and Discussion.....	72
3.5.1. General Considerations.....	72
3.5.2. Conformational Properties of the C1-C2 Bond.....	76
3.5.3. ^1H - ^1H Spin-Couplings.	78
3.5.4. ^{13}C - ^1H Spin-Couplings.	81
3.5.5. ^{13}C - ^{13}C Spin-Couplings.....	89
3.5.6. Conformation About the C6-C7 Bond.....	94
3.5.7. Comparison of JCC in 2 _β , 3-deoxy-β-D-fructopyranose (11) and β-D-fructopyranose (12).	95
3.5.8. Effect of Solvation on Computed Couplings in 9 and 10	96
3.6. Conclusions	98
3.7. Supporting Information.	101
3.8. Acknowledgements.....	106
3.9. References	106
Chapter 4: Correlated C-C and C-O Bond Conformations in Saccharide Hydroxymethyl Groups: Parametrization and Application of Redundant ^1H - ^1H , ^{13}C - ^1H , and ^{13}C - ^{13}C NMR <i>J</i> -Couplings.....	109
4.1. Abstract	109
4.2. Introduction	110
4.3. Experimental Section	115

4.3.1. Synthesis of Labeled Methyl Aldohexopyranosides.	115
4.3.2. NMR Spectroscopy.	117
4.3.3. Theoretical Calculations.	117
4.3.4. Equation Parametrization.	120
4.4. Results and Discussion.	121
4.4.1. General Considerations.	121
4.5. Calculated NMR Scalar Coupling Constants and Parametrization.	124
4.5.1. Two-Bond ^{13}C - ^1H Spin-Spin Coupling Constants.	124
4.5.2. Three-Bond ^{13}C - ^1H Spin-Spin Coupling Constants.	131
4.5.3. Three- and Two-Bond ^1H - ^1H Spin-Spin Coupling Constants.	136
4.5.4. Two-Bond ^{13}C - ^{13}C Spin-Spin Coupling Constants.	139
4.5.5. One-Bond ^{13}C - ^{13}C Spin-Spin Coupling Constants and Bond-Length Considerations.	141
4.5.6. Three-Bond ^{13}C - ^{13}C Spin-Spin Coupling Constants.	143
4.5.7. Experimental Validation of Computed Couplings and Proposed Equations.	144
4.5.8. Average Computed J-Couplings in Staggered Hydroxymethyl Rotamers.	146
4.6. Experimental J -Couplings in 1-4 and Conformational Analysis.	148
4.6.1. Qualitative Treatment and Comparison to Theory.	148
4.6.2. Hydroxymethyl Rotamer (ω) Analysis in 1-4.	154
4.6.3. Distribution of Nine (ω, θ) Rotamers in 1-4 Through Multilinear Fit.	158
4.7. Conclusions.	163
4.8. Acknowledgment.	167
4.9. Supporting Information.	168
4.10. References.	184

Chapter 5: Geminal $^2J_{\text{CCH}}$ Spin-Spin Coupling Constants As Probes of the ϕ Glycosidic Torsion Angle in Oligosaccharides.	188
5.1. Abstract.	188
5.2. Introduction.	189
5.3. Computations.	193
5.4. Results and Discussion.	194
5.4.1. Energetics.	194
5.4.2. $^2J_{\text{CCH}}$ Spin-Couplings in 1-4	198
5.4.3. $^2J_{\text{CCH}}$ Spin-Couplings in 5-8.	203
5.4.4. Other Structural Factors Influencing $^2J_{\text{CCH}}$ in Saccharides.	208
5.4.5. Quantitative Treatment of $^2J_{\text{C1,H2}}$ and $^2J_{\text{C2,H1}}$	212
5.5. Conclusions.	216
5.6. Acknowledgements.	220
5.7. Supporting Information.	220
5.8. References.	224

Chapter 6: ^{13}C - ^{13}C NMR Spin-Couplings in Saccharides: New Correlations with	
Molecular Structure	227
6.1. Abstract	227
6.2. Introduction	228
6.3. Experimental.....	230
6.3.1. Synthesis of ^{13}C -Labeled D-Aldoses and Methyl D-Aldopyranosides	
.....	230
6.3.2. Measurement of ^{13}C - ^{13}C Spin-Coupling Constants.....	232
6.4. Computational.....	233
6.4.1. Selection and Geometric Optimization of Model Compounds.....	233
6.4.2. Theoretical Calculations of ^{13}C - ^{13}C Spin-Coupling Constants	234
6.5. Results and Discussion.....	235
6.5.1. General Observations in 1 and 2	235
6.5.2. $^2J_{\text{CC}}$ Coupling Constants.....	237
6.5.3. $^3J_{\text{CC}}$ Coupling Constants.....	246
6.5.4. $^3+^3J_{\text{CC}}$ Coupling Constants.....	250
6.5.5. $^1J_{\text{CC}}$ Coupling Constants.....	254
6.5.6. General Observations on Computed J_{CC} Values	254
6.6. Conclusions	256
6.7. Acknowledgements.....	261
6.8. Supporting Information.....	261
6.9. References	269

Volume II

Figures	ix
Tables	xxiv
Schemes	ccxciii

Chapter 7: Hydroxyl Group Configuration / Conformation and $^2J_{\text{CCC}}$ Spin-Couplings in	
Saccharides: DFT, NJC and NSA Analyses of Experimental Data	272
7.1. Abstract	272
7.1.1. Introduction.....	273
7.2. Experimental.....	277
7.2.1. Experimental ^{13}C - ^{13}C Spin-Coupling Measurements in DMSO	277
7.3. NMR titration of experimental $^2J_{\text{C1,C3}}$ by ionization of the O2 hydroxyl	278
7.4. Computational	278

7.4.1. Selection and Geometric Optimization of Model Compounds	278
7.4.2. Theoretical Calculations of ^{13}C - ^{13}C Spin-Coupling Constants	282
7.4.3. Natural Bonding Orbital Calculations	282
7.4.4. Theoretical SSCC Parameterization and Analysis of Experimental Couplings	282
7.5. Results and Discussion	283
7.5.1. The Dependence of $^2J_{\text{C1,C3}}$ on Configuration	283
7.5.2. The Dependence of $^2J_{\text{C1,C3}}$ on Conformation	284
7.5.3. The Effect of Deoxygenation on $^2J_{\text{CC}}$	291
7.5.4. The Effect of <i>N</i> -acetylation on $^2J_{\text{CC}}$	296
7.5.5. C-C Bond Angle and Bond Length Considerations Regarding $^2J_{\text{CC}}$	297
7.5.6. NBO Analysis: Lone Pair Donation into C-C σ^* Orbitals	301
7.5.7. The Influence of C-O rotation on $^2J_{\text{C2,C4}}$ in β -Glc	310
7.5.8. Natural <i>J</i> -coupling Analysis I: Configurational Dependence of $^2J_{\text{C1,C3}}$	314
7.5.9. Natural <i>J</i> -coupling Analysis II: Conformational Dependence of $^2J_{\text{C1,C3}}$	323
7.5.10. Coupling Trend Validation in Conformationally Determined Lacotside System	337
7.5.11. O2 Ionization and $^2J_{\text{C1,C3}}$	338
7.5.12. The Conformational Analysis of ϕ , ξ and ζ in Methyl- β -D- glucopyranose	339
7.6. Conclusions	399
7.7. References	406

Chapter 8: Crystal Structure Methyl β -allolactoside (Methyl 6-O-beta-D-[1- ^{13}C]- galactopyranosyl-beta-D-glucopyranoside) Monohydrate	415
8.1. Introduction	415
8.2. Comment	416
8.3. Experimental	426
8.3.1. Reagents	426
8.3.2. Synthesis of o-Nitrophenyl β -D-[1- ^{13}C]-galactopyranoside (2)	427
8.3.3. Synthesis of Disaccharide I_{E} via Enzyme-catalyzed Transglycosylation	427
8.3.4. Crystal growth of I_{E}	428
8.3.5. Data Collection	429
8.3.6. Instrumentation	430
8.3.7. Refinement	430
8.3.8. Crystal Data	430
8.4. References	431

Chapter 9: Synthesis	434
9.1. Definition of Terms.....	434
9.2. Primary Structure	436
9.3. Secondary Structure	437
9.4. Higher Order Structure.....	438
9.5. Modular Conformational Analysis.....	442
9.6. Biological Applications.....	444
9.7. References	446

FIGURES

- Figure 2.1. Partial $^{13}\text{C}\{^1\text{H}\}$ NMR spectrum of $[2\text{-}^{13}\text{C}]\mathbf{1}$ (150 MHz) at pH 2.0 and 25 °C showing signal assignments. (A) Anomeric region. X1 and X2 are putative C2 signals of the acyclic hydrate form ($\mathbf{1h}$). (B) Region containing labeled C2 *keto* ($\mathbf{1k}$) and *enol* ($\mathbf{1e}$) carbons, and the natural abundance amide CO (CO_{am}) and C1 (COOH) carbons of $\mathbf{1}\alpha p$ and $\mathbf{1}\beta p$. The C1 signals appear as doublets due to the presence of $^1J_{\text{C1,C2}}$. Several weak signals in this region were not identified....35
- Figure 2.2 Partial ^1H -coupled ^{13}C NMR spectrum (150 MHz) of $[2\text{-}^{13}\text{C}]\mathbf{1}$ at pH 2.0 and 25 °C. (A) Labeled C2 signals of $\mathbf{1}\alpha p$, $\mathbf{1}\beta p$ and the two putative C2 $\mathbf{1h}$ (X1 and X2). (B) C2 *keto*. (C) C2 *enol* forms.37
- Figure 2.3. Partial $^{13}\text{C}\{^1\text{H}\}$ NMR spectrum of $[3\text{-}^{13}\text{C}]\mathbf{1}$ at pH 2.0 and 25 °C. (A) Region showing the natural abundance C1 and amide CO signals of $\mathbf{1}\alpha p$ and $\mathbf{1}\beta p$, and the labeled C3 signal of $\mathbf{1e}$. (B) C3 signal of $\mathbf{1e}$ in the ^1H -coupled ^{13}C spectrum, showing the $^1J_{\text{CH}}$ and longer-range J_{CH}41
- Figure 2.4 (A) Partial $^{13}\text{C}\{^1\text{H}\}$ NMR spectrum of $[1,2,3\text{-}^{13}\text{C}_3]\mathbf{1}$ showing the putative C2 and C3 enol signals. Signals labeled as “u” are unknown species, possibly other enols. (B) and (C) Expansions of the C2 and C3 signals showing their multiplicities and constituent $^1J_{\text{CC}}$ and $^2J_{\text{CC}}$ values.43
- Figure 2.5 Titration of the C2 chemical shifts of $\mathbf{1}\alpha p$ (A), $\mathbf{1}\beta p$ (B), $\mathbf{1k}$ (C) and $\mathbf{1e}$ (D). Filled blue circles and blue line are fits to experimental points shown in either red or green.47
- Figure 2.6 Partial ^1H NMR spectrum (600 MHz) of $\mathbf{1}$ immediately upon dissolution in $^2\text{H}_2\text{O}$ (A) and after incubation at 25 °C for 150 h (B). Signals from H2_{ax} in $\mathbf{1}\alpha p$ and $\mathbf{1}\beta p$ are nearly absent, whereas those from H2_{eq} are still observable.49

Figure 2.7 (S1) $^{13}\text{C}\{^1\text{H}\}$ NMR spectra (150 MHz) of (A) pyruvic acid and (B) sodium pyruvate. Note the significant reduction in the *hydrate/keto* ratio in aqueous solutions of the sodium salt. Weak signals in both spectra were not assigned; in (A), signals at ~ 130 ppm may be due to *enol* forms.55

Figure 2.8. (S2) Effect of the C2-C3-C4-C5 torsion angle on calculated total energies, $^2J_{\text{C2,H3R/S}}$ and $^1J_{\text{CC}}$ values in **2**. (A) Total energies (brown); $^2J_{\text{C2,H3R}}$ (blue); $^2J_{\text{C2,H3S}}$ (green). (B) $^1J_{\text{C1,C2}}$ (blue); $^1J_{\text{C2,C3}}$ (green).56

Figure 2.9. (S3) Partial $^{13}\text{C}\{^1\text{H}\}$ NMR spectrum (150 MHz) of $[1,2,3-^{13}\text{C}_3]\mathbf{1}$ at pH 2.0 showing the relatively intense C1 signals of **1ap** (offscale at 173.1 ppm) slightly downfield of the C1 signals of **1e** (172.4 ppm). The latter doublet of doublets contains $^1J_{\text{C1,C2}}$ and $^2J_{\text{C1,C3}}$ values identical to those observed at C2 of **1e** (Figure 2.4). The upfield doublet at 171.3 ppm contains a $^1J_{\text{C1,C2}}$ equal that observed in the C2 signal of hydrate species X₁ (Figure S4), thus identifying C1 of this species. Comparison of these data to those in Figure 2.1B reveals the low levels of **1e** and X₁ relative to that of **1ap**.57

Figure 2.10. (S4) Partial $^{13}\text{C}\{^1\text{H}\}$ NMR spectrum (150 MHz) of $[1,2,3-^{13}\text{C}_3]\mathbf{1}$ at pH 2.0 showing the very intense C2 signals of **1βp** (a; doublet of doublets; $^1J_{\text{C1,C2}} = 70.1$ Hz, $^1J_{\text{C2,C3}} = 41.0$ Hz), the upfield half of the C2 signals of **1ap** (b; $^1J_{\text{C1,C2}} = 67.6$ Hz, $^1J_{\text{C2,C3}} = 41.7$ Hz), and the C2 signals of hydrate species X₁ (c). Note that the $^1J_{\text{CC}}$ values measured from C2 of X₁ are identical to those observed at C1 of X₁ (Figure S3). Signals a' arise from the $[1,2-^{13}\text{C}_2]$ isotopomer of **1** present in the sample.58

Figure 2.11. (S5) Effect of the C2-C3-C4-C5 torsion angle on calculated J_{CH} values in **5** and **6**. (A) $^1J_{\text{C3,H3}}$ in **5**. (B) $^2J_{\text{C2,H3}}$ in **5**. (C) $^1J_{\text{C3,H3}}$ in **6**. (D) $^2J_{\text{C2,H3}}$ in **6**. Blue circles; O1-C1-C2-C3 torsion angle of 90° (fixed). Green squares; O1-C1-C2-C3 torsion angle of 180° (fixed).59

Figure 2.12. (S6) Effect of the C2-C3-C4-C5 torsion angle on calculated $^1J_{\text{CC}}$ values in **5** and **6**. Blue circles, $^1J_{\text{C1,C2}}$. Green squares, $^1J_{\text{C2,C3}}$. (A) **5** with the C1-C2-C3-C4 torsion angle at 90° . (B) **5** with the C1-C2-C3-C4 torsion angle at 180° . (C) **6** with the C1-C2-C3-C4 torsion angle at 90° . (D) **6** with the C1-C2-C3-C4 torsion angle at 180°60

Figure 2.13. (S7) Effect of the C2-C3-C4-C5 torsion angle on calculated $^2J_{C1,C3}$ values in **5** and **6**. (A) **5** with the C1-C2-C3-C4 torsion angle at 90°. (B) **5** with the C1-C2-C3-C4 torsion angle at 180°. (C) **6** with the C1-C2-C3-C4 torsion angle at 90°. (D) **6** with the C1-C2-C3-C4 torsion angle at 180°.....61

Figure 3.1. Expanded regions of the resolution-enhanced 1H NMR spectrum of $[2-^{13}C]\mathbf{2}$ at p 2H 2.0 and 25 °C showing signal assignments. The amide signals in (D) were very weak due to the small percentage of molecules containing 1H at the NH site in 2H_2O . The H7 β signal in (B) is expanded in (E) to show the presence of two $^3J_{HH}$ and the long-range $^4J_{C2,H7}$73

Figure 3.2. Expanded regions of the $^{13}C\{^1H\}$ NMR spectrum of $[1-^{13}C]\mathbf{2}$ at p 2H 2.0 and 25 °C. The C2 signals (C) show the presence of the large $^1J_{C1,C2}$, and smaller longer range couplings are observed at C6 β ($^3J_{C1,C6}$) (D) and C3 α/β ($^2J_{C1,C3}$) (F).75

Figure 3.3. The effect of C1-C2 bond rotation on the total energies of protonated **7** (A) and **9** (B). *In vacuo* data are shown as solid lines, and solvated (water) data are shown as dotted lines. Black symbols = FX series, blue symbols = FL series. ...76

Figure 3.4. The effect of C1-C2 bond rotation on total energies of **8** (A) and **10** (B). *In vacuo* data are shown as solid lines, and solvated (water) data are shown as dotted lines. Black symbols = FX series, blue symbols = FL series.77

Figure 3.5 Effect of C1-C2 bond rotation on calculated $^1J_{C1,H3ax/eq}$ in **7/8** (A) and **9/10** (B). Squares = H3 $_{ax}$, circles = H3 $_{eq}$. Black symbols = protonated form; blue symbols = ionized form. Data taken from the FXS series.84

Figure 3.6. Effect of C1-C2 bond rotation on calculated $^2J_{C2,H3eq/ax}$ in **7/8** (A) and **9/10** (B). Squares = H3 $_{ax}$, circles = H3 $_{eq}$. Black symbols = protonated form; blue symbols = ionized form. Data taken from the FXS series.....85

Figure 3.7. Effect of C1-C2 bond rotation on calculated $^1J_{C3,H3eq/ax}$ in **7/8** (A) and **9/10** (B). Squares = H3 $_{ax}$, circles = H3 $_{eq}$. Black symbols = protonated form; blue symbols = ionized form. Data taken from the FXS series.....87

- Figure 3.8 Effect of C1-C2 bond rotation on $r_{C1,C2}$ in **7/8** (A) and **9/10** (B). Squares = protonated form; circles = ionized form. Black/red symbols = FX/FL series; green/purple symbols = FXS/FLS series. 89
- Figure 3.9. Effect of C1-C2 bond rotation on $^1J_{C1,C2}$ in **7/8** (A) and **9/10** (B). Squares = protonated form; circles = ionized form. Black/red symbols = FX/FL series; green/purple symbols = FXS/FLS series. 90
- Figure 3.10. Effect of C1-C2 bond rotation on $^2J_{C1,C3}$ (A) and $^1J_{C2,C3}$ (B) in **7/8** (circles) and **9/10** (squares). Black symbols = protonated form; blue symbols = ionized form. Data taken from the FXS series. 92
- Figure 3.11. Effect of C1-C2 bond rotation on $^2J_{C2,C4}$ (A), $^2J_{C2,C6}$ (B) and $^3J_{C2,C7}$ (C) in **7/8** (circles) and **9/10** (squares). Black symbols = protonated form; blue symbols = ionized form. Data taken from the FXS series. 93
- Figure 3.12. (S1) (A) Amide 1H signals of **2** at p^2H 2.0 and 20 °C. Assignment of the weaker αp signal is tentative. Resonance linewidth ($\Delta\nu_{0.5}$) of the βp signal is 2.4 Hz. $^3J_{H5,NH}$ are 9.2 Hz and 9.4 Hz for the αp and βp , respectively. These signals were very weak, since they represent the small fraction of **2** containing an N^1H rather than an N^2H at the amide site. (B) Amide 1H signals of **2** at pH 8.0 and 20 °C. The $NH\beta$ signal has collapsed into a broadened singlet due to rapid chemical exchange of the NH proton with solvent H_2O . Resonance linewidth ($\Delta\nu_{0.5}$) is 19.6 Hz. Raw FIDs used to generate spectra in (A) and (B) were treated with a 0.1 Hz exponential apodization function prior to FT..... 104
- Figure 3.13. (S2) (A) $H5$ signal of **2** βp at p^2H 2.0 and 20 °C showing a pseudotriplet pattern due to the nearly equal values of $^3J_{H4,H5}$ (10.1 Hz) and $^3J_{H5,H6}$ (10.3 Hz). Resonance linewidths ($\Delta\nu_{0.5}$) range from 1.5-1.7 Hz. No J -coupling to the NH proton is observed since the latter is essentially fully exchanged with solvent 2H . (B) $H5$ signal of **2** βp at pH 8.0 and 20 °C. The pseudotriplet has broadened considerably (compare to data in Fig. 1A) due to rapid chemical exchange of the adjacent NH proton with solvent H_2O . Resonance linewidth ($\Delta\nu_{0.5}$) is estimated at ~17 Hz. Raw FIDs used to generate spectra in (A) and (B) were treated with a 0.1 Hz exponential apodization function prior to FT..... 105
- Figure 4.1. Conformational Energy Hypersurface Generated from 30° Rotations of ω and θ in **5** (144 optimized structures) determined by DFT (B3LYP/6-31G*)..... 122

Figure 4.2. (A) Dependence of ${}^2J_{C5,H6R}$ on ω . (B) Dependence of ${}^2J_{C5,H6S}$ on ω . (C) Dependence of ${}^2J_{C6,H5}$ on ω . Circles, data from **5** (Table 4.1); open diamonds, data from **6** (Table S1). For **5** in plots A and B, data are divided into two groups to emphasize the enhanced coupling (open circles) observed in one θ conformation (see Scheme 4.5). 125

Figure 4.3. (A) The dependence of ${}^2J_{C5,H6R/S}$ on both ω and θ , determined by varying both torsion angles in **5** systematically through 360° in 30° increments. The vertical spread of points at discrete ω values demonstrates the sensitivity of these ${}^2J_{CH}$ to θ . Superimposed are coupling data computed in the fully (staggered) and partially (eclipsed) optimized structures reported in Table 4.1. Filled circles, ${}^2J_{C5,H6R}$; open squares, ${}^2J_{C5,H6S}$; stars and open circles, respective couplings taken from Table 4.1. (B) Data similar to that in part A for ${}^2J_{C6,H5}$ in **5**. Closed triangles, hypersurface data; open circles, data from Table 4.1. (C) Hypersurface (ω/θ) calculated for ${}^2J_{C5,H6R}$ in **5**. (D) Hypersurface (ω/θ) calculated for ${}^2J_{C5,H6S}$ in **5**. (E) Hypersurface (ω/θ) calculated for ${}^2J_{C6,H5}$ in **5**. 130

Figure 4.4. (A) Dependence of ${}^3J_{C4,H6R}$ and ${}^3J_{C4,H6S}$ on ϕ in **5**. Filled squares, ${}^3J_{C4,H6R}$ (hypersurface data); open diamonds, ${}^3J_{C4,H6S}$ (hypersurface data); filled circles, ${}^3J_{C4,H6R/S}$ curve reported by Tvaroska and Gadjos;³¹ open triangles, ${}^3J_{C4,H6R}$ in **6**; filled triangles, ${}^3J_{C4,H6S}$ in **6**; open circles, ${}^3J_{C4,H6R}$ in **7**; open squares, ${}^3J_{C4,H6S}$ in **7**. Small black + (${}^3J_{C4,H6R}$) and \times (${}^3J_{C4,H6S}$) define Karplus curves predicted from eqs 4.2 and 4.3. The vertical spread of points at discrete ϕ indicates the effect of θ . (B) Hypersurface calculated for ${}^3J_{C4,H6R}$ in **5**. (C) Hypersurface calculated for ${}^3J_{C4,H6S}$ in **5**. (D) Dependence of ${}^3J_{C6,H4}$ in **5** on the C6-C5-C4-H4 torsion angle (Table S2). Filled circles, ${}^3J_{C6,H4ax}$; filled squares, ${}^3J_{C6,H4eq}$. The vertical spread of points at discrete C-C-H torsions shows the effect of θ . Data for corresponding couplings in **6** (open squares) and **7** (open circles) are also shown. 133

Figure 4.5. (A) Dependence of ${}^3J_{H5,H6R}$ and ${}^3J_{H5,H6S}$ on ω in **5** (open circles, ${}^3J_{H5,H6R}$; open triangles, ${}^3J_{H5,H6S}$). The vertical spread of points at discrete ω torsions indicates the effect of θ . Curves derived from eqs 4.4 and 4.5 (+ and \times), and curves derived from previously reported empirically derived Karplus equations³³ (filled upright and inverted triangles) are also shown. (B) Dependence of ${}^2J_{H6R,H6S}$ on ω in **5**. The vertical spread of points at discrete C-C- C-H

torsions indicates the effect of θ . (C) The dependence of ${}^2J_{H6R,H6S}$ in **5** on ω in the three perfectly staggered θ rotamers (open squares, $\theta = 60^\circ$; open circles, $\theta = -60^\circ$; filled circles, $\theta = 180^\circ$). (D) Dependence of ${}^2J_{H6R,H6S}$ in **5** on θ in the three perfectly staggered ω rotamers (open squares, $\omega = 60^\circ$; open circles, $\omega = -60^\circ$; filled circles, $\omega = 180^\circ$). 137

Figure 4.6. (A) Hypersurface (ω/θ) calculated for ${}^3J_{H5,H6R}$ in **5**. (B) Hypersurface (ω/θ) calculated for ${}^3J_{H5,H6S}$ in **5**. (C) Hypersurface (ω/θ) calculated for ${}^2J_{H6R,H6S}$ in **5**. 138

Figure 4.7. (A) Dependence of ${}^2J_{C4,C6}$ in **5** on ω . The vertical spread of points at discrete ω torsions (smaller open circles) indicates the effect of θ . Larger open circles are data taken from Table S3 for staggered and eclipsed conformations about ω . Data in triangles and diamonds were obtained from **6** and **7**, respectively (Table S1). (B) Hypersurface (ω/θ) calculated for ${}^2J_{C4,C6}$ in **5**. 140

Figure 4.8. (A) Dependencies of ${}^1J_{C5,C6}$ and ${}^1J_{C4,C5}$ in **5** on ω (data taken from Table S3). Filled circles, ${}^1J_{C5,C6}$ when $\theta = 60^\circ$ and -60° ; open circles, ${}^1J_{C5,C6}$ when $\theta = 180^\circ$; open squares, ${}^1J_{C4,C5}$ (staggered ω rotamers only). (B) Similar plot as in part A but using data obtained from the full hypersurface. The vertical spread of points at discrete ω torsions (filled circles) indicates the effect of θ . Open circles identify perfectly staggered θ rotamers. (C) Hypersurface (ω/θ) calculated for ${}^1J_{C5,C6}$ in **5**. 142

Figure 4.9. (S1) (A) The dependence of $r_{C5,C6}$ in **5** on ω . (B) Correlations between ${}^1J_{C5,C6}$ in **5** and $r_{C5,C6}$. The vertical spread of points at discrete ω torsions indicates the degree of sensitivity of the coupling to changes in θ . Open squares, staggered conformers; filled squares, eclipsed conformers. 180

Figure 4.10. (S2) Correlation between $r_{C6,H6R/S}$ and ω in **5**. Filled squares, $r_{C6,H6R}$; open squares, $r_{C6,H6S}$. (B) Correlation between $r_{C6,O6}$ and ω in **5**. (C) Correlation between $r_{C5,O5}$ and ω in **5**. In all plots, data were taken from the 18 staggered and eclipsed structures identified in Table 1 180

Figure 4.11. (S3) The dependencies of ${}^3J_{C1,C6}$ (filled circles) and ${}^3J_{C3,C6}$ (open circles) in **5** on ω . The vertical spread of points at discrete ω torsions indicates the effect of θ . Perfectly staggered θ rotamers at individual ω values are indicated by open circles and diamonds. 181

Figure 4.12. (S4) Portions of the 600-MHz ^1H NMR spectrum of methyl α -D-[4- ^{13}C]galactopyranoside **4** (upper trace) superimposed on simulated data (lower trace). (A) H1. (B) downfield half of H4. (C) H6R, upfield half of H4, and H6S. (D) H5 and H3. (E) H2..... 182

Figure 4.13. (S5) The 150-MHz $^{13}\text{C}\{^1\text{H}\}$ NMR spectrum of methyl α -D-[6- ^{13}C]galactopyranoside **3**, showing (A) $^3J_{\text{CC}}$ (to C1), $^1J_{\text{CC}}$ and $^3J_{\text{CC}}$ (B) and (to C5 and C3, respectively), and no coupling to C2 and C4. No splitting was observed in the aglycone methyl carbon signal (not shown). Only the natural abundance carbon signals are shown. 183

Figure 5.1. (A) Plot of computed $^2J_{\text{C5,H6R}}$ and $^2J_{\text{C5,H6S}}$ in **1** (Scheme 5.1) as a function of ω (defined as the O5-C5-C6-O6 torsion angle). The scatter of points at discrete values of ω is caused by the effect of θ (defined as the C5-C6-O6-H torsion angle). Note the unimodal behavior with respect to ω . Closed blue circles, $^2J_{\text{C5,H6R}}$; open black squares, $^2J_{\text{C5,H6S}}$. (B) Hypersurface showing the effect of ω and θ on $^2J_{\text{C5,H6R}}$ in **1**. (C) Hypersurface showing the effect of ω and θ on $^2J_{\text{C5,H6S}}$ in **1**. Data taken from ref 9. 191

Figure 5.2. Plot showing the effect of ϕ on the calculated total energy E of **1** and **2** determined by DFT (B3LPY/6-31G*, in vacuo)..... 195

Figure 5.3. Plots showing the effect of ϕ on the calculated total energy E of **5** (A), **6** (B), **7** (C), and **8** (D) determined by DFT (B3LYP/6-31G*, in vacuo). The scatter of points at discrete values of ϕ is caused by the effect of α ; data points in blue are for perfectly staggered values of α . Superimposed on each plot is the corresponding curve derived from either **1** (A and C) or **2** (B and D). 196

Figure 5.4. Plots showing the effect of α on the calculated total energy E of **5** (A), **6** (B), **7** (C), and **8** (D) determined by DFT (B3LYP/6-31G*, in vacuo). The scatter of points at discrete values of α is caused by the effect of ϕ ; data points in blue are for perfectly staggered values of ϕ 197

Figure 5.5. (A) Correlations between $^2J_{\text{C1,H2}}$ and ϕ in **1** (open symbols) and **3** (closed blue symbols). Squares, $^2J_{\text{C1,H2a}}$; circles, $^2J_{\text{C1,H2e}}$ (H2a = H2S; H2e = H2R; see Scheme 5.2). (B) Correlations between $^2J_{\text{C1,H2e}}$ and ϕ in **2** (open circles) and **4** (closed blue circles). (C) Correlations between $^2J_{\text{C1,H2a}}$ and ϕ in **2** (open squares) and **4** (closed blue squares). (D) Correlations between $^2J_{\text{C2,H1}}$ and ϕ in

1 (open squares) and 3 (closed blue squares). (E) Correlations between ${}^2J_{C2,H1}$ and ϕ in 2 (open squares) and 4 (closed blue squares).....	199
Figure 5.6. (A) Effect of ϕ on $r_{C1,O1}$ (open squares) and $r_{C1,O5}$ (closed blue squares) in 1. (B) Effect of ϕ on $r_{C1,O1}$ (open squares) and $r_{C1,O5}$ (closed blue squares) in 2.	201
Figure 5.7. (A) Effect of ϕ on $r_{C1,H1}$ (open squares) and $r_{C1,C2}$ (closed blue squares) in 1. (B) Effect of ϕ on $r_{C1,H1}$ (open squares) and $r_{C1,C2}$ (closed blue squares) in 2.	201
Figure 5.8. (A) Effect of ϕ on $r_{C1,H1}$ (open squares) and ${}^2J_{C2,H1}$ (closed squares) in 1. (B) Effect of ϕ on $r_{C1,H1}$ (open squares) and ${}^2J_{C2,H1}$ (closed squares) in 2...	203
Figure 5.9. (A) Effect of α on ${}^2J_{C1,H2}$ in 5. Point scatter at discrete values of α is due to the effect of ϕ ; highlighted points (open blue circles) are for perfectly staggered values of ϕ . (B) Effect of ϕ on ${}^2J_{C1,H2}$ in 5. Point scatter at discrete values of ϕ is due to the effect of α ; highlighted points (open blue circles) are for perfectly staggered values of α . (C) Effect of ϕ on ${}^2J_{C2,H1}$ in 5. Point scatter at discrete values of ϕ is due to the effect of α ; highlighted points (open blue circles) are for perfectly staggered values of α . (D) Effect of α on ${}^2J_{C2,H1}$ in 5. Point scatter at discrete values of α is due to the effect of ϕ ; highlighted points (open blue circles) are for perfectly staggered values of ϕ	204
Figure 5.10. Same data as in Figure 5.9 for 6.	205
Figure 5.11. Same data as in Figure 5.9 for 7.	206
Figure 5.12. Same data as in Figure 5.9 for 8.	207
Figure 5.13. Computed hypersurfaces showing the dependencies of ${}^2J_{C1,H2}$ and ${}^2J_{C2,H1}$ on ϕ and α in 5 (A and B, respectively), and in 6 (C and D, respectively).	213
Figure 5.14. Computed hypersurfaces showing the dependencies of ${}^2J_{C1,H2}$ and ${}^2J_{C2,H1}$ on ϕ and α in 7 (A and B, respectively), and in 8 (C and D, respectively).	214

- Figure 5.15. (S1) Contour maps showing preferred ϕ/α populations for **5** (A), **6** (B), **7** (C), and **8** (D) derived from total energies obtained from DFT calculations (B3LYP/6-31G*).221
- Figure 5.16. (S2) (A) Plot of $r_{C1,H1}$ (closed circles) and ${}^2J_{C2,H1}$ (open triangles) as a function of ϕ in **6**. Note the anomalous behavior of ${}^2J_{C2,H1}$ at $\phi = -60^\circ$. (B) A plot of $r_{C2,H2}$ (closed circles) and ${}^2J_{C1,H2}$ (open triangles) as a function of α in **6**. Note the anomalous behavior of ${}^2J_{C1,H2}$ at $\alpha = 180^\circ$. The shift to more negative couplings in both cases is attributed to oxygen lone-pair effects on $r_{C1,C2}$ (see text); in both cases, the lack of a vicinal lone-pair effect reduces $r_{C1,C2}$, thus shifting ${}^2J_{CCH}$ to more negative (less positive) values.222
- Figure 5.17. (S3) (A) Correlation between the C1-C2-H2 bond angle and ${}^2J_{C1,H2}$ in **6**. Open circles; $\alpha = 60^\circ$; closed squares, $\alpha = -60^\circ$; open squares, $\alpha = 180^\circ$. (B) Correlation between the C2-C1-H1 bond angle and ${}^2J_{C2,H1}$ in **6**. Open circles; $\phi = 60^\circ$; closed squares, $\phi = -60^\circ$; open squares, $\phi = 180^\circ$222
- Figure 5.18. (S4) (A) Plot of ${}^1J_{C1,H1}$ in **6** as a function of $r_{C1,H1}$ (closed squares), showing decreasing ${}^1J_{CH}$ with increasing r_{CH} . The value of $r_{C1,H1}$ was systematically varied in 0.001 Å increments and held fixed; all other molecular parameters were optimized. Superimposed on this plot is the effect of varying $r_{C1,C2}$ (open circles) and $r_{C2,H2}$ (closed circles) on ${}^1J_{C1,H1}$; both bond lengths were varied systematically and separately in 0.001 Å increments and held fixed; all other molecular parameters were optimized. Note the small effect of $r_{C1,C2}$ and $r_{C2,H2}$, and the large influence of $r_{C1,C2}$, on ${}^1J_{C1,H1}$. (B) Plot of ${}^1J_{C1,C2}$ in **6** as a function of $r_{C1,C2}$ (closed squares), showing decreasing ${}^1J_{CC}$ with increasing r_{CC} . The value of $r_{C1,C2}$ was systematically varied in 0.001 Å increments and held fixed; all other molecular parameters were optimized. Superimposed on this plot is the effect of varying $r_{C1,H1}$ (open circles) and $r_{C2,H2}$ (close circles) (performed as described in A) on ${}^1J_{C1,C2}$. Note the modest effect of r_{CH} on ${}^1J_{CC}$. (C) Plot of ${}^1J_{C1,H1}$ as a function of $r_{C1,H1}$ in *fully optimized geometries* of **6**. Changes in r_{CH} were induced by rotating ϕ and α (only perfectly staggered rotamers are shown). Note the enhanced slope of this plot relative to that found in A. (D) Plot of ${}^1J_{C1,C2}$ as a function of $r_{C1,C2}$ in *fully optimized geometries* of **6**. Changes in r_{CC} were induced by rotating ϕ and α (only perfectly staggered rotamers are shown). While data scatter is significant, the average slope of this plot is greater than that found in B.223

Figure 6.1. (A) Effect of hydroxymethyl group conformation on calculated $^3J_{C1,C6}$ in **20** (blue circles), **21** (black circles), **22** (blue squares), and **23** (black squares). (B) Effect of hydroxymethyl conformation on calculated $^3J_{C3,C6}$ (same symbols as in (A))......249

Figure 6.2. Effect of exocyclic hydroxymethyl group conformation on calculated $^{3+3}J_{C1,C4}$ in **20** (blue circles), **21** (black circles), **22** (blue squares), and **23** (black squares)......252

Figure 6.3. Effect of exocyclic hydroxymethyl group conformation on calculated $^{3+3}J_{C2,C5}$ in **20** (blue circles), **21** (black circles), **22** (blue squares), and **23** (black squares)......253

Figure 6.4. (S1) $^{13}C\{^1H\}$ NMR spectrum (150 MHz) of an aqueous solution of methyl glycosides generated from Fischer glycosidation of D-[1- ^{13}C]galactose. Four forms are present (see adjacent structures): Gal α p, Gal β p, Gal α f and Gal β f. Expanded regions of the spectrum are shown in A-D, with signal assignments shown in blue and J_{CC} values shown in red.264

Figure 6.5. (S2) Effect of exocyclic hydroxymethyl group conformation on calculated $^2J_{C1,C3}$ in **20** (blue circles), **21** (black circles), **22** (blue squares), and **23** (black squares). The most negative coupling is observed in **22**, which bears two axial C-O bonds at C1 and C3. In contrast, the most positive coupling is observed in **21**, which bears two equatorial C-O bonds at C1 and C3. Intermediate couplings are observed in **20** and **23** which contain one axial and one equatorial C-O bond at C1 and C3. These findings validate the predictions based on the empirical PR rule.⁶265

Figure 6.6. (S3) Effect of exocyclic hydroxymethyl group conformation on calculated $^2J_{C1,C5}$ in **20** (blue circles), **21** (black circles), **22** (blue squares), and **23** (black squares). A dependence of this coupling on anomeric configuration is observed, with α -anomers (**20**, **22**) giving couplings of ~ -2 Hz and β -anomers giving couplings of ~ -0.5 Hz. These data are consistent with experimental data (Table 1) and PR predictions.⁶265

Figure 6.7. (S4) Effect of exocyclic hydroxymethyl group conformation on calculated $^2J_{C3,C5}$ in **20** (blue circles), **21** (black circles), **22** (blue squares), and **23** (black squares). Changing the orientation of O3 from equatorial to axial results in a significant shift in $^2J_{C3,C5}$ to more negative values. The remote effect of anomeric configuration on $^2J_{C3,C5}$ is also evident, with the coupling in **21** ~ -0.6

Hz larger than in 20 . However, a related remote effect in 22 and 23 is not observed. These results are consistent with experimental observations (Tables 1 and 3).....	266
Figure 7.1. Conformational Dependence of $^2J_{C1,C3}$ on ξ . Definitions of ϕ , ξ and ζ are found in the text. Specific values for ϕ and ζ are represented by the coloration indicated in the legend.	286
Figure 7.2. Comparison of Spin-Spin Couplings Calculated <i>In Vacuo</i> and <i>In Solvo</i> as a Function of ξ in 2^C . Data depicted with circles and squares are structures in which C2-C3-O3-H (ζ) = 60° and 180° respectively. Solid and outlined shapes were data calculated <i>In Vacuo</i> and <i>In Solvo</i> respectively. Definition of ξ in the text.....	290
Figure 7.3. Projection Resultant for $^2J_{C1,C3}$ as a Function of C1, C2 and C3 Hydroxyl Substitution. The projection resultant is a unitless measure. C1 through C3 hydroxyl substitutions patterns are indicated by color where ‘Exptl.’ denotes an experimentally measured coupling and ‘DFT’ an averaged ab initio value. C1 through C3 hydroxyls not mentioned are absent (i.e. O1, O3 indicates a 2-deoxy structure). Data is not sorted by configuration.	295
Figure 7.4. Comparison of Experimental and DFT $^2J_{C1,C3}$ Values in 14 - 17 . Diamonds represent <i>ab initio</i> coupling values from the Series 6 calculations, whereas the horizontal lines are experimental couplings. Color representations are blue: b-GlcNAc (15), green: a-GlcNAc (14), orange: b-AlloNAc (17), and red: a-AlloNAc (16).....	297
Figure 7.5. The Subtended Bond Angle and Length Dependence of $^2J_{C1,C3}$, $^1J_{C1,C2}$ and $^1J_{C2,C3}$ in 1^C - 8^C . Geometric parameters and spin-spin coupling constants derived from Series 1 calculations. Colors indicate C1 through C3 hydroxyl configuration as per legend.	298
Figure 7.6. Dependence of $^2J_{C1,C3}$ on Additive Subtended Bond Lengths for 1^C , 2^C and 5^C . Color scheme for data is identical to Figure 7.1.	301
Figure 7.7. Electron Occupancy in C-O σ^* NBO’s in 1^C and 2^C as a Function of C2-C1-O1-H Dihedral. Panels A and C depict data for 1^C and panels C and D contain data for 2^C . The labeling color scheme is the same as Figure 7.1. The clustering in panels A and B are indicative of the exoanomeric effect, whereas the relative	

ranges in the electron occupancy in panels C and D is indicative of the presence (panel C) or absence (panel D) of the endoanomeric effect.....303

Figure 7.8. Principal Component Analysis (PCA) of NBO Occupancies in **2C**305

Figure 7.9. Combined NBO Electron Occupancy for **1C**, **2C** and **5C** as a Function of ξ . Combined electron occupancy is the sum of the individual occupancies for the $\sigma_{C1,C2}$, $\sigma_{C2,C3}$, $\sigma_{C1,C2}^*$ and $\sigma_{C2,C3}^*$ NBOs. Coloring scheme is identical to that in Figure 7.1. Dihedral ξ defined in text.307

Figure 7.10. Normalized Plots of $^2J_{C1,C3}$ vs. Sums of Selected NBO Occupancies in **2C**. The conformational color scheme is identical to Figure 1. (A) The $s_{C1,C2}$, $s_{C2,C3}$, $s_{C1,C2}^*$ and $s_{C2,C3}^*$ NBO occupancies were summed for a given conformer. The grey dotted lines indicate geometrically related conformers. (B) The s and s* NBO occupancies for the C1-O5, C1-C2, C2-C3, C3-C4, C1-H1, C3-H3 bonds were summed along with $s_{C2,H2}$ for the 27 conformers of **2C**. ...309

Figure 7.11. Calculated $^2J_{C2,C4}$ in **9C** as a function of the H3-C3-O3-H dihedral. Color scheme is analogous to that found in Fig. 7.1, except shifted with respect to the coupling path. For example, the C1-O1 torsion in Fig. 7.1 is the C2-O2 torsion here, etc.312

Figure 7.12 Configuration Dependent Variation in the Vicinal $J(\sigma_{C,C})$. The differences in the pairwise steric exchange energy between $\sigma_{C2,C3}$ and $\sigma_{C1,O1}$ (A) and $\sigma_{C1,C2}$ and $\sigma_{C3,O3}$ (B) are significant contributors to the configuration dependent changes in the magnitude of $^2J_{C1,C3}$ between the epimeric pairs **2C** and **1C**, and **1C** and **5C** respectively. The orbitals depicted are pre-orthogonal NBOs. The bonding (σ) orbitals have three lobes with a node at each of the bonded carbon or oxygen nuclei. The coloration denotes orbital phasing and is consistent only within an individual PNBO. The schematic diagrams show the relative hydroxyl orientations obscured by the presence of orbitals.318

Figure 7.13. Configuration Dependence of $^2J_{C1,C3}$ as Mediated by Vicinal $J(\text{deloc})$. The differences in orbital interactions $\sigma_{C2,C3} \rightarrow \sigma_{C1,O1}^*$ (A) and $\sigma_{C1,C2} \rightarrow \sigma_{C3,O3}^*$ (B) are the largest contributors to the configuration dependent changes in the magnitude of $^2J_{C1,C3}$ between the epimeric pairs **2C** and **1C**, and **1C** and **5C** respectively. The bonding (σ) orbitals have three lobes with a node at each of the bonded carbon nuclei, and the antibonding (σ^*) orbitals have four lobes with a node each at the bonded carbon and oxygen nuclei, as well as a third node between them. The coloration denotes orbital phasing and is consistent only

within an individual PNBO. The schematic diagrams show the relative hydroxyl orientations obscured by the presence of orbitals.....321

Figure 7.14. O2 Lone Pair Orbitals from NBO Analysis of **2^C**. Pseudo π shaped orbital (A) and pseudo σ shaped orbital (B) on O2 are the largest contributors to the ξ conformation dependent changes in the magnitude of ${}^2J_{C1,C3}$ between the two gauche and the trans conformers in **2^C**. The dihedrals ϕ , ξ and $\zeta = 180^\circ$ for both structures depicted. The coloration denotes orbital phasing.325

Figure 7.15. The ξ Dependent Variation in the Pairwise Steric Exchange Energy Between O2lp π and $\sigma_{C1,C2}$ or $\sigma_{C2,C3}$. The overlap in the **2^C** PNBOs for O2lp π and $\sigma_{C1,C2}$ (A) or O2lp π and $\sigma_{C2,C3}$ (B) are a reflection of the angle between the bilateral plane of symmetry for O2lp π (dotted line in central scheme) and either the C1-C2 or C2-C3 bond vectors respectively. This in turn is directly related to the pairwise steric exchange energies ($E_{i,j}$) which are listed in kcal/mol. An entry of *bt* indicates that the $E_{i,j}$ was below the 0.2 kcal/mol threshold. The corresponding $\mathcal{J}^{(L)}$ contributions are listed in Hz for comparison. The bar above the E and the J indicates that the reported value is averaged over the 9 conformers of C1-O1 and C3-O3. The number in the parenthesis is the standard deviation in the last reported digit. The orbital coloration denotes phasing and is consistent only within an individual PNBO. The ϕ and ζ conformations depicted (definitions in text) all = 180° , whereas ξ conformation is consistent within a column.328

Figure 7.16. The ξ Dependent Variation in the Second Order Perturbation Energy Between O2lp π and $\sigma_{C1,C2}^*$ or $\sigma_{C2,C3}^*$ in **2^C**. The overlap in the 2C PNBOs for O2lp π and $\sigma_{C1,C2}^*$ (A) or O2lp π and $\sigma_{C2,C3}^*$ (B) vary as a function of ξ . This in turn is directly related to the 2nd-order perturbation energy ($E_{i,j}$) which are listed in kcal/mol. The corresponding $\mathcal{J}^{(deloc)}$ is listed in Hz for comparison. An entry of *bt* indicates that the $E_{i,j}$ or the $\mathcal{J}^{(deloc)}$ were below the respective 0.2 kcal/mol or 0.1 Hz thresholds. The bar above the E and the J indicates that the reported value is averaged over the 9 conformers of C1-O1 and C3-O3. The number in the parenthesis is the standard deviation in the last digit. The antibonding ($\sigma_{C,C}^*$) orbitals have four lobes with a node at each of the bonded carbon nuclei, as well as a third node between them. The ϕ and ζ conformations depicted (definitions in text) are all = 180° , whereas ξ conformation is consistent within a column.333

Figure 7.17. The Normalized Relationship Between ${}^2J_{C1,C3}$ and the Sum of Select ${}^2J_{C1,C3}^{(L)}$ and ${}^2J_{C1,C3}^{(deloc)}$. The select ${}^2J_{C1,C3}^{(L)}$ and ${}^2J_{C1,C3}^{(deloc)}$ terms summed and normalized for the 27 conformations of **2^C** (A) are $\sigma_{C1,C2}$, $\sigma_{C2,C3}$ and

$\sigma_{C1,C2}^*$, $\sigma_{C2,C3}^*$, $\sigma_{C1,O1}^*$, $\sigma_{C3,O3}^*$ respectively with the removal of $\sigma_{C1,O1}^*$ for **1C** (B) and the removal of both $\sigma_{C,O}^*$ terms for **5C** (C).....336

Figure 7.18. Calculated ${}^2J_{C1,C3}$ as a Function of ϕ , ξ and ζ with Parameterization Overlays. The ξ (H2-C2-O2-H) and ϕ (C2-C1-O1-H) dimensions are explicitly indicated while the ζ (C2-C3-O3-H) dimension is implicitly indicated by the vertical stacking of the hypersurfaces. Magenta and teal spheres indicate ${}^2J_{C1,C3}$ calculated by DFT for $\zeta = \pm 180^\circ$ and 0° respectively. Spheres have a 0.5 Hz diameter. DFT data for intermediate ζ values omitted for clarity. Solid surfaces represent best fit to the DFT data for $z = \pm 180^\circ$ (indigo), $\pm 150^\circ$ (blue), $\pm 120^\circ$ (green), $\pm 90^\circ$ (yellow), $\pm 60^\circ$ (orange), $\pm 30^\circ$ (fuchsia) and 0° (red).....341

Figure 7.19. Isosurface of ${}^2J_{C1,C3}$ in the ϕ , ξ and ζ conformational space. Grey spheres are combinations of ϕ , ξ and ζ (definitions in text) that lead to a ${}^2J_{C1,C3}$ of 4.6 Hz as determined by DFT. The spheres have a 15° radius and are digitized every 5° in the ϕ and ξ dimensions and every 30° in the ζ dimension.....348

Figure 7.20. The Effect of μ , σ and w on Population Distribution. The parameter μ controls the location of the peak maximum across the rotational itinerary whereas σ dictates the peak width (A). The parameter w dictates the fractional weighting of a peak with respect to others about the same rotational itinerary (B). The two curves in (B) bound areas of different size whereas the two curves in (A) have the same area.351

Figure 7.21. Population Histograms for Conformational Models about the Dihedrals ϕ , ξ and ζ in **9C**. The dihedrals for ϕ (A), ξ (B) and ζ (C) are shown in degrees whereas population is shown in arbitrary units. The raw data for the three simulations is shown rather than the best fit gaussian models for the simulations represented in Tables 7.10 and 7.11. The bin size for the three simulation histograms was every 1° . The definitions for models **I**, **II** and **III** are given in the text.....364

Figure 7.22. Bond Length, Relative Energy, and Dipole Hypersurfaces as a Function of ϕ , ξ and ζ for the *ccw* and *cw* H-bonding Conformers in **9C**. The dihedrals ϕ and ξ are measured in degrees. The global dipole is represented as the non-directional scalar quantity. Putative *ccw* and *cw* H-bonding geometries are depicted for the **II** and **III** models and are indicated on the various hypersurfaces by open squares and circles respectively. The 0 kcal/mol global relative energy minimum used as a reference for panels C and G occurred in a slice through the ζ dimension not shown. The hydroxymethyl group, the O4 hydroxyl and all non-hydroxyl protons

are omitted from the molecular models for clarity, except for H2 which was retained as a reference.....377

Figure 7.23. Radial Population Density Histograms about ϕ , ξ and ζ for **II** and **III** with Correlated Rotameric Transition Paths for the *ccw* and *cw* H-bonding Networks. Polar coordinates defined with arbitrary radial population units and a polar angle corresponding to the ϕ (A), ξ (B) or ζ (C) dihedrals measured in degrees. The annulus containing the nested Newman projections represents zero population. Black solid line represents model **II** and the grey line represents model **III**. Rotameric transition paths for the interconversion between *ccw* and *cw* conformers of **II** (D) and **III** (E) assume transitions proceed through adjacent rotameric regimes. Half arrows indicate transitional continuity about the entire rotational itinerary. The value for μ_ϕ used in the **III**_{*ccw*} model (E) is the weighted average of the μ_{ϕ_1} and μ_{ϕ_2} peaks from Table 7.11.....386

Figure 7.24. The Goodness of Fit Error for ${}^2J_{C1,C3}$ in **9C** as a Function of Dihedral. The definitions for the x and y values in panels B-D are found in panel A, where θ represents one of the dihedrals ζ , ϕ or ξ respectively. Data in panels B-D are color coded by virtue of the respective ζ_{DFT} , ϕ_{DFT} or ξ_{DFT} angles used to calculate $\Delta_{DFT-Fit}{}^2J_{C1,C3}$. The percentage of the 1728 DFT data points whose coupling magnitude was outside the range of the parameterization thereby precluding the calculation of $\theta_{\pm error}$ is indicated in parenthesis beside the panel label. Definitions for ζ , ϕ and ξ are found in the text.395

Figure 8.1. Atomic Numbering for **I_E**417

Figure 8.2. Northern Hemispheric Stereographical Projection of Pyranose Pseudorotational Itinerary with Ring Puckering Coordinates for I-V. ³Ring at the non-reducing end of the disaccharide **II** is *glucopyranose* instead of *galactopyranose*. The ring puckering parameters φ and θ are represented by angular and radial displacements about the ⁴*C*₁ origin (center point) respectively. The displacements for all crystal data in the main figure are based upon individual total puckering amplitudes, Q , while displacements in the inset are based upon an average amplitude for the depicted data ($Q_{avg} = 0.5734$). The inner and outer black circumferential rings represent the minimal and maximal Q values for the total data set, while the colored rings correspond to the Q values for the galacto and gluco rings of **I_E** and424

TABLES

Table 3.1. ^1H - ^1H Spin-Coupling Constants ^a in 2 at p ² H 2.0 and pH 8.0.	79
Table 3.2 Calculated ^1H - ^1H Spin-Coupling Constants ^a in 7-10	80
Table 3.3. ^{13}C - ^1H Spin-Coupling Constants in 2 at p ² H 2.0 and pH 8.0.	82
Table 3.4. Calculated ^{13}C - ^1H Spin-Coupling Constants in 7-10	83
Table 3.5. ^{13}C - ^{13}C Spin-Coupling Constants ^a in 2 at p ² H 2.0 and pH 8.0.....	88
Table 3.6. Calculated ^{13}C - ^{13}C Spin-Coupling Constants ^a in 7-10	91
Table 3.7. J_{CC} Values in 3-Deoxy- β -D-Fructopyranose 11 and β -D- Fructopyranose 12	96
Table 3.8. Effect of Solvent on Calculated Spin-Couplings.....	97
Table 3.9. ^1H Chemical Shifts ^a of 2 at p ² H 2.0 and pH 8.0.	104
Table 3.10. ^{13}C Chemical Shifts ^a of 2 at p ² H 2.0 and pH 8.0.....	104
Table 4.1. Torsion Angles, ω and θ , Calculated $^2J_{\text{CH}}$ Values.....	126
Table 4.2. Experimental J -Couplings in C-Labeled 4,6- <i>O</i> -Ethylidene- α and β -D-Gluco- (8) and Galactopyranoses (9) and Comparison with Calculated Couplings	145
Table 4.3. Averaged Calculated J -Couplings in Hydroxymethyl Group Fragments for Staggered Rotamers about ω and θ ^a	147

Table 4.4. Experimental ^1H - ^1H Spin-Spin Coupling Constants in 1-4	149
Table 4.5. Experimental ^{13}C - ^1H Spin-Spin Coupling Constant ^a in 1-4	150
Table 4.6. Experimental ^{13}C - ^{13}C Spin-Spin Coupling Constants in 1-4	153
Table 4.7. Summary of ω and θ Rotamer Populations Determined by Single ω Analysis and Correlated ω/θ Analysis ^a in 1-4	155
Table 4.8. Summary of θ Rotamer Populations in Different ω Rotamers in 1-4	161
Table 4.9. (S1) Calculated Scalar couplings in 6 and 7	169
Table 4.10. (S2) Torsions, ω and θ , Calculated $^3J_{\text{CH}}$ Values in 5	170
Table 4.11. (S3) Torsion Angles, ω and θ , and Calculated $^1J_{\text{CC}}$ and $^2J_{\text{CC}}$ Values in 5	171
Table 4.12. (S4) Populations of ω Rotamers in 1 : Analysis of $^3J_{\text{H5,H6R/S}}$, $^3J_{\text{C4,H6R/S}}$, $^2J_{\text{C4,C6}}$ and/or $^2J_{\text{C6,H5}}$	172
Table 4.13. (S5) Populations of ω Rotamers in 2 from an Analysis of $^3J_{\text{H5,H6R/S}}$, $^3J_{\text{C4,H6R/S}}$, $^2J_{\text{C4,C6}}$ and/or $^2J_{\text{C6,H5}}$	173
Table 4.14. (S6) Populations of ω Rotamers in 3 from an Analysis of $^3J_{\text{H5,H6R/S}}$, $^3J_{\text{C4,H6R/S}}$, $^2J_{\text{C4,C6}}$ and/or $^2J_{\text{C6,H5}}$	174
Table 4.15. (S7) Populations of ω Rotamers in 4 from an Analysis of $^3J_{\text{H5,H6R/S}}$, $^3J_{\text{C4,H6R/S}}$, $^2J_{\text{C4,C6}}$ and/or $^2J_{\text{C6,H5}}$	175
Table 4.16. (S8) Multilinear Fit of Experimental Couplings in α -D-Glc (1) to Assess ω and θ Rotamer Populations	176
Table 4.17. (S9) Multilinear Fit of Experimental Couplings in β -D-Glc (2) to Assess ω and θ Rotamer Populations	177

Table 4.18. (S10) Multilinear fit of Experimental Couplings in α -D-Gal (3) to Assess ω and θ Rotamer Populations	178
Table 4.19. (S11) Multilinear Fit of Experimental Couplings in α -D-Gal (4) to Assess ω and θ Rotamer Populations	179
Table 5.1. Coefficients in Parameterized Equations for ${}^2J_{C1,H2}$ and ${}^2J_{C2,H1}$ in 1 , 2 , and 5-8 , and χ^2 and RMS Values Derived from the Fit.....	215
Table 6.1. ${}^{13}C$ - ${}^{13}C$ Spin-Couplings in Selectively ${}^{13}C$ -Labeled D-Gluco- (1α , 1β) and D-Mannopyranoses (2α , 2β) and Methyl β -D-Allopyranoside 3¹	236
Table 6.2. ${}^{13}C$ - ${}^{13}C$ Spin-Couplings Involving C2 of Aldohexopyranoses and Alkyl Aldohexopyranosides.....	238
Table 6.3. Computed ${}^2J_{CC}$ Values in Model Aldopyranosides and Comparison with Experimental Couplings.....	239
Table 6.4. ${}^{13}C$ - ${}^{13}C$ Spin-Couplings Involving C3 of Aldohexopyranoses and Methyl Aldohexopyranosides.....	245
Table 6.5. Computed ${}^3J_{CC}$ and ${}^{3+3}J_{CC}$ in Model Aldohexopyranosides and Comparison with Experimental Couplings.....	247
Table 6.6. (S1) Fermi Contact and Non-Fermi Contact Contributions to Total Calculated J_{CC} Values in 11^C	267
Table 6.7. (S2) Calculated J_{CC} values in 6^C in the 4C_1 conformation.....	268
Table 7.1. Comparison of Experimental ${}^2J_{C1,C3}$ Values in Hz for Selectively ${}^{13}C$ -Labeled Hexo-Pyranoses with Theory as a Function of Coupled Site Configuration.....	276
Table 7.2. Theoretical ${}^2J_{C1,C3}$ Values ^a as a Function of C2-O2 Rotamer Conformation Averaged Across All Staggered C1-O1 and C3-O3 Rotamer Conformations....	288

Table 7.3. Comparison between Calculated ${}^2J_{C1,C3}$ in 11C , 12C and 14C as a function of C2-C1-O1-H and C2-C3-O3-H dihedral.	292
Table 7.4. Statistical Comparison ^a between Calculated ${}^2J_{C1,C3}$ in 2C and ${}^2J_{C2,C4}$ in 9C	313
Table 7.5. Configuration dependence ^a of $J(L)$ in 2C , 1C and 5C	316
Table 7.6. Configuration dependence ^a of $J(\text{deloc})$ in 2C , 1C and 5C	320
Table 7.7. Comparison of the Difference Between Averaged H2-C2-O2-H <i>trans</i> and <i>gauche</i> $J(L)$ and $J(\text{deloc})$ with DFT Total ${}^2J_{C1,C3}$ as a Function of Coupled Site Configuration ^a	326
Table 7.8. ξ Conformational Dependence of O2 lp $\rightarrow\sigma_j^*$ as a Function of Coupled Site Configuration ^a	332
Table 7.9. Generalized Spin-Spin Coupling Equation ^a and Coefficients ^b for the Parameterization of Couplings Sensitive to C1 Through C3 Hydroxyl Orientation.	343
Table 7.10. Spin-spin Coupling Constant Comparisons between Experiment and Various Conformational Models.	362
Table 7.11. Conformational Model Parameters for ϕ , ξ and ζ in 9C	363
Table 8.1. Geometric Parameters for I_E and I_C (Å, °) with select comparisons to II-V.	419
Table 8.2. Hydrogen-bond geometry (Å, °) in Crystalline I_E	422
Table 8.3. Cremer-Pople Pyranose Ring Puckering Parameters ²⁵ for I-V.	426

SCHEMES

Scheme 1.1. Fisher Projectons of Common Aldoses and Ketoses.....	4
Scheme 1.2. Ring Interconversion of α -D-Altropyranose	5
Scheme 1.3. Rotameric Definitions of Hydroxymethyl Dihedral ω	8
Scheme 1.4 Conceptual Map of Spin Coupling Based Conformational Analysis.....	13
Scheme 2.1 Anomerization o <i>N</i> -acetylneuraminic acid (1) and abundances of forms in aqueous solution at pH 2.0.	28
Scheme 2.2 Enol forms of 1	40
Scheme 2.3 $^nJ_{CH}$ values in 3 and 4	42
Scheme 2.4 Structure of <i>cis</i> (5) and <i>trans</i> (6) enol model compounds.	44
Scheme 2.5 Potential lactones of 1 (keto, keto hydrate, and enol forms).	52
Scheme 2.6 (S1) Projections for $^2J_{C2,H3ax}$ and $^2J_{C2,H3eq}$ in 1h conformers and predicted couplings.	54
Scheme 3.1. α -(2 \rightarrow 3) and α -(2 \rightarrow 6) Glycosidic Linkages Involving 2 , and Trans-Glycoside <i>J</i> -Couplings Across an α -(2 \rightarrow 3) Linkage.	68
Scheme 3.2. ^{13}C Isotopomers if 2 and Atomic Numbering.....	70

Scheme 3.3. Projections for $^3J_{C1,H3ax}$ and $^3J_{C1,H3eq}$ in 2 α and 2 β	81
Scheme 3.4. Hyperconjugative effects on $r_{C1,C2}$ and $^1J_{C1,C2}$ in the ionized form of 2 αp	90
Scheme 3.5. (S1) Monomeric forms of 2 and their abundances in aqueous solution at pH 2. (R= -CHOH-CHOH-CH ₂ OH).	101
Scheme 3.6. (S2) Initial geometries of 7-10 used in DFT calculations of J -couplings in 2 . All ring conformations are 1C_4 ; see text for the initial values of the exocyclic torsions.	102
Scheme 3.7. (S3) Deuterium exchange of C3 protons of 2 in mild aqueous base.	102
Scheme 3.8. (S4) Preferred C1-C2 Bond Conformations in the protonated and ionized forms of 2 αp and 2 βp	103
Scheme 3.9. (S5) Projections for $^2J_{C2,H3ax}$ and $^2J_{C2,H3eq}$ in 2 αp and 2 βp	103
Scheme 4.1. Part of the Core Structure of Glycoprotein <i>N</i> -Glycans, showing 1,3- and 1,6-Linkages and the ψ / ϕ Redundancy in the Latter	111
Scheme 4.2. The Synthesis of D-[4- ¹³ C]Glucose.	116
Scheme 4.3. Idealized Staggered Rotamers (ω) about the C5-C6 Bond of Aldohexopyranosyl Rings.	119
Scheme 4.4. Idealized Staggered Rotamers (θ) about the C6-O6 Bond of Aldohexopyranosyl Rings.	123
Scheme 4.5. θ Rotamers that Make a Positive Contribution to $^2J_{C5,H6R}$ (A), $^2J_{C5,H6S}$ (B), and $^2J_{H6R,H6S}$ (C) ^a	127
Scheme 4.6. C4 Configuration Dependence of $^2J_{C6,H5}$	128
Scheme 5.1. Rotamer Definitions	191
Scheme 5.2. Model Compound Structures 1-8	192

Scheme 5.3. Experimental $^2J_{C1,H2}$ and $^2J_{C2,H1}$ in 9-14	202
Scheme 5.4. Lone-pair effects on r_{CH}	209
Scheme 6.1. Representative $^1J_{CC}$, $^2J_{CC}$, $^3J_{CC}$ and $^{3+3}J_{CC}$ in methyl β -D-glucopyranoside. Coupling pathways are highlighted in red and blue.	229
Scheme 6.2. Application of the Projection Resultant (PR) Method to $^2J_{C4,C6}$ in D-Aldohexopyranosyl Rings (4C_1)	240
Scheme 6.3. Projections for $^2J_{C4,C6}$ in D-Aldohexopyranosyl Rings (1C_4)	241
Scheme 6.4. Application of the Projection Resultant (PR) Method to $^2J_{C3,C5}$ in D-Glucopyranosyl Rings.....	243
Scheme 6.5. Application of the Projection Resultant (PR) Method to $^2J_{C3,C5}$ in Other D-Aldohexopyranosyl Rings	244
Scheme 6.6. Projections About the C1-O1 Bond in a β -(1 \rightarrow 4) Glycosidic Linkage Showing the Two Arrangements that Orient C2 and C4' Gauche	252
Scheme 6.7. C-C and C-O Bond Lengths (Å) in 11C	255
Scheme 6.8. Summary of $^2J_{CC}$ behaviour in Aldopyranosyl Rings. Coupling pathways and direct substituent effects are shown in blue, and remote substituent effects are shown in red.	257
Scheme 6.9. Summary of $^3J_{CC}$ behaviour in Aldopyranosyl Rings. Coupling pathways and direct substituent effects are shown in blue and pink, and remote substituent effects are shown in red.....	258
Scheme 6.10. (S1) DFT-Optimized Structures (B3LYP/6-31G*) – FIXED Series	261
Scheme 6.11. (S2) DFT-Optimized Structures (B3LYP/6-31G*) – FLOAT Series	262
Scheme 6.12. (S3) Projections for $^2J_{C4,C6}$ in D-alдохexopyranosyl rings (1C_4)	262

Scheme 6.13. (S4) Application of the projection resultant (PR) method to $^2J_{C3,C5}$ in glucopyranosyl rings.	263
Scheme 6.14. (S5) Application of the projection resultant (PR) method to $^2J_{C3,C5}$ in other aldohexopyranosyl rings.	263
Scheme 6.15. (S5) Structures of 6C (4C_1) FIXED and FLOAT	268
Scheme 7.1. Structures for model compounds 1C-18C (A) and experimental compounds 1E-7E , 11E-17E , and LE (B)	279
Scheme 7.2. Rotameric Definitions of the Dihedrals ζ , ξ and ϕ	285
Scheme 7.3. Explanation of $^2J_{C1,C3}$ Karplus Profile Shape Based on O2lp π Disposition	330
Scheme 7.4. Orbital Interpretations of Models II and III	379
Scheme 8.1. Coupling Reaction for the Synthesis of IE	428
Scheme 9.1. Complex <i>N</i> -Glycan.....	444
Scheme 9.2. Structure of <i>Campylobacter jejuni</i> Serotype O:19 Antigenic Lipopolysaccharide OH 4384-C1 and Related Human Neolacto Series Gangliosides. Residues in blue are structurally related portions of the antigenic terminus of the OH 4384-C1 LPS. Select abbreviations: LDHep, L- <i>glycero</i> -D- <i>manno</i> -heptose; PEA, <i>O</i> -phosphoethanolamine; KDO, 3-deoxy-D- <i>manno</i> -octulosonic acid.	445

PREFACE

“And while I stood there I saw more than I can tell and I understood more than I saw; for I was seeing in a sacred manner the shapes of all things in the spirit, and the shape of all shapes as they must live together like one being.”

– Black Elk

“Five senses cannot sense the fact of our existence.

And that’s the only fact. In fact, there are no facts.”

– Saul Williams: Gaia Child

"One had to cram all this stuff into one's mind for the examinations, whether one liked it or not. This coercion had such a deterring effect on me that, after I had passed the final examination, I found the consideration of any scientific problems distasteful to me for an entire year."

– Albert Einstein

When I first came to study at Notre Dame in May of 2000, it was a exciting experience. I had left my graduate studies at the University of Virginia two years previously. I had completed my coursework in immunology and begun to conduct research in a lab that studied atopic dermatitis, a skin disorder that I have had since childhood. I did not gel well with the structure of the program in Virginia and chose to leave to pursue my artistic endeavors, however after two years of this I realized how

much I missed science. When I arrived at Notre Dame, I found a much more integrated academic community, at least in proximity if not in practice. I realized that it was the sequestration of science from considerations of philosophy and the humanities that I abhorred in Virginia.

Through my artistic explorations I had begun to crystallize the content of my aspirations. Simply and perhaps naïvely I wanted to understand the fiber of experience. Experience involves interaction, verbal, visual or otherwise. The scientific part of my mind translated this as a question: ‘*What is the biological origin of language?*’ A friend of mine, Vincent Harris, whose struggle with ALS had originally contributed to my decision to attend graduate school, had been studying linguistics before his death. I began to read the writings of Ferdinand de Saussure. These helped me formulate a concept of language in its simplest elements. Language requires an entity isolated from its surroundings. This isolation requires a boundary capable of transmitting the state of the external system to the interior of the entity in a manner that internally represents the external condition. The entity must be capable of processing this information and responding in an appropriate manner. This concept seemed abstract enough to be transferable across the many size scales of biology such that it applied equally well to the complex verbal discourse of humans or to equally complex interactions between seemingly simple single cellular prokaryotes. Language requires meaningful boundaries.

The problem that I ran into was the chicken and the egg of informational content and awareness. The pieces of art that I was making at the time were all small light boxes, constructions that you could look into through tiny peepholes to see a lit diorama of the found world in miniature. They often had external handles or knobs with which you

could manipulate the contents. I had been making such constructions since my childhood. The pieces of art were my unconscious attempt at creating responsive organisms. Despite the increasing sophistication of these constructions, I hardly considered them conscious organisms, capable of experience. I came to conclude that consciousness preceded informational content and meaning. So my question became: '*What is the biological origin of consciousness?*' I needed to define some terms. What was meant by consciousness?

Through conversations with my father, who was trained as a neurologist and a neurophamologist I was led to the work of Dr. Antonio Damasio, the head of neurology at the university of Iowa. I began to separate the notions of proto- and extended consciousness; proto-consciousness being the primary feeling of being, '*...I am*', extended consciousness being this fundamental state layered with the many varied qualia of an enriched experience, '*I think, therefore...*'. Damasio talked in his book *Descartes Error* of the essential role of emotion in conscious experience; '*I emote, therefore I am.*' To me the more fundamental point, thinking or affect regardless, was that either of these was predicated upon being, however the feeling of being did not necessarily require either thinking or emotions in the manner in which ordinary human experience implies. Certainly thinking and emotion both require a temporal binding of experience – memory, however is it not conceivable that there is experience that is atemporal. The deepest levels of meditation approach this, a constant experience of strictly the present moment. As organismal consciousness emerged throughout evolution, this must be closer to actual experience.

Again my question transformed itself: *‘What is the biophysical origin of consciousness?’* Through a friend I came into contact with the work of Drs. Roger Penrose and Stuart Hameroff, a famous physicist and anesthesiologist respectively. They had been collaborating on a model for non-deterministic consciousness called orchestrated objective reduction (OrchOR). This model seeks a definition for consciousness as a property fundamental to matter and integrated into an attempt at a physical unified field theory. They argued that fundamental consciousness cannot be an emergent property of a complex system because complexity implies informational content and it is a simple argument to show that consciousness must precede information. This jived with my own intuition on the matter. Their model identifies the non-temporal collapse of the wave equation as the fundamental event of consciousness. The extended consciousness experienced by higher organisms such as humans results from the orchestrated collapse of the single wave function governing an ensemble of macromolecular assemblies in quantum coherence. They were exploring the neuronal microtubule lattice as being the cellular structure responsible for this quantum process. The arguments as presented are persuasive however the concept is in its infancy. One of the problems that this theory has is the seeming trouble with quantum decoherence at the temperatures of life. A second is how does this quantum coherence extend across macroscopic tissue tracks in the brain. Perhaps the most significant weakness is the absolute lack of experimental techniques for testing any of the theories.

My consideration of cellular ‘language’ and how it might be mediated by the interfacial phenomena at the membrane in neurons, led me to a consideration of the behaviour of glycolipids. I imagined the individual glycolipids in the ganglioside

microdomains that decorate the surface of neurons as moving in a coordinated manner under the influence of interstitial flow as if they were a field of wheat swaying in waves under a strong wind. In fact carbohydrates could be found at all interfacial boundaries in living systems. They preceded life, are ubiquitous within and across organisms, intimately interact with the aqueous milieu and are the most conformationally mobile biopolymer. Could carbohydrates be in some manner facilitating conscious processes through their interactions with other biomolecules, the solvent, and each other? I became interested in the function of carbohydrates. However, as I describe in the conclusion, ‘...*form ever follows function.*’ An understanding of function requires a commensurate understanding of structure. For carbohydrates this requires knowledge of their conformational profiles as a function of time. From my undergraduate research with the NMR of triazoles, I was familiar with the power of magnetic resonance to offer important information on the structure and dynamics of small molecules. In my naïveté I imagined that I might be able to remedy the lack of empirical tools for the study of conscious processes on the biomolecular level while breaking ground by elucidating an occult function of saccharides. Thus began my time at Notre Dame with Dr. Serianni studying the conformational behaviour of simple mono- and disaccharides with NMR.

Now, eight years later I have been humbled. I do not eschew my beliefs or intuitions from before, quite the contrary, I just have a much more realistic perspective on what constitutes careful and achievable research goals. Above I mentioned that language requires meaningful boundaries. During my graduate studies I have navigated many boundaries, found them meaningful, and learned to communicate. In the process I have become a scientist.

ACKNOWLEDGMENTS

“True dignity is a grace of the spirit that transcends all limitations of age and race and birth and opportunity; it is bestowed, as it were, out of the universal loving kindness of God as a visible token of that noble order of beings who, respecting themselves and reverencing the unknown, have achieved maturity within themselves.”

– Rockwell Kent

I would like to acknowledge the patience and support of my mentor and advisor, Dr. Anthony S. Serianni, without whose constant guidance I would have been utterly lost. He has served as the highest example of scientific research integrity throughout the many years that I have known him. His faith in my potential was a leap that I hope was rewarded. I count myself lucky to have worked with him. Sincerely, thank you.

I also extend the deepest gratitude to Dr. Ian Carmichael of the Notre Dame Radiation Lab for his jovial patience, impressive scientific understanding, and at times miraculous problem solving skills. I have considered him as a co-advisor and friend throughout my time at Notre Dame.

I wish to thank all of my fellow lab mates that have shared space with my at times capacious personality. I know it wasn't always easy. In particular I want to thank Dr. Qinfeng Pan for his humor, knowledge and kindness, Xiaosong Hu for his patience, forgiveness and generosity, Wenhui Zhang for his wit, helpfulness and pleasant

demeanor, Hongqiu Zhao for his total cooperation, inspirational and unflagging smile, Peter Nizner, *moj slovenski brat*, for his moral support and humorous commiserations, and Dr. Christophe Thibadeau for his tutelage, technical expertise and occasional donuts.

I am deeply indebted to the entire staff at Omicron Biochemicals for their formidable synthetic capability and generosity. Much more than half of the chemicals discussed in this dissertation started there. I owe a particular acknowledgement to Meredith Reed and Gail Bondo for their significant contributions to the work presented herein.

I thank the members of my graduate committee, Drs. Tom Nowak, Olaf Weist and Holly Goodson for their meaningful insights on matters scientific and otherwise, patience and support. I apologize to Dr. Goodson for forcing her to endure so much technical material in a field so divergent from her own, but my interest in her own work was too much for me to resist involving her in my committee and for her fortitude I am greatly appreciative.

I am thankful for the technical support that I received from Drs. Jaroslav Zajicek and Igor Veretennikov in the NMR facility and from Dr. Bruce Noll in the crystallography division. I am also indebted to Dr. John Brady and his lab for hosting me at Cornell University in the summer of 2003.

During my first two years at Notre Dame I took the medical school sequence at the South Bend Center for Medical Education. The following two years I was privileged to be a teaching assistant in the anatomy lab there. For the gift of this experience I wish to thank Drs. John F. O'Malley, Robert E. Kingsley and David A. Halperin. Those were perhaps the most enjoyable classroom experiences of my life.

While it was the love of science that enabled me to get up in the morning, it was the love of my family and friends that allowed me to sleep at night. I thank my family for the depth of their patience, the endurance of their support and the kindness of their love. In particular I wish to thank my father, Dr. Garron L. Klepach ('63), for his spiritual guidance, stimulating conversation and personal example that helped me gain focus and become a better person. πατερ αμων, ο εν το ουρανω...

I am blessed with many truly wonderful friends who each enrich my life in unique ways. Although they each deserve recognition I cannot begin to list them all here. I trust that each knows how much I appreciate them individually. I do however wish to particularly acknowledge the love, support and patience of Dr. Denise Bruesewitz. She has been an inspiration and a blessing.

Finally I thank you who are reading this. You must have a significant purpose driving you to wade through this tome of numbers and figures. It is that purpose, whatever it may be, which rewards my efforts.

CHAPTER 1: INTRODUCTION

*“These high wild hills and rough uneven ways
Draw out our miles and make them wearisome;
But yet your fair discourse hath been as sugar,
Making the hard way sweet and delectable.”*

– William Shakespeare

“It is important to eat some carbohydrates at breakfast, because the brain needs fuel right away, and carbohydrates are the best source.”

– Andrew Weil

1.1. Background

1.1.1. Carbohydrate Chemistry

The prebiotic synthesis of simple carbohydrates via inorganic thermodynamic cycling anticipated life on Earth and was an important part of early geochemistry^{1a}. These ancient organic molecules were an explicit prerequisite to the development of other classes of biopolymers such as the nucleic acids. Now carbohydrates are one of the major

classes of biomolecules and represent approximately 85% of the biomass on the Earth^{1b}. Carbon fixation in the form of cellulose through the process of photosynthesis is one of the major links in the elemental carbon cycle that is so crucial to the regulation of the planetary climate¹ and essential to the sustenance of life.

Carbohydrates are able to form branched heterogeneous polymers with a potential for structural and sequence diversity that far surpasses similarly long polymers of either nucleic acids or peptides. A variety of factors influence this including the large number biologically significant monomers. Biologically, this structural diversity is further expanded by modifications such as amination, *N*-acetylation, phosphorylation, oxidation or deoxygenation. Other equally important factors are the extraordinary potential for linkage variety and the opportunity for highly branched polymers. Carbohydrates serve numerous commonly accepted biological functions such as energy storage, cellular structural support, and can be directly involved in biomolecular binding events. Glycosylation can act as a biomolecular switch to affect protein function.^{1c} Additionally, it has been suggested that an occult function of saccharides is to dynamically perturb solvent layers around glycoconjugates or to otherwise mediate intermolecular interactions by virtue of its unique solvation properties^{2a}.

As the name implies, carbohydrates are essentially ‘hydrated carbon’ with the empirical formula $(C \cdot H_2O)_n$, chemically characterized as poly-hydroxylated aldehydes or ketones, designated aldoses or ketoses respectively (Scheme 1.1). The simplest aldose is the three-carbon glyceraldehyde, an aldotriose, whereas the simplest ketose is the three-carbon dihydroxyacetone. The standard aldose and ketose trees are built by adding a –CHOH– within the carbon backbone of the growing saccharide. The open-chain members

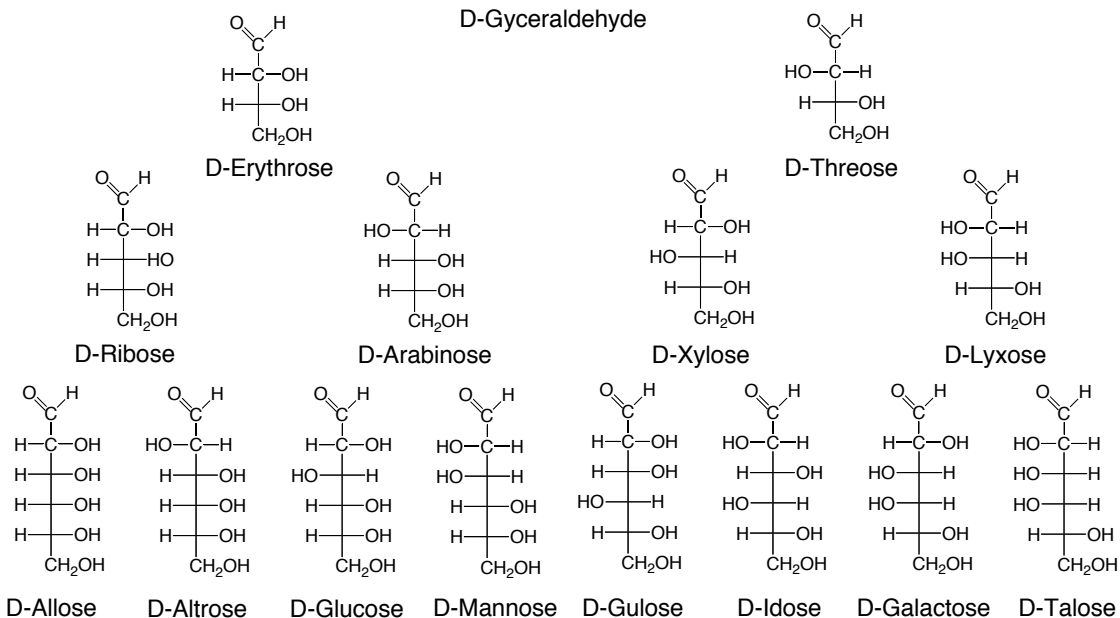
of the aldose or ketose series with the same number of carbons in the backbone are distinguished from one another by the configuration about carbons intervening between the carbonyl carbon and the terminal $-\text{CH}_2\text{OH}$ group. Carbohydrates are designated as D or L by virtue of the configuration about the penultimate carbon in the chain (Fischer convention). The vast majority of naturally occurring saccharides have the D configuration, with a few notable exceptions, such as L-fucose.

In solution the acyclic aldopentoses and aldohexoses form cyclic hemiacetals by an intramolecular acid or base catalyzed nucleophilic attack of the carbonyl carbon by a hydroxyl group. Five and six membered ring structures (furanosyl and pyranosyl respectively) are thermodynamically favored upon formation of the hemiacetal^{1d}. The configuration of the hemiacetal carbon in the ring-closed sugar is determined by which face of the planar carbonyl group is attacked by the nucleophilic hydroxyl. D-Pyranohexoses are said to have adopted the ' α ' configuration if the hydroxyl group in the hemiacetal is on the opposite side of the ring as the exocyclic hydroxymethyl group, and ' β ' when they are on the same side of the ring (this is the converse in L-sugars). Two carbohydrates are called anomers if they differ only in the configuration of the hydroxyl group at C1.

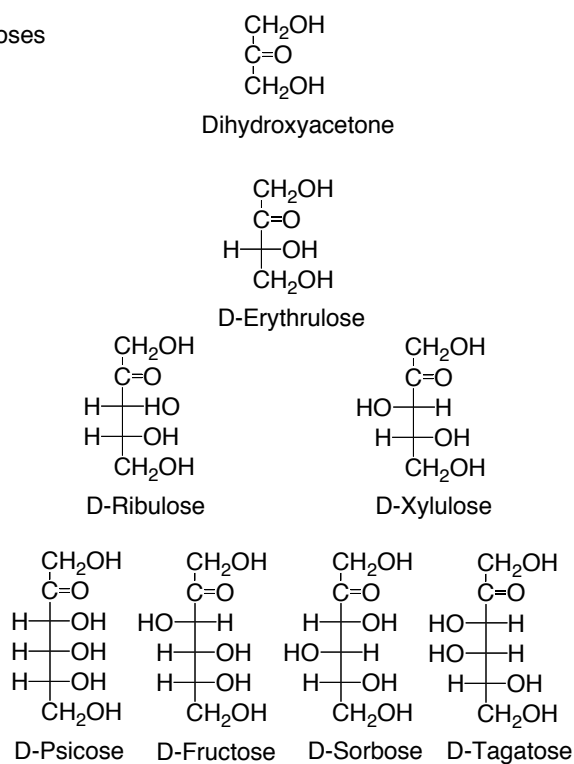
In aqueous solution there are at least six tautomeric forms of D-glucose in equilibrium with one another; four cyclic structures (α/β furanose and pyranose) and the open chain aldehyde and its hydrate. Spontaneous interconversion between the α and β anomers proceeds through the acyclic aldehyde and is termed mutarotation. A sugar is considered to be reducing if the anomeric hydroxyl is free and is able to form the reductive aldehydic or ketonic species. The 'reducing end' of a di- or oligosaccharide

$$\begin{array}{c} \text{O} & \text{H} \\ & \diagdown \quad \diagup \\ & \text{C} \\ & | \\ \text{H}-\text{C}-\text{OH} \\ & | \\ & \text{CH}_2\text{OH} \end{array}$$

D-Gyceraldehyde



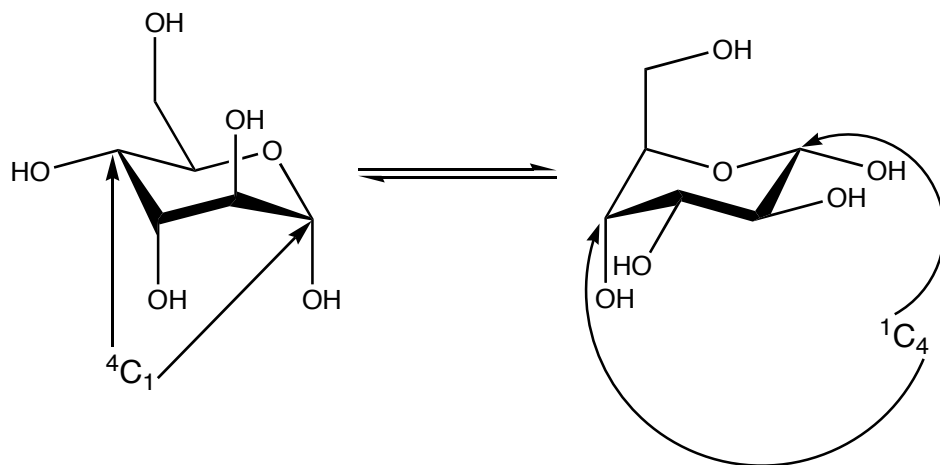
B. Ketoses



Scheme 1.1. Fisher Projectons of Common Aldoses and Ketoses

refers to the end of the glycan that has a free anomeric hydroxyl. This term is often applied to the end of a polymeric glycan that is glycosidically linked to an aglycone such as a lipid, protein or alkyl group.

The tautomeric equilibria in glucose strongly favor pyranose ring forms. There are three categories of pyranose ring conformation, the rigid chair (C) form and the more flexible boat (B) and skew (S) forms. Additionally there are intermediate ring conformations such as the envelope (E) or half chair (H). In the absence of contravening contextual forces, the C ring form is more stable than the B or S due to a variety of steric concerns. The biologically significant hexopyranoses such as glucose, mannose or galactose are typically found in the 4C_1 form, although some of the more unusual simple sugars such as the α anomers of altrose and idose exist to a high degree in the ring flipped 1C_4 conformation which allows the majority of their hydroxyl groups to adopt an equatorial orientation that minimizes a 1,3-diaxial steric clash present in the 4C_1 form (Scheme 1.2).



Scheme 1.2. Ring Interconversion of α -D-Altropyranose

In contrast to the relative stability of the 4C_1 pyranose chair, furanose rings undergo facile interconversion between twenty-one distinct idealized ring conformers. These break up into three categories, the planar ring geometry, and two types of non-planar forms, the envelope (E) which has four coplanar ring members (the fifth situated either above or below the ring), or the twist (T) which has three coplanar ring members (the two remaining nuclei are situated on opposing faces of the ring). Interconversion between these numerous energetically similar idealized ring forms is referred to as pseudorotation, and leads to numerous non-idealized geometries. The studies contained in this dissertation are primarily limited to saccharides with the pyranose ring form with an additional discussion of the acyclic tautomers of sialic acid in chapter 2. For this reason further discussion of furanosyl ring forms will be limited.

A clear understanding of the various functions of carbohydrates requires a detailed understanding of their structure. Static structures alone are not a sufficient description of the time-averaged fluctuations in carbohydrate conformation. There is significant torsional sampling about the C-O bonds of hydroxyl groups and glycosides, as well sampling about the C-C bonds of exocyclic groups. Saccharides can be viewed as residue specific scaffolds for spatial and temporal lone pair distribution and reorientation. Stereoelectronic, electrostatic, and steric factors govern configurational stabilities and conformational preferences. The most well known of these factors is called the anomeric effect that manifests as either the *endo*-^{2b,4} or *exo*-anomeric^{3,4} effect. Other effects include the equatorial versus axial substituent preference, exocyclic conformation and the gauche effect.⁵⁻⁷

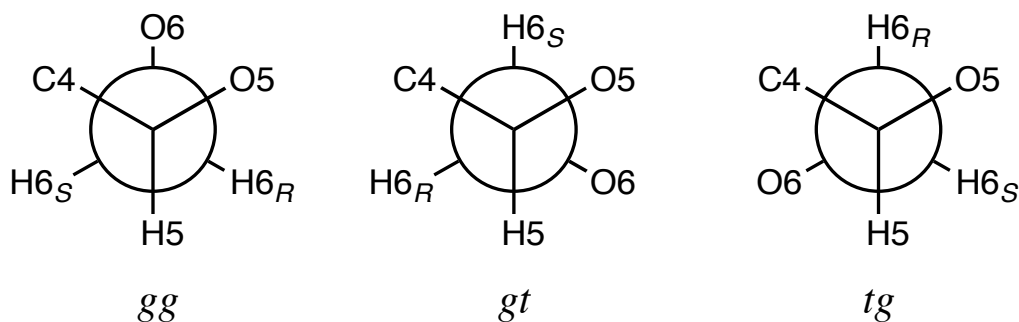
The anomeric effect, later termed the *endo*-anomeric effect in contrast to the *exo*-anomeric effect, was first described by Lemieux and Chü in 1958 as the proclivity of electronegative substituents at C1 of D-glucose to adopt the axial or α orientation over the equatorial β disposition counterintuitive to other steric considerations⁸⁻⁹. This generalized effect is directly correlated to the electronegative strength of the anomeric substituent. There have been a number of rationalizations of this phenomenon such as an electrostatic dipole-dipole interaction between the C1-O5 and C1-O1 bond vectors. The most common interpretation of the effect is stereoelectronic in nature and describes the electron density from the trans lone pair orbital of O5 donating into the σ^* orbital of the C1-O1 bond^{4,10}.

As the stereoelectronic description of the *endo*-anomeric effect depicts the delocalization of lone pair electron density from the ring oxygen, so the *exo*-anomeric effect originates from an analogous delocalization of O1 lone pair electron density into the C1-O5 σ^* orbital. Phenomenologically this manifests as the preferential orientation of the anomeric hydroxyl proton *anti* to either C2 or H1 in β -D-glucose, with C2-C1-O1-H $\approx 180^\circ$ being the most favored conformation. Lemieux and coworkers¹¹ have argued that the *endo*-anomeric effect is more strongly manifest in equatorial anomeric hydroxyls than axial due to a lack of competition in the equatorial configuration from the O5 *endo*-anomeric effect for delocalization into the electron deficient aldehydic C1, although this notion has been challenged based upon arguments related to the orthogonality of the orbitals involved¹².

There is a sterically driven tendency to maximize the number of equatorial and minimize the number of axial substituents in a pyranose ring structure. A bulky axial substituent such as a hydroxyl or hydroxymethyl encounters steric clashes with other

axial ring components through 1,3 diaxial interactions. The minimization of these steric interactions determines the equilibrium between 4C_1 and 1C_4 ring conformations. This propensity towards ring conformations that maximize the number of equatorial substituents is enhanced by the phenomenon called the *gauche* effect. This effect describes the preferential stability of the *gauche* conformation over the *anti* in R-C-C-R' *sp*³ hybridized fragments where R and R' are electronegative substituents. In 1978 Baranenkov and coworkers demonstrated using Perturbational MO theory that this phenomenon could not be explained by invoking either steric or electrostatic arguments alone, and must involve an additional stereoelectronic component⁶.

In addition to the conformational averaging of C-O rotamers, a further degree of conformational freedom in hexopyranoaldoses is in the orientation of the exocyclic hydroxymethyl group. Scheme 1.3 depicts the three idealized staggered rotamers about the C-C bond of the hydroxymethyl group. Each of the three rotamers is named by a two letter descriptor. For example in the *gt* conformation O6 is oriented *gauche* to the ring oxygen O5 and *trans* to the vicinal carbon C4. The sampling about C5-C6 is dictated by steric interactions with O4 and through the presence of the stereoelectronic *gauche* effect between O6 and O5.



Scheme 1.3. Rotameric Definitions of Hydroxymethyl Dihedral ω

Determinants of monosaccharide structure are no less important within the context of an oligosaccharide. Carbohydrate polymers are formed through a condensation reaction between the hemiacetal hydroxyl of a reducing sugar and any other hydroxyl group from a second sugar moiety. This reaction is usually acid catalyzed and results in the release of a single water molecule per glycosidic linkage formed. The geometry of a glycosidic linkage is described by the two dihedrals, ϕ and ψ . A dihedral is defined as the minimal angle between two intersecting planes and is uniquely described by four sequentially bonded nuclei, although a dihedral can be non-uniquely referred to as a rotation about the central two atoms. For example, in all glycosidic linkages the dihedral ϕ describes the torsion about the two central atoms, the anomeric carbon and the linkage oxygen, with the actual measurement describing the dihedral angle between the attachment point carbon of the reducing end sugar and, depending upon the convention used, one of the other three nuclei bound to the anomeric carbon. The glycosidic dihedral ψ describes the angle between the anomeric carbon and one of the three nuclei three bonds away from the anomeric carbon across the linkage. The choice of which of the three nuclei is the reference is again dependent upon the convention adopted. When the glycosidic linkage involves the primary alcohol of the exocyclic hydroxyl methyl group, the additional degree of conformational mobility about the C5-C6 torsion can also affect global structure and the conformational preferences of the two glycosidic torsions. This dihedral is typically designated ω , and is most often defined as the angle between the linkage oxygen and the ring oxygen of the reducing end sugar.

The relatively free rotation about these dihedrals gives rise to a considerable degree of structural flexibility in the typical oligosaccharide. Because of this, a serious

account of the structure function relationships in saccharides must address the various time averaged conformational states present in solution. As a consequence of their polyhydroxylated nature, conformational reorientation in saccharides is likely to involve significant solvent redistribution in the solvation sphere¹³. Additionally, the high density of lone pair electrons throughout the glycosyl framework leads to numerous stereo-electronic and electrostatic phenomena that are only partly understood. For these reasons, a comprehensive investigation of the conformational behavior of saccharides requires the complimentary usage of diverse theoretical and experimental technologies.

1.1.2. Experimental and Theoretical Methods

Crystallography has been an indispensable tool to the protein structural biologist, however static structures, while providing important insights, offer only a small part of the information necessary for a thorough understanding of the structure-function relationships in saccharides.

The advent of high field nuclear magnetic resonance spectroscopy (NMR) has enabled significant strides in the solution state study of saccharides¹⁴⁻¹⁶. The NMR phenomenon arises from the quantum mechanical magnetic properties of nuclei with an odd number of protons and neutrons that are in an external magnetic field¹⁷. Such nuclei have an intrinsic magnetic moment and angular momentum. This magnetic moment aligns with the external magnetic field such that there is a small net polarization that can be perturbed by an orthogonally applied alternating magnetic field¹⁷. When the nuclear spins relax to their ground state, the energy that they absorbed is released at a

characteristic resonant frequency that is proportional to the external magnetic field strength.

There are numerous magnetic resonance parameters that contain structural information. The most commonly recognized of these is the chemical shift (δ). This is the specific frequency at which a particular nucleus resonates due to the unique magnetic shielding properties experienced by that nucleus within the molecular framework. The second most commonly recognized NMR parameter is the spin-spin coupling constant (nJ). This is the splitting of a resonant peak due to the slightly different magnetic shieldings experienced by the resonant nucleus as a result of having its spin either parallel or anti-parallel to another nearby spin $\frac{1}{2}$ nucleus to which it is coupled. The transfer of spin density information from one nucleus to another is mediated by the molecular orbital electronic distribution. Thus, the magnitude of this splitting is dependent upon the geometry of the intervening molecular framework¹⁷. This is the NMR parameter that I will be utilizing more than any other throughout this dissertation.

Another common NMR parameter that can yield structural information is the nuclear Overhauser effect (NOE)¹⁷. This is the through space transfer of spin polarization from one spin $\frac{1}{2}$ nucleus to another by means of cross relaxation. The magnitude of the NOE varies by a factor of $\sim 1/r^6$, ultimately limiting the reliability and usefulness of this parameter. Two other useful parameters are the longitudinal spin-lattice (R_1^X) and the transverse spin-spin (R_2^X) relaxation rate constants for nucleus X. These parameters can give a rough estimate of the relative conformational mobility that a particular nucleus is experiencing within the molecular framework.

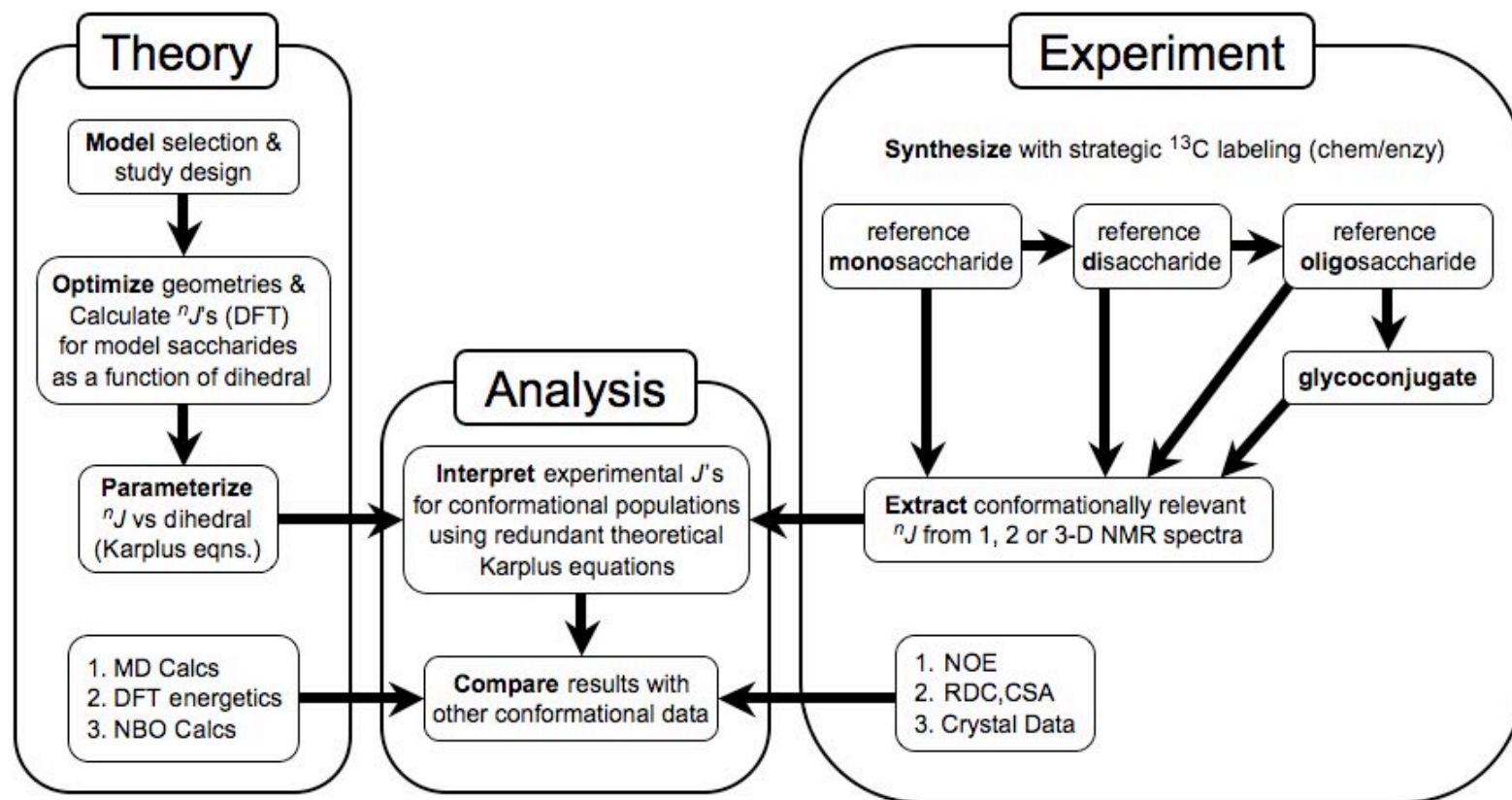
The development of sample alignment media has allowed the potential measurement of a host of other useful parameters typically averaged out by the isotropic tumbling of the molecule. These include the orientational order parameters (S_n), residual dipolar (D) and Quadripolar (χ) couplings and residual chemical shift anisotropy (ζ)¹⁷⁻¹⁸. One hurdle to the widespread use of many of these NMR techniques is the need for strategic ¹³C isotopic enrichment of sample compounds, however significant strides in the requisite synthetic technology have been made in the Serianni lab¹⁹.

The interpretation of these experimental observables in structural terms is greatly facilitated by the use of a variety of theoretical and computational techniques. There have been an extensive number of computational studies involving saccharides. These include a variety of force-field applications²⁰, quantum mechanical calculations^{13b,21} and calculation of crystalline structures^{21a,22}. Each of these techniques is of course subject to its unique set of strengths and weaknesses. In general there is a tradeoff between the accuracy of the physical representation returned by the calculation and the computational cost of the theoretical method.

1.2. Dissertation Outline

1.2.1. Conceptual Research Approach

Scheme 1.4 depicts the conceptual research flow utilized in the Serianni lab. This method incorporates synthetic, experimental and theoretical technologies into a comprehensive conformational analysis protocol for mono-, di- and oligosaccharides. Broadly speaking, my dissertation describes the expanded application and refinement of



Scheme 1.4 Conceptual Map of Spin Coupling Based Conformational Analysis

this integrated research approach, with a particular focus on the theoretical and analytic aspects.

The most common theoretical method used in my dissertation is quantum mechanical density functional theory (DFT) calculations. The calculations are conducted *ab initio* meaning that they are based upon a first principles treatment that invokes the Schrödinger equation rather than using an empirical data set as the starting point²³. The Schrödinger equation,

$$H\Psi = E\Psi, \quad (1.1)$$

describes the relationship between the electronic molecular Hamiltonian (H) and the total electronic energy (E) of the system, as satisfied by the molecular wavefunction (Ψ). Modern DFT methods were preceded by Hartree-Fock methods in which the approximate ground state wavefunction and ground state energies are determined for many-electron system. Hohenberg and Kohn showed that for a many electron system there is a direct mapping of the ground state electron density onto the ground state wave function, and that this single ground state electron density represents the minimization of the total electronic energy of the system²⁴. This led to the replacement of the many-body electronic wavefunction with the electronic density as the fundamental quantity²³.

The functional most frequently used in the geometric optimizations described in this dissertation is the hybrid functional, B3LYP. The ‘B’ refers to the physical chemist Axel Becke, who developed the exchange portion of the functional, whereas ‘LYP’ refer to Lee, Yang and Parr who developed the electron correlation portion of the functional. It is termed a hybrid functional because the exchange density functional is combined with the exact Hartree-Fock energy as specified by three parameters²³. The molecular orbitals

are constructed from a collection of functions called the basis set. These functions are typically atomic orbitals, the coefficients of which determine the electron density²³. Since it is typically the valence electrons that participate in bonding, representing these orbitals by multiple basis functions permits the electron density to adjust to the spatial distribution appropriate to the specific molecular context. The number of basis functions comprising the valence orbitals in these so-called ‘split-valence’ basis sets is an example of the tradeoff between physical accuracy and computational cost²³. The vast majority of the *in vacuo* DFT geometry optimizations presented in this dissertation used the 6-31G* basis set²⁵. This double-zeta split-valence basis set represents the core atomic orbital basis functions with six primitive Gaussian functions, whereas the valence orbitals are comprised of two basis functions apiece, hence double-zeta. The first valence basis function has three primitive Gaussian functions and the second has one. The asterisk indicates the presence of polarization functions for the heavy atoms. This basis set was designed to accurately represent the valence energetics with a maximum of computational efficiency by using an inflexible representation of the 1s cores on carbon and oxygen. In contrast, the calculation of indirect spi-spin couplings requires a more flexible and balanced representation of the core and valence contributions to the Fermi contact term in the coupling. This was achieved through the use of a specially designed [5s2p1d|3s1p] extended double-zeta basis set that has returned *in vacuo* results estimated to deviate by less than 5% of the total coupling when compared to experimental values²⁶. Additionally the spin-spin coupling calculations were conducted using an unrestricted open-shell wavefunction²⁷. This indicates that different molecular orbitals are used to represent the α and β electrons.

Given a set of experimental spin-spin couplings sensitive to the geometrical features of interest in a particular glycan, the theoretical component of the study begins by the selection of an appropriate model system. This model system should adequately reproduce the salient molecular features of the glycan, while making simplifications to the molecular framework that are appropriate for the theoretical method employed. For example, such simplifications for the DFT calculation of indirect spin-spin couplings can reasonably include the removal of hydroxyl groups distal to the conformational aspect of interest that are expected to have little impact on the parameterization of the relevant experimental couplings. These simplifications reduce the computational cost of the calculations and avoid spurious effects such as incidental H-bonding.

Once an appropriate model system has been selected, the specifics of the conformational sampling must be determined. This is dictated by the size of the conformational space and can be facilitated by a simple hard sphere van der Waals radii determination of the conformational contact map as a function of the dihedrals of interest. The one or more dihedrals are then constrained while the rest of the molecule is allowed to relax during an energetic minimization. Depending upon the available conformational space, the dihedrals are iteratively scanned about their respective rotational itineraries maintaining their geometric constraints while continuously allowing the rest of the molecule to relax into an energy minimum. Once an ensemble of optimized geometries has been obtained, the indirect spin-spin coupling constants can be calculated for each energetically optimized molecular conformation.

The collection of spin-spin couplings resulting from the ensemble of sampled geometries is then parameterized as a function of one or more dihedrals utilizing a

Karplus-like trigonometric function²⁸. These parameterized coupling profiles can subsequently be used to interpret experimental couplings in structural terms. Finally these results can be compared with those from parallel theoretical and experimental data to form conclusions. These parallel methods include the theoretical information returned by molecular dynamics simulations, DFT energetics, and natural bonding orbital (NBO) calculations, as well as other experimental spectroscopic and crystallographic data.

Within this conceptual framework, the ultimate research goals are ideally guided by biological structure function questions that identify specific complex glycans as targets for conformational analysis, however such analysis is predicated upon a significant amount of preliminary basic research on the molecular fragments of the target glycan. In this spirit the majority of the dissertation work presented here is restricted primarily to studies on monosaccharides, while the final two chapters focus on efforts in disaccharides.

1.2.2. Research Objectives

Investigations of higher order structure in saccharides (*i.e.* global conformation in dimers and oligomers as dictated minimally by the ensemble of glycosidic torsions) is predicated upon an understanding of the conformational behaviour of the constituent monosaccharides in isolation. Due to the significant potential for intra-molecular H-bonding in saccharides, there is an equally significant potential for correlated conformational behaviour. One theme that will arise throughout this dissertation (particularly in chapters 4, 5 and 7) is the notion that there are spin couplings that are sensitive to the orientation of multiple molecular features with respect to the coupling

path and as a result these coupling constants simultaneously report on the conformation of more than one dihedral in the molecular framework. Thus, the accurate interpretation of such experimental measurements requires a consideration of the correlated conformations of these related structural parameters to which the couplings are sensitive. Given the astronomical degree of freedom in the total molecular conformational space of even a simple monosaccharide, the theoretical parameterization of the ensemble of coupling constants in this complete conformational space is totally unfeasible. Fortunately there are essentially no coupling constants that are sensitive to all of these geometric features. In fact, the majority of possible spin couplings are sensitive to usually no more than three dihedrals at most, all of which are proximal to the coupling pathway in consideration. This allows for a modular approach to coupling parameterization in which a single hexopyranose ring can be divided up into overlapping regions. Since the ring oxygen provides a relatively conformationally immobile spacer between the anomeric center and the hydroxymethyl group, the hexopyranose ring can be broken up into three regions which can be independently conformationally analysed. The two extreme regions are defined by the dihedrals about *a*) C1-O1, C2-O2 and C3-O3 and *b*) C4-O4, C5-C6 and C6-O6 with a third bridging region defined by *c*) C2-O2, C3-O3 and C4-O4. In the following chapters I will directly address regions *a* and *b*, and lay some groundwork for the conformational analysis of region *c*.

As alluded to earlier, knowledge of the tautomeric distribution in a reducing monosaccharide can often add important basic information to the study of that saccharide in various chemical and macromolecular contexts. In chapter 2, through the use of quantitative 1-D NMR and *ab initio* DFT calculations, the solution behavior of a

biologically important C₉ α -*keto* acid, *N*-acetyl-neuraminic acid (sialic acid), was investigated in terms of its tautomeric distribution with particular attention to the quantification of the minor open chain forms. Specifically these acyclic forms are the *keto*, *enol*, and *keto* hydrate (*gem*-diol). The relative amount of each form present in solution was explored as a function of pH, and the pK_a's of the acid functionality on each of the forms was determined by NMR chemical shift titration. These studies involved the use of unlabeled sialic acid isolated from edible barn swiftlet nest (*Aerodramus fuciphagus*), and the C1, C2 or C3 ¹³C-labeled isotopomeric sialic acids prepared via the aldol condensation between the appropriately ¹³C-enriched pyruvic acid and *N*-acetyl-mannosamine. Chapter 3 expanded on these studies in sialic acid by exploring all carbon and proton based spin-spin couplings to C1 through C3 for the α - and β -pyranose tautomers, again as a function of pH. This involved the measurement of the experimental couplings at pH \approx 2 and 8 in an aqueous solution of 5% ²H₂O. Additionally the effect of the α -*keto* acid moiety orientation (rotation about C1-C2) on proximal scalar couplings was assessed via *ab initio* DFT calculations utilizing a solvent continuum model with the carboxylic acid either protonated or ionized. These two chapters set the groundwork for further studies of more complex sialic acid containing glycans.

Chapter 4 explores the conformational preferences of the hydroxymethyl group in the α and β anomers of D-gluco- and D-galactopyranose through the interpretation of redundant experimental ¹H-¹H, ¹H-¹³C and ¹³C-¹³C spin-spin couplings with theoretically derived coupling parameterizations. The multi-linear grid search analysis protocol is introduced within the context of the program *Chymesa*, specifically designed for the conformational analysis of the C5-C6 and C6-O6 rotamers (ω and θ respectively)

in pyranose rings. The conformational analysis includes an account of the correlation between the two dihedrals as based on the multiple couplings that show a dual dependence on ω and θ .

By analogy to the θ dependence of $^2J_{C5,H6R/S}$ in the hydroxymethyl studies of chapter 4, the dependence of $^2J_{C1,H2}$ and $^2J_{C2,H1}$ on the C1-O1 and C2-O2 dihedrals in the α and β anomers of D-gluco- and D-mannopyranose is discussed in chapter 5. Full theoretical parameterization of these couplings as a function of their dual conformational dependencies is presented and the possible utility of these couplings in the conformational analysis of C1 and C2 hydroxyl orientation is discussed with particular emphasis on the potential application of $^2J_{C2,H1}$ to an analysis of the glycosidic torsion ϕ .

The usefulness of carbon based couplings having been established, chapter 6 reports on the full ensemble of experimental $^1J_{CC}$, $^2J_{CC}$ and $^3J_{CC}$ values throughout the pyranose ring in the majority of C1 through C4 epimers. Empirical correlations between coupling magnitude and sign with configuration at carbons proximal to the coupling path are discussed in the context of theoretical validations. Also discussed is the modulation of various $^3J_{CC}$ values as a function of ω conformation.

The empirically observed correlation between coupling sign and magnitude with configuration is investigated in detail for $^2J_{C1,C3}$ in chapter 7. Experimental $^2J_{C1,C3}$ values for the eight C1 through C3 hexopyranose stereoisomers are sorted into three structural groups depending upon configuration at the coupled carbons. A comprehensive battery of *ab initio* DFT calculations validated the observed trend in the coupling. This phenomenon is extended to structurally analogous situations for $^2J_{C2,C4}$. The DFT

calculations also reveal an additional dependence of this coupling on the conformation of hydroxyls appended to the carbons along the coupling pathway. Both the configurational and conformational dependencies of $^2J_{C1,C3}$ are dissected in terms of two distinct modes of orbital interaction as defined in the natural bonding orbital (NBO) paradigm; destabilizing steric (through-space) and a stabilizing hyperconjugative (through-bond) interactions. The merits and weaknesses of the NBO interpretation are briefly discussed. Chapter 8 goes on to report all 1H - 1H , 1H - ^{13}C and ^{13}C - ^{13}C spin-spin couplings sensitive to the C1-O1, C2-O2 and C3-O3 rotamers in *O*-methyl- β -D-glucopyranoside including the 2 and 3 bond proton and carbon based couplings to the hydroxyl protons on O2 and O3 as measured at 25 °C in a DMSO- d_6 solvent system. Each of the couplings in the ensemble of 15 are then parameterized as a function of the C1-O1, C2-O2 and C3-O3 rotamers from a DFT data set that explores 1728 distinct conformations about these dihedrals in a 6-deoxy- β -D-glucopyranose model. The experimental couplings are then interpreted in structural terms through the use of the multiple redundant theoretical coupling profiles in a combined stochastic and deterministic trajectory optimization analysis of the C1-O1, C2-O2 and C3-O3 rotamer conformations. The results are compared to those from a variety of molecular mechanics and molecular dynamics simulations and discussed in terms of intra-molecular H-bonding patterns, rotameric transition pathways, and various interpretations of the *exo*-anomeric effect.

The work in previous chapters on monosaccharides is applied to the conformational analysis of the ϕ and ψ glycosidic torsions in aqueous solution for the *O*-methyl- α -D-mannopyranosyl-(1 \rightarrow 2)- α -D-mannopyranoside disaccharide in chapter 8. This analysis is based on a set of six experimentally measured trans-glycoside $^3J_{CH}$, $^3J_{CC}$

and $^2J_{CC}$ couplings in disaccharide strategically ^{13}C -enriched in the linkage carbons. These couplings were parameterized using a set of DFT optimized geometries which sampled the available ϕ and ψ conformational space with a 30° resolution. The multi-linear grid search protocol for conformational analysis in the hydroxymethyl group presented in chapter 4 is adapted to the glycosidic torsions ϕ and ψ in a program called *Glyfit*. Various conformational models are proposed and the results are compared with those from previously reported conformational studies on this linkage.

The final data chapter (9) reports on the crystallization and subsequent X-ray structure determination of methyl 6-*O*- β -D-[1- ^{13}C]-galactopyranosyl- β -D-glucopyranoside•mono-hydrate (methyl-allolactoside). A novel crystallization protocol involving the use of a λ -tube is described. Structural comparisons between the methyl-allolactoside crystal structure, a fully unconstrained DFT optimized geometry for methyl-allolactoside, the crystal structure of allolactose as a co-crystal with β -galactosidase, and crystal structures of the related disaccharides gentiobiose and methyl-lactoside are presented including a discussion of the pyranose ring puckering parameters.

1.3. References

1. (a) Fenchel, T.; Blackburn, T.H.; King, G.M. *Bacterial Biogeochemistry: The Ecophysiology of Mineral Cycling*, 2nd edition, **1998**, Academic Press, San Diego, California (b) Kaufman, D.G.; Franz, C.M. *Biosphere 2000: Protecting our Global Environment* **2000**, Kendall Hunt, Dubuque, Iowa (c) Ernst, B; Hart, G.W.; Sinaÿ, P. (eds) *Carbohydrates in Chemistry and Biology, Part II: Biology of Saccharides, Vol IV: Lectins and Saccharide Biology*, **2000**, Wiley-Interscience, New York, New York (d) Collins, P.; Ferrier, R. *Monosaccharides: Their Chemistry and Their Roles in Natural Products* **1995**, Wiley-Interscience, New York, New York

2. (a) Lemieux, R.U. *Acc. Chem. Res.* **1996**, 29, 373-380 (b) Lemieux, R.U. *Molecular Rearrangements* (ed. De Mayo, P.) **1963**, p.713. Wiley-Interscience, New York, New York
3. Lemieux, R.U. *Pure Appl. Chem.* **1971**, 25, 527-548
4. Graczyk, P.P.; Mikolajczyk, M. Anomeric Effect: Origin and Consequences. In *Topics In Stereochemistry, Volume 21*, (eds. Eliel, E.L.; Wilen, S.H.) **1994**, 159 – 349. John Wiley & Sons, Inc. New York, New York
5. Wolfe, S. *Acc. Chem. Res.* **1972**, 5, 102 – 111
6. Zefirov, N.S.; Samoshin, V.V.; Subbotin, O.A.; Baranenko, V.I.; Wolfe, S. *Tetrahedron* **1978**, 34, 2953 – 2959
7. Kirby, A.J. *The Anomeric Effect and Related Stereoelectronic Effects at Oxygen* **1983**, Springer, New York, New York
8. Lemieux, R.U.; Chü, N.J. *Abstracts of Papers*, 133rd National Meeting of the American Chemical Society, San Francisco, CA, April **1958**, American Chemical Society: Washington D.C., **1958**; p. 31 N
9. Lemieux, R.U. *Abstr. Papers Am. Chem. Soc.* **1959**, 135, 5E
10. Juaristi, E.; Cuevas, G. *The Anomeric Effect*, **1995**, CRC Press, Boca Raton
11. Praly, J.P.; Lemieux, R.U. *Can. J. Chem.* **1987**, 65, 213 – 223
12. Bitzer, R.S.; Barbosa, A.G.H.; Silva, C.O.d.; Nascimento, M.A.C. *Carbohydr. Res.* **2005**, 340, 2171–2184
13. (a) Çarçabal, P.; Jockusch, R.A.; Hünig, I.; Snoek, L.C.; Kroemer, R.T.; Davis, B.G.; Gamblin, D.P.; Compagnon, I.; Oomens, J.; Simons, J.P. *J. Am. Chem. Soc.* **2005**, 127, 11414-11425 (b) Suzuki, T. *Phys. Chem. Chem. Phys.* **2008**, 10, 96–105
14. (a) Krivdin, L.B.; Shcherbakov, V.V.; Kalabin, G.A. *Zh. Org. Khim.*, **1986**, 22, 342 (b) Krivdin, L.B.; Zinchenko, S.V.; Shcherbakov, V.V.; Kalabin, G.A.; Contreras, R.H.; Tufro, M.F.; Ruiz De Azuna, M.C.; Giribet, C.G. *J. Magn. Reson.* **1989**, 84, 1 (c) Krivdin, L.B.; Della, E.W. *Progress in NMR Spectroscopy*, **1991**, 23, 301 – 610 (d) Danilova, V.A.; Krivdin, L.B. *Russ. J. Org. Chem.*, **2003**, 39, 663 (e) Danilova, V.A.; Isotomina, N.V.; Krivdin, L.B. *Russ. J. Org. Chem.*, **2004**, 40, 1194
15. (a) Tvaroska, I.; Hricovini, H.; Petrakova, E. *Carbohydr. Res.* **1989**, 189, 359-362 (b) Mulloy, B.; Frenkiel, T. A.; Davies, D. B. *Carbohydr. Res.* **1988**, 184, 39-46 (c) Tvaroska, I.; Gadjos, J. *Carbohydr. Res.* **1995**, 271, 151-162 (d) Tvaroska, I.; Taravel, F. R.; Utile, J. P.; Carver, J. P. *Carbohydr. Res.* **2002**, 337, 353-367

16. (a) Cloran, F.; Carmichael, I.; Serianni, A. S. *J. Am. Chem. Soc.* **1999**, *121*, 9843-9851 (b) Stenutz, R.; Carmichael, I.; Widmalm, G.; Serianni, A. S. *J. Org. Chem.* **2002**, *67*, 949-958 (c) Thibaudeau, C.; Stenutz, R.; Hertz, B.; Klepach, T.; Zhao, S.; Wu, Q.; Carmichael, I.; Serianni, A. S. *J. Am. Chem. Soc.* **2004**, *126*, 15668-15685
17. (a) Claridge, T.D.W. *High-Resolution NMR Techniques in Organic Chemistry* **1999**, Elsevier, Netherlands (b) van de Ven, F.J.M. *Multidimensional NMR in Liquids: Basic Principles and Experimental Methods* **1995**, John Wiley & Sons, Ltd, San Francisco, California
18. Lipsitz, R.S.; Tjandra, N. New Applications for Residual Dipolar Couplings: Extending the Range of NMR in Structural Biology. In *Modern Magnetic Resonance Part I: Applications in Chemistry, Biological and Marine Sciences* (ed. Webb, G.A.) **2006**, 653-660. Springer, Netherlands
19. (a) Serianni, A. S.; Nunez, H. A.; Barker, R. *Carbohydr. Res.* **1979**, *72*, 71-78 (b) Hayes, M. L.; Pennings, N. J.; Serianni, A. S.; Barker, R. *J. Am. Chem. Soc.* **1982**, *104*, 6764-6769 (c) Serianni, A. S.; Vuorinen, T.; Bondo, P. J. *Carbohydr. Chem.* **1990**, *9*, 513-541 (d) King-Morris, M. J.; Bondo, P. B.; Mrowca, R. A.; Serianni, A. S. *Carbohydr. Res.* **1988**, *175*, 49-58 (e) Podlasek, C. A.; Wu, J.; Stripe, W. A.; Bondo, P. B.; Serianni, A. S. *J. Am. Chem. Soc.* **1995**, *117*, 8635-8644 (f) Serianni, A. S.; Clark, E. L.; Barker, R. *Carbohydr. Res.* **1979**, *72*, 79-91
20. (a) Brady, J.W. *J. Am. Chem. Soc.* **1986**, *108*, 8153-8160 (b) Brady, J.W. *Carbohydr. Res.* **1987**, *165*, 306-312 (c) Ha, S.N.; Giammona, A.; Field, M.; Brady, J.W. *Carbohydr. Res.* **1988**, *180*, 207-221 (d) Dashnau, J.L.; Sharp, K.A.; Vanderkooi, J.M. *J. Phys. Chem. B* **2005**, *109*, 24152-24159 (e) Dowd, M.K.; French, A.D.; Reilly, P.J. *Carbohydr. Res.* **1994**, *264*, 1-19 (f) Astley, T.; Birch, G.G.; Drew, M.G.B.; Rodger, P.M. *J. Phys. Chem. A* **1999**, *103*, 5080-5090
21. (a) Barrows, S.E.; Dulles, F.J.; Cramer, C.J.; French, A.D.; Truhlar, D.G. *Carbohydr. Res.* **1995**, *276*, 219-251 (b) Cramer, C. J.; Truhlar, D. G. *J. Am. Chem. Soc.* **1993**, *115*, 5745-5753. (c) Cramer, C. J.; Truhlar, D. G.; French, A. D. *Carbohydrate Res.* **1997**, *298*, 1-14 (d) French, A.D.; Dowd, M.K.; Reilly, P.J. *J. Mol. Struct.: Theochem.* **1997**, *395*, 271-287 (e) Csonka, G. I.; Elias, K.; Csizmadia, I. G. *Chem. Phys. Lett.* **1996**, *257*, 49-60 (f) Brown, J. W.; Wladkowski, B. D. *J. Am. Chem. Soc.* **1996**, *118*, 1190-1993 (g) Polavarapu, P. L.; Edwig, C. S. *J. Comput. Chem.* **1992**, *13*, 1255-1261 (h) Momany, F.A.; Appell, M.; Strati, G.; Willett, J.L. *Carbohydrate Res.* **2004**, *339*, 553-567 (i) Jebber, K.A.; Zhang, K.; Cassady, C.J.; Chung-Phillips, A. *J. Am. Chem. Soc.* **1996**, *118*, 10515-10524 (j) Zuccarello, F.; Buemi, G. *Carbohydrate Res.* **1995**, *273*, 129-145 (k) Bagno, A.; Rastrelli, F.; Saielli, G. *J. Org. Chem.* **2007**, *72*, 7373-7381 (l) Suzuki, T.; Kawashima, H.; Sota, T. *J. Phys. Chem. B* **2006**, *110*, 2405-2418

22. (a) Molteni, C.; Parrinello, M. *Chem. Phys. Lett.* **1997**, 275, 409-413 (b) Kouwijzer, M.L.C.E.; van Eijck, B.P.; Kroes, S.J.; Kroon, J. *J. Comput. Chem.* **1993**, 14, 1281-1289 (c) Kouwijzer, M.L.C.E.; van Eijck, B.P.; Kooijman, H.; Kroon, J. *Acta Crystallogr. B* **1995**, 51, 209-220
23. (a) Parr, R.G.; Yang, W. *Density-Functional Theory of Atoms and Molecules* **1989**, Oxford University Press, New York (b) Dreizler, R.; Gross, E. *Density Functional Theory* **1995**, Plenum Press, New York (c) Koch, W.; Holthausen, M.C. *A Chemist's Guide to Density Functional Theory* **2002**, Wiley-VCH, Weinheim, ed. 2 (d) Fiolhais, C.; Nogueira, F.; Marques, M. (eds.) *A Primer in Density Functional Theory* **2003**, Springer-Verlag (e) Kohanoff, J. *Electronic Structure Calculations for Solids and Molecules: Theory and Computational Methods* **2006**, Cambridge University Press
24. Hohenberg, P.; Kohn, W. *Phys. Rev. B* **1964**, 136, 864
25. Hehre, W.J.; Ditchfield, R.; Pople, J.A. *J. Chem. Phys.* **1972**, 56, 2257 – 2261
26. (a) Serianni, A.S.; Wu, J.; Carmichael, I. *J. Am. Chem. Soc.* **1995**, 117, 8645-8650 (b) Cloran, F.; Carmichael, I.; Serianni, A.S. *J. Phys. Chem. A* **1999**, 103, 3783
27. Pople, J.A.; Nesbet, R.K. *Journal of Chemical Physics* **1954**, 22, 571
28. (a) Karplus, M. *J. Am. Chem. Soc.* **1963**, 85, 2870 (b) Karplus, M. *J. Am. Chem. Soc.* **1969**, 91, 1-10

CHAPTER 2:

¹³C-LABELED *N*-ACETYL-NEURAMINIC ACID IN AQUEOUS SOLUTION:
DETECTION AND QUANTIFICATION OF ACYCLIC KETO, KETO HYDRATE
AND ENOL FORMS BY ¹³C NMR¹

“Where shall I start, please your majesty?” he asked.

*“Begin at the beginning,” the king said gravely, “and go on till you come to the end:
then stop”*

– Lewis Carroll

2.1. Abstract

N-Acetyl-neuraminic acid (**1**) labeled with ¹³C at C1-C3 was analyzed by ¹³C NMR to detect and quantify the acyclic forms (keto, keto hydrate, enol) in aqueous solution at varying pHs. In addition to pyranoses, solutions contained keto form based on the detection of C2 signals at ~198 ppm (~0.7% at pH 2). Spectra of [2-¹³C] and [3-¹³C] isotopomers contained labeled carbons at ~143 and ~120 ppm, respectively, which were attributed to enol form. Studies with [1,2,3-¹³C₃]**1** substantiated the existence of enol

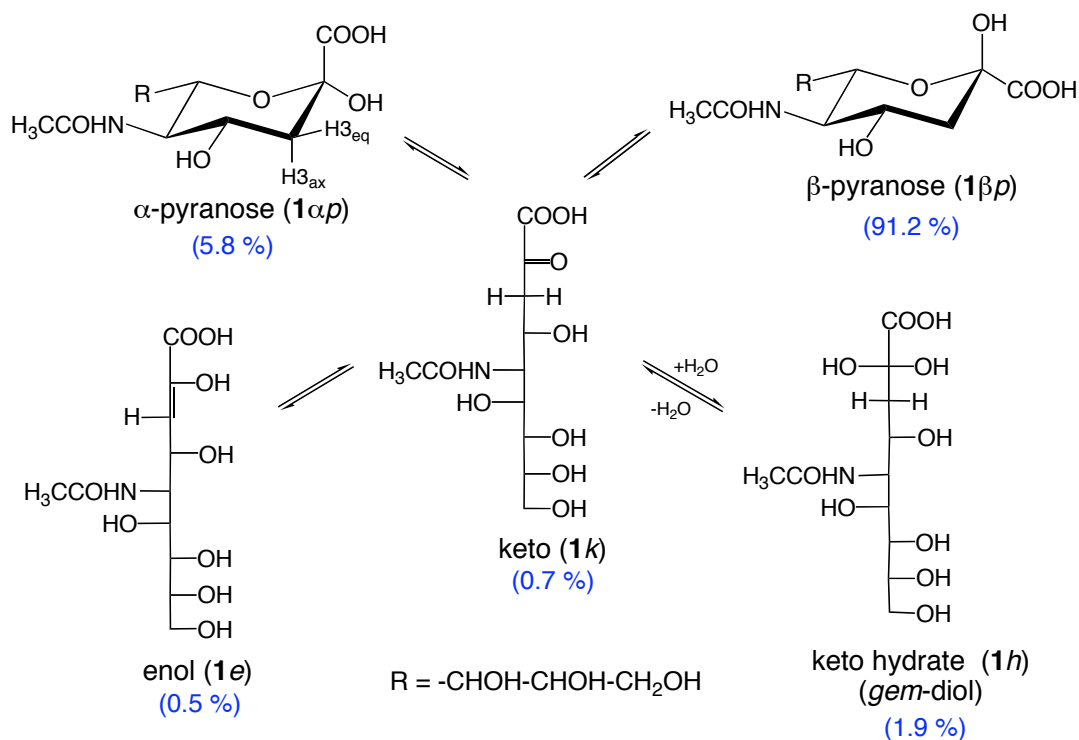
¹ I gratefully acknowledge my co-authors Ian Carmichael and Anthony S. Serianni for their assistance in preparing this chapter, which is submitted to the Journal of the American Chemical Society. I also wish to acknowledge Meredith Reed from Omicron Biochemicals for her synthetic efforts in this report.

(~0.5% at pH 2). Enol was not detected at pH values > 6.0. A C2 signal observed at ~94 ppm was identified as C2 of the keto hydrate (~1.9 % at pH 2) based partly on its abundance as a function of solution pH. Density functional theory (DFT) calculations were used to study the effect of enol and hydrate structure on J_{CH} and J_{CC} values involving C2 and C3 of these forms. DFT calculations showed that $^2J_{C2,H3}$ in cis and trans enols have similar magnitudes but opposite signs, making this J -coupling potentially useful to distinguish enol configurations. Solvent deuterium exchange studies of **1** showed selective incorporation of 2H from 2H_2O at $H3_{axial}$ in the pyranoses at p 2H 8.0. The acyclic keto form, which presumably participates in this reaction, must assume a pseudo-cyclic conformation in order to account for the exchange selectivity. Weak ^{13}C signals arising from labeled species were also observed consistently and reproducibly in aqueous solutions of ^{13}C -labeled **1**, possibly arising from lactonization or intermolecular esterification.

2.2. Introduction

N-Acetyl-neuraminic acid **1** (NeuAc; sialic acid; SA) (Scheme 2.1) is a C_9 α -ketoacid often encountered as the terminal residue of complex-type *N*-glycans covalently bound to human glycoproteins such as IgG.^{1,2} It is commonly installed on glycoproteins and glycolipids in 2→3 or 2→6 linkage with terminal β -Gal residues via the involvement of the biologically activated donor of NeuAc, CMP-sialic acid (CMP-SA), and CMP-SA sialyltransferase (E.C. 2.4.99.1, 2.4.99.4).³ The presence of SA on glycoproteins has been shown to influence their biological functions. For instance, the anti- and pro-inflammatory activities of human IgG have been shown recently to be correlated with the

presence and absence of SA, respectively, on the Fc fragment.⁴ Sialic acid is derived from C₆ and C₃ metabolites *in vivo*, although the specific forms of these building blocks depends on the organism. In *E. coli*, NeuAc is produced from *N*-acetyl-D-mannosamine (ManNAc) and pyruvate in an aldol condensation catalyzed by the enzyme, *N*-acetylneuraminate lyase (E.C. 4.1.3.3).⁵ In other organisms, ManNAc or ManNAc-6P,



Scheme 2.1 Anomerization of *N*-acetylneuraminic acid (1) and abundances of forms in aqueous solution at pH 2.0.

and PEP (phosphoenolpyruvate), are substrates for sialic acid synthases, yielding NeuAc or NeuAc-9P as products, respectively.⁶

Studies in this laboratory of the conformational and dynamics properties of biologically important oligosaccharides containing NeuAc glycosidic linkages required **1** containing specific sites of ¹³C-enrichment to allow measurements of NMR parameters

such as trans-glycoside J_{CH} and J_{CC} spin-spin coupling constants. The availability of NeuNAc singly-labeled with ^{13}C at C1, C2 and C3 stimulated tangential ^{13}C NMR investigations of the solution composition of **1**. Prior work has shown that selective ^{13}C -labeling at anomeric carbons of aldoses and ketoses allows the detection and quantification not only of major tautomeric forms in solution, which are often cyclic, but also of acyclic forms (aldehyde and keto forms and their hydrates), which are normally present in very low abundance.⁷⁻⁹ Knowledge of the solution behavior of **1** contributes to a better understanding of its biological properties, especially with respect to identifying potential monomeric forms bound by SA-recognizing proteins, enzymes and receptors. We describe herein ^{13}C NMR studies of aqueous solutions of NeuAc ^{13}C -isotopomers, and show that these solutions contain detectable amounts of acyclic keto, enol, and keto hydrate forms.

2.3. Experimental

2.3.1. ^{13}C -Labeled Sialic acids.

[1- ^{13}C]-, [2- ^{13}C]-, [3- ^{13}C]- and [1,2,3- $^{13}C_3$]sialic acid were obtained from Omicron Biochemicals Inc. (South Bend, IN) and used without further purification.

2.3.2. Preparation of Unlabeled Sialic Acid.

Unlabeled **1** was prepared by a modification of the procedure described by Czarniecki and Thornton.¹⁰ Two batches of edible bird's nest (batch **A**, 27.68 g; batch **B**, 28.10 g), obtained from Hsu's Ginseng Enterprises, Inc. (<http://english.hsuginseng.com>),

were each homogenized in 50 mL of distilled H₂O using a Waring blender. The homogenate was diluted to a final volume of 3 L containing H₂SO₄ at a concentration of 0.025 M. The solution was stirred at 60-70 °C for 2.5 h. A saturated aqueous solution of Ba(OH)₂ was then slowly added to the mixture until the pH was between 5 and 6. The mixture was set at 4 °C overnight and then vacuum filtered through a glass microfiber filter. The clear filtrate was concentrated *in vacuo* to ~250 mL and passed through a 0.3 µm filter, which was washed with water after filtration. The combined filtrate and washings were split into two equal volumes and individually loaded (~130 mL) onto a Dowex 1 × 8 (200-400 mesh) ion-exchange column (3.0 × 30.0 cm) in the formate form. After loading, the column was washed with 1 L of distilled water, and then eluted with a 1.5 L linear formic acid gradient (0-2 M). Fractions (23 mL) were collected and assayed by spotting fraction aliquots on silica gel TLC plates, spraying with molybdate reagent (1% (w/v) CeSO₄ – 2.5% (w/v) (NH₄)₆Mo₇O₂₄ – 10% aq H₂SO₄)¹¹ and charring. Fractions testing positive for sialic acid were combined and the resulting solution lyophilized. Total yield of *N*-acetylneuraminic: ~1.7 g each from batches A and B. The white powder had a melting point of 184 – 186 °C and was shown to be >98% pure by 1D ¹H and ¹³C NMR.

2.3.3. Preparation of 2-*O*-Methyl-β-D-N-Acetylneuraminic acid (**2**).

Unlabeled **1** (100 mg, 0.32 mmol) was dissolved in 80 mL of dry methanol, 3 g of Dowex 50 x 8 (200-400 mesh) ion-exchange resin in the H⁺ form were added, and the suspension was refluxed at 76 °C. The reaction was monitored by silica gel TLC (butanol:acetic acid:H₂O, 2:1:1) using molybdate reagent for visualization¹¹ (see above).

The reaction was stopped after 48 h, cooled and filtered to remove the resin, and the filtrate was concentrated *in vacuo* to give ~85 mg of crude syrup. 1D ^1H and ^{13}C NMR revealed methyl 2-*O*-methyl- β -D-*N*-acetylneuraminate methyl ester as the primary product. ^{13}C NMR: 171.81 (C1); 100.60 (C2); 40.61 (C3); 67.82, 53.11, 71.93, 69.41, 71.24, 64.77 (C4-C9); 176.21 (acetyl CO); 23.48 (acetyl CH_3); 52.40 (glycoside CH_3); 54.94 (ester CH_3).

The methyl ester was saponified for 12 h in 1 *M* NaOH, after which the pH was lowered to 1.4 with the addition of Dowex (H^+) ion-exchange resin. 1D ^1H and ^{13}C NMR showed conversion to the free acid methyl glycoside **2**. ^{13}C NMR: 171.46 (C1); 95.40 (C2); 38.74 (C3); 66.72, 52.13, 70.40, 68.26, 70.15, 63.22 (C4-C9); 174.86 (acetyl CO); 22.15 (acetyl CH_3); 53.56 (ester CH_3).

2.3.4. NMR Spectroscopy.

Solutions (~300 μL , ~0.1 *M*) of ^{13}C -labeled compounds in 95:5 v/v $^1\text{H}_2\text{O}$: $^2\text{H}_2\text{O}$ solvent were prepared and transferred to 3-mm NMR tubes. Quantitative 1D $^{13}\text{C}\{^1\text{H}\}$ NMR spectra were obtained at 25 $^\circ\text{C}$ on a Varian Unity*Plus* 600-MHz FT-NMR spectrometer operating at 150.856 MHz for ^{13}C and equipped with a 3-mm $^{13}\text{C}/^1\text{H}$ microprobe (Nalorac).

For non-quantitative measurements, $^{13}\text{C}\{^1\text{H}\}$ NMR spectra were typically obtained with a 36,496 Hz spectral window and 27.75 s recycle time (^{13}C T_1 s were not longer than ~5 s under the experimental solution conditions as determined from τ_{null} values in an inversion-recovery T_1 experiment). FIDs were zero-filled once or twice to

give final digital resolutions of <0.05 Hz/pt, and FIDs were processed with resolution enhancement (Gaussian or sine-bell functions) to improve resolution and facilitate the measurement of small J -couplings. The degree of enhancement was chosen empirically based on the observed spectral S/N and quality.

For quantitative measurements, ^{13}C NMR spectra were collected in a ^1H -decoupled – NOE mode with 35 s interpulse delays to allow for more reliable determinations of % forms in solution. A minimal line broadening window function was applied prior to signal integration.

2.4. Calculations

2.4.1. Selection and Geometric Optimization of Model Compounds.

Structures **2** and **3-6** were chosen as mimics of **1h** and **1e**, respectively. DFT calculations were conducted within *Gaussian03*¹² using the B3LYP functional¹³ and 6-31G* basis set¹⁴ for geometric optimization, as described previously.^{15,16} Initial torsion angle constraints in **2** were as follows: C2-C3-C4-C5 torsion fixed at -165° ; C3-C2-O2-H, C3-C2-O2'-H, C3-C4-O4-H and C2-C1-O1'-H torsions fixed at 180° ; O1-C1-C2-C3 torsion set initially at 90° and allowed to optimize. For **3-4**, the C3-C4-O4-H, C2-C1-O1-H and C3-C2-O2-H torsions were fixed at 180° . For **5-6**, the C3-C4-O4-H, C3-C2-O2-H and C2-C1-O1-H torsions were fixed at 180° . For cis enol **3**, the C1-C2-C3-C4 torsion angle was fixed at 0° , whereas this torsion was fixed at 180° in **4**. Two orientations of the COOH group in **3** and **4** were examined wherein the double bonds were conjugated (O1-C1-C2-C3 torsion fixed at 180°) and where the O1-C1-C2-C3

torsion was fixed at 90° (unconjugated). In **5-6**, the C2-C3-C4-C5 torsion angle was rotated systematically in 30° increments through 360° and all remaining geometric parameters optimized except those identified above.

2.4.2. Theoretical Calculations of ^{13}C - ^1H and ^{13}C - ^{13}C Spin-Coupling Constants.

J_{CH} and J_{CC} values were calculated in **2-6** with *Gaussian03*¹² using DFT (B3LYP)¹³. Finite field double perturbation theory^{17,18} was used to recover the Fermi contact, diamagnetic and paramagnetic spin-orbit, and spin-dipole terms¹⁹ with a [5s2p1d|3s1p] basis set²⁰, and the raw (unscaled) calculated couplings are reported.

2.5. Results and Discussion

2.5.1. Cyclic pyranose and acyclic keto forms of **1**.

NeuAc ^{13}C -labeled at the anomeric carbon (C2) was used to detect and quantify monomeric forms present in aqueous solution (Scheme 2.1). The $^{13}\text{C}\{^1\text{H}\}$ NMR spectrum of [2- ^{13}C]**1** at pH 2.0 contained intense labeled signals attributed to the α -pyranose (**1** αp ; 96.53 ppm) and β -pyranose (**1** βp ; 95.97 ppm)²¹ (Figure 2.1A). The β -pyranose is significantly more abundant (91.2%) than the α -pyranose (5.8%) at pH 2.0; these percentages are 92.1% and 7.5%, respectively, at pH 8.0. Preference for the β -pyranose presumably derives from the anomeric effect,²²⁻²⁴ which favors an axial C2-O2 bond, and from the greater steric demand of the COOH group relative to OH, which favors an equatorial C1-C2 bond. Both effects are reinforcing. The $\alpha p/\beta p$ ratio at pH 2.0 (0.064) is slightly smaller than the same ratio at pH 8.0 (0.081).

The $^{13}\text{C}\{^1\text{H}\}$ NMR spectrum of $[2\text{-}^{13}\text{C}]\mathbf{1}$ at pH 2.0 also contained a relatively intense labeled signal at 198.20 ppm (Figure 2.1B) which was attributed to the acyclic *keto* (carbonyl) form ($\mathbf{1k}$). This signal appeared further upfield than observed previously for the acyclic *keto* forms of D- $[2\text{-}^{13}\text{C}]\text{ribulose-5P}$ (213.7 ppm),²⁵ D- $[2\text{-}^{13}\text{C}]\text{ribulose-1,5-bisphosphate}$ (211.7 ppm)²⁵ and the D- $[2\text{-}^{13}\text{C}]\text{pentuloses}$ (~ 214 ppm),²⁶ and probably reflects the effect of C1 structure on $\delta_{\text{C}2}$ (COOH vs $\text{CH}_2\text{OH}/\text{CH}_2\text{OP}$). Integration of the spectrum acquired at pH 2.0 and 25 °C indicated that $\mathbf{1k}$ comprises $\sim 0.7\%$ of the total forms in solution; this percentage decreased to $\sim 0.4\%$ at pH 8.0. At pH 2.0, an $\alpha\text{p}:\beta\text{p}:\text{keto}$ ratio of 8:128:1 was observed, whereas at pH 8.0, the ratio was 19:228:1.

2.5.2. Acyclic hydrate form of $\mathbf{1}$.

The anomeric region of the $^{13}\text{C}\{^1\text{H}\}$ NMR spectrum of $[2\text{-}^{13}\text{C}]\mathbf{1}$ at pH 2.0 contained two relatively strong labeled signals at 95.90 and 93.60 ppm (Figure 2.1A; signals denoted X_1 and X_2 , respectively). These chemical shifts are consistent with that expected for the acyclic keto hydrate form, $\mathbf{1h}$.²⁵ The latter signal was assigned tentatively to C2 of $\mathbf{1h}$ based on its relative abundance (1.9%) and on the observed keto hydrate/keto ratio of ~ 2.7 , which is comparable to the same ratio reported for pyruvic acid (2.31 ± 0.02).²⁷ By comparison, 2-ketose phosphates gave keto hydrate/keto ratios of < 1 (e.g., 0.14 for D-ribulose-1,5-bisphosphate; $\delta_{\text{C}2}$ 97.6 ppm), while no keto hydrate form was detected by ^{13}C NMR in aqueous solutions of D- $[2\text{-}^{13}\text{C}]\text{2-pentuloses}$.^{25,26}

Since C2 $_{\mathbf{1h}}$ is unprotonated, experimental support for its assignment could not be obtained by examining the magnitude of $^1J_{\text{CH}}$, which was used previously to identify

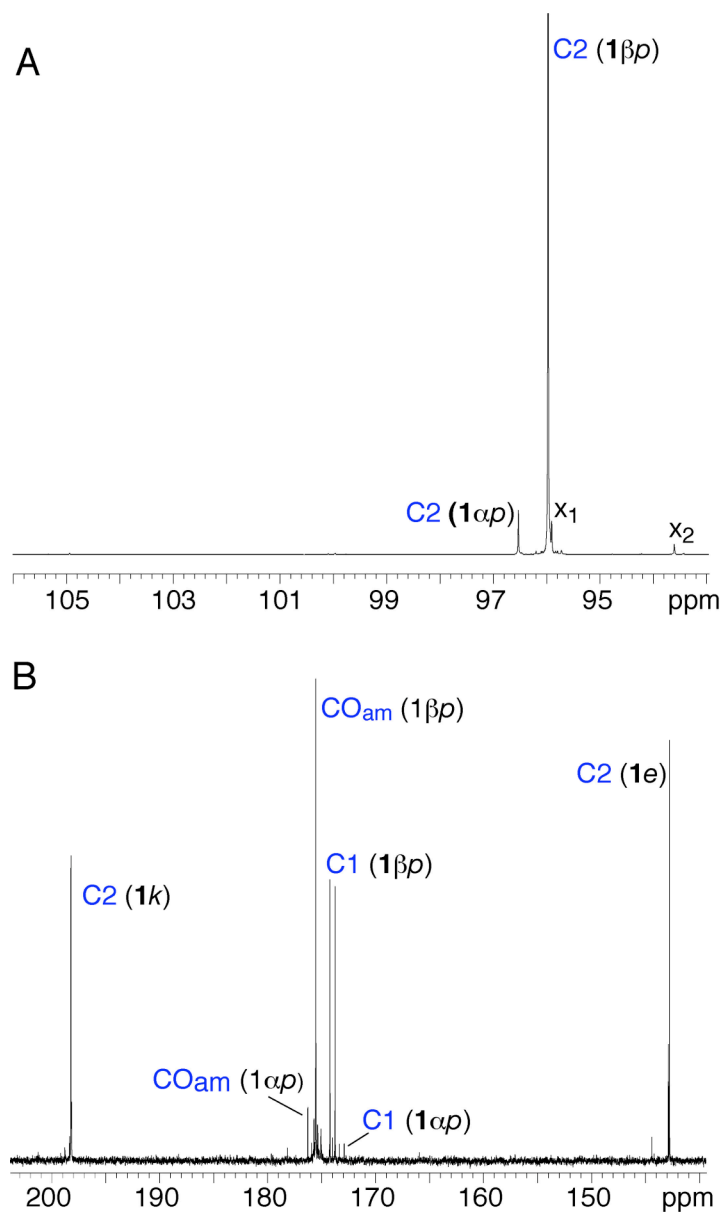


Figure 2.1. Partial $^{13}\text{C}\{^1\text{H}\}$ NMR spectrum of $[2\text{-}^{13}\text{C}]\mathbf{1}$ (150 MHz) at pH 2.0 and 25 °C showing signal assignments. (A) Anomeric region. X_1 and X_2 are putative C2 signals of the acyclic hydrate form ($\mathbf{1h}$). (B) Region containing labeled C2 *keto* ($\mathbf{1k}$) and *enol* ($\mathbf{1e}$) carbons, and the natural abundance amide CO (CO_{am}) and C1 (COOH) carbons of $\mathbf{1}\alpha\text{p}$ and $\mathbf{1}\beta\text{p}$. The C1 signals appear as doublets due to the presence of $^1J_{\text{C1,C2}}$. Several weak signals in this region were not identified.

hydrate C1 carbons in aqueous solutions of [1- ^{13}C]aldoses.^{8,9} Therefore, two alternative assignment strategies were investigated.

Studies of pyruvate have shown that pyruvate anion is much less extensively hydrated than pyruvic acid in aqueous solution (keto hydrate/keto ratio in the anion ranges from 0.054 – 0.087).²⁷⁻³⁰ This behavior was confirmed by inspection of ^{13}C NMR spectra of pyruvic acid and sodium pyruvate (Figure S1). By analogy to pyruvate, the intensity of the authentic C2_{1h} signal should decrease significantly upon raising the solution pH from 2.0 to 7.0. Titration of a solution of [2- ^{13}C]**1** at pH 2.0 with NaOH caused the disappearance of signals X_1 and X_2 at pH ~6-7, but only X_2 reappeared at 93.60 ppm upon relowering the pH of the same solution back to 2.0 with HCl. These results suggest that X_2 is the correct C2_{1h} carbon signal.

A second approach to assign C2_{1h} involved interpretation of X_1 and X_2 signal multiplicities in the ^1H -coupled ^{13}C NMR spectrum of [2- ^{13}C]**1**. The C2 signals of **1** αp and **1** βp showed the expected multiplicities (Figure 2.2A) and served as internal controls. The $\text{C2}_{1\alpha p}$ signal appeared as a doublet of doublets with J_{CH} values of ~3.9 and ~7.5 Hz, whereas the $\text{C2}_{1\beta p}$ signal appeared as a pseudo-triplet containing J_{CH} values of ~3.5 Hz. These couplings were consistent with the more accurate $^2J_{\text{C2,H3ax}}$ and $^2J_{\text{C2,H3eq}}$ values measured directly from the ^1H NMR spectrum of [2- ^{13}C]**1**.³¹ $^3J_{\text{C2,H4}}$ and $^3J_{\text{C2,H6}}$ values in **1** αp and **1** βp associated with C2-C3-C4-H4 and C2-O6-C6-H6 torsion angles of ~60° and ~60°, respectively, are small and appeared as line-broadening in the ^{13}C multiplets. Signal X_1 appeared broadened, whereas X_2 , appeared as a doublet with a splitting of ~2.9

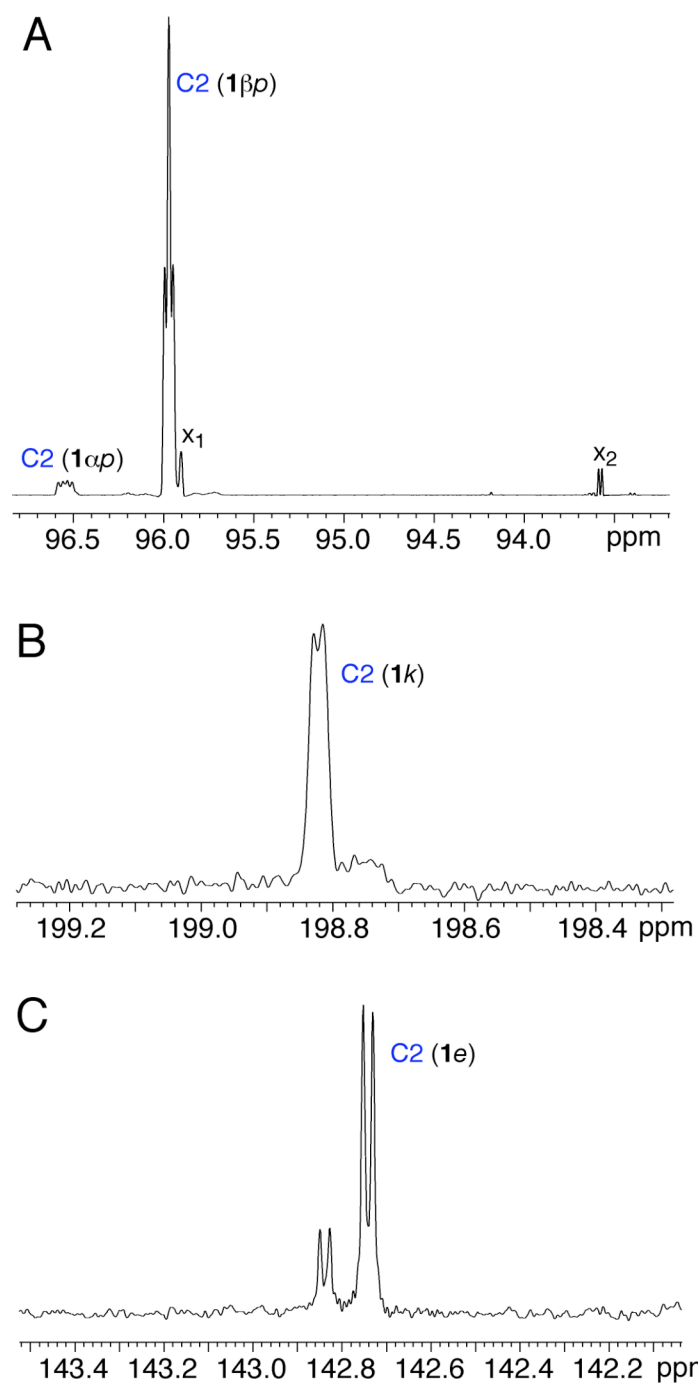
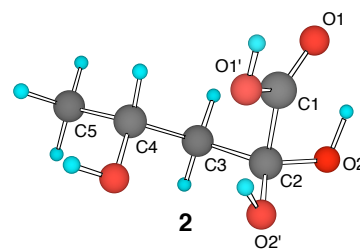


Figure 2.2 Partial ^1H -coupled ^{13}C NMR spectrum (150 MHz) of $[2\text{-}^{13}\text{C}]\mathbf{1}$ at pH 2.0 and 25 $^\circ\text{C}$. (A) Labeled C2 signals of $\mathbf{1}\alpha\text{p}$, $\mathbf{1}\beta\text{p}$ and the two putative C2_{1h} (X_1 and X_2). (B) C2 *keto*. (C) C2 *enol* forms.

Hz (Figure 2.2A). By comparison, C2_{1k} appeared as a broadened doublet with a splitting of ~2.1 Hz (Figure 2.2B).

Inspection of molecular models of **1h** showed that, in geometries having C2 anti to H4, destabilizing 1,3-interactions exist between the C2 and C4 substituents that are likely to render this conformation unstable. Conformations having C2 and H4 gauche would yield a small $^3J_{C2,H4}$ which would be undetectable in the 1H -coupled ^{13}C spectrum. Thus, non-zero J_{CH} values involving C2_{1h} are predicted to involve only the geminal C3 protons. If the signal at 93.60 ppm (X₂) is C2_{1h}, then one $^2J_{CH}$ is ~2.9 Hz and the other is small or zero. Application of the projection rule³² to the three staggered C2-C3 rotamers of **1h** predicted zero values for both $^2J_{CH}$ in one rotamer (that having C1 anti to C4), whereas the remaining two rotamers yielded a zero coupling to one H3 and a negative coupling to the other (Scheme S2). Thus, the observation of a single non-zero $^2J_{CH}$ is consistent with **1h** having C2 gauche to H4, and C1 gauche to C4 (either gauche conformation appears consistent with the experimental couplings). The second putative C2_{1h} signal, X₁, showed small or zero $^2J_{CH}$ values, consistent with **1h** having C2 anti to C5, and C1 anti to C4.



DFT calculations on SA hydrate mimic **2** were conducted to evaluate the effect of C2-C3 bond rotation on calculated $^2J_{C2,H3R/S}$ values and total energies. In these calculations, the C2-C3-C4-C5 torsion angle was fixed at -165° , which gave calculated $^3J_{C2,H4}$ values of ~0.6 Hz consistent with the NMR results. This treatment assumes that the small experimental $^3J_{C2,H4}$ correlates with a relatively rigid C2-C3-C4-H4 torsion

angle of $\sim 75^\circ$ in solution. Conformations of **2** containing a C1-C2-C3-C4 torsion angle of 60° and -60° were found to be lower in energy than that containing a torsion angle of 180° (Figure S7A), favoring assignment of the hydrate C2 signal to X₂. However, calculated $^2J_{C2,H3R/S}$ couplings show that, for torsions near 90° , one coupling is ~ -1.5 Hz and the other ~ -7.5 Hz. These results are in modest agreement with experiment (~ 0 Hz and 3 Hz) for X₂. Other conformational variables not investigated here (e.g., conformation about the C1-C2 bond), and contributions to the experimental couplings made by the ionized form in solution may contribute to the discrepancy.

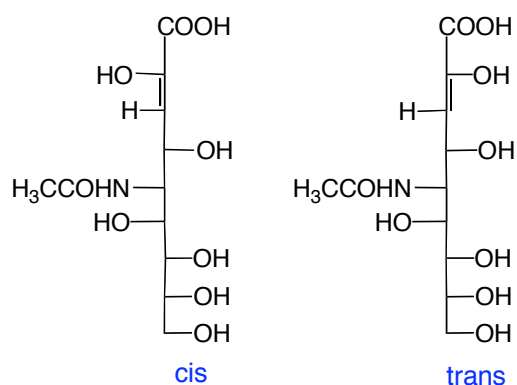
$^1J_{C1,C2}$ and $^1J_{C2,C3}$ values were also computed in **2** as a function of the C2-C3-C4-C5 torsion angle (Figure S7B). Both couplings are relatively insensitive to the C2-C3 bond torsion, with the former considerably larger than the latter. The computed couplings are in reasonable agreement with those observed experimentally for X₂ ($^1J_{C1,C2} = 69.5$ Hz; $^1J_{C2,C3} = 44.0$ Hz).

2.5.3. Acyclic enol forms of **1**.

The $^{13}C\{^1H\}$ NMR spectrum of $[2-^{13}C]\mathbf{1}$ contained relatively strong *labeled* signals at 142.75 and 142.85 ppm (Figure 2.1B). Signals in this spectral region commonly arise from unsaturated carbons. Possible candidates are enol forms **1e** (Scheme 2.1) which exist in cis (E-isomer) and trans (Z-isomer) configurations (Scheme 2.2). Two signals were observed at 150 MHz (a small unassigned signal also appeared at 144.39 ppm; Figure 2.1B), and integration of these signals at pH 2.0 gave a total abundance of $\sim 0.5\%$.

Experimental support for the presence of **1e** was obtained from the $^{13}\text{C}\{^1\text{H}\}$ NMR spectrum of $[\text{3-}^{13}\text{C}]\mathbf{1}$. This spectrum contained intense signals at 40.70 and 39.50 ppm attributed to $\text{C3}_{1\alpha p}$ and $\text{C3}_{1\beta p}$, respectively (data not shown). While additional weaker signals appeared in the same region, they could not be assigned confidently to **1k** and **1h** forms. However, a moderately strong *labeled* signal was observed at 119.85 ppm (Figure 2.3A) which was tentatively assigned to C3 of **1e**.

¹H-Coupled ¹³C NMR spectra of [2-¹³C]**1** and [3-¹³C]**1** were obtained to measure J_{CH} values involving the putative C2 and C3 carbons of **1e**. The putative C2 signals appeared as doublets with $J_{\text{CH}} = 3.2$ Hz (major signal) and 3.4 Hz (minor signal) (Figure 2.2C), consistent with C2 being coupled to H3 ($^2J_{\text{C2,H3}}$) or to H4 ($^3J_{\text{C2,H4}}$). The putative enol C3 signal was split into a doublet of doublets with $^1J_{\text{C3,H3}} = 177.5$ Hz and a longer-range $J_{\text{CH}} = 4.7$ Hz (Figure 2.3B), results consistent with the structure of **1e**. These data indicate that one of the two possible longer-range J_{CH} involving C2 ($^2J_{\text{C2,H3}}$, $^3J_{\text{C2,H4}}$) and C3 ($^2J_{\text{C3,H4}}$, $^3J_{\text{C3,H5}}$) must be small or zero.



Scheme 2.2 Enol forms of 1.

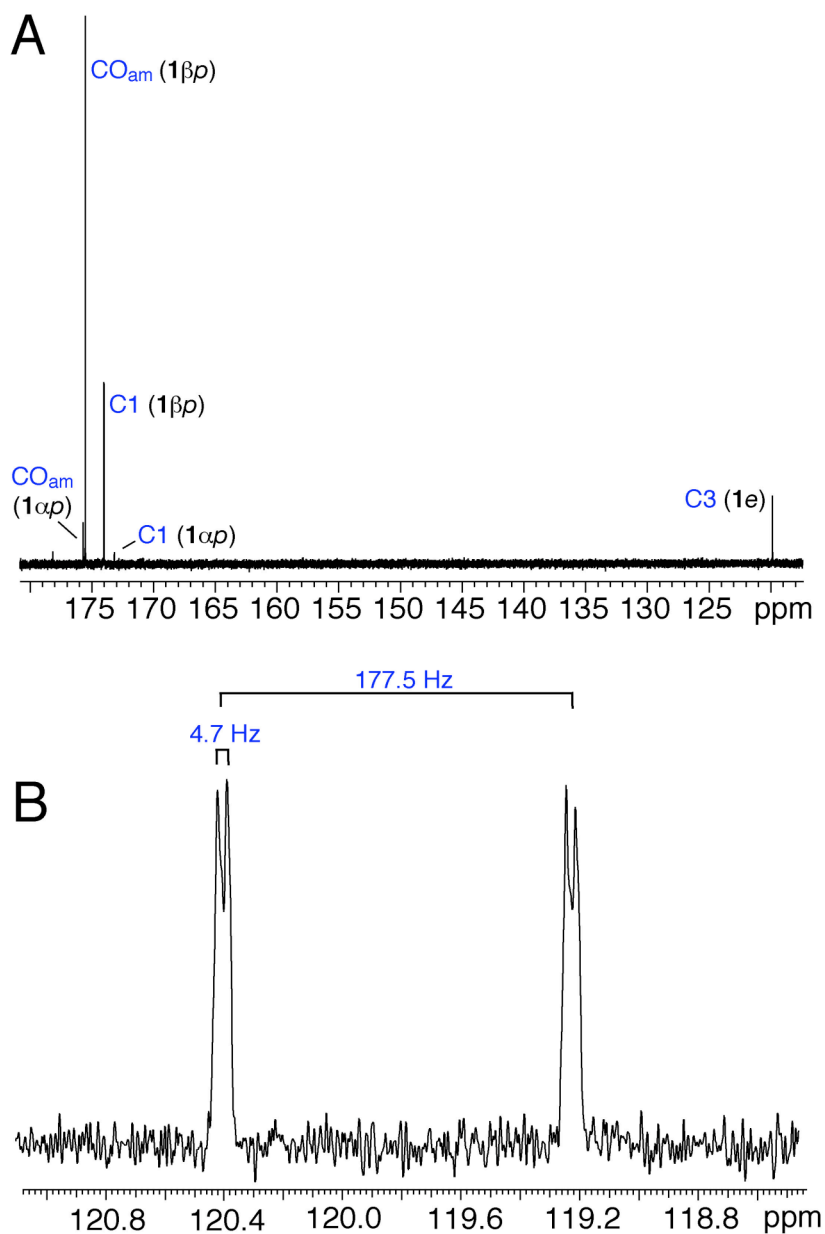
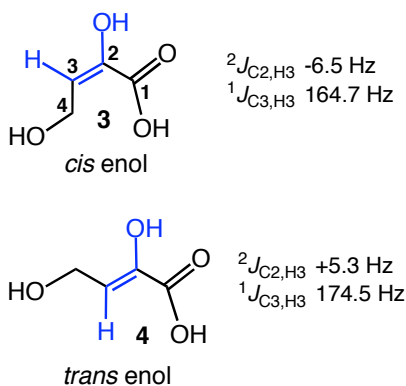


Figure 2.3. Partial $^{13}\text{C}\{^1\text{H}\}$ NMR spectrum of $[3\text{-}^{13}\text{C}]\mathbf{1}$ at pH 2.0 and 25 $^{\circ}\text{C}$. (A) Region showing the natural abundance C1 and amide CO signals of $1\alpha p$ and $1\beta p$, and the labeled C3 signal of $1e$. (B) C3 signal of $1e$ in the ^1H -coupled ^{13}C spectrum, showing the $^1J_{\text{CH}}$ and longer-range J_{CH} .

Given the low intensities of the putative C2 and C3 enol signals and the possibility of attributing their presence to low level contamination, **1** was prepared with contiguous ^{13}C -labeling at C1-C3 to confirm backbone C-C connectivities via $^1J_{\text{CC}}$ and $^2J_{\text{CCC}}$ values. ^{13}C NMR of the tri-labeled sample showed the simultaneous presence of C2 and C3 signals at the expected chemical shifts, in comparable intensities, and with the expected signal multiplicities (Figure 2.4). Backbone connectivity between C2 and C3 was established from the mutual $^1J_{\text{CC}}$ observed in each carbon signal ($^1J_{\text{C2,C3}} = 80.6$ Hz). $^1J_{\text{C1,C2}} = 76.6$ Hz as measured at C2, and $^2J_{\text{C1,C3}} = 12.4$ Hz as measured at C3 (sign unknown).³³ The large $^1J_{\text{C2,C3}}$ is consistent with one-bond couplings in C=C fragments, and $^1J_{\text{C1,C2}}$ is ~ 10 Hz larger than the corresponding coupling in **1** αp and **1** βp at pH 2.0.³⁴ The distinctive values of these couplings also allowed assignment of the weak C1 carbon signal of the enol form at 172.41 ppm (Figure S3). Overall, these results support the conclusion that **1e** is present in aqueous solutions of **1** at low pH.

J_{CH} Values were calculated in enol structural mimics **3** and **4** in their protonated states and with O1 anti to C3 to optimize conjugation of the double bonds (Scheme 2.3).



Scheme 2.3 $^nJ_{\text{CH}}$ values in **3** and **4**

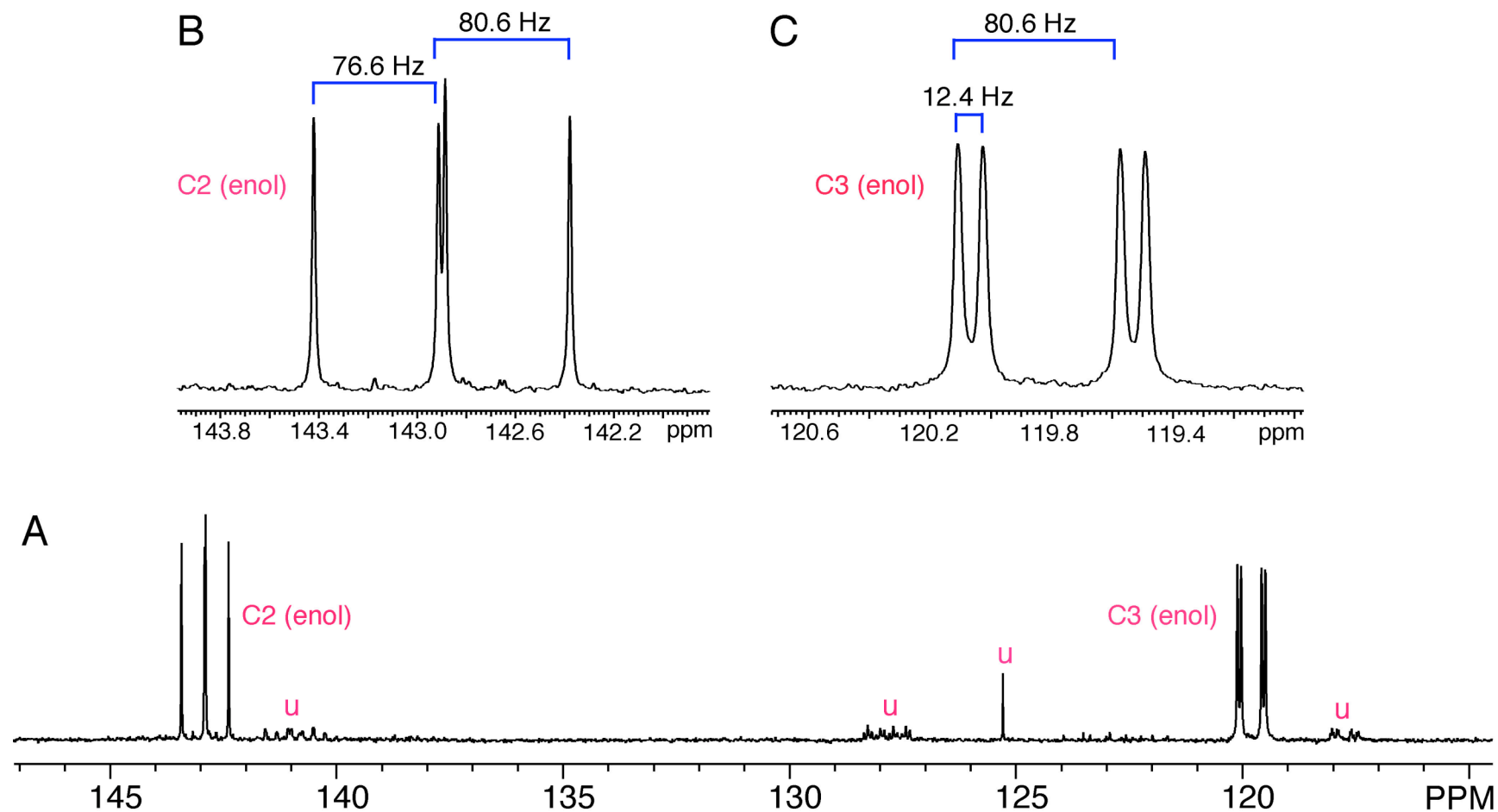
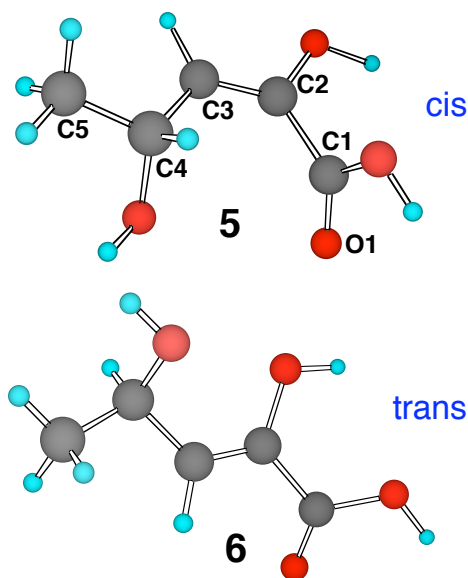


Figure 2.4 (A) Partial $^{13}\text{C}\{^1\text{H}\}$ NMR spectrum of $[1,2,3-^{13}\text{C}_3]\mathbf{1}$ showing the putative C2 and C3 enol signals. Signals labeled as “u” are unknown species, possibly other enols. (B) and (C) Expansions of the C2 and C3 signals showing their multiplicities and constituent $^1J_{\text{CC}}$ and $^2J_{\text{CC}}$ values.

Calculated $^2J_{C2,H3}$ values in **3** and **4** were found to be similar in magnitude, but the coupling in cis enol **3** was negative while that in trans enol **4** was positive. This result suggests that the sign of $^2J_{C2,H3}$ could be used to distinguish between cis and trans enol configurations. $^1J_{C3,H3}$ is ~ 10 Hz larger in the trans enol (Scheme 2.3). Calculations of total energies of both structures showed that the trans configuration **4** is more stable than **3** by ~ 3 kcal/mol.

The effect of C1-C2 and C3-C4 bond rotation on calculated J_{CH} values was investigated in simplified enol mimics **5** and **6** (Scheme 2.4). These structures were geometrically optimized as a function of the C2-C3-C4-C5 torsion angle (90° - 270°) in two O1-C1-C2-C3 torsions (90° and 180°). The latter torsions were chosen to evaluate the effect of double-bond conjugation on the calculated couplings. In most cases, *trans*



Scheme 2.4 Structure of *cis* (**5**) and *trans* (**6**) enol model compounds.

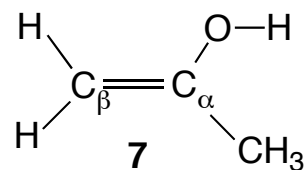
enol **6** was lower in energy than cis enol **5**, although in a few cases the opposite was observed, presumably due to the presence of intramolecular H-bonding in **5** that was not available in **6**. $^2J_{C2,H3}$ values show a significant dependence on the C2-C3-C4-C5 torsion angle (Figure S2). Calculated $^2J_{C2,H3}$ show behavior similar to that found in **4** and **5**; couplings are negative in **5** and positive in **6**. $^2J_{C2,H3}$ values shifted to more negative (less positive) values as the C1-O1 bond was brought into conjugation with the C2-C3 bond. Calculated $^1J_{C3,H3}$ values shift to smaller values in the conjugated form of **5**, whereas conjugation increased $^1J_{C3,H3}$ in **6**. $^1J_{C3,H3}$ is uniformly larger in **6** than in **5** in conjugated systems. The effect of ene configuration is reduced considerably in non-conjugated structures.

$^3J_{C2,H4}$ values calculated in **5** and **6** gave a minimal value of ~ 2 Hz in **6**. The experimental value is predicted to be small or zero (see above). However, it should be noted that the electronegative *N*-acetyl substituent at C5 in **1** will probably affect this coupling, especially if it prefers to orient anti to H4. The latter conformation would reduce $^3J_{C2,H4}$ by > 1 Hz, thus rendering it more consistent with the experimental data.

$^1J_{C1,C2}$, $^1J_{C2,C3}$ and $^2J_{C1,C3}$ values were calculated in **5** and **6** as a function of the C2-C3-C4 C5 torsion angle (Figures S5 and S6). Calculated $^1J_{C2,C3}$ values were larger than $^1J_{C1,C2}$ values, in agreement with experimental observations, although the difference was accentuated in the calculations. Calculated $^2J_{C1,C3}$ values were positive in sign and assumed an average magnitude of ~ 7 Hz compared to the experimental value of 12.4 Hz. It should be appreciated, however, that the effect of the C2-O2 bond torsion on these couplings could be appreciable, mediated by O2 lone-pair effects on C1-C2 and C2-C3

bond lengths. In the present calculations, only one C3-C2-O2-H torsion angle was examined (180°), and presumably appropriate averaging of this torsion that mimics behavior in solution would improve the agreement between experiment and theory.³⁵

Detection of the putative C2 and C3 enol signals in ¹³C NMR spectra of [2-¹³C]**1** and [3-¹³C]**1**, respectively, depended on solution pH. Signals were observed in spectra obtained on solutions at pH 2.0 but not on the same solutions adjusted to pH 7.0. Enol signal detection could be recovered by adjusting solutions at pH 7.0 back to pH 2.0 with HCl.



These observations are consistent with those made for the enol-keto equilibrium of pyruvate, in which the [enol]/[keto] ratio is approximately 100-fold greater for pyruvic acid than for pyruvate anion. An explanation has been offered for this behavior that hinges on the relative stabilities of the keto form in the COOH and COO⁻ forms of pyruvate.²⁷

¹³C NMR chemical shifts for the enol forms of α -ketoacids like **1** have not been well documented in the literature. However, the ¹³C shifts of propen-2-ol **7** (acetone enol) show C α at 156.8 ppm and C β at 95.3 ppm in 2-propanol solvent at 44 °C.³⁶ These shifts provide a crude calibration for the putative C2 and C3 shifts in **1**, and suggest that C2**1_e** should be downfield of C3**1_e**, as observed experimentally.

2.5.4. pK_a Values of tautomers of **1**.

The C2 chemical shifts of **1 α _p**, **1 β _p**, **1 k** and **1 e** exhibited sufficient pH dependencies to allow estimations of pK_a values. Titration data (Figure 2.5) obtained on

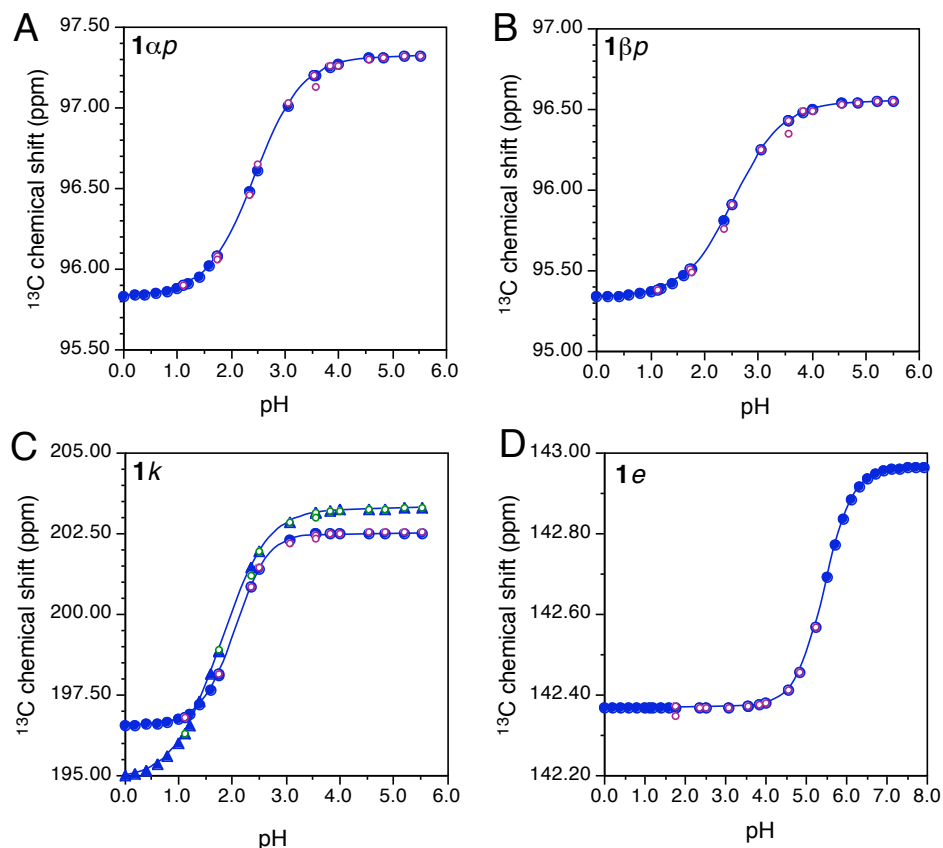


Figure 2.5 Titration of the C2 chemical shifts of $1\alpha p$ (A), $1\beta p$ (2), $1k$ (C) and $1e$ (D). Filled blue circles and blue line are fits to experimental points shown in either red or green.

$[2-^{13}\text{C}]\mathbf{1}$ and fit to a modified form of the Henderson-Hasselbach equation³⁷ gave the following results: $1\alpha p$, 2.5 ± 0.1 ; $1\beta p$, 2.6 ± 0.1 ; $1k$, 2.1 ± 0.1 and 1.8 ± 0.1 ; $1e$, 5.5 ± 2.6 . The large error in the pK_a of $1e$ results from the lack of data points at the higher pHs of the titration (signal detection is lost at the higher pHs). The true pK_a is expected to be close to 5.5 based on visual inspection of the curve (Fig. 5D).

The nearly identical pK_a values for $1\alpha p$ and $1\beta p$ were intermediate in magnitude between those for $1k$ and $1e$, with $1k$ being most acidic. These results are comparable to observations made on pyruvic acid, where pK_a values of keto and enol forms have been

reported to be 1.97 and 3.79, respectively.²⁷ It was not possible to estimate the pK_a of the putative hydrate form of **1** (X_2) since signal intensity decreased rapidly with increasing pH, preventing sufficient digitization of a titration curve.

2.5.5. Exchange Rates Between Tautomers of **1**.

^{13}C Saturation-transfer (ST) experiments³⁷ were conducted on an aqueous solution of $[2-^{13}\text{C}]\mathbf{1}$ at pH 2.0 and 30 °C to identify species in chemical exchange with the open-chain keto form. Selective irradiation of the C2 signal of **1k** did not result in detectable loss of C2 signal intensities of **1 α p**, **1 β p**, **1e** or **1h**, suggesting that the unidirectional rate constants for ring-opening, dehydration and enolization are very slow ($< 0.05\text{ s}^{-1}$). Control ^{13}C ST experiments on aqueous solutions of D- $[1-^{13}\text{C}]\text{threose}$ at pH 2.0 showed strong reduction of the C1 signals from furanose and hydrate forms upon selective irradiation of C1 of the open-chain aldehydo form, as expected.³⁸ ST experiments on SA at higher temperature were not conducted to avoid thermal degradation of the sample.

2.5.6. Solvent Deuterium exchange in **1**.

Given the relatively high abundance of *enol* forms of **1** in aqueous solution, ^1H NMR studies were conducted on unlabeled **1** in $^2\text{H}_2\text{O}$ solvent at $p^2\text{H}$ 8.0 to evaluate the propensity for solvent deuterium exchange at C3. The H3_{ax} and H3_{eq} signals in **1 α p** and **1 β p** were readily detected in $^1\text{H}_2\text{O}$ solvent at pH 8.0 and assigned based on the relative magnitudes of $^3J_{\text{H3ax,H4}}$ and $^3J_{\text{H3eq,H4}}$ (Figure 2.6A). Solvent deuterium exchange was very rapid at $p^2\text{H}$ 8.0 and 25 °C (Figure 2.6B), with virtually full and selective exchange

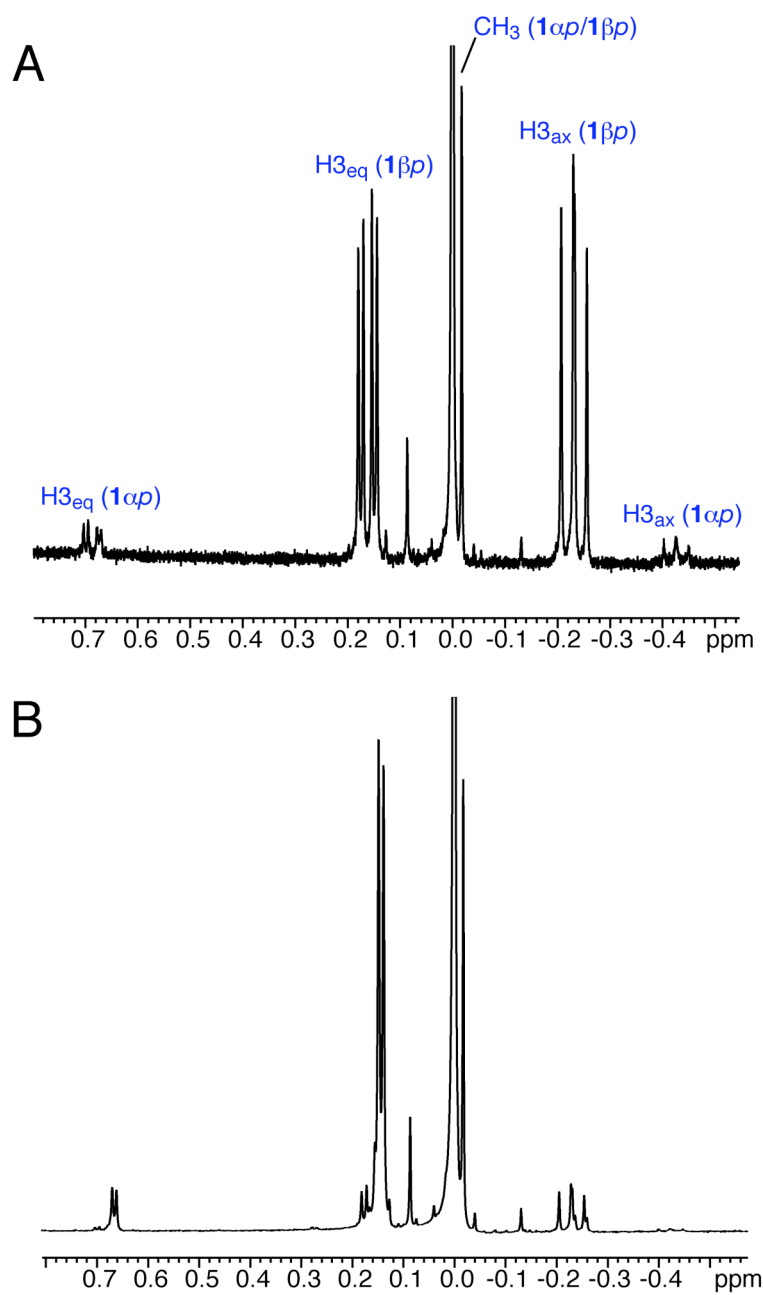
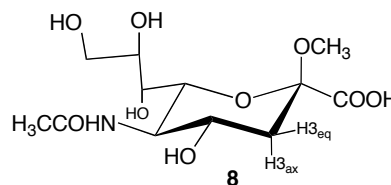


Figure 2.6 Partial ^1H NMR spectrum (600 MHz) of **1** immediately upon dissolution in $^2\text{H}_2\text{O}$ (A) and after incubation at 25 °C for 150 h (B). Signals from H2_{ax} in **1** α *p* and **1** β *p* are nearly absent, whereas those from H2_{eq} are still observable.

observed at H3_{ax} under these conditions after 47 min. ¹H NMR data obtained after extended incubation of the same reaction mixture for 6 days were identical to those obtained after 47 min (spectrum not shown).

The facile and selective exchange of H3_{ax} in **1** α *p* and **1** β *p* presumably occurs via the acyclic *keto* form **1k**. If so, **1k** probably assumes a relatively stable *pseudo-cyclic* conformation in solution containing relatively distinct and persistent C3-H3_{ax} and C3-H3_{eq} bond orientations to account for the observed selectivity. ¹H/²H Exchange



via cyclic structures was eliminated through studies of 2-*O*-methyl- β -D-*N*-acetylneuraminic acid (**8**). A ²H₂O solution of **8** was titrated from an initial p²H of 1.8 to 12.0 with NaO²H. In contrast to the exchange properties of **1**, solvent exchange was not observed in **8** at either H3_{ax} or H3_{eq} after 21 days at p²H 12.0 and 25 °C.

2.6.Conclusions

Aqueous solutions of *N*-acetyl-neuraminic acid **1** contain mainly β -pyranose form, with the α -pyranose second in abundance. In addition to cyclic forms, three acyclic forms can be detected at low levels (0.5 - 1.9% at pH 2). These acyclic forms are difficult to observe by ¹³C NMR at natural abundance, but measurement with ¹³C-labeled samples, especially singly labeled at C2, greatly improves their detection and quantification.

The characteristic ¹³C chemical shifts of the keto form make its detection and quantification relatively straightforward, whereas the presence of hydrate and enol forms

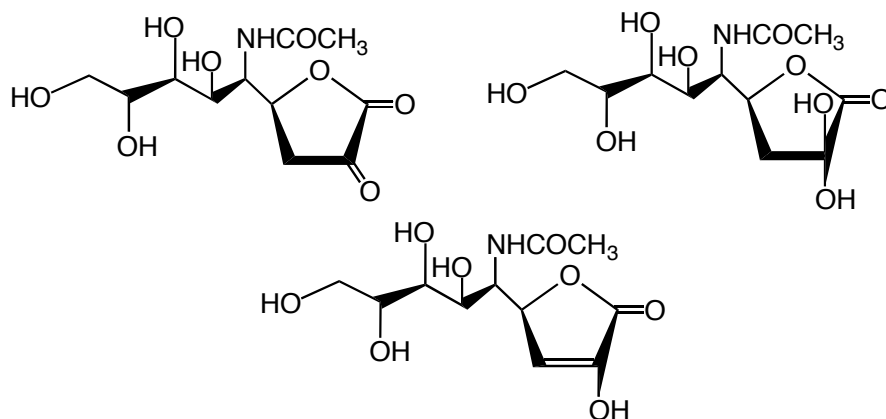
is not easily confirmed. The latter is due to the relatively scant literature of ^{13}C chemical shifts for these forms, and the underlying concern that weak signals observed in spectra may be due to low-level contamination of the sample.

Observation of C2 signals consistent with SA enol form in solution were followed up by measurements on the $[3-^{13}\text{C}]$ and $[1,2,3-^{13}\text{C}_3]$ isotopomers. The data, when taken in total, strongly support the presence of detectable levels of SA enol in solution. While the dominant configuration could not be confirmed, DFT measurements suggest that the trans form is likely to be preferred. DFT calculations further predict that the two enol configurations can be distinguished based on the different signs of $^2J_{\text{C2,H3}}$ in their structures. This observation may prove useful in further characterization of these and related species.

Of the three acyclic monomeric forms of SA, confirmation of the presence of keto hydrate proved most challenging, and the present data might not be considered unequivocal. However, when the present data are viewed in total, a likely C2 hydrate signal emerges (X_2).

Exploitation of the pH dependencies of the C2 chemical shifts yielded pK_a values for the cyclic, keto and enol forms of SA. The enol form is least acidic, and it is assumed that this titration is of the COOH group, not the enol C2 OH. Presumably raising the pH above 6-7, where enol form abundance decays, results in the ionization of the enol C2 OH, thus destabilizing the enol due to the presence of two negative charges in close proximity.

Particularly striking about ^{13}C NMR spectra of ^{13}C -labeled SA is the presence of weak but reproducible signals that cannot be attributed to the major cyclic and acyclic monomeric forms of the molecule. This is in direct contrast to prior studies of ^{13}C -labeled aldopentoses⁸ and aldohexoses⁹ where essentially all signals arising from labeled species could be assigned to monomeric forms. Identification of these unknown species was not attempted, but it is noted that SA lactonization can potentially occur in aqueous solution, especially at low pH, giving structures shown in Scheme 2.5. These species may account for the “extra” keto, enol and hydrate signals observed in ^{13}C spectra of ^{13}C -labeled SA. In addition to monomeric lactones, intermolecular dimerization and oligomerization (esterification) involving COOH and OH functionalities in different SA molecules could also contribute to these weak signals, with their relative intensities dependent on SA concentration.



Scheme 2.5 Potential lactones of **1** (keto, keto hydrate, and enol forms).

DFT calculations conducted on structural mimics of **1h** and **1e** served to provide supplemental information on which to base signal assignments. It should be appreciated,

however, that these calculations have some inherent assumptions at their core which were not fully tested, especially with regard to preferred conformation in solution. Related to this is the fact that SA experiences facile solvent deuterium exchange in aqueous solution, and this exchange occurs considerably more rapidly at the axial H3 site in **1 α p** and **1 β p**. This rapid exchange correlates with the fairly high abundance of keto form in solution. The selective exchange implies that the acyclic keto form probably retains some cyclic character, possibly assuming a pseudo-cyclic conformation in which H3_{ax} and H3_{eq} retain orientations similar to those found in the cyclic pyranoses.

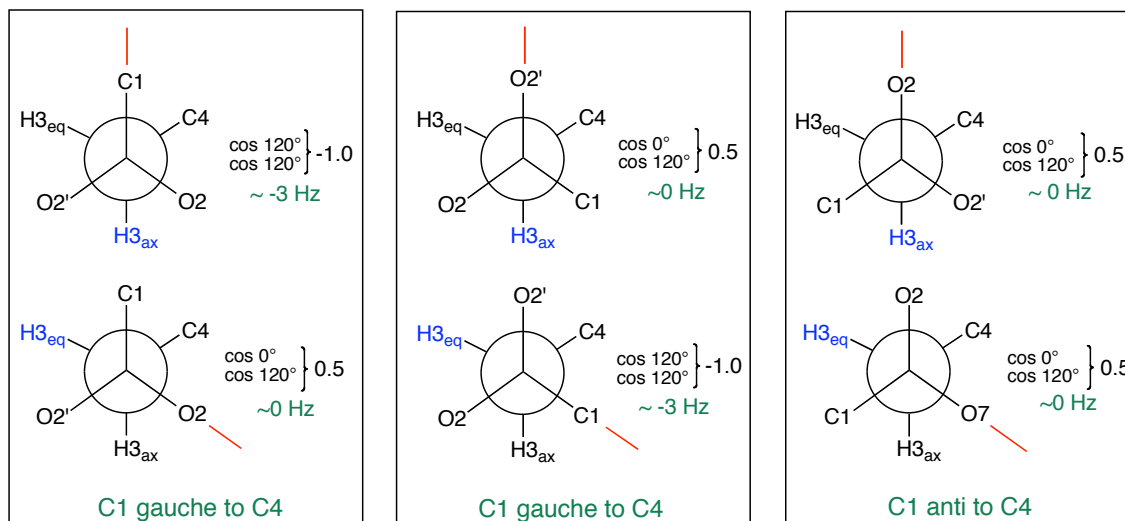
The fact that solutions of SA contain acyclic keto, hydrate and enol forms may have implications for its biological functions. At low pHs uncharacteristic of most biological environments, enol and hydrate forms are relatively abundant in aqueous solution. However, as pH approaches the physiological value of ~ 7.0 , these forms decrease substantially, thus reducing (but not necessarily eliminating) the likelihood of their functioning as substrates in enzyme catalyzed reactions. However, in subcellular regions of low pH (e.g., lysosomes) or in the low pH environment of stomach, these forms are more prevalent and could play a role in biological catalysis. The extent to which these solution behaviors influence SA biological function remains to be explored.

2.7. Acknowledgements

This work was supported by a grant (to A.S.) from the National Institutes of Health (GM059239). The Notre Dame Radiation Laboratory is supported by the Office of Basic Energy Sciences of the United States Department of Energy. This is Document

No. NDRL-4742 from the Notre Dame Radiation Laboratory. The authors thank Omicron Biochemicals Inc. for the generous gift of the ^{13}C -labeled sialic acids.

2.8.Supporting Information



Scheme 2.6 (S1) Projections for $^2J_{\text{C2},\text{H3}_{\text{ax}}}$ and $^2J_{\text{C2},\text{H3}_{\text{eq}}}$ in **1h** conformers and predicted couplings.

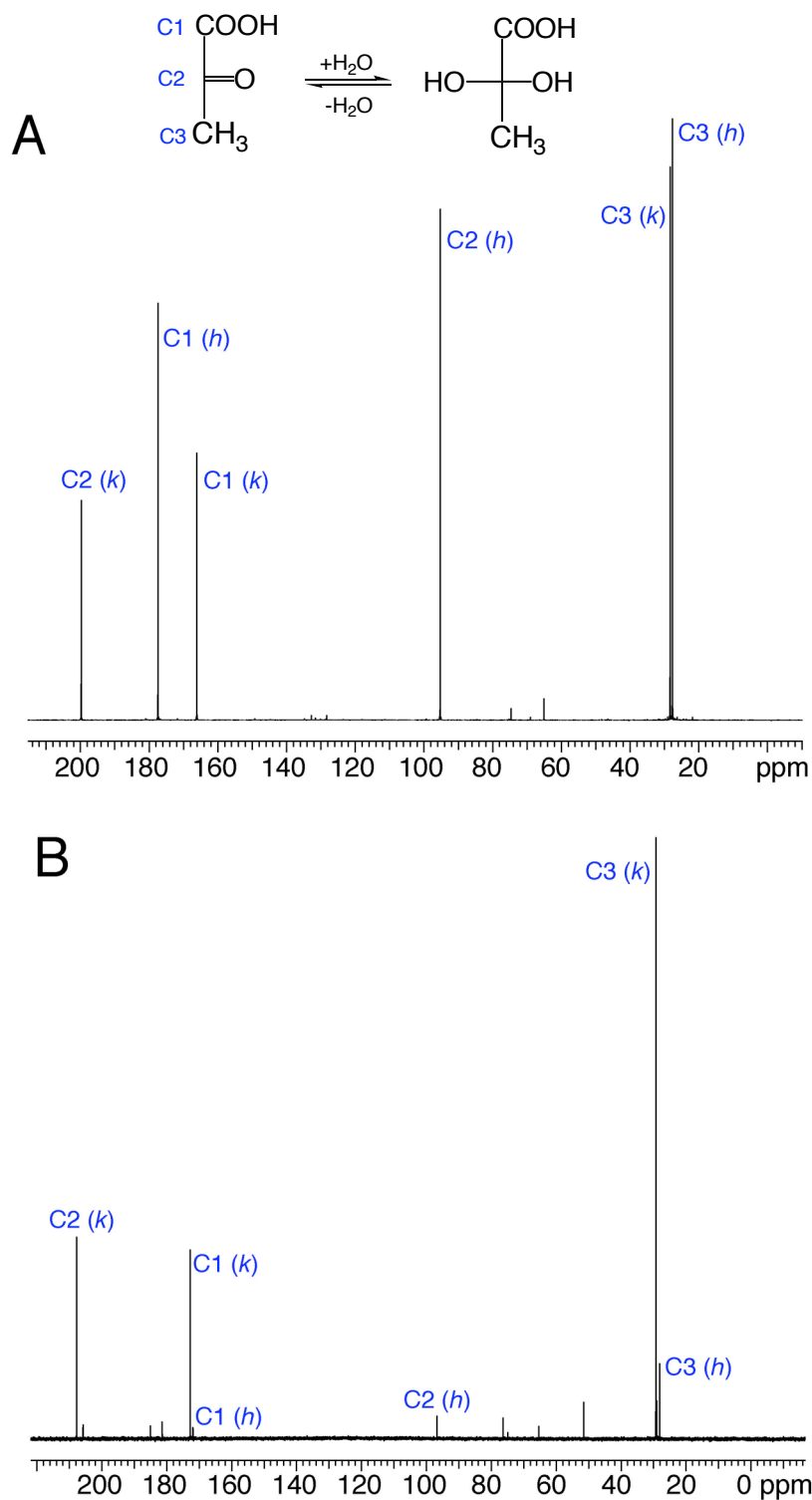


Figure 2.7 (S1) $^{13}\text{C}\{^1\text{H}\}$ NMR spectra (150 MHz) of (A) pyruvic acid and (B) sodium pyruvate. Note the significant reduction in the *hydrate/keto* ratio in aqueous solutions of the sodium salt. Weak signals in both spectra were not assigned; in (A), signals at ~130 ppm may be due to *enol* forms.

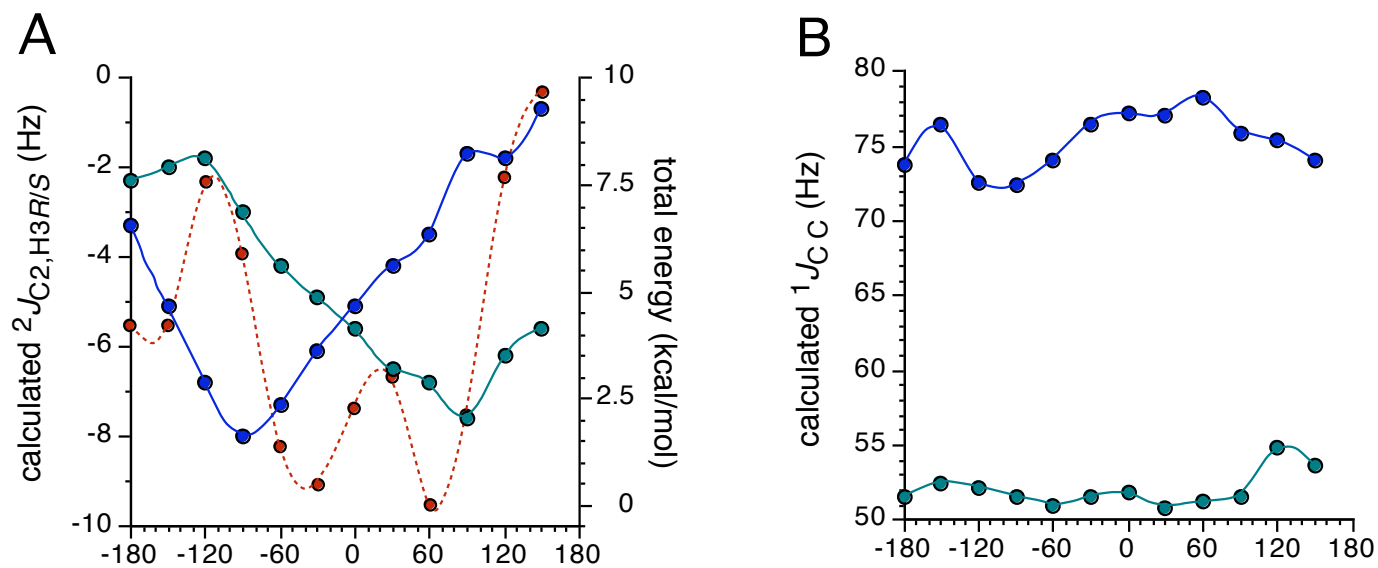


Figure 2.8. (S2) Effect of the C2-C3-C4-C5 torsion angle on calculated total energies, ${}^2J_{C2,H3R/S}$ and ${}^1J_{CC}$ values in **2**. (A) Total energies (brown); ${}^2J_{C2,H3R}$ (blue); ${}^2J_{C2,H3S}$ (green). (B) ${}^1J_{C1,C2}$ (blue); ${}^1J_{C2,C3}$ (green).

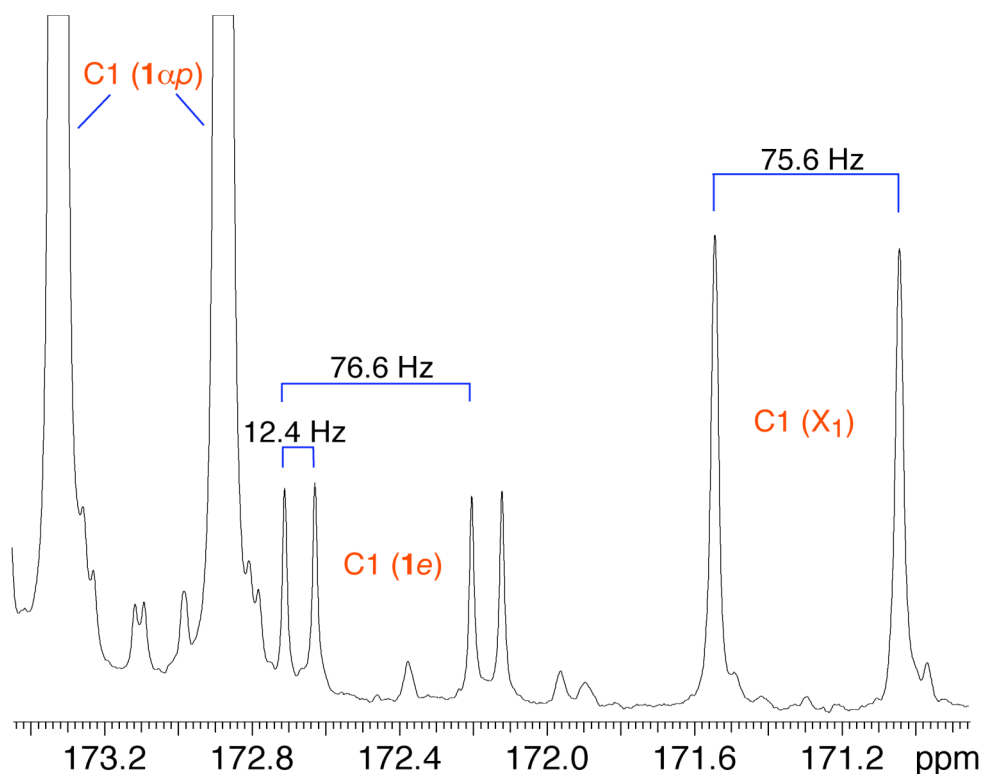


Figure 2.9. (S3) Partial $^{13}\text{C}\{^1\text{H}\}$ NMR spectrum (150 MHz) of $[1,2,3\text{-}^{13}\text{C}_3]\mathbf{1}$ at pH 2.0 showing the relatively intense C1 signals of $\mathbf{1}\alpha p$ (offscale at 173.1 ppm) slightly downfield of the C1 signals of $\mathbf{1e}$ (172.4 ppm). The latter doublet of doublets contains $^1J_{\text{C1,C2}}$ and $^2J_{\text{C1,C3}}$ values identical to those observed at C2 of $\mathbf{1e}$ (Figure 2.4). The upfield doublet at 171.3 ppm contains a $^1J_{\text{C1,C2}}$ equal that observed in the C2 signal of hydrate species X_1 (Figure S4), thus identifying C1 of this species. Comparison of these data to those in Figure 2.1B reveals the low levels of $\mathbf{1e}$ and X_1 relative to that of $\mathbf{1}\alpha p$.

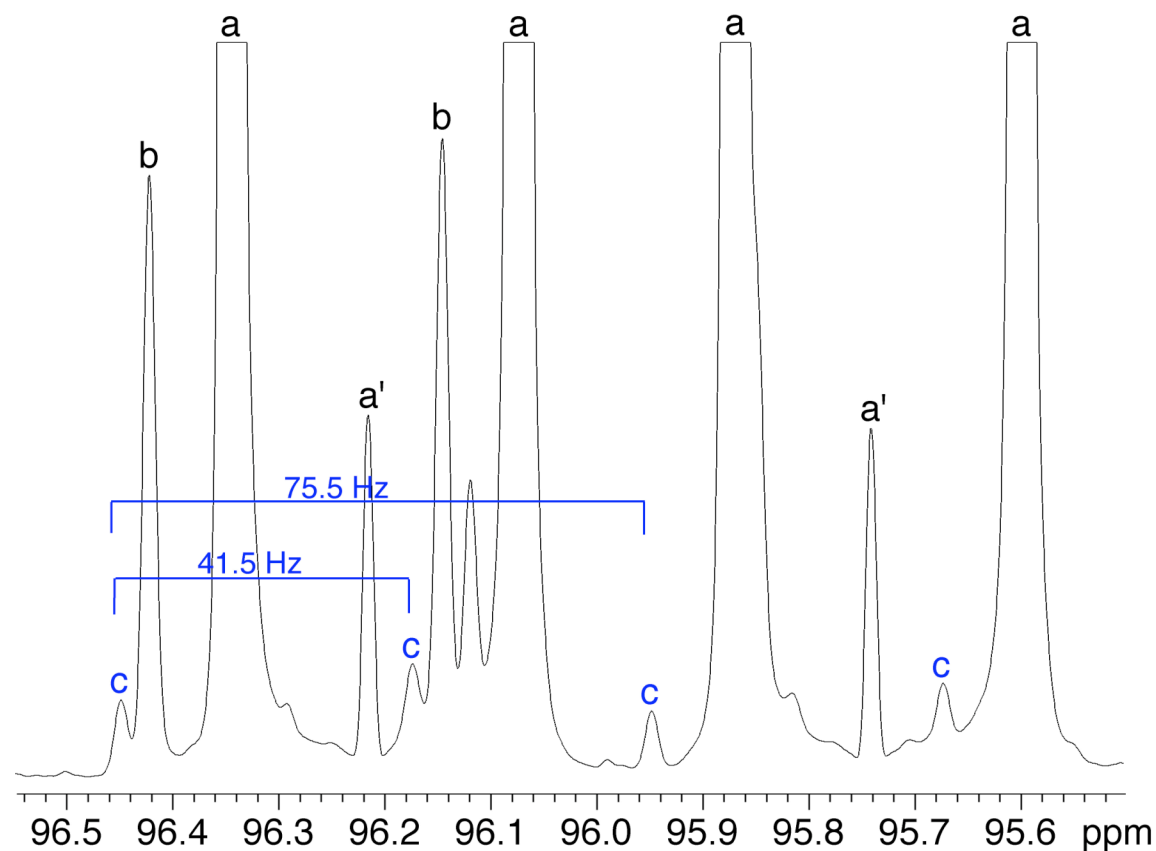


Figure 2.10. (S4) Partial $^{13}\text{C}\{^1\text{H}\}$ NMR spectrum (150 MHz) of $[1,2,3-^{13}\text{C}_3]\mathbf{1}$ at pH 2.0 showing the very intense C2 signals of $\mathbf{1}\beta p$ (a; doublet of doublets; $^1J_{\text{C1,C2}} = 70.1$ Hz, $^1J_{\text{C2,C3}} = 41.0$ Hz), the upfield half of the C2 signals of $\mathbf{1}\alpha p$ (b; $^1J_{\text{C1,C2}} = 67.6$ Hz, $^1J_{\text{C2,C3}} = 41.7$ Hz), and the C2 signals of hydrate species X_1 (c). Note that the $^1J_{\text{CC}}$ values measured from C2 of X_1 are identical to those observed at C1 of X_1 (Figure S3). Signals a' arise from the $[1,2-^{13}\text{C}_2]$ isotopomer of $\mathbf{1}$ present in the sample.

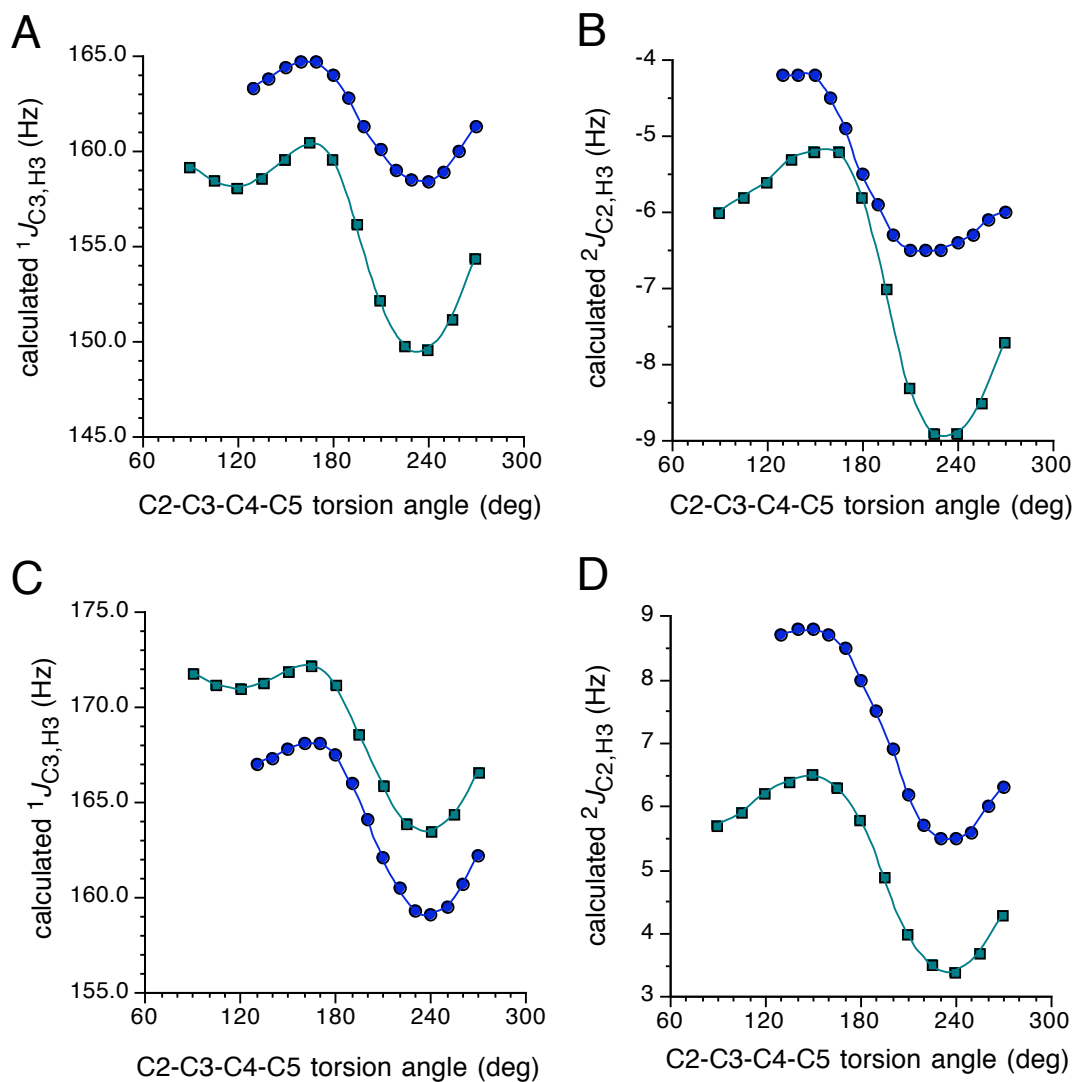


Figure 2.11. (S5) Effect of the C2-C3-C4-C5 torsion angle on calculated J_{CH} values in **5** and **6**. (A) $^1J_{C3,H3}$ in **5**. (B) $^2J_{C2,H3}$ in **5**. (C) $^1J_{C3,H3}$ in **6**. (D) $^2J_{C2,H3}$ in **6**. Blue circles; O1-C1-C2-C3 torsion angle of 90° (fixed). Green squares; O1-C1-C2-C3 torsion angle of 180° (fixed).

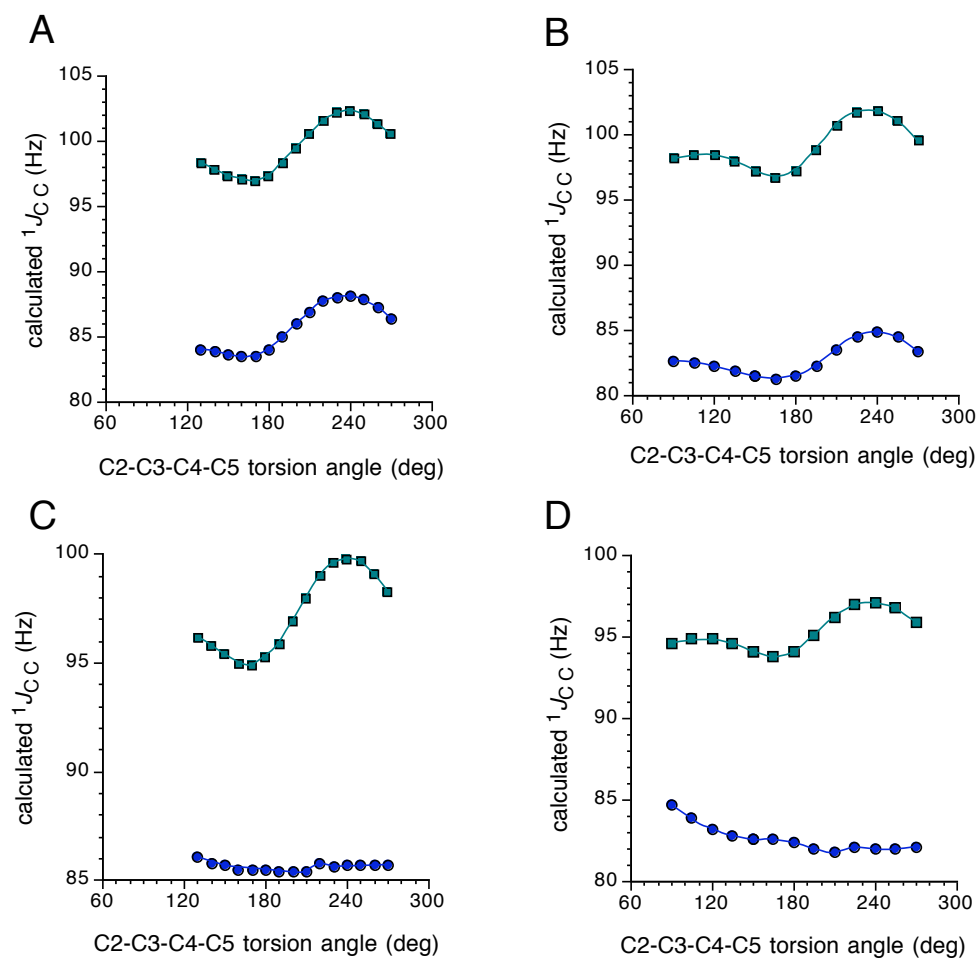


Figure 2.12. (S6) Effect of the C2-C3-C4-C5 torsion angle on calculated $^1J_{CC}$ values in **5** and **6**. Blue circles, $^1J_{C1,C2}$. Green squares, $^1J_{C2,C3}$. (A) **5** with the C1-C2-C3-C4 torsion angle at 90°. (B) **5** with the C1-C2-C3-C4 torsion angle at 180°. (C) **6** with the C1-C2-C3-C4 torsion angle at 90°. (D) **6** with the C1-C2-C3-C4 torsion angle at 180°.

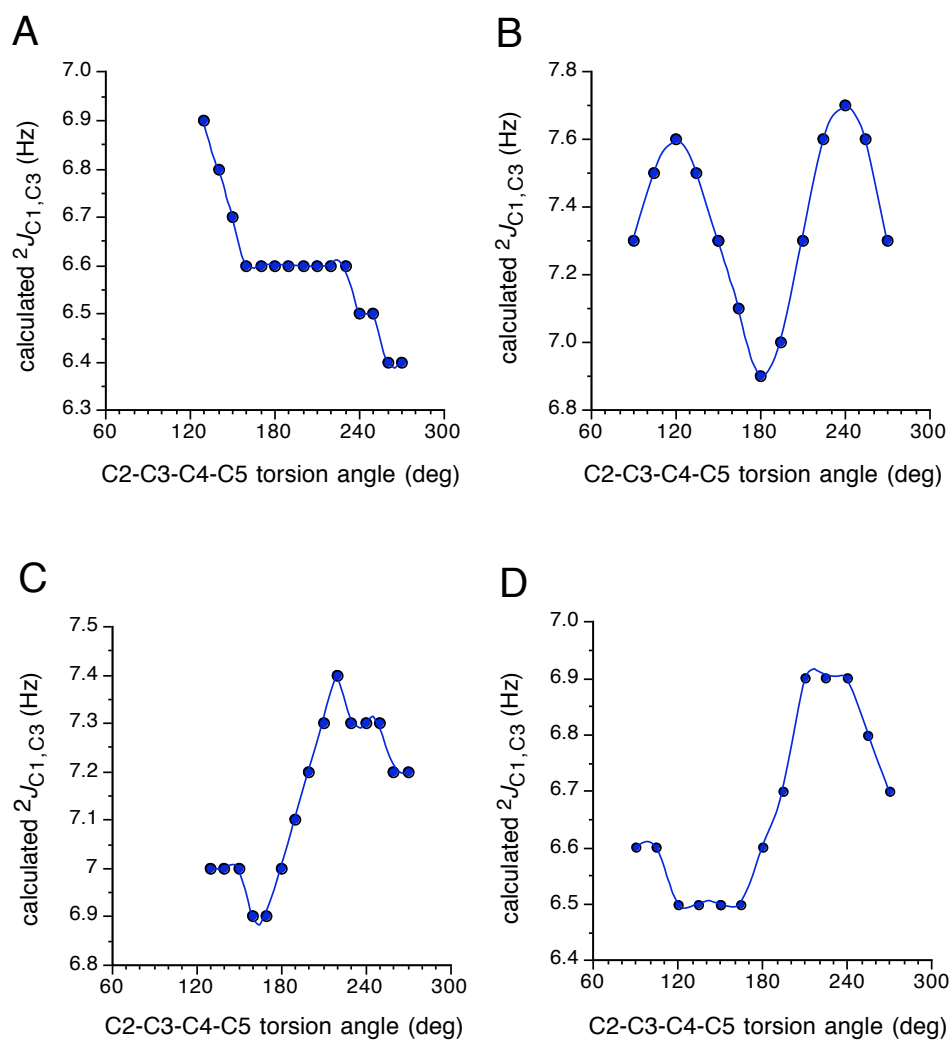


Figure 2.13. (S7) Effect of the C2-C3-C4-C5 torsion angle on calculated $^2J_{C1,C3}$ values in **5** and **6**. (A) **5** with the C1-C2-C3-C4 torsion angle at 90° . (B) **5** with the C1-C2-C3-C4 torsion angle at 180° . (C) **6** with the C1-C2-C3-C4 torsion angle at 90° . (D) **6** with the C1-C2-C3-C4 torsion angle at 180° .

2.9.References

1. Dwek, R.A.; Lellouch, A.C.; Wormald, M.R. *J. Anat.* **1995**, *187*, 279-292.
2. Wormald, M.R.; Rudd, P.M.; Harvey, D.J.; Chang, S.-C.; Scragg, I.G.; Dwek, R.A. *Biochemistry* **1997**, *36*, 1370-1380.
3. Breton, C.; Snajdrova, L.; Jeanneau, C.; Koca, J.; Imberty, A. *Glycobiology* **2006**, *16*, 29R - 37R.
4. Kaneko, Y.; Nimmerjahn, F.; Ravetch, J.V. *Science* **2006**, *313*, 670-673.
5. Maru, I.; Ohnishi, J.; Ohta, Y.; Tsukada, Y. *J. Biosci. Bioeng.* **2002**, *93*, 258-265.
6. Tanner, M.E. *Bioorg. Chem.* **2005**, *33*, 216-228.
7. Maple, S.R.; Allerhand, A. *J. Am. Chem. Soc.* **1987**, *109*, 3168-3169.
8. Drew, K.N.; Zajicek, J.; Bondo, G.; Bose, B.; Serianni, A.S. *Carbohydr. Res.* **1998**, *307*, 199-209.
9. Zhu, Y.; Zajicek, J.; Serianni, A.S. *J. Org. Chem.* **2001**, *66*, 6244-6251.
10. Czarniecki, M.F.; Thornton, E.R. *J. Am. Chem. Soc.* **1977**, *99*, 8273-8279.
11. Tropper, F. D.; Andersson, F. O.; Grand-Maitre, C.; Roy, R. *Carbohydr Res.* **1992**, *229*, 149-154
12. Frisch, M.J.; Trucks, G.W.; Schlegel, H.B.; Scuseria, G.E.; Robb, M.A.; J.R.; Montgomery, Jr., J.A.; Vreven, T.; Kudin, K.N.; Burant, J.C.; Millam, J.M.; Iyengar, S.S.; Tomasi, J.; Barone, V.; Mennucci, B.; Cossi, M.; Scalmani, G.; Rega, N.; Petersson, G.A.; Nakatsuji, H.; Hada, M.; Ehara, M.; Toyota, K.; Fukuda, R.; Hasegawa, J.; Ishida, M.; Nakajima, T.; Honda, Y.; Kitao, O.; Nakai, H.; Klene, M.; Li, X.; Knox, J.E.; Hratchian, H.P.; Cross, J.B.; Adamo, C.; Jaramillo, J.; Gomperts, R.; Stratmann, R.E.; Yazyev, O.; Austin, A.J.; Cammi, R.; Pomelli, C.; Ochterski, J.W.; Ayala, P.Y.; Morokuma, K.; Voth, G.A.; Salvador, P.; Dannenberg, J.J.; Zakrzewski, V.G.; Dapprich, S.; Daniels, A.D.; Strain, M.C.; Farkas, O.; Malick, D.K.; Rabuck, A.D.; Raghavachari, K.; Foresman, J.B.; Ortiz, J.V.; Cui, Q.; Baboul, A.G.; Clifford S.; Cioslowski, J.; Stefanov, B.B.; Liu, G.; Liashenko, A.; Piskorz, P.; Komaromi, I.; Martin, R.L.; Fox, D.J.; Keith, T.; Al-Laham, M.A.; Peng, C.Y.; Nanayakkara, A.; Challacombe, M.; Gill, P.M.W.; Johnson, B.; Chen, W.; Wong, M.W.; Gonzalez, C.; Pople, J.A. *Gaussian03*, Revision A.1, Gaussian, Inc., Pittsburgh PA, 2003.

13. Becke, A.D. *J. Chem. Phys.* **1993**, *98*, 5648-5652.
14. Hehre, W.J.; Ditchfield, R.; Pople, J.A. *J. Chem. Phys.* **1972**, *56*, 2257-2261.
15. Cloran, F.; Zhu, Y.; Osborn, J.; Carmichael, I.; Serianni, A.S. *J. Am. Chem. Soc.* **2000**, *122*, 6435-6448.
16. Cloran, F.; Carmichael, I.; Serianni, A.S. *J. Am. Chem. Soc.* **2001**, *123*, 4781-4791.
17. Kowalewski, J.; Laaksonen, A.; Roos, B.; Siegbahn, P. *J. Chem. Phys.* **1979**, *71*, 2896-2902.
18. Helgaker, T.; Watson, M.; Handy, N. C. *J. Chem. Phys.* **2000**, *113*, 9402.
19. Sychrovsky, V.; Grafenstein, J.; Cremer, D. *J. Chem. Phys.* **2000**, *113*, 3530.
20. Stenutz, R.; Carmichael, I.; Widmalm, G.; Serianni, A.S. *J. Org. Chem.* **2002**, *67*, 949-958.
21. The chemical shift of C2_{1βp} (free acid) was assigned as described previously (Gervay, J.; Batta, G. *Tetrahedron Lett.* **1994**, *35*, 3009-3012) using internal dioxane (δ 67.4 ppm) as the reference. All ¹³C NMR spectra of **1** at pH 2 were referenced in this fashion.
22. Edward, J.T. *Chem. Ind.* **1955**, 1102.
23. Lemieux, R.U. in *Molecular Rearrangements*, de Mayo, P., ed., Interscience Publishers, New York, 1964, p. 709.
24. Juaristi, E.; Cuevas, G. *The Anomeric Effect*, CRC Press, Boca Raton, 1995.
25. Serianni, A.S.; Pierce, J.; Barker, R. *Biochemistry* **1979**, *18*, 1192-1199.
26. Vuorinen, T.; Serianni, A.S. *Carbohydr. Res.* **1990**, *209*, 13-31.
27. Chiang, Y.; Kresge, A.J.; Pruszyński, P. *J. Am. Chem. Soc.* **1992**, *114*, 3103-3107.
28. Greenzaid, P.; Luz, Z.; Samuel, D. *J. Am. Chem. Soc.* **1967**, *89*, 749-756.
29. Pocker, Y.; Meany, J.E.; Nist, B.J.; Zadorojny, C. *J. Phys. Chem.* **1969**, *73*, 2872-2882.
30. Cooper, A.J.L.; Redfield, A.G. *J. Biol. Chem.* **1975**, *250*, 527-532.

31. ^1H NMR data showed significantly different (absolute) $^2J_{\text{C2,H3ax}}$ and $^2J_{\text{C2,H3eq}}$ values in **1 α p** (7.7 Hz and 4.3 Hz, respectively), whereas nearly identical couplings were observed in **1 β p** (\sim 3.6 Hz). As reported previously for $^3J_{\text{C1,H3ax}}$ and $^3J_{\text{C1,H3eq}}$ (Hori, H.; Nakajima, T.; Nishida, Y.; Ohru, H.; Meguro, H. *Tetrahedron Lett.* **1988**, 29, 6317-6320), $^2J_{\text{C2,H3ax}}$ and $^2J_{\text{C2,H3eq}}$ can be used to distinguish between **1 α p** and **1 β p** (Klepach, T.; Zhang, W.; Carmichael, I.; Serianni, A.S., submitted)
32. Bock, K.; Pedersen, C. *Acta Chem. Scand.* **1977**, B31, 354-358.
33. These values differ from those measured in **1k** ($^1J_{\text{C1,C2}} \cong 65.1$ Hz, $^1J_{\text{C2,C3}} \cong 42.2$ Hz) and for **1h** (**X**₂) ($^1J_{\text{C1,C2}} = 69.5$ Hz, $^1J_{\text{C2,C3}} = 44.0$ Hz).
34. Klepach, T.; Zhang, W.; Carmichael, I.; Serianni, A.S., submitted.
35. DFT calculations on **6** in which the C1-C2-O2-H and C3-C2-O2-H torsion angles were fixed at 60° and -60° , respectively, gave calculated $^2J_{\text{C1,C3}}$ values of +8.8 and +9.0 Hz, respectively (C2-C3-C4-C5 torsion fixed at 180°). These results confirm that the effect of the C2-O2 bond torsion on $^2J_{\text{CCC}}$ values in unsaturated systems mimics that observed in saturated systems (Klepach T.; Carmichael, I.; Serianni, A.S., unpublished results).
36. Moniz, W.B.; Sojka, S.A.; Poranski, Jr., C.F.; Birkle, D.L. *J. Am. Chem. Soc.* **1978**, 100, 7940.
37. The following equation was used to fit the NMR chemical shift data: δ (pH) = $[\delta_{\text{base}} + \delta_{\text{acid}} \times 10^{n(\text{pKa}-\text{pH})}] / [1 + 10^{n(\text{pKa}-\text{pH})}]$, where δ_{acid} and δ_{base} are the chemical shifts at the acid and base plateaus and n = Hill coefficient. Parameters δ_{base} , δ_{acid} , pK_a and n were optimized simultaneously during the data fit using the Solver Routine in Microsoft *Excel*.
38. Serianni, A.S.; Pierce, J.; Huang, S.-G.; Barker, R. *J. Am. Chem. Soc.* **1982**, 104, 4037 – 4044.

CHAPTER 3:

^{13}C - ^1H AND ^{13}C - ^{13}C NMR J -COUPLINGS IN ^{13}C -LABELED N -ACETYL-NEURAMINIC ACID: CORRELATIONS WITH MOLECULAR STRUCTURE²

“Truth, in Science, can be defined as the working hypothesis best fitted to open the way to the next better one.”

–Konrad Lorenz

3.1. Abstract

N -Acetyl-neuraminic acid (**2**) was prepared enzymatically containing single sites of ^{13}C -enrichment at C1, C2 and C3. Aqueous solutions of the three ^{13}C isotopomers were studied by ^1H and ^{13}C NMR spectroscopy at p²H 2 and pH 8 to obtain J_{CH} and J_{CC} values involving the labeled carbons. Experimental studies were complemented by DFT calculations of the same set of J -couplings in protonated and ionized structural mimics of **2** to determine how well theoretical predictions match the experimental findings in saccharide systems bearing ionizable functionality. Results show that (a) $^2J_{\text{C2,H3ax/eq}}$ values in **2** depend on anomeric configuration, complementary to $^3J_{\text{C1,H3ax/eq}}$ behavior,

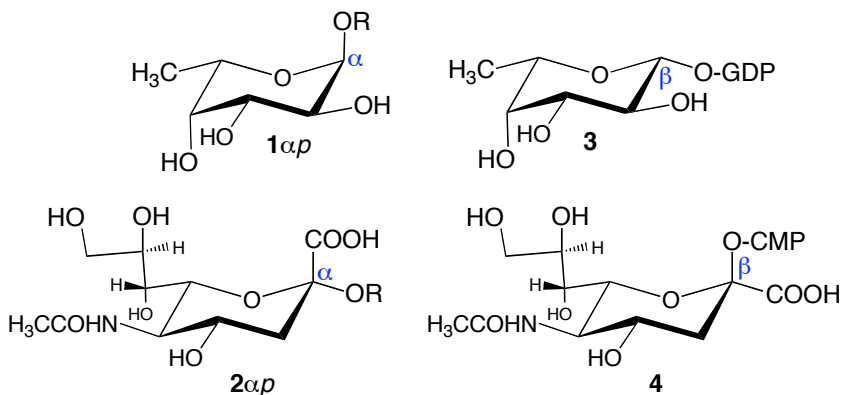
² I gratefully acknowledge my co-authors Wenhui Zhang, Ian Carmichael and Anthony S. Serianni for their assistance in preparing this chapter, which is submitted to the Journal of Organic Chemistry.

(b) J_{CH} and J_{CC} values involving C2 depend on anomeric configuration, the C1-C2 bond torsion and on solution pH, and (c) long-range $^4J_{C2,H7}$ can be used to evaluate glycerol side-chain conformation. All intra-ring J_{HH} values in **2** appear largely unaffected by solution pH. *In vacuo* DFT calculations of J_{CH} and J_{CC} values do not reproduce the experimental data well. When solvent is included in these calculations, however, the theoretical results are in much better agreement with experiment. The present work provides new information for the future treatment of trans-glycoside couplings involving NeuAc residues by (a) providing new standard values of intra-ring J_{CC} having coupling pathways that mimic those for trans-glycoside J_{CC} , (b) identifying the potential effects of solution pH on trans-glycoside couplings inferred through the behavior of related intra-ring couplings, and (c) providing specific guidelines for more accurate DFT calculations of J_{CH} and J_{CC} values in ionizable saccharides.

3.2. Introduction

Mammalian glycobiology can be distinguished from the glycobiology of other organisms based on the involvement of two monosaccharide building blocks, L-fucose (6-deoxy-L-galactose, Fuc) (**1**) and *N*-acetyl-neuraminic acid (NANA, NeuAc, sialic acid, SA) (**2**). Glycoproteins such as human IgG¹ contain **1** in the α -pyranosyl form (**1 α p**), whereas the biological glycosyl donor, GDP-L-fucose (**3**), contains **1** in the β -configuration. The α -ketoacid, NeuAc, is also incorporated into glycoproteins in its α -pyranose configuration (**2 α p**), and like **3**, the corresponding biological glycosyl donor, CMP-sialic acid (**4**), contains **2** in the β -configuration. Incorporation of both

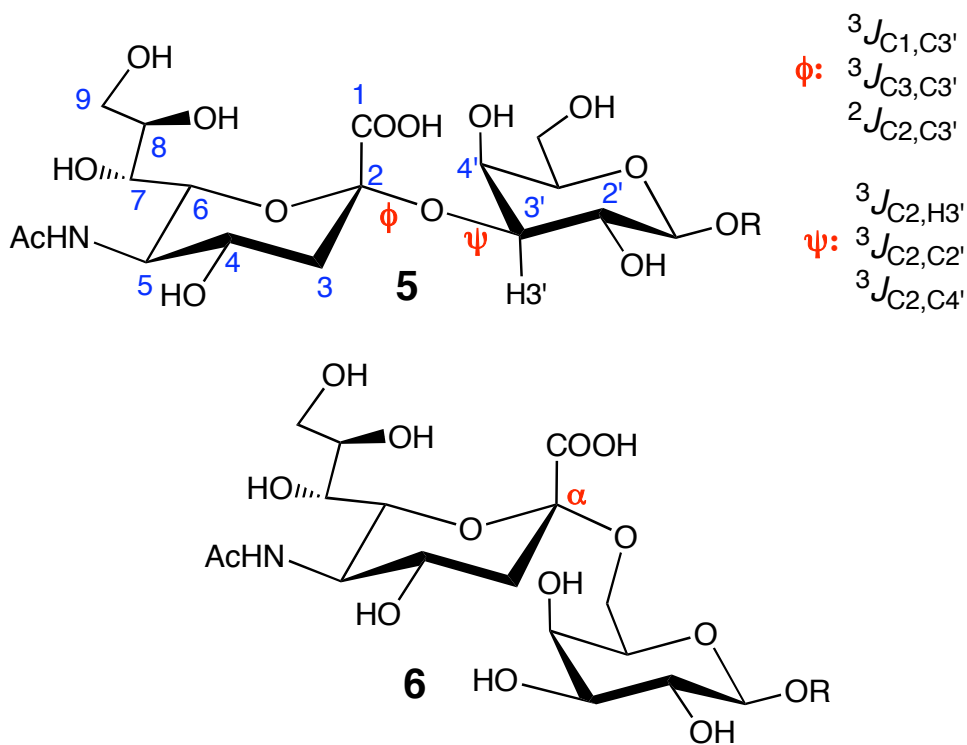
monosaccharides into a growing oligosaccharide chain, catalyzed by appropriate glycosyltransferases, involves inversion of configuration at the anomeric center of both donor sugars.²⁻⁴



NeuAc residues are important in human biology and pathology. These residues are commonly found as terminal residues on N-linked oligosaccharide chains of glycoproteins or glycolipids, and are accessible for binding to various biological agents. For example, NeuAc residues found on the outer lining of the stomach cavity during inflammation serve as binding sites for *H. pylori*, the causative agent of peptic ulcers.⁵ The H₅N₁ virus associated with avian flu is released from its host cell membrane through the action of a viral neuraminidase (sialidase), which cleaves the cell surface viral NeuAc receptor.⁶ The antiviral agent, oseltamivir (TamifluTM), inhibits this enzyme, thus preventing the release of viral progeny and stifling the proliferation of the disease.^{6,7} Removal of terminal NeuAc residues from human glycoproteins such as IgG targets the protein for clearance and degradation.⁸

NeuAc in N-glycans of human glycoproteins is commonly found linked glycosidically to Gal in either α -(2 \rightarrow 3) (**5**) or α -(2 \rightarrow 6) (**6**) linkages (Scheme 3.1). The conformational properties of these linkages remain poorly characterized, partly because

only one $^3J_{\text{COCH}}$ coupling exists across them (Scheme 3.1) (this also pertains to linkages involving 2-ketosugars), in contrast to two $^3J_{\text{COCH}}$ across linkages involving aldopyranosyl rings. The common ^1H - ^1H NOE in oligosaccharides between protons

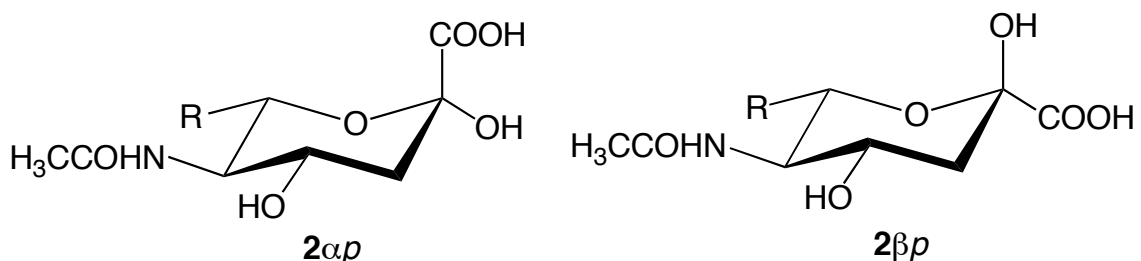


Scheme 3.1. α -(2 \rightarrow 3) and α -(2 \rightarrow 6) Glycosidic Linkages Involving **2**, and Trans-Glycoside J -Couplings Across an α -(2 \rightarrow 3) Linkage.

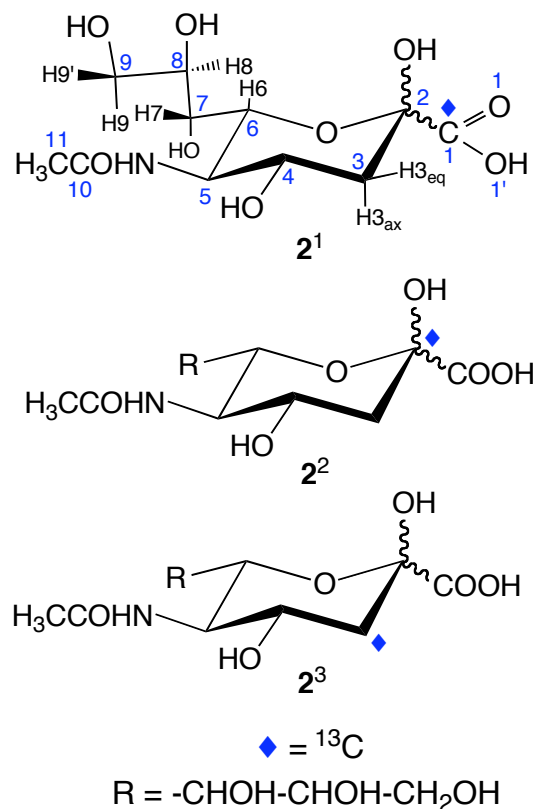
appended to the linkage carbons is also absent. However, useful structural information is potentially available from the five trans-glycoside (inter-residue) J_{CC} values across NeuAc glycosidic linkages (Scheme 3.1). A prerequisite to the use of these couplings as potential probes of linkage conformation is knowledge of their structural dependencies, and a first step towards achieving this aim is an understanding of J_{CC} values within NeuAc itself. For example, intra-ring coupling in **5** between C1 and C6 is similar in character to the trans-glycoside J -coupling between C1 and C3'. Likewise, intra-ring

coupling between C2 and C7 in **5** is similar to the trans-glycoside J -coupling between C2 and C2'/C4' (Scheme 3.1).

Free NeuAc exists in aqueous solution in five monomeric forms: α - (**2 α p**) and β - (**2 β p**) pyranoses, keto (**2k**), keto hydrate (**2h**), and enol (**2e**) (Scheme S1).⁹ The β -



pyranose **2 β p** is highly predominant (~91%), followed by **2 α p** (~6%). In the presentwork, three NeuAc isotopomers containing selective ¹³C-labeling at C1, C2 and C3 (denoted **2¹**, **2²** and **2³**, respectively; Scheme 3.3) were employed to permit measurements of intra-ring J_{CH} and J_{CC} values in aqueous solution involving the labeled carbons of **2 α p** and **2 β p**. Since ionization state may influence these couplings, measurements were conducted at p²H 2.0 and pH 8.0 where the carboxyl group is largely protonated and deprotonated, respectively. Experimental studies were complemented by density functional theory (DFT) calculations of J_{CH} and J_{CC} in structural mimics in protonated and ionized states. Since the experimental ¹³C-¹H and ¹³C-¹³C J -couplings in **2** pertain to conformationally rigid pathways, they can be compared to corresponding calculated couplings to determine the accuracy of the latter in a saccharide capable of ionization. This type of comparison has not been reported previously and contributes to the long-term goal of interpreting trans-glycoside J_{CH} and J_{CC} across NeuAc glycosidic linkages where conformational flexibility is possible and reliance on theoretical calculations to predict their magnitudes essential.



Scheme 3.2. ^{13}C Isotopomers of **2** and Atomic Numbering.

3.3. Experimental Methods

3.3.1. ^{13}C -Labeled N-Acetyl-neuraminic Acid (**2**¹, **2**² and **2**³).

Compounds **2**¹⁻³ were obtained from Omicron Biochemicals, Inc. (South Bend, IN) and were used without further purification.

3.3.2. NMR Spectroscopy.

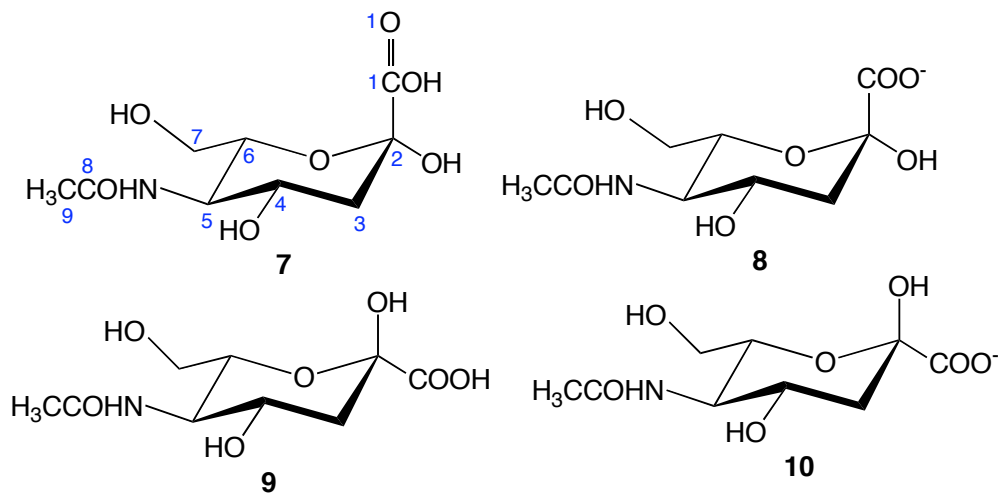
For solutions at p²H 2.0 or 8.0, solid samples of **2**¹, **2**² or **2**³ were dissolved in ²H₂O and the solution p²H was adjusted to 2.0 or 8.0 using NaO²H. For solutions at pH 2.0 or 8.0, solid samples were dissolved in distilled water and adjusted to pH 2.0 or 8.0

with NaOH. Sample concentrations were ~ 100 mM for ^1H and ~ 300 mM for ^{13}C NMR analyses.

High-resolution ^1H and $^{13}\text{C}\{^1\text{H}\}$ NMR spectra were collected at 600 and 150 MHz, respectively at ~ 25 °C in 3-mm NMR tubes using a 3-mm $^{13}\text{C}/^1\text{H}$ microprobe (Nalorac). Digital resolutions for ^1H and $^{13}\text{C}\{^1\text{H}\}$ spectra were typically <0.02 Hz/pt and <0.1 Hz/pt, respectively. Spectra were processed with different degrees of resolution enhancement to improve the detection and measurement of smaller J_{HH} , J_{CH} and J_{CC} values.

3.4. Computational Methods

Model structures **7-10** were chosen for theoretical studies of J_{HH} , J_{CH} and J_{CC} . These structures mimic the protonated and ionized forms of **2** in the α - (**7/8**) and β -pyranose (**9/10**) in the $^1\text{C}_4$ ring conformation. Geometric optimization was performed in *Gaussian03*¹⁰ using density functional theory (DFT) with the B3LYP functional¹¹ and the 6-31G* basis set¹² as described previously.^{13,14a}



Four series of calculations were conducted to give a total of 16 data sets (four per structure). In all sets, the O1-C1-C2-O6 torsion angle (see structure 7 for atom numbering) was varied in 30° increments through 360°. In all sets, the C6-C7-O7-H and H4-C4-O4-H torsion angles were fixed at 180°, the O6-C6-C7-O7 torsion angle was fixed at 60°, and the H5-C5-N5-H and C5-N5-C8-C9 torsion angles were set initially at 180° and allowed to optimize (Scheme S2). The C3-C2-O2-H torsion was fixed at 180° in Series 1 and 3, whereas it was set initially at 180° and allowed to optimize in Series 2 and 4. Series 1/2 and 3/4 were otherwise identical except that the former pair involved *in vacuo* calculations, whereas the latter pair included the effects of solvent water (see below). Data from each series are distinguished throughout the manuscript with the following symbolism, illustrated here for structure 7: **7^{FX}** (Series 1), **7^{FL}** (Series 2), **7^{FXS}** (Series 3) and **7^{FLS}** (Series 4).

J-Couplings were calculated in *Gaussian03* using DFT (B3LYP) and a [5s2p1d|3s1p] basis set.^{14b} The reported couplings contain both Fermi and non-Fermi contact contributions and are unscaled. The effect of solvent water on the computed couplings (Series 3 and 4) was evaluated using the Self-Consistent Reaction Field (SCRF)^{14c} and the Integral Equation Formalism (polarizable continuum) model (IEFPCM)^{14d} and the [5s2p1d|3s1p] basis set as implemented in *Gaussian03*.

3.5. Results and Discussion

3.5.1. General Considerations.

The ¹H NMR spectrum of NeuAc is dominated by signals arising from **2βp** (Figure 3.1);¹⁵⁻¹⁷ signal assignments are given in Table S1 at p²H 2.0 and pH 8.0. The detection of **2αp** was difficult, and only H3_{ax}, H3_{eq} and the *N*-acetyl methyl protons

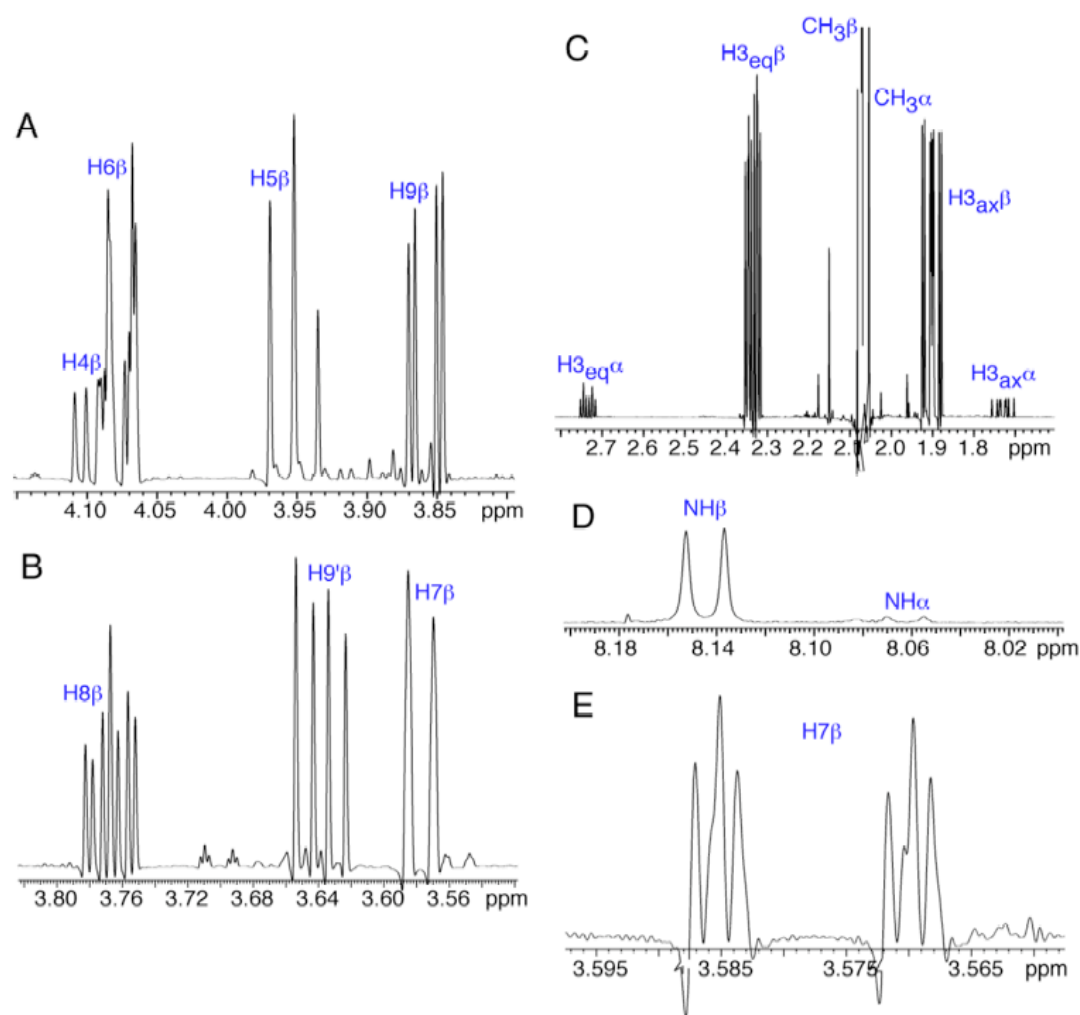


Figure 3.1. Expanded regions of the resolution-enhanced ^1H NMR spectrum of $[2-^{13}\text{C}]\mathbf{2}$ at $p^2\text{H}$ 2.0 and 25°C showing signal assignments. The amide signals in (D) were very weak due to the small percentage of molecules containing ^1H at the NH site in $^2\text{H}_2\text{O}$. The $\text{H}_{7\beta}$ signal in (B) is expanded in (E) to show the presence of two $^3J_{\text{HH}}$ and the long-range $^4J_{\text{C}2,\text{H}7}$.

could be assigned with confidence to this form. In **2** α *p* and **2** β *p*, the H3_{ax} signal is more shielded than that of H3_{eq}, and the difference in their chemical shifts is more pronounced for **2** α *p* (~1 ppm) than for **2** β *p* (~0.4 ppm). ¹H signals arising from the exchangeable NH protons of the *N*-acetyl side chain were observed at ~8 ppm, appearing as a weak doublet at p²H 2.0 and an exchange-broadened singlet at pH 8.0 (Figure S1). The effect of amide proton exchange was also evident at the H5 β signal, which appeared as a well-resolved triplet at p²H 2.0 and an exchange-broadened triplet at pH 8.0 in unlabeled **2** (Figure S2).

¹H NMR spectra of **2**¹⁻³ were initially obtained at p²H 2.0 and p²H 8.0. While the former spectra were interpretable (Figure 3.1) and are discussed below, the latter spectra were devoid of H3_{ax}/H3_{eq} signals, and contained a doublet for the H4 signal of **2** β *p*, when solutions were allowed at stand for extended time prior to analysis. Similar effects were observed in ¹³C NMR spectra at p²H 8.0, with the C3 signals difficult to detect under these conditions. Further investigation confirmed that solvent deuterium exchange at C3 is facile (Scheme S3), with more rapid exchange observed for H3_{ax} than for H3_{eq} in **2** α *p* and **2** β *p*.¹⁶ The present *J*-coupling studies at high pH were conducted in 95/5 (v/v) H₂O/²H₂O to eliminate this complication.

The ¹³C NMR spectrum of **2** (Figure 3.2) contained well resolved signals for both pyranoses,¹⁷⁻²⁰ allowing complete signal assignments at p²H 2.0 and pH 8.0 (Table S2). ¹³C{¹H} NMR spectra of **2**¹, **2**² and **2**³ contained doublets due to ¹*J*_{CC} which were used to confirm the C1-C4 signal assignments. The C5-C7 signals were assigned based on an analysis of longer-range *J*_{CC}. The C8 and C9 signals were assigned based on the expected chemical shifts of 1° and 2° alcoholic carbons.

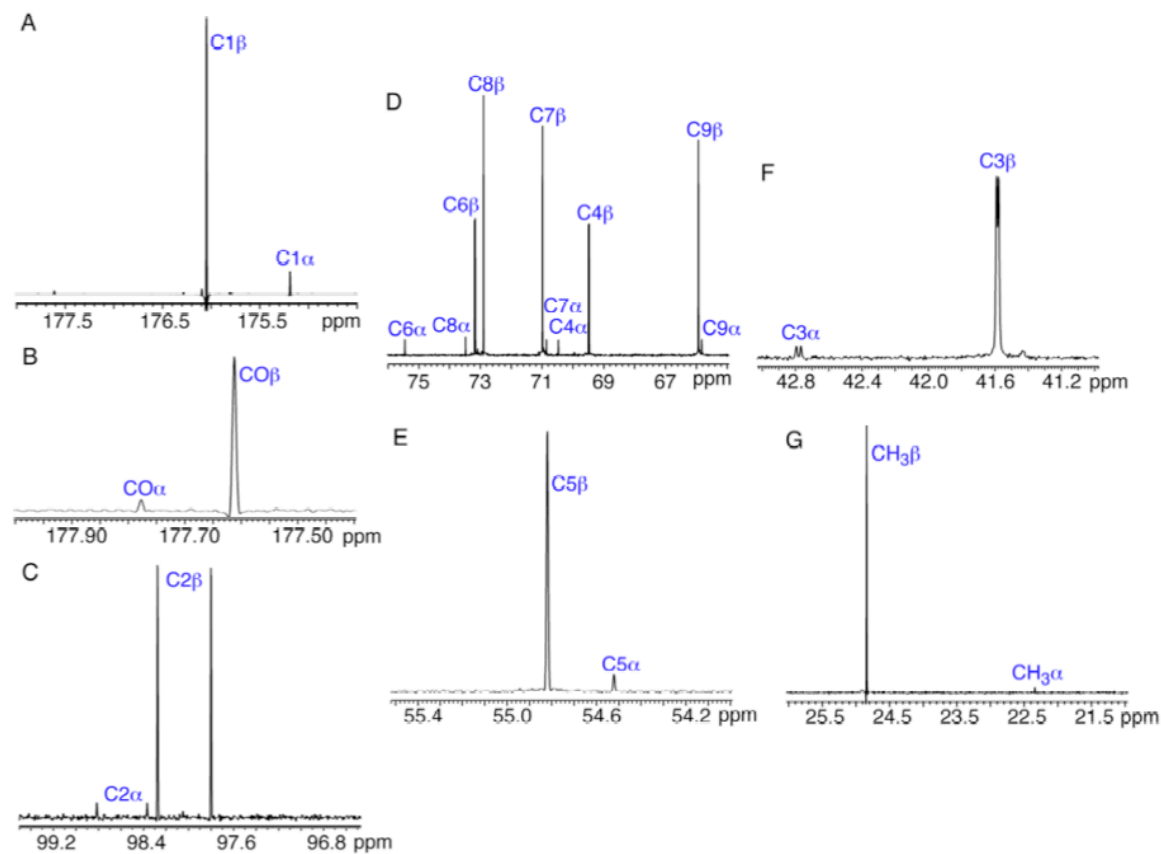


Figure 3.2. Expanded regions of the $^{13}\text{C}\{^1\text{H}\}$ NMR spectrum of $[1-^{13}\text{C}]\mathbf{2}$ at $p^2\text{H}$ 2.0 and 25 $^\circ\text{C}$. The C2 signals (C) show the presence of the large $^1J_{\text{C1,C2}}$, and smaller longer range couplings are observed at C6 β ($^3J_{\text{C1,C6}}$) (D) and C3 α/β ($^2J_{\text{C1,C3}}$) (F).

3.5.2. Conformational Properties of the C1-C2 Bond.

The energetics of C1-C2 bond rotation in **2** was investigated by DFT since this rotation could affect *J*-couplings involving carbons and protons near the carboxyl group.

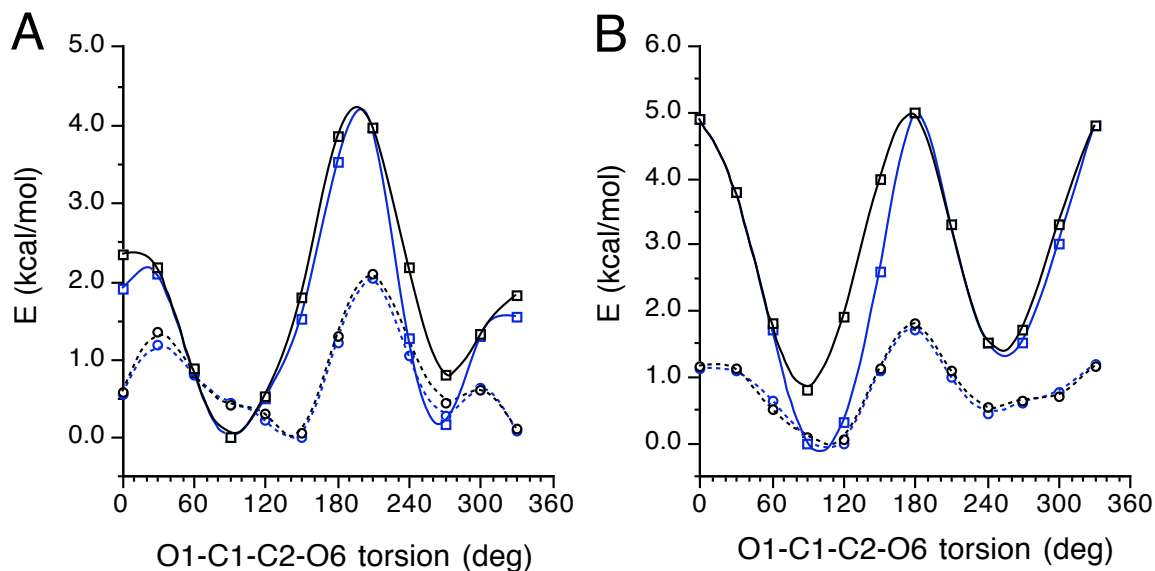


Figure 3.3. The effect of C1-C2 bond rotation on the total energies of protonated **7** (A) and **9** (B). *In vacuo* data are shown as solid lines, and solvated (water) data are shown as dotted lines. Black symbols = FX series, blue symbols = FL series.

The effect of C1-C2 bond rotation in protonated **2 α p** and **2 β p** on total energy is shown in Figure 3.3. *In vacuo* energy profiles show significantly larger amplitudes than do solvated profiles. The effect of fixing the C2-O2 bond torsion is small, and some phase-shifting was observed possibly due to H-bonding in some *in vacuo* conformations. This H-bonding is presumably suppressed in the corresponding solvated conformations. For **2 β p**, *in vacuo* and solvated data show the same global minimum at ~90°, and a local minimum at ~-90°. The dampened barriers in the solvated data suggest considerable

conformational sampling. For **2** αp , *in vacuo* and solvated data differ with respect to the location of the global minimum and the shape of the curve near this minimum. The solvated data suggest that torsions between 90° - 150°, and between 0° - -90°, are nearly isoenergetic, with the global minimum at ~150°. Conformational flexibility about the C1-C2 bond appears greater in **2** αp than in **2** βp . In **2** αp , multiple steric interactions between the COOH group and the pyranose ring are possible, and exert a leveling effect on the energetics, whereas in **2** βp , the equatorial COOH group is subject to less steric interactions and is thus more likely to favor a more limited set of conformations.

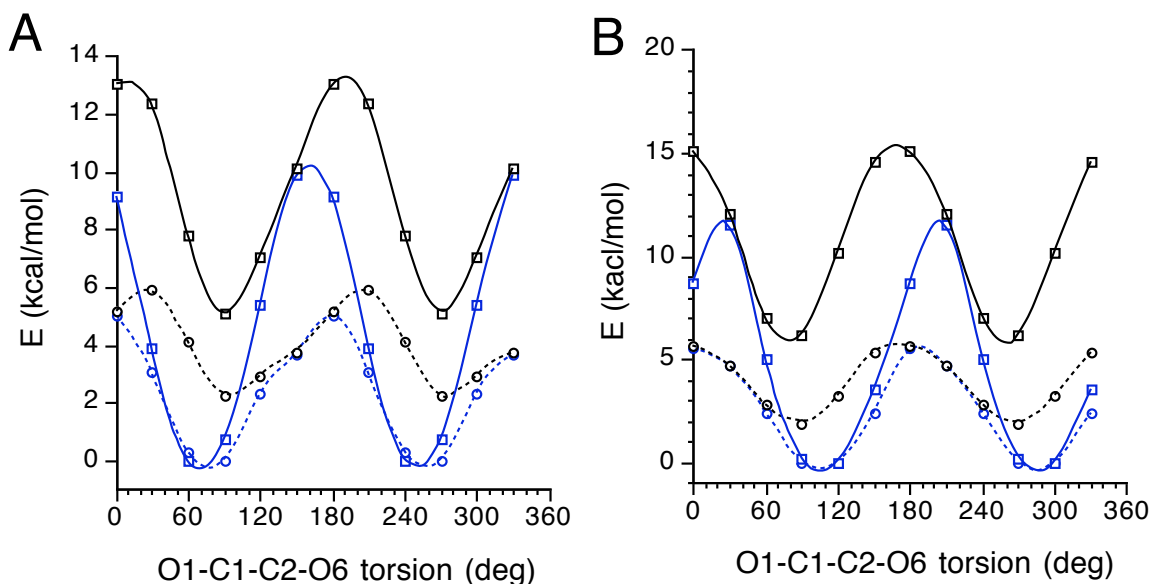


Figure 3.4. The effect of C1-C2 bond rotation on total energies of **8** (A) and **10** (B). *In vacuo* data are shown as solid lines, and solvated (water) data are shown as dotted lines. Black symbols = FX series, blue symbols = FL series.

Energy curves for the carboxylate anions are shown in Figure 3.4. As observed in the COOH forms, inclusion of solvent dampens curve amplitude substantially, but barrier heights appear generally greater for the COO⁻ forms than for COOH forms. Phase-

shifting for $2\beta p$ is more apparent between the FX and FL series, and is still observable in the FXS and FLS data sets. Phase-shifting is observed in $2\alpha p$ in the anion in both the *in vacuo* and solvated data, whereas it is absent in the protonated form. For $2\beta p$, a single well defined minimum is observed at $\sim \pm 90^\circ - 120^\circ$. For $2\alpha p$, this minimum is located at $\sim \pm 60^\circ - 90^\circ$.

Preferred C1-C2 conformations in $2\alpha p$ and $2\beta p$ are summarized in Scheme S4, with the caveat that, in both structures, significant averaging about the C1-C2 bond probably occurs in solution, particularly for the protonated forms.

3.5.3. ^1H - ^1H Spin-Couplings.

^1H - ^1H spin-couplings in $2\beta p$ range from 1.2 Hz to 11.5 Hz for $^3J_{\text{HH}}$ and -11.9 to -13.1 Hz for $^2J_{\text{HH}}$ (Table 3.1). The large intra-ring $^3J_{\text{H3ax,H4}}$, $^3J_{\text{H4,H5}}$ and $^3J_{\text{H5,H6}}$ are consistent with trans arrangements of the coupled hydrogens, consistent with a preferred $^1\text{C}_4$ ring conformation. The small $^3J_{\text{H6,H7}}$ (1.2 Hz) and large $^3J_{\text{H7,H8}}$ (9.1-9.3 Hz) are noteworthy, with the former suggesting a preferred gauche/orthogonal torsion angle between H6 and H7, and the latter suggesting a preferred near-trans arrangement between H7 and H8. These couplings place significant constraints on exocyclic glycerol side-chain conformation,¹⁵ which will be discussed below when J_{CH} and J_{CC} are considered. The magnitudes of the J_{HH} values in $2\beta p$ are largely independent of ionization state even for couplings involving nuclei close to the site of ionization (*e.g.*, H3_{ax}, H3_{eq}). The available J_{HH} values in $2\alpha p$ are similar in magnitude to those observed in $2\beta p$.

TABLE 3.1. ^1H - ^1H SPIN-COUPLING CONSTANTS^A IN **2** AT P²H 2.0 AND PH 8.0

<i>J</i>-coupling (Hz)	$2\alpha p$		$2\beta p$	
	p²H 2.0	pH 8.0	p²H 2.0	pH 8.0
$^3J_{\text{H3ax,H4}}$	11.4	11.4	11.4	11.5
$^3J_{\text{H3eq,H4}}$	4.6	~4.1	4.9	4.9
$^2J_{\text{H3ax,H3eq}}$	-12.8	-12.5	-13.1	-13.0
$^3J_{\text{H4,H5}}$	<i>obsc</i>	<i>obsc</i>	10.1	9.9
$^3J_{\text{H5,NH}}$	9.2	<i>obsc</i>	9.4	<i>nm</i>
$^3J_{\text{H5,H6}}$	<i>obsc</i>	<i>obsc</i>	10.3	10.5
$^3J_{\text{H6,H7}}$	<i>obsc</i>	<i>obsc</i>	1.2	1.2
$^3J_{\text{H7,H8}}$	<i>obsc</i>	<i>obsc</i>	9.3	9.1
$^3J_{\text{H8,H9}}$	<i>obsc</i>	<i>obsc</i>	2.8	2.7
$^3J_{\text{H8,H9'}}$	<i>obsc</i>	<i>obsc</i>	6.4	6.4
$^2J_{\text{H9,H9'}}$	<i>obsc</i>	<i>obsc</i>	-11.9	-11.9

^aIn Hz \pm 0.1 Hz at ~ 25 °C; *obsc* denotes *obscured* signal; *nm* denotes *not measurable*.

Doublets were observed at ~8 ppm for the NH protons of **2 α p** and **2 β p** at p²H 2.0 (Figure 3.1D). ³J_{H5,NH} values of 9.2 Hz and 9.4 Hz were measured for **2 α p** and **2 β p**, respectively. These couplings are assumed to be unaffected by exchange broadening since NH exchange with solvent water was slow under the conditions used for the determinations.

TABLE 3.2 CALCULATED ¹H-¹H SPIN-COUPLING CONSTANTS^A IN **7-10**.

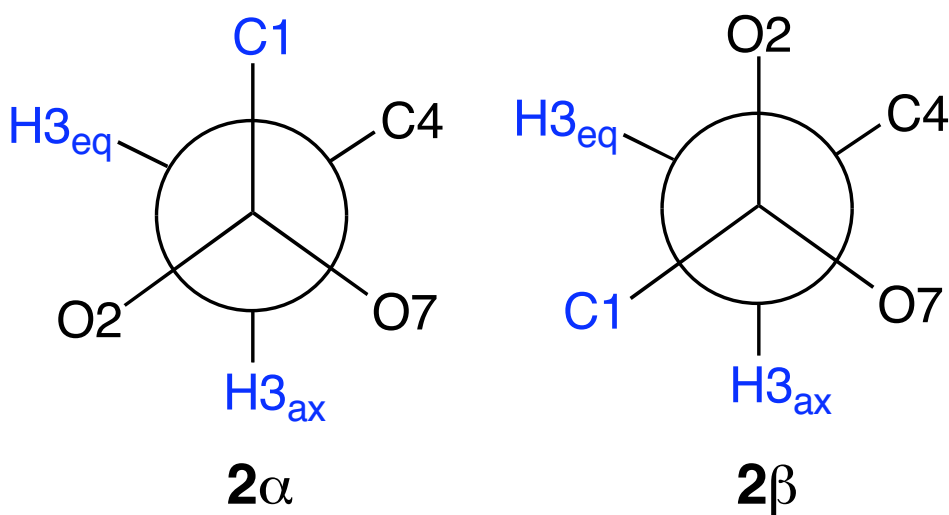
<i>J</i> -coupling (Hz)	cmpd			
	7 ^{FXS}	8 ^{FXS}	9 ^{FXS}	10 ^{FXS}
³ J _{H3ax,H4}	12.0 (11.4)	11.7 (11.4)	11.5 (11.4)	11.8 (11.5)
³ J _{H3eq,H4}	5.2 (4.6)	5.2 (~4.1)	5.3 (4.9)	5.4 (4.9)
² J _{H3ax,H3eq}	-13.0 (-12.8)	-11.8 (-12.5)	-12.9 (-13.1)	-13.1 (13.0)
³ J _{H4,H5}	10.0	9.8	9.9 (10.1)	9.8 (9.9)
³ J _{H5,NH}	(9.2)		(9.4)	
³ J _{H5,H6}	10.6	10.5	10.7 (10.3)	10.7 (10.5)
³ J _{H6,H7}	1.8	1.9	1.9 (1.2)	1.9 (1.2)

^aReported couplings were obtained by averaging the couplings calculated in the twelve C1-C2 rotamers of each structure. Blue values are experimental.

Computed ¹H-¹H couplings (Table 3.2) show very good agreement with experiment. For example, computed couplings in **9** are within 0.3-0.4 Hz of experimental values except for ³J_{H6,H7} and ³J_{H5,NH}. The larger deviation for the former is likely caused by the different exocyclic structures in **2 β p** and **9**, and to differences in the C6-C7 bond torsion.

3.5.4. ^{13}C - ^1H Spin-Couplings.

Vicinal ^{13}C - ^1H couplings between C1 and H_{3ax}/H_{3eq} differ in 2α and 2β as described previously.^{19a,b} In 2α , $^3J_{\text{C1,H3ax}}$ is large (7.0 Hz) (Table 3.3), indicative of an anti arrangement, whereas $^3J_{\text{C1,H3eq}}$ is essentially zero, consistent with a gauche arrangement. In 2β , both gauche couplings are < 1.6 Hz. The three gauche couplings are non-equivalent, with $^3J_{\text{C1,H3ax}}$ in 2β larger than $^3J_{\text{C1,H3eq}}$ in 2α and 2β at p²H 2.0 and pH 8.0. Newman projections about the C2-C3 bond (Scheme 3.3) show the presence of an electronegative substituent anti to the gauche-coupled C3 proton in all three cases, so this anti effect cannot explain the observed results. The ring oxygen O7 may be more

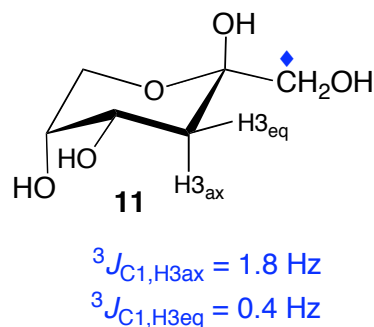


Scheme 3.3. Projections for $^3J_{\text{C1,H3ax}}$ and $^3J_{\text{C1,H3eq}}$ in 2α and 2β .

effective at reducing gauche $^3J_{\text{CCCH}}$ than O2, possibly due to different stereoelectronic properties at the two oxygens. The appended carboxyl group at C2 may also reduce the effectiveness of O2, but this explanation was eliminated through studies of 3-deoxy- β -D-[1- ^{13}C]fructopyranose **11**. In **11**, $^3J_{\text{C1,H3ax/eq}}$ values are virtually identical to those in

2βp. Alternatively, the different gauche couplings may be caused by slightly different C-C-C-H torsion angles in the chair forms of **2αp**, **2βp** and **11**.

Inspection of crystal structures of **11**^{20a} and the methyl ester of **2βp**^{20b} give C1-C2-C3-H3_{ax} torsions



of -49.2°/-46.7° and C1-C2-C3-H3_{eq} torsion angles of 68.6°/61.9°. If similar torsions exist in solution, they would produce $^3J_{C1,H3ax}$ values larger than $^3J_{C1,H3eq}$ values, consistent with the experimental observations.

TABLE 3.3. ^{13}C - ^1H SPIN-COUPLING CONSTANTS IN **2** AT P²H 2.0 AND PH 8.0.

J-coupling (Hz)	2αp		2βp	
	p²H 2.0	pH 8.0	p²H 2.0	pH 8.0
$^3J_{C1,H3ax}$	7.0	6.2	1.6	1.0
$^3J_{C1,H3eq}$	~ 0	~ 0	~ 0	~ 0
$^2J_{C2,H3ax}$	± 7.7	± 7.4	± 3.6	± 3.4
$^2J_{C2,H3eq}$	~ ± 4.3	~ ± 4.1	± 3.9	± 3.5
$^3J_{C2,H4}$	<i>obsc</i>	<i>obsc</i>	0.5	<i>nc</i>
$^3J_{C2,H6}$	<i>obsc</i>	<i>obsc</i>	~1.3	1.2
$^4J_{C2,H7}$	<i>obsc</i>	<i>obsc</i>	0.8	<i>br</i>
$^1J_{C3,H3ax}$	129.4	~128.3	129.8	129.1
$^1J_{C3,H3eq}$	134.1	~133.5	133.5	132.5
$^2J_{C3,H4}$	<i>obsc</i>	<i>obsc</i>	~ ± 2.1	± 2.1
$^3J_{C3,H5}$	<i>obsc</i>	<i>obsc</i>	1.0	<i>nm</i>

^aIn Hz ± 0.1 Hz; *obsc* denotes *obscured* signal; *nm* denotes *not measureable*; *br* denotes *broadened* signal; *nc* denotes *no coupling* ($J < 0.6 \text{ Hz}$).

Calculated $^3J_{C1,H3ax/eq}$ in **7** and **9** (Table 3.4) are in moderate agreement with the experimental findings. In **7**, $^3J_{C1,H3ax}$ and $^3J_{C1,H3eq}$ are 7.4 and 1.5 Hz, respectively,

whereas in **9**, the respective couplings are 2.0 and 0.5 Hz. These data display the expected relative couplings in **9**, but $^3J_{C1,H3eq}$ is larger than expected in **7**. However, the magnitudes of these $^3J_{CCCH}$ depend C1-C2 bond conformation (Figure 3.5), making

Table 3.4. Calculated ^{13}C - 1H Spin-Coupling Constants in **7-10**.

J -coupling (Hz)	cmpd			
	7 ^{FXS}	8 ^{FXS}	9 ^{FXS}	10 ^{FXS}
$^3J_{C1,H3ax}$	7.4 (7.0)	5.5 (6.2)	2.0 (1.6)	1.6 (1.0)
$^3J_{C1,H3eq}$	1.5 (~0)	1.0 (~0)	0.5 (~0)	0.5 (~0)
$^2J_{C2,H3ax}$	-7.0 (-7.7)	-6.2 (-7.4)	-2.7 (-3.6)	-3.0 (-3.4)
$^2J_{C2,H3eq}$	-2.3 (~-4.3)	-2.1 (-4.1)	-2.7 (-3.9)	-2.5 (-3.5)
$^3J_{C2,H4}$	0.7	0.7	0.7 (0.5)	0.6 (<i>nc</i>)
$^3J_{C2,H6}$	1.0	1.2	1.8 (~1.3)	1.8 (1.2)
$^4J_{C2,H7}$	1.5	1.2	1.0 (0.8)	0.7 (<i>br</i>)
$^1J_{C3,H3ax}$	133.1 (129.4)	130.4 (~128.3)	132.0 (129.8)	130.4 (129.1)
$^1J_{C3,H3eq}$	138.3 (134.1)	135.4 (~133.5)	138.4 (133.5)	135.2 (132.5)
$^2J_{C3,H4}$	-1.5	-1.8	-1.7 (-2.1)	-1.7 (-2.1)
$^3J_{C3,H5}$	1.9	1.8	1.7 (1.0)	1.6 (<i>nm</i>)

^aReported couplings were obtained by averaging the couplings calculated in the twelve C1-C2 rotamers of each structure. Blue values are experimental; *nc* denotes *no* coupling ($J < 0.6$ Hz); *br* denotes *broadened* signal; *nm* denotes *not measureable*.

quantitative comparisons between computed and experimental couplings difficult.

Ionization of the COOH group generally reduces experimental $^3J_{C1,H3ax/eq}$ (Table 3.3), and a similar shift to smaller couplings is observed in the calculated couplings (Table 3.4).

Like $^3J_{C1,H3ax/eq}$, $^2J_{C2,H3ax}$ and $^2J_{C2,H3eq}$ can be used to distinguish between **2 αp** and **2 βp** . $^2J_{C2,H3ax} > ^2J_{C2,H3eq}$ in **2 αp** , whereas $^2J_{C2,H3ax} \approx ^2J_{C2,H3eq}$ in **2 βp** . Application of the projection rule²¹ (Scheme S5) yields projections of +0.5 for both couplings in **2 βp** and for $^2J_{C2,H3eq}$ in **2 αp** , and the projection for $^2J_{C2,H3ax}$ in **2 αp** is –

1.0. Projections of +0.5 and -1.0 correlate with ~ 0 and very negative values of ${}^2J_{\text{CCH}}$, respectively. The large ${}^2J_{\text{C2,H3ax}}$ in **2** αp is thus probably negative, but the projection rule cannot predict the remaining signs reliably. Since C2 is unprotonated, ${}^1\text{H}$ - ${}^1\text{H}$ TOCSY data could not be used to determine the signs.²² Therefore, DFT calculations were used to make these determinations.

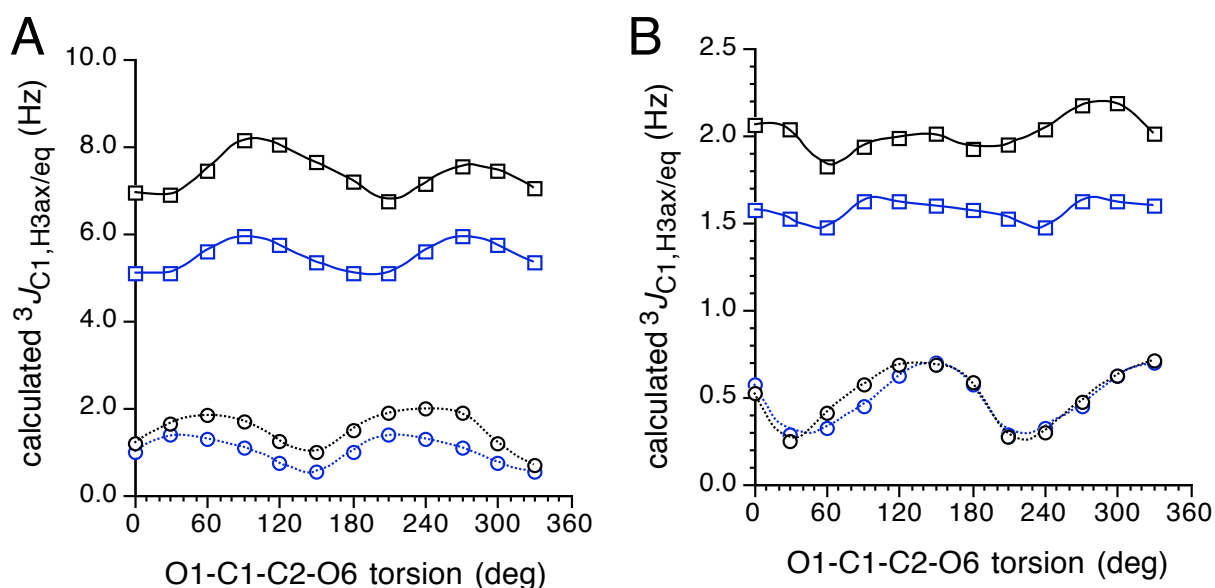


Figure 3.5 Effect of C1-C2 bond rotation on calculated ${}^1J_{\text{C1,H3ax/eq}}$ in **7/8** (A) and **9/10** (B). Squares = H3_{ax}, circles = H3_{eq}. Black symbols = protonated form; blue symbols = ionized form. Data taken from the FXS series.

Negative signs were obtained for $^2J_{\text{CH}}$ involving C2 and H3_{ax}/eq in **7-10** (Table 3.4). Experimental coupling trends were maintained in the calculations, with very different couplings observed in **7/8** compared to **9/10**. These geminal couplings show differential sensitivities to rotation of the C1-C2 bond, with the large $^2J_{\text{C2,H3ax}}$ in **7** much less sensitive than the remaining three couplings (Figure 3.6). Proximity to the COOH group appears to be a determinant, since H3_{ax} in **7** is anti to C1, whereas the remaining three H3 protons are gauche to C1. Modulation of the three gauche $^2J_{\text{CCH}}$ appears to occur via a through-space pathway that presumably involves anisotropy of the COOH group.

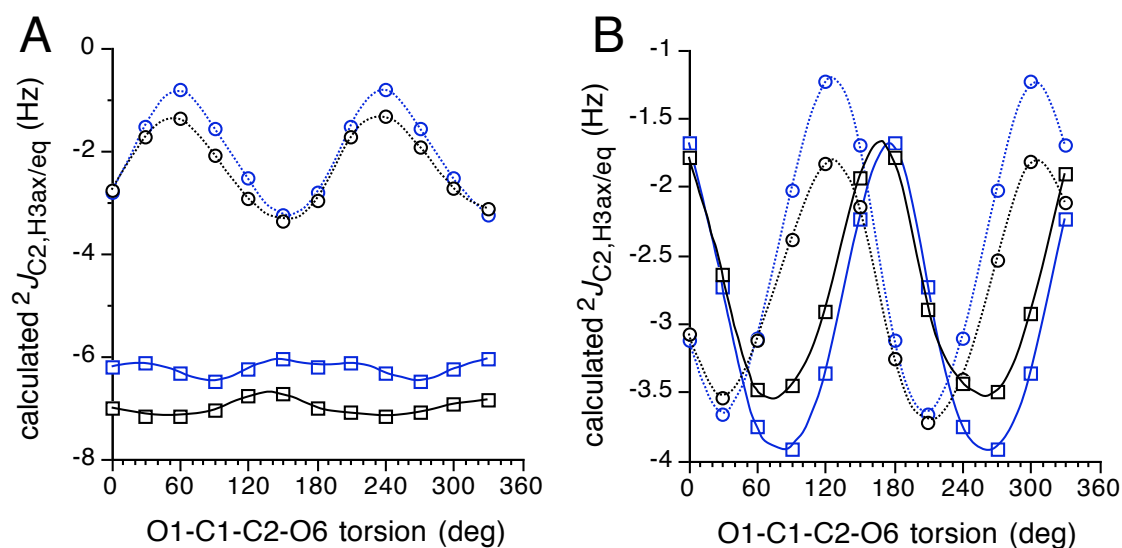


Figure 3.6. Effect of C1-C2 bond rotation on calculated $^2J_{\text{C2,H3eq/ax}}$ in **7/8** (A) and **9/10** (B). Squares = H3_{ax}, circles = H3_{eq}. Black symbols = protonated form; blue symbols = ionized form. Data taken from the FXS series.

$^3J_{\text{C2,H4}}$ is small in **2βp** (0.5 Hz) and corresponds to a C2-C3-C4-H4 torsion angle of $\sim 60^\circ$; the computed coupling is ~ 0.5 Hz. This coupling is consistent with the

analogous $^3J_{C1,H3}$ in aldopyranosyl rings, which varies from 0-1.3 Hz.²² $^3J_{C2,H6}$ in **2βp** (1.2 - 1.3 Hz) is also consistent with a C2-O6-C6-H6 torsion angle of $\sim +60^\circ$ and is comparable to $^3J_{C1,H5}$ in aldopyranosyl rings (~ 2.0 Hz).²² Computed couplings of 1.6 Hz were obtained in **8/10**, in agreement with experiment. Interestingly, values < 0.9 Hz were computed for **7/9**, suggesting that the “in-plane” O2 in **8/10** enhances this coupling. Interestingly, C2 is also coupled to H7 in **2βp** (Figure 3.1E). This long-range $^4J_{COCCH}$ is related to the $^4J_{C1,H6R/S}$ values involving the exocyclic hydroxymethyl protons of aldohexopyranosyl rings,²³ and its presence constrains conformation about the C6-C7 bond (see discussion below).

$^1J_{C3,H3eq}$ is ~ 4 Hz larger than $^1J_{C3,H3ax}$ in **2αp** and **2βp**. The equatorial C3-H3 bond is expected to be shorter than the axial C3-H3 bond, and the resulting enhanced *s*-character is expected to produce a larger $^1J_{CH}$.²⁴ Both $^1J_{CH}$ are relatively insensitive to the COOH ionization state; changes of only ~ 1 Hz are observed.

DFT calculations show $^1J_{C3,H3ax/eq}$ to be sensitive to C1-C2 bond conformation in **2αp** and **2βp** (Figure 3.7). This sensitivity is largest for $^1J_{C3,H3eq}$ in the ionized form of both anomers, showing a change of 5-7 Hz as the bond is rotated. This effect is probably mediated by through-bond and through-space mechanisms, given that both anomers appear equally responsive to the rotation. DFT calculations also predict a decrease in both couplings upon COOH ionization, and on average, larger couplings for the C3-H3_{eq} bonds. The *relative* difference between $^1J_{C3,H3ax}$ and $^1J_{C3,H3eq}$, however, is predicted to depend on C1-C2 bond conformation, with some conformations of **2βp** giving identical couplings in the COO⁻ form.

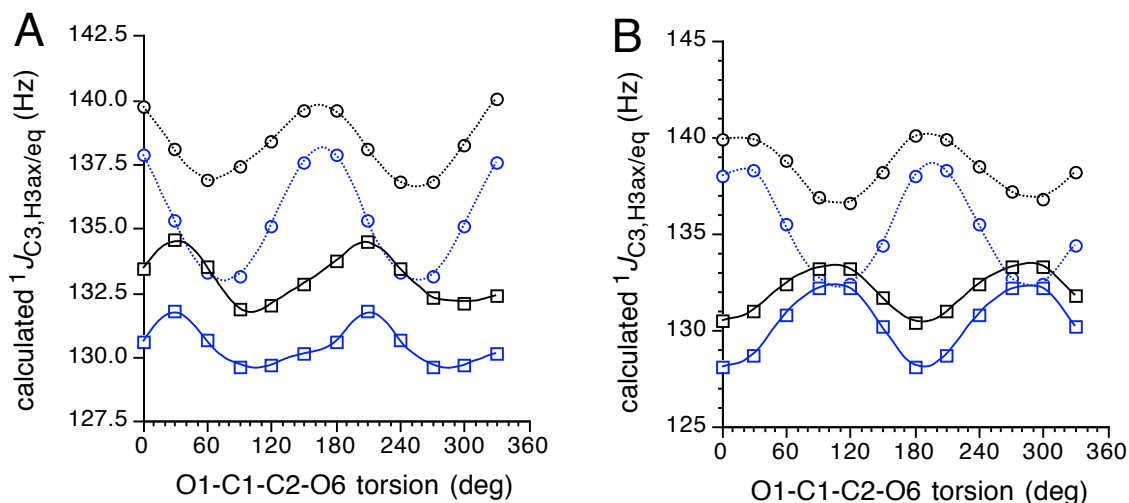


Figure 3.7. Effect of C1-C2 bond rotation on calculated $^1J_{C3,H3eq/ax}$ in **7/8** (A) and **9/10** (B). Squares = $H3_{ax}$, circles = $H3_{eq}$. Black symbols = protonated form; blue symbols = ionized form. Data taken from the FXS series.

$^2J_{C3,H4}$ is 2.1 Hz in **2 βp** , and the projection rule²¹ yields a projection of +0.5.

This coupling is expected to be negative since the analogous $^2J_{C2,H3}$ in the 2-deoxy- α -D-glucopyranosyl ring is -2.0 Hz (projection of +0.5)²⁵ This result is confirmed by the DFT calculations (Table 3.4). The gauche $^3J_{C3,H5}$ in **2 βp** of 1.0 Hz is similar to the gauche $^3J_{C2,H4}$ observed in 2-deoxy- α -D-glucopyranosyl (~0 Hz) and 2-deoxy- β -D-allopyranosyl (~0 Hz) rings.²

TABLE 3.5. ^{13}C - ^{13}C SPIN-COUPLING CONSTANTS^A IN **2** AT p²H 2.0 AND pH 8.0.

<i>J</i>-coupling (Hz)	$2\alpha p$		$2\beta p$	
	p²H 2.0	pH 8.0	p²H 2.0	pH 8.0
$^1J_{\text{C1,C2}}$	67.4	62.6	71.7	66.3
$^2J_{\text{C1,C3}}$	(+) 4.1	(+) 3.8	~ (+) 1.7	(+) 1.4
$^3J_{\text{C1,C4}}$	0	0	3.3	3.1
$^3J_{\text{C1,C6}}$	0	0	3.3	3.1
$^1J_{\text{C2,C3}}$	41.7	42.3	41.0	41.1
$^2J_{\text{C2,C4}}$	0 or <i>br</i>		±1.5	± 1.5
$^2J_{\text{C2,C6}}$	<i>br</i>	0	±1.9	± 2.1
$^{3+3}J_{\text{C2,C5}}$	0	0	0	0
$^3J_{\text{C2,C7}}$	3.5	3.6	3.2	3.1
$^1J_{\text{C3,C4}}$	35.8		35.8	35.6
$^2J_{\text{C3,C5}}$	0	0	0	0
$^{3+3}J_{\text{C3,C6}}$	0 or <i>br</i>	0	0	0

^aIn Hz ± 0.1 Hz; *obsc* denotes *obscured* signal; *nm* denotes *not measureable*; *br* denotes *broadened* signal. Coupling signs in () were predicted by DFT.

3.5.5. ^{13}C - ^{13}C Spin-Couplings.

$^1J_{\text{C1,C2}}$ in $2\alpha p$ and $2\beta p$ range from 63-72 Hz and depend on anomeric configuration, with $2\alpha p$ giving smaller couplings by ~ 4 Hz (Table 3.5). Solution pH influences $^1J_{\text{C1,C2}}$, with couplings ~ 5 Hz smaller in the ionized forms. If s -character of the C1-C2 bond largely determines $^1J_{\text{C1,C2}}$, then the smaller coupling in the ionized state implies less s -character, and the latter should lead to a longer C1-C2 bond. DFT calculations confirm this expectation (Figure 3.8), with $r_{\text{C1,C2}}$ consistently shorter in the protonated forms by ~ 0.03 and $\sim 0.02\text{\AA}$ in *in vacuo* and solvated calculations, respectively. C1-C2 bond length also varies somewhat with C1-C2 bond rotation, with $2\alpha p$ showing a more systematic dependence in both its protonated and ionized forms.

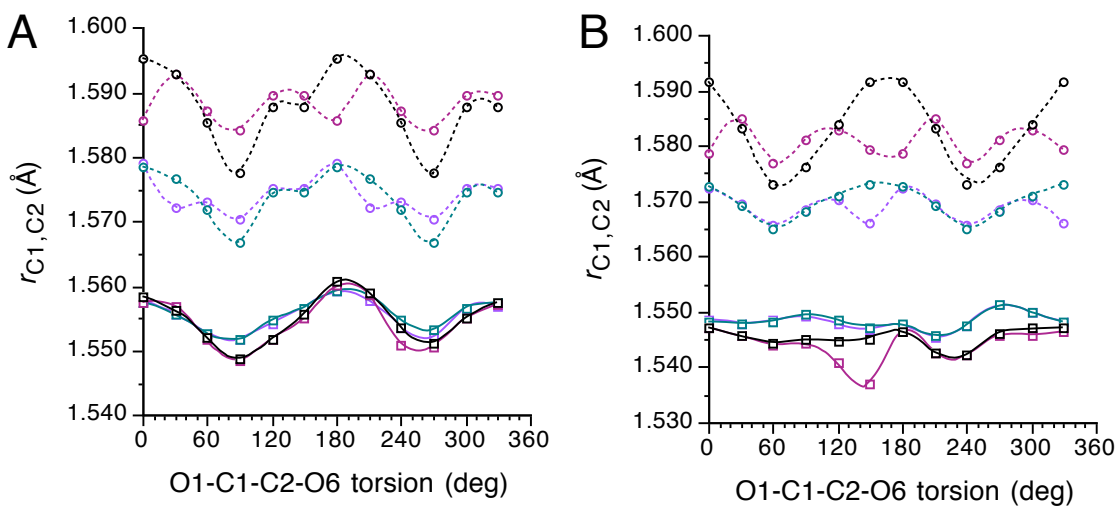


Figure 3.8 Effect of C1-C2 bond rotation on $r_{\text{C1,C2}}$ in **7/8** (A) and **9/10** (B). Squares = protonated form; circles = ionized form. Black/red symbols = FX/FL series; green/purple symbols = FXS/FLS series.

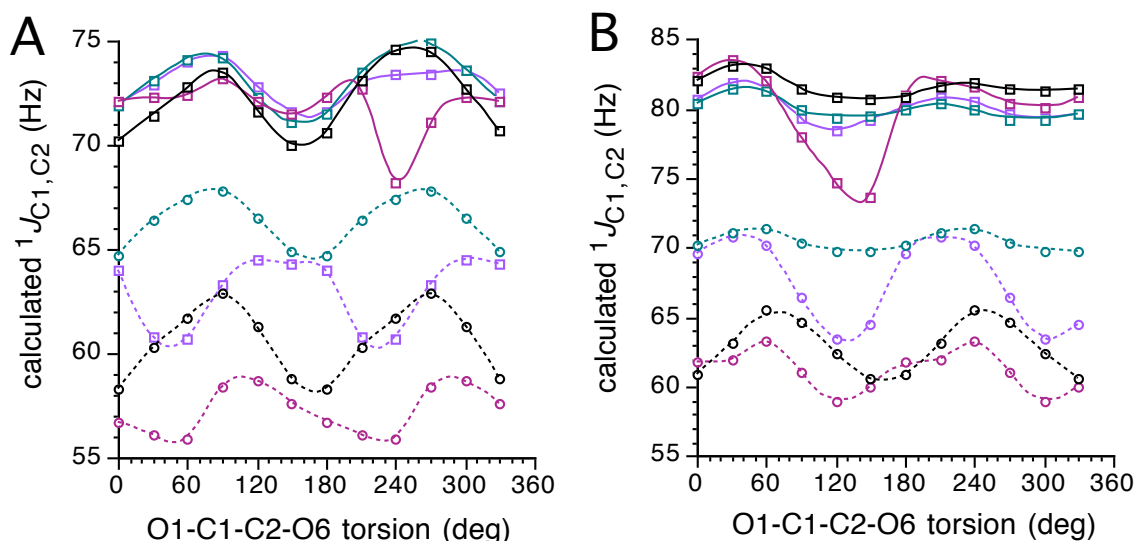
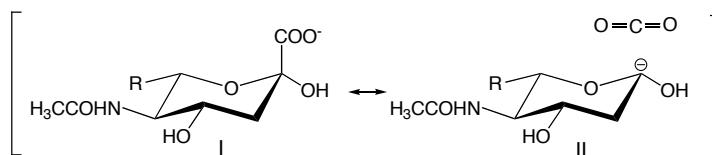


Figure 3.9. Effect of C1-C2 bond rotation on $^1J_{C1,C2}$ in **7/8** (A) and **9/10** (B). Squares = protonated form; circles = ionized form. Black/red symbols = FX/FL series; green/purple symbols = FXS/FLS series.

DFT calculations show that $^1J_{C1,C2}$ scales with $r_{C1,C2}$, with larger couplings observed in the protonated forms (Figure 3.9). $^1J_{C1,C2}$ is smaller in the ionized forms, and the amount of decrease depends on whether the calculations were conducted *in vacuo* or with solvent. The solvated data are in better agreement with experiment, suggesting that neglecting solvent accentuates (localizes) the charged properties of the carboxylate anion, which in turn produces hyper-extension of $r_{C1,C2}$ and hyper-reduction of $^1J_{C1,C2}$. A hyperconjugative mechanism may explain $r_{C1,C2}$ elongation in the anion (Scheme 4.4),



Scheme 3.4. Hyperconjugative effects on $r_{C1,C2}$ and $^1J_{C1,C2}$ in the ionized form of **2αp**.

where contributions from resonance structure **II** are responsible for weakening (lengthening) the C1-C2 bond in the anion and for the concomitant reduction in $^1J_{C1,C2}$.

$^2J_{C1,C3}$ depends on anomeric configuration, with absolute couplings in **2 α p** larger than in **2 β p** by ~ 2 Hz. The projection resultant method²⁶ could not be used to predict their signs due to the sp^2 character of C1. DFT calculations predict positive signs for $^2J_{C1,C3}$ in **2 α p** and **2 β p**, a dependence on anomeric configuration that mirrors the experimental findings, and a dependence on the C1-C2 torsion angle, especially in the protonated state (Table 3.6, Figure 3.10A). $^2J_{C1,C3}$ may be slightly reduced in the ionized state (Table 3.5), which is also suggested from the calculations.

TABLE 3.6. CALCULATED ^{13}C - ^{13}C SPIN-COUPLING CONSTANTS^A IN **7-10**.

J -coupling (Hz)	cmpd			
	7 ^{FXS}	8 ^{FXS}	9 ^{FXS}	10 ^{FXS}
$^1J_{C1,C2}$	73.1 (67.4)	66.4 (62.7)	80.0 (71.7)	70.4 (66.2)
$^2J_{C1,C3}$	4.9 (4.1)	4.1 (3.8)	2.1 (1.9)	1.9 (1.4)
$^3J_{C1,C4}$	-0.2 (0)	-0.2 (0)	3.4 (3.3)	2.7 (3.1)
$^3J_{C1,C6}$	-0.2 (0)	-0.1 (0)	4.1 (3.3)	3.1 (3.1)
$^1J_{C2,C3}$	43.7 (41.7)	43.8 (42.3)	44.9 (41.0)	45.8 (41.1)
$^2J_{C2,C4}$	1.5 (<i>br</i>)	1.7	-1.1 (-1.5)	-1.4 (1.5)
$^2J_{C2,C6}$	-1.7 (<i>br</i>)	-1.3 (0)	-1.9 (-1.9)	-2.6 (2.1)
$^{3+3}J_{C2,C5}$	0.3 (0)	0.3 (0)	0.3 (0)	0.3 (0)
$^3J_{C2,C7}$	4.0 (3.5)	3.7 (3.6)	3.9 (3.2)	3.5 (3.1)
$^1J_{C3,C4}$	36.3 (35.8)	36.7	36.0 (35.8)	36.4 (35.6)
$^2J_{C3,C5}$	2.1 (0)	1.9 (0)	2.1 (0)	2.0 (0)
$^{3+3}J_{C3,C6}$	0.1 (<i>br</i>)	0.1 (0)	0.3 (0)	0.4 (0)

^aReported couplings were obtained by averaging the couplings calculated in the twelve C1-C2 rotamers of each structure. Blue values are experimental; *br* denotes broadened signals.

$^3J_{C1,C4}$ and $^3J_{C1,C6}$ differ significantly in $2\alpha p$ and $2\beta p$, with essentially zero couplings observed in the former and 3.1-3.3 Hz couplings observed in the latter (Table 3.5). These couplings show a small dependence on COOH ionization state. Similar trends are predicted by DFT (Table 3.6), and both vicinal couplings show little dependence on

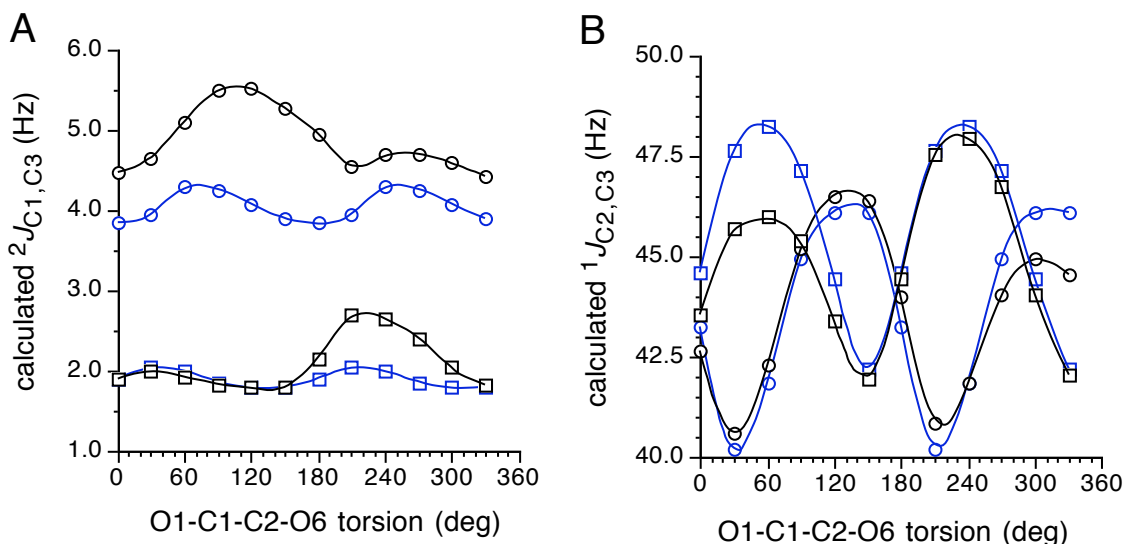


Figure 3.10. Effect of C1-C2 bond rotation on $^2J_{C1,C3}$ (A) and $^1J_{C2,C3}$ (B) in **7/8** (circles) and **9/10** (squares). Black symbols = protonated form; blue symbols = ionized form. Data taken from the FXS series.

C1-C2 bond rotation (data not shown). The 3.1-3.3 couplings in $2\beta p$ are associated with C1-C2-C3-C4 and C1-C2-O6-C6 torsion angles of $\sim 180^\circ$, and the ~ 0 Hz couplings in 2α with corresponding torsion angles of $\sim 60^\circ$. Anti couplings $^3J_{C1,C4}$ and $^3J_{C1,C6}$ in $2\beta p$ are virtually identical, implying that oxygen along the coupling pathway exerts a minimal effect on the coupling (assuming similar torsion angles). This behavior is similar to that of $^3J_{C1,C6}$ and $^3J_{C3,C6}$ in aldohexopyranosyl rings, which exhibit a similar Karplus dependency.²⁷

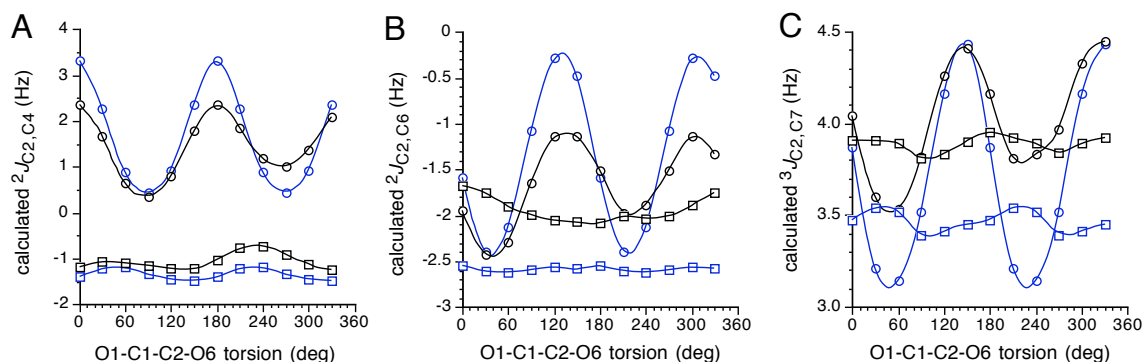


Figure 3.11. Effect of C1-C2 bond rotation on ${}^2J_{C2,C4}$ (A), ${}^2J_{C2,C6}$ (B) and ${}^3J_{C2,C7}$ (C) in **7/8** (circles) and **9/10** (squares). Black symbols = protonated form; blue symbols = ionized form. Data taken from the FXS series.

${}^1J_{C2,C3}$ ranges from 41-42 Hz and shows little sensitivity to anomeric configuration and to COOH ionization state. ${}^1J_{C2,C3}$ depends on the C1-C2 bond torsion (Figure 3.10B), with maximal couplings observed at $\sim 120^\circ$ in **2 α p** and $\sim 60^\circ$ in **2 β p** regardless of the carboxyl ionization state.

${}^2J_{C2,C4}$ is very small in **2 α p**, slightly larger in **2 β p**, and is not significantly affected by ionization at C1. DFT computations predict a positive sign in **2 α p** and a negative sign in **2 β p** (Table 3.6). The sensitivity of ${}^2J_{C2,C4}$ to C1-C2 bond rotation (Figure 3.11A) is significantly greater in **2 α p** than in **2 β p**, and may explain the apparent greater disparity between computed and experimental ${}^2J_{C2,C4}$ in **2 α p** (Table 3.6).

Like ${}^2J_{C2,C4}$, ${}^2J_{C2,C6}$ is larger in **2 β p** than in **2 α p**, and DFT calculations indicate negative signs (Table 3.6). ${}^2J_{C2,C6}$ is analogous to ${}^2J_{C1,C5}$ in aldopyranosyl rings in the 4C_1 conformation, which shows a dependence on anomeric configuration (~ 0 Hz in β -pyranoses, ~ -2 Hz in α -pyranoses).²⁸ The axial O2 in **2 β p** mimics the axial O1 in α -aldohexopyranosyl rings and elicits a measurable coupling, whereas the equatorial O2 in

$2\alpha p$ mimics that in β -aldopyranoses and little or no coupling is observed. The magnitude of $^2J_{C2,C6}$ in $2\beta p$ is similar to that observed in α -aldopyranosyl rings (~ 2 Hz). DFT calculations (Figure 3.11B) show $^2J_{C2,C6}$ in $2\alpha p$ to be considerably more sensitive to C1-C2 bond rotation than $2\beta p$, mimicking behavior observed for $^2J_{C2,C4}$.

$^3J_{C2,C7}$ is large in $2\alpha p$ and $2\beta p$ (3.1-3.6 Hz), consistent with a C2-O6-C6-C7 torsion angle of $\sim 180^\circ$. The coupling is slightly larger in $2\alpha p$, since the terminal “in-plane” equatorial O2 enhances this $^3J_{COCC}$ as expected from in work.²⁹ Ionization state affects this coupling minimally. DFT calculations (Figure 3.11C) show $^3J_{C2,C7}$ to be more sensitive to C1-C2 bond rotation in $2\alpha p$ than in $2\beta p$, a pattern observed for $^2J_{C2,C4}$ and $^2J_{C2,C6}$.

$^1J_{C3,C4}$ is 35.7 Hz in $2\alpha p$ and $2\beta p$, and shows no sensitivity to the state of COOH ionization. Of the three $^1J_{CC}$ measured in this study, $^1J_{C3,C4}$ is smallest, $^1J_{C1,C2}$ largest, and $^1J_{C2,C3}$ intermediate in magnitude. $^2J_{C3,C5}$ and $^{3+3}J_{C3,C6}$ are very small or zero in $2\alpha p$ and $2\beta p$.

3.5.6. Conformation About the C6-C7 Bond.

Prior studies have addressed the conformation of the exocyclic glycerol fragment of NeuAc. Czarniecki and Thornton^{18,19} concluded that the favored C6-C7 bond conformation is that having H6 roughly anti to C8, a conformation presumably stabilized by two H-bonds between O6 (acceptor) and O8H, and between N5H and O7 (acceptor). In this conformation, H6 and H7 are approximately gauche, which is consistent with the small $^3J_{H6,H7}$ (1.2 Hz; Table 3.1). In contrast, Brown and coworkers¹⁵ concluded, based

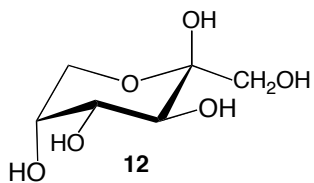
on steric arguments, that of the two potential gauche O6-C6-C7-O7 conformations consistent with a small $^3J_{\text{H6,H7}}$, that having O7 approximately anti to H6 is preferred.

In the present work, an additional long-range ^{13}C - ^1H coupling, $^3J_{\text{C2,H7}}$, was observed in $2\beta p$ (Table 3.3) that serves to distinguish between the two potential gauche O6-C6-C7-O7 conformations. Analogous $^4J_{\text{CCCCCH}}$ have been reported recently in D-galactopyranosyl rings ($^4J_{\text{C1,H6S}}$) and were shown to depend highly on geometry about the C1-O5-C5-C6-H6*R/S* fragment, with in-plane (W-shaped) arrangements leading to measureable couplings.²³ In this prior work, couplings as large as 1.1 Hz were observed in conformationally constrained compounds. Observation of $^4J_{\text{C2,H7}}$ in $2\beta p$ supports the contention that the C6-C7 conformation orienting H6 approximately anti to O7 is highly populated in solution. If the very small value of $^3J_{\text{H6,H7}}$ is interpreted as support for a relatively stable torsion angle of $\sim 70^\circ$ - 80° , then the magnitude of $^3J_{\text{H6,H7}}$ would be consistent with a geometry with H7 slightly out-of-plane, although we cannot dismiss a two-state exchange involving both O6-C6-C7-O7 gauche conformers, with one highly favored. Other J -couplings not measured in this work (*e.g.*, $^3J_{\text{C5,H7}}$, $^3J_{\text{C5,C8}}$) might shed further light on this problem.

3.5.7. Comparison of J_{CC} in $2\beta p$, 3-deoxy- β -D-fructopyranose (**11**) and β -D-fructopyranose (**12**).

The preferred chair conformations of 3-deoxy- β -D-fructopyranose (**11**), β -D-fructopyranose (**12**), and $2\beta p$ are similar (*i.e.*, $^1\text{C}_4$), allowing meaningful comparisons of related couplings in these structures. $^1J_{\text{C1,C2}}$ is ~ 22 Hz larger in $2\beta p$ at pH 2.0 than in **11**

and **12** (Table 3.7). In contrast, $^1J_{C2,C3}$ and $^1J_{C3,C4}$ are 4-6 Hz larger in **12** than in **2βp**, presumably due to the additional hydroxyl group on C3 in **12**.³⁰ $^2J_{C1,C3}$ is 3.4 Hz in **11**



and $\sim(+)$ 1.7 Hz in **2βp**. $^3J_{C1,C4}$ and $^3J_{C1,C6}$ are larger in **2βp** than in **11** and **12**; since the dihedral angles are similar, these differences are probably due mainly to different

electronegative substituent effects at the terminal (C1) carbon. $^2J_{C2,C6}$ is very similar in **2βp** and **12**, but $^2J_{C2,C4}$ is smaller in **12**. $^2J_{C3,C5}$ is small in **2βp** and **12**.

TABLE 3.7. J_{CC} VALUES IN 3-DEOXY-β-D-FRUCTOPYRANOSE **11** AND β-D-

J -coupling (Hz)	compd 11	compd 12	compd 2βp^b
$^1J_{C1,C2}$	50.2	49.8	71.7
$^2J_{C1,C3}$	3.4	2.4	$\sim(+)$ 1.7
$^3J_{C1,C4}$	2.7	1.8	3.3
$^3J_{C1,C6}$	2.7	2.4	3.3
$^1J_{C2,C3}$		47.5	41.0
$^2J_{C2,C4}$		<i>nc</i>	± 1.5
$^2J_{C2,C6}$		2.1	± 1.9
$^1J_{C3,C4}$		39.8	35.8
$^2J_{C3,C5}$		<i>nc</i>	0

^aIn Hz \pm 0.1 Hz; *nc* denotes *no* coupling ($J < 0.6$ Hz). Data were taken from ref. 29. ^bAt pH 2.0; data from Table 5.

FRUCTOPYRANOSE **12**.

3.5.8. Effect of Solvation on Computed Couplings in **9** and **10**.

The effect of solvent water on calculated J -couplings in **9** and **10** is summarized in Table 3.8. Comparisons were drawn between coupling data obtained in the FX and FXS series of calculations. Inclusion of solvent caused only minor changes in computed

J_{HH} , J_{CH} and J_{CC} values in the protonated form **9**. In contrast, some of the computed couplings in **10** were considerably more sensitive to the presence or absence of solvent. In **10**, J_{HH} values were little affected by the inclusion of solvent, presumably because these pathways are relatively far removed from the site of ionization. At the other extreme, $^1J_{C1,C2}$ increases significantly in the solvent calculations. The difference in $^1J_{C1,C2}$ between **9** and **10** is 18.8 Hz for FX data and 9.6 Hz for FXS data; the experimental difference is 5.5 Hz. These results show that, although the computed $^1J_{CC}$ are not quantitative in any data set (they are consistently overestimated), the solvated data provide a closer approximation to experiment than do the *in vacuo* data. In general, J_{CC} and J_{CH} values in **10** involving C1 and C2 shift to more positive values when solvent is included. These results point to the importance of including solvent in J -couplings calculations in the ionized forms of saccharides.

TABLE 3.8. EFFECT OF SOLVENT ON CALCULATED SPIN-COUPPLINGS
IN **9** AND **10**.

Table 8. Effect of Solvent on Calculated Spin-Couplings in **9** and **10**.

J -coupling (Hz)	9			10		
	FX	FXS	Exp	FX	FXS	Exp
$^1J_{C1,C2}$	81.7	80.0	71.7	62.9	70.4	66.2
$^1J_{C2,C3}$	44.5	44.9	41.0	45.2	45.8	41.1
$^1J_{C3,C4}$	35.6	36.0	35.8	36.3	36.4	35.6
$^2J_{C1,C3}$	2.0	2.1	1.9	1.8	1.9	1.4
$^3J_{C1,C4}$	3.4	3.4	3.3	2.2	2.7	3.1
$^3J_{C2,C7}$	4.5	3.9	3.2	2.6	3.5	3.1
$^3J_{C1,C6}$	4.0	4.1	3.3	3.2	3.1	3.1
$^3J_{C1,H3ax}$	2.0	2.0	1.6	1.2	1.6	1.0
$^3J_{C1,H3eq}$	0.6	0.5	~0	0.5	0.5	~0
$^2J_{C2,H3ax}$	-2.8	-2.7	-3.6	-3.7	-3.0	-3.4
$^2J_{C2,H3eq}$	-2.9	-2.7	-3.9	-2.6	-2.5	-3.5
$^1J_{C3,H3ax}$	131.9	132.0	129.8	131.5	130.4	129.1
$^1J_{C3,H3eq}$	139.6	138.4	133.5	135.6	135.2	132.5
$^2J_{C3,H4}$	-1.9	-1.7	-2.1	-2.0	-1.7	-2.1
$^3J_{H3ax,H4}$	11.4	11.5	11.4	11.9	11.8	11.5
$^3J_{H3eq,H4}$	5.2	5.3	4.9	5.4	5.4	4.9

3.6. Conclusions

Many biologically important oligosaccharides attached to glycoproteins contain NeuAc glycosidically linked as a terminal residue. The conformational properties of NeuAc-containing linkages are still poorly understood, largely due to the limited number of experimental parameters available for such studies. The present work was conducted to set the stage for studies of trans-glycoside J -couplings involving NeuAc residues, which hold the potential for better defining these linkages. In contrast to trans-glycoside J -couplings involving Glc, Gal, Fuc and GlcNAc residues, J -couplings involving NeuAc are potentially subject to the effects of solution pH, since an ionizable COOH functionality is proximal to the glycosidic linkage. The present work aimed in part to evaluate the effect of this factor on intra-residue J_{HH} , J_{CH} and J_{CC} as a means of predicting related effects on trans-glycoside J_{CH} and J_{CC} . This work also provided useful new information on J_{CH} and J_{CC} involving C1, C2 and C3 of NeuAc for coupling pathways having defined structure imposed by the pyranosyl ring. These “fixed pathway” couplings provide a means to validate calculated trans-glycoside couplings since some of their pathways mimic those across the linkage and, importantly, are associated with known torsions.

Several key findings emerged from this work. ^1H - ^1H J -couplings in $2\alpha p$ and $2\beta p$ are largely independent of solution pH, presumably because these coupling pathways are relatively remote from the site of ionization. DFT calculations in the presence of solvent reproduce intra-ring J_{HH} very well.

Geminal J_{CH} involving C2 and H3_{ax}/H3_{eq} are negative in sign and can be used to distinguish between NeuAc pyranose anomers in a manner similar to that reported for

$^3J_{C1,H3ax/H3eq}$.^{19a,b} Regarding the latter vicinal couplings, the different coupling magnitudes observed for the three gauche C-C-C-H pathways in **2** αp and **2** βp is not attributable to effects of C1 functionality but rather to differences in the torsion angles associated with these couplings.

$^1J_{C1,C2}$ values in **2** depend on pyranose anomeric configuration and on solution pH. Couplings are generally larger in the β -pyranose and decrease with increasing pH. DFT calculations showed that the reduction in $^1J_{C1,C2}$ with increasing pH is accompanied by an increase in the C1-C2 bond length. The latter correlation can be explained by a hyperconjugative mechanism in which the C1-C2 bond is weakened in the ionized state.

Rotation of the C1-C2 bond exerts significant effects on $^1J_{CC}$, $^2J_{CC}$ and $^3J_{CC}$ values involving C2 of NeuAc. The extent of this effect depends on anomeric configuration for the latter two coupling types. Generally, these couplings are more sensitive to C1-C2 bond rotation in the α -pyranose for reasons that are presently unclear.

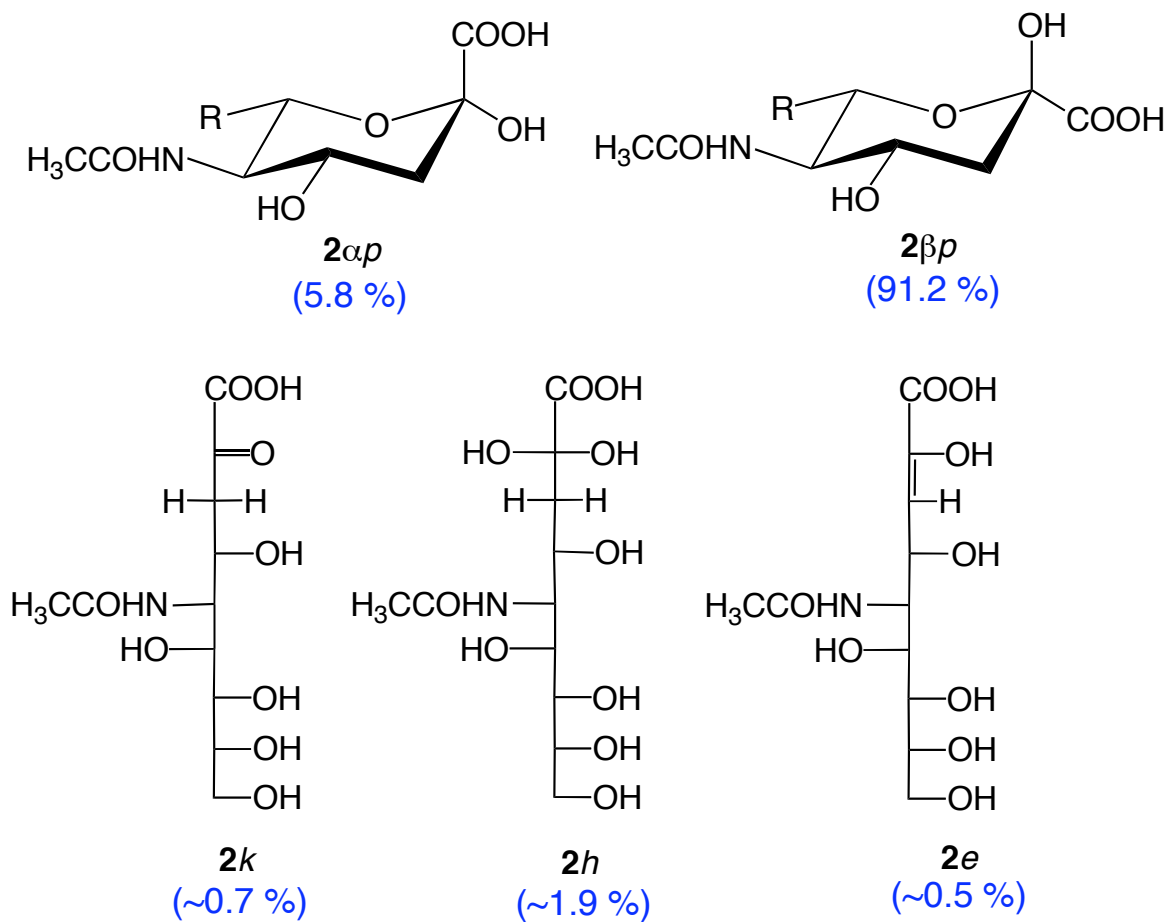
Recent studies in aldohexopyranosyl rings have shown that $^4J_{CCCCH}$ involving C1 can be used to evaluate exocyclic CH₂OH conformation.²³ A related effect exists in NeuAc pyranosyl rings, where analogous coupling is observed between C2 and H7. This observation provides constraints on the C6-C7 bond torsion in **2** βp in solution, favoring a conformation having H6 approximately anti to O7.

DFT calculations of J -couplings in **2** appear less accurate when solvent is excluded from the calculations. This effect is particularly apparent for $^1J_{C1,C2}$ but extends to couplings more remote from the site of ionization. These findings have

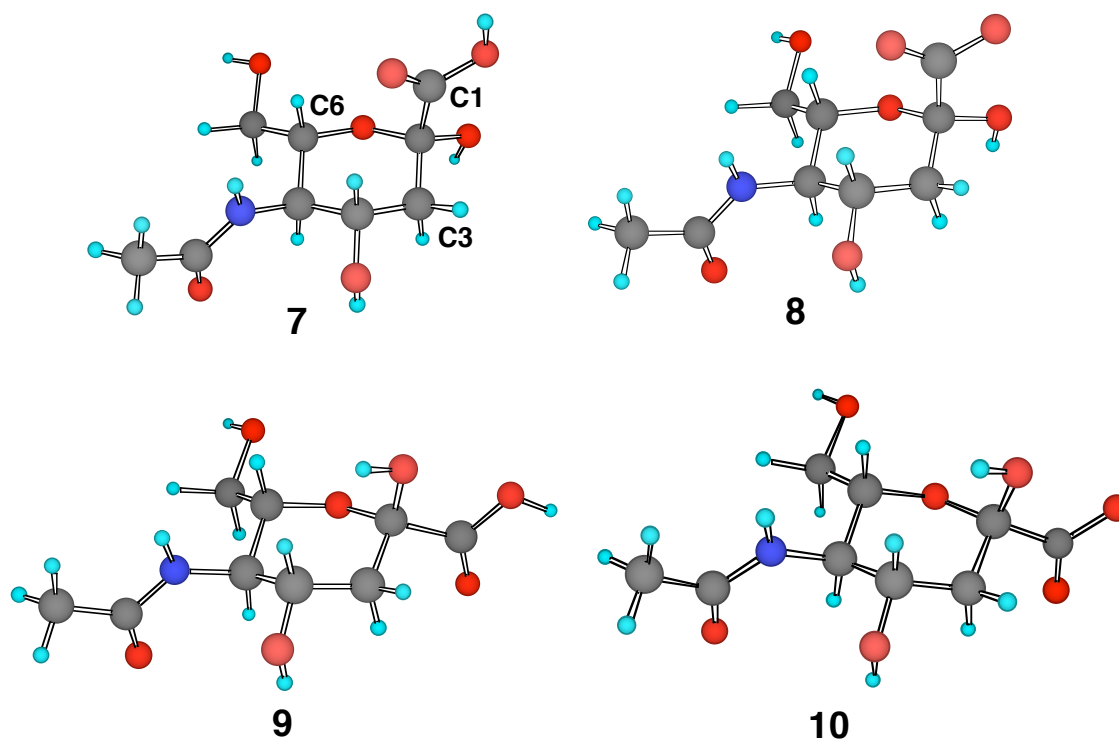
important implications for future theoretical studies of trans-glycoside J -couplings involving **2**. Specifically, DFT calculations of the latter must be performed with solvent in order to be of use in interpreting experimental data. The same approach will probably be required for DFT calculations of J -couplings in other ionizable sugars such as uronic acids.

The present work provides a set of standard J_{CH} and J_{CC} values involving C1-C3 in **2** that will assist in studies of trans-glycoside J -couplings. Intra-residue $^3J_{C1,C6}$ in **2** αp is related to $^3J_{C1,C3'}$ in **5**; the experimental value of $^3J_{C1,C6}$ is associated with a torsion angle of $\sim 60^\circ$, providing a reference value in the construction of a $^3J_{C1,C3'}$ Karplus curve. Likewise, $^3J_{C2,C7}$ in **2** αp mimics trans-glycoside $^3J_{C2,C2'}$ and $^3J_{C2,C4'}$ in **5**, providing standard couplings for torsions of $\sim 180^\circ$. These couplings are expected to be relatively unaffected by the state of ionization of the COOH group, thus eliminating this factor in their analysis. On the other hand, the present results suggest that rotation about the C1-C2 of **2** significantly affects J_{CH} and J_{CC} values, and this factor will need to be considered in studies of trans-glycoside couplings. Present data suggest that conformational preferences about the C1-C2 bond differ in NeuAc anomers, that inclusion of solvent water significantly reduces the activation barriers for C1-C2 bond rotation, and that activation barriers to C1-C2 bond rotation are much higher for the carboxylate anion compared to the protonated acid. At present, it is not possible to evaluate the disposition of the COOH/COO⁻ group in NeuAc anomers experimentally, and this problem remains to be addressed in future work.

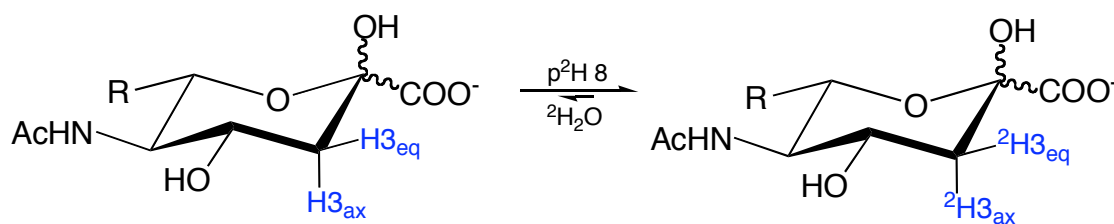
3.7. Supporting Information.



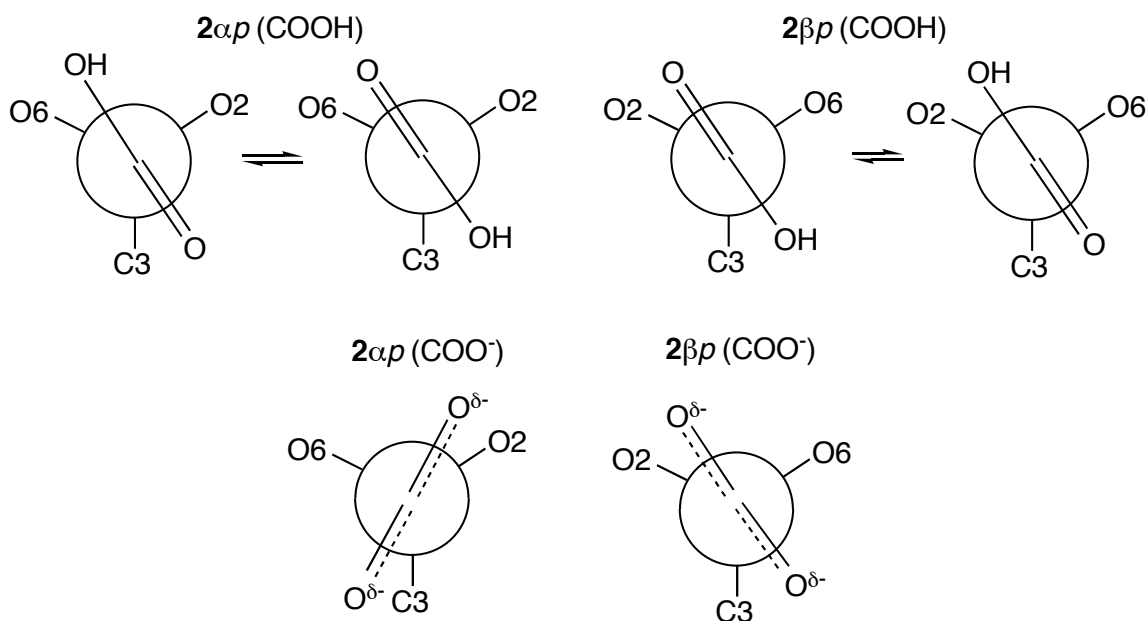
Scheme 3.5. (S1) Monomeric forms of **2** and their abundances in aqueous solution at pH 2. (R= -CHOH-CHOH-CH₂OH)



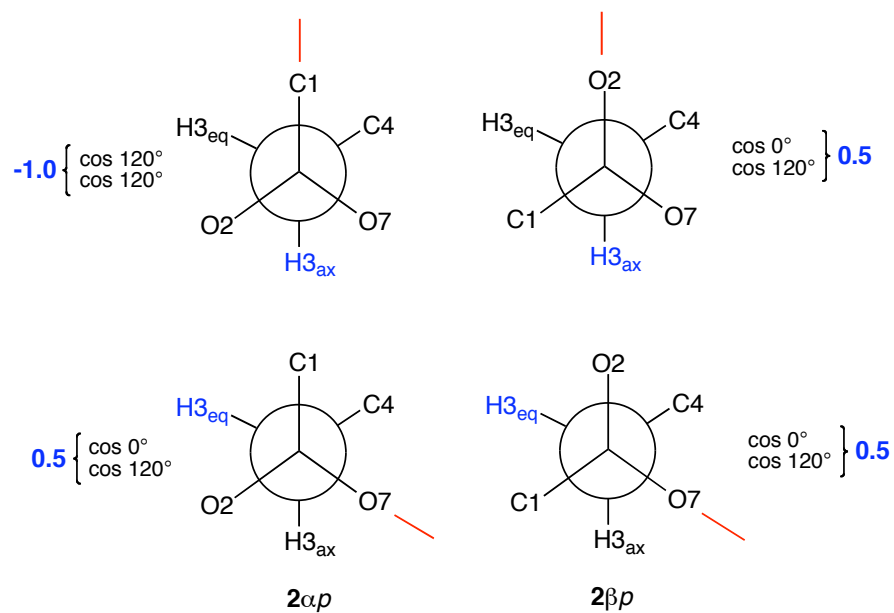
Scheme 3.6. (S2) Initial geometries of **7-10** used in DFT calculations of J -couplings in **2**. All ring conformations are 1C_4 ; see text for the initial values of the exocyclic torsions.



Scheme 3.7. (S3) Deuterium exchange of C3 protons of **2** in mild aqueous base.



Scheme 3.8. (S4) Preferred C1-C2 Bond Conformations in the protonated and ionized forms of $2\alpha p$ and $2\beta p$.



Scheme 3.9. (S5) Projections for $^2J_{C2,H3_{ax}}$ and $^2J_{C2,H3_{eq}}$ in $2\alpha p$ and $2\beta p$.

TABLE 3.9. ^1H CHEMICAL SHIFTS^a OF **2** AT P²H 2.0 AND PH 8.0.

cmpd	Nucleus										
	H3 _{ax}	H3 _{eq}	H4	H5	H6	H7	H8	H9	H9'	CH ₃	NH
2 α (pD 2.0)	1.493	2.497	<i>obsc</i>	<i>obsc</i>	<i>obsc</i>	<i>obsc</i>	<i>obsc</i>	<i>obsc</i>	<i>obsc</i>	1.816	~7.801
2 α (pH 8.0)	1.400	2.505	<i>obsc</i>	<i>obsc</i>	<i>obsc</i>	<i>obsc</i>	<i>obsc</i>	<i>obsc</i>	<i>obsc</i>	1.809	
2 β (pD 2.0)	1.664	2.098	3.849	3.715	3.839	3.339	3.529	3.620	3.400	1.833	~7.885
2 β (pH 8.0)	1.588	1.985	3.804	3.682	3.751	3.294	3.528	3.616	3.390	1.828	

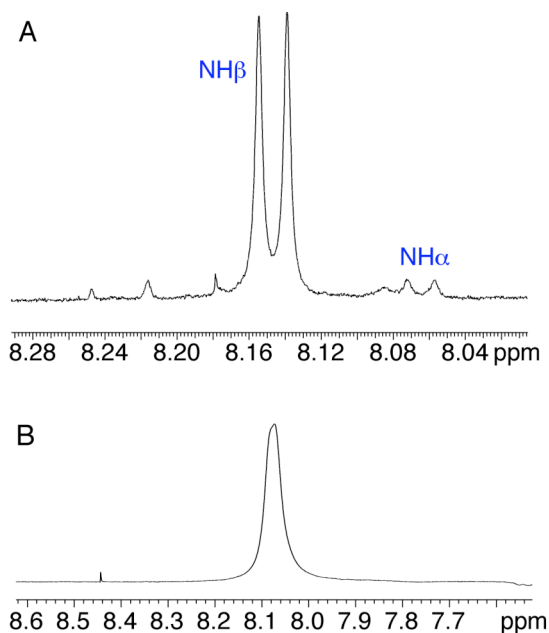
^aIn ppm at 25 °C; ± 0.001 ppm. *Obsc* denotes obscured signal. Shifts were referenced to those reported in ref. 17 for the β -pyranose in the free acid and sodium salt forms.

TABLE 3.10. ^{13}C CHEMICAL SHIFTS^a OF **2** AT P²H 2.0 AND PH 8.0.

cmpd	nucleus										
	C1	C2	C3	C4	C5	C6	C7	C8	C9	C10	C11
2 α (pD 2.0)	173.2	96.6	40.8	68.5	52.5	73.5	68.9	71.5	63.8	175.8	20.3
2 α (pH 8.0)	176.2	98.0	41.6	67.7	52.7	73.4	69.0	72.4	63.7	176.0	22.9
2 β (pD 2.0)	174.1	96.0	39.6	67.5	52.8	71.2	69.0	70.9	63.9	175.6	22.8
2 β (pH 8.0)	177.7	97.2	40.3	68.1	53.1	71.1	69.4	71.2	64.2	175.6	23.0

^aIn ppm at 25 °C, ± 0.1 ppm. Shifts were referenced to those reported in ref. 17 for the β -pyranose in the free acid and sodium salt forms.

Figure 3.12. (S1) (A) Amide ^1H signals of **2** at p²H 2.0 and 20 °C. Assignment of the weaker αp signal is tentative. Resonance linewidth ($\Delta\nu_{0.5}$) of the βp signal is 2.4 Hz. $^3J_{\text{H5,NH}}$ are 9.2 Hz and 9.4 Hz for the αp and βp , respectively. These signals were very weak, since they represent the small fraction of **2** containing an N¹H rather than an N²H at the amide site. (B) Amide ^1H signals of **2** at pH 8.0 and 20 °C. The NH β signal has collapsed into a broadened singlet due to rapid chemical exchange of the NH proton with solvent H₂O. Resonance linewidth ($\Delta\nu_{0.5}$) is 19.6 Hz. Raw FIDs used to generate spectra in (A) and (B) were treated with a 0.1 Hz exponential apodization function prior to FT.



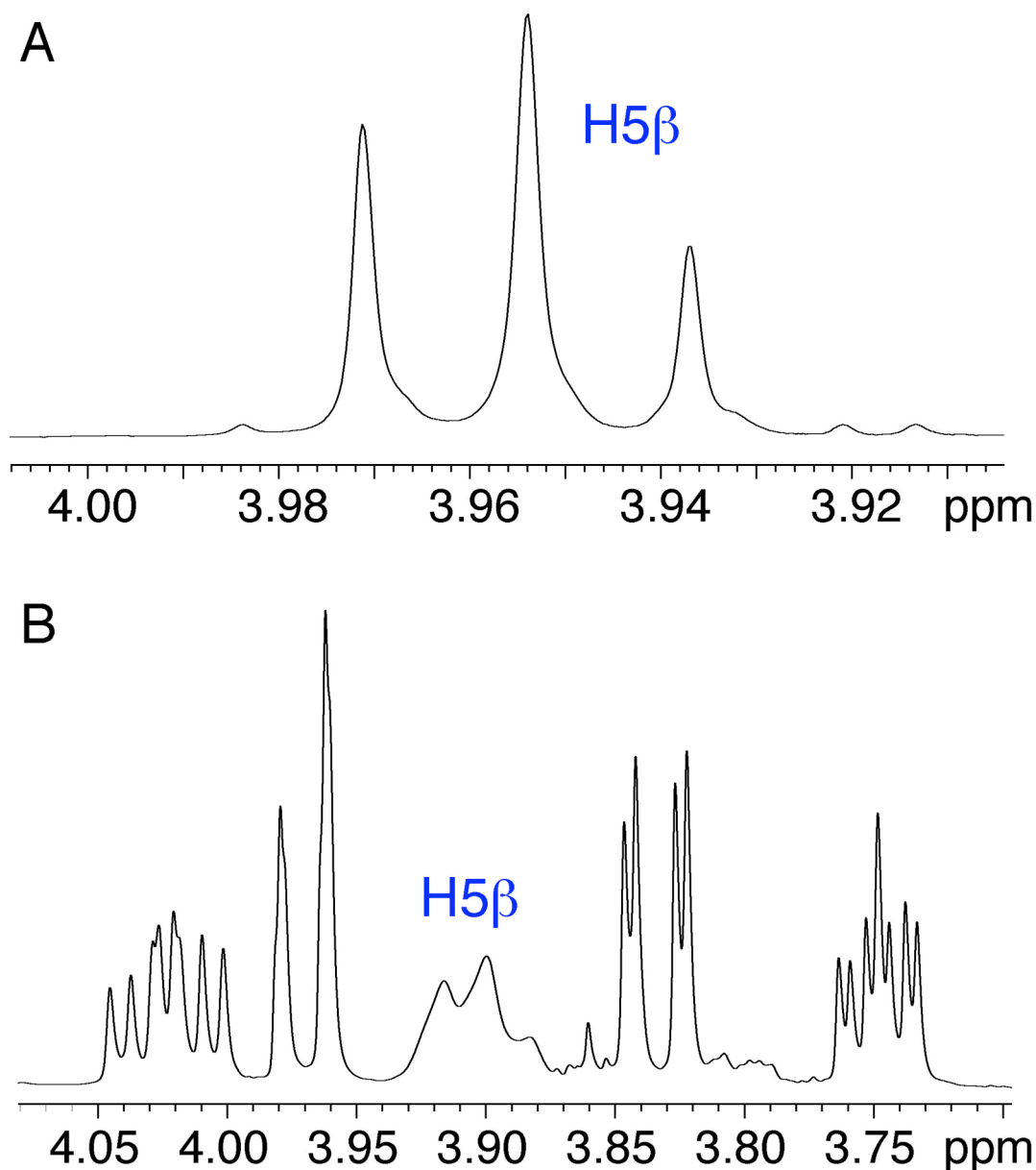


Figure 3.13. (S2) (A) H5 signal of 2βp at p²H 2.0 and 20 °C showing a pseudotriplet pattern due to the nearly equal values of $^3J_{\text{H4,H5}}$ (10.1 Hz) and $^3J_{\text{H5,H6}}$ (10.3 Hz). Resonance linewidths ($\Delta\nu_{0.5}$) range from 1.5-1.7 Hz. No J -coupling to the NH proton is observed since the latter is essentially fully exchanged with solvent ^2H . (B) H5 signal of 2βp at pH 8.0 and 20 °C. The pseudotriplet has broadened considerably (compare to data in Fig. 1A) due to rapid chemical exchange of the adjacent NH proton with solvent H_2O . Resonance linewidth ($\Delta\nu_{0.5}$) is estimated at ~17 Hz. Raw FIDs used to generate spectra in (A) and (B) were treated with a 0.1 Hz exponential apodization function prior to FT.

3.8. Acknowledgements.

This work was supported by a grant from the National Institutes of Health (GM) (to A.S.). The Notre Dame Radiation Laboratory is supported by the Office of Basic Energy Sciences of the United States Department of Energy. This is Document No. NDRL-4743 from the Notre Dame Radiation Laboratory.

3.9. References

1. Fujii, S.; Nishiura, T.; Nishikawa, A.; Miura, R.; Taniguchi, N. *J. Biol. Chem.* **1990**, *265*, 6009-6018.
2. Wormald, M.R.; Rudd, P.M.; Harvey, D.J.; Chang, S.-C.; Scragg, I.G.; Dwek, R.A. *Biochemistry* **1997**, *36*, 1370-1380.
3. Masuda, K.; Yamaguchi, Y.; Kato, K.; Takahashi, N.; Shimada, I.; Arata, Y. *FEBS* **2000**, *473*, 349-357.
4. (a) Breton, C.; Snajdrova, L.; Jeanneau, C.; Koca, J.; Imberty, A. *Glycobiology* **2006**, *16*, 29R-37R. (b) Lairson, L.L.; Wakarchuk, W.W.; Withers, S.G. *Chem. Commun.* **2007**, 365-367.
5. Mahdavi, J.; Sondén, B.; Hurtig, M.; Olfat, F.O.; Forsberg, L.; Roche, N.; Ångström, J.; Larsson, T.; Teneberg, S.; Karlsson, K.-A.; Altraja, S.; Wadström, T.; Kersulyte, D.; Berg, D.E.; Dubois, A.; Petersson, C.; Magnusson, K-E.; Norberg, T.; Lindh, F.; Lundskog, B.B.; Arnqvist, A.; Hammarström, L.; Borén, T. *Science* **2002**, *297*, 573-578.
6. (a) Russell, R.J.; Haire, L.F.; Stevens, D.J.; Collins, P.J.; Lin, Y.P.; Blackburn, G.M.; Hay, A.J.; Gamblin, S.J.; Skehel, J.J. *Nature* **2006**, *443*, 45-49. (b) Rameix Welti, M.A.; Agou, F.; Buchy, P.; Mardy, S.; Aubin, J.T.; Veron, M.; van der Werf, S.; Naffakh, N. *Antimicrobial Agents and Chemotherapy* **2006**, *50*, 3809 - 3815.
7. (a) Palese, P.; Ueda, M.; Tobita, K; Compans, R.W. *Virology* **1974**, *61*, 397-410. (b) Kim, C.U.; Williams, M.A.; Lui, H.; Zhang, L.; Swaminathan, S.; Bischofberger, N.; Chen, M.S.; Mendel, D.B.; Tai, C.Y.; Laver, W.G.; Stevens, R.C. *J. Am. Chem. Soc.* **1997**, *119*, 681-690.

8. Morell, A.G.; Gregoriadis, G.; Scheinberg, H.; Hickman, J.; Ashwell, G. *J. Biol. Chem.* **1971**, *246*, 1461-1467.
9. Klepach, T.; Carmichael, I.; Serianni, A.S., submitted for publication.
10. Frisch, M.J.; Trucks, G.W.; Schlegel, H.B.; Scuseria, G.E.; Robb, M.A.; J.R.; Montgomery, Jr., J.A.; Vreven, T.; Kudin, K.N.; Burant, J.C.; Millam, J.M.; Iyengar, S.S.; Tomasi, J.; Barone, V.; Mennucci, B.; Cossi, M.; Scalmani, G.; Rega, N.; Petersson, G.A.; Nakatsuji, H.; Hada, M.; Ehara, M.; Toyota, K.; Fukuda, R.; Hasegawa, J.; Ishida, M.; Nakajima, T.; Honda, Y.; Kitao, O.; Nakai, H.; Klene, M.; Li, X.; Knox, J.E.; Hratchian, H.P.; Cross, J.B.; Adamo, C.; Jaramillo, J.; Gomperts, R.; Stratmann, R.E.; Yazyev, O.; Austin, A.J.; Cammi, R.; Pomelli, C.; Ochterski, J.W.; Ayala, P.Y.; Morokuma, K.; Voth, G.A.; Salvador, P.; Dannenberg, J.J.; Zakrzewski, V.G.; Dapprich, S.; Daniels, A.D.; Strain, M.C.; Farkas, O.; Malick, D.K.; Rabuck, A.D.; Raghavachari, K.; Foresman, J.B.; Ortiz, J.V.; Cui, Q.; Baboul, A.G.; Clifford S.; Cioslowski, J.; Stefanov, B.B.; Liu, G.; Liashenko, A.; Piskorz, P.; Komaromi, I.; Martin, R.L.; Fox, D.J.; Keith, T.; Al-Laham, M.A.; Peng, C.Y.; Nanayakkara, A.; Challacombe, M.; Gill, P.M.W.; Johnson, B.; Chen, W.; Wong, M.W.; Gonzalez, C.; Pople, J.A. *Gaussian03*, Revision A.1, Gaussian, Inc., Pittsburgh PA, 2003.
11. Becke, A.D. *J. Chem. Phys.* **1993**, *98*, 5648-5652.
12. Hehre, W.J.; Ditchfield, R.; Pople, J.A. *J. Chem. Phys.* **1972**, *56*, 2257-2261.
13. Pan, Q.; Klepach, T.; Carmichael, I.; Reed, M.; Serianni, A.S. *J. Org. Chem.* **2005**, *70*, 7542-7549.
14. (a) Zhao, H.; Pan, Q.; Zhang, W.; Carmichael, I.; Serianni, A.S. *J. Org. Chem.* **2007**, in press. (b) Stenutz, R.; Carmichael, I.; Widmalm, G.; Serianni, A.S. *J. Org. Chem.* **2002**, *67*, 949-958. (c) Cancés, M.T.; Mennucci, B.; Tomasi, J. *J. Chem. Phys.* **1997**, *107*, 3032. (d) Cammi, R.; Mennucci, B.; Tomasi, J. *J. Phys. Chem.* **2000**, *104A*, 5631.
15. Brown, E.B.; Brey, Jr., W.S.; Weltner, Jr., W. *Biochim. Biophys. Acta* **1975**, *399*, 124-130.
16. Schmidt, H.; Friebohn, H. *J. Carbohydr. Chem.* **1983**, *2*, 405-413.
17. Gervay, J.; Batta, G. *Tetrahedron Lett.* **1994**, *35*, 3009-3012.
18. Czarniecki, M.; Thornton, E.R. *J. Am. Chem. Soc.* **1976**, *98*, 1023-1025.
19. (a) Czarniecki, M.; Thornton, E.R. *J. Am. Chem. Soc.* **1977**, *99*, 8273-8279. (b) Hori, H.; Nakajima, T.; Nishida, Y.; Ohru, H.; Meguro, H. *Tetrahedron Lett.* **1988**, *29*, 6317-6320.

20. (a) Szarek, W.A.; Roszak, A.W.; Crone, G.M.; Martin, O.R. *Acta Cryst.* **1997**, *C53*, 1921-1923. (b) O'Connell, A.M. *Acta Cryst.* **1973**, *B29*, 2320-2328.
21. Bock, K.; Pedersen, C. *Acta Chem. Scand.* **1977**, *B31*, 354-358.
22. Podlasek, C.A.; Wu, J.; Stripe, W.A.; Bondo, P.B.; Serianni, A.S. *J. Am. Chem. Soc.* **1995**, *117*, 8635-8644.
23. Pan, Q.; Klepach, T.; Carmichael, I.; Reed, M.; Serianni, A.S. *J. Org. Chem.* **2005**, *70*, 7542-7549.
24. Klepach, T.; Carmichael, I.; Serianni, A.S. *J. Am. Chem. Soc.* **2005**, *127*, 9781
25. Bose, B.; Serianni, A.S., unpublished results.
26. Church, T.; Carmichael, I.; Serianni, A.S. *Carbohydr. Res.* **1996**, *280*, 177-186.
27. Bose, B.; Klepach, T.; Bondo, G.; Bondo, P.B.; Zhang, W.; Carmichael, I.; Serianni, A.S., *J. Org. Chem.* **2007**, in press.
28. King-Morris, M.; Serianni, A.S. *J. Am. Chem. Soc.* **1987**, *109*, 3501-3508.
29. Bose, B.; Zhao, S.; Stenutz, R.; Cloran, F.; Bondo, P.B.; Bondo, G.; Hertz, B.; Carmichael, I.; Serianni, A.S. *J. Am. Chem. Soc.* **1998**, *120*, 11158-11173.
30. Duker, J.; Serianni, A.S. *Carbohydr. Res.* **1993**, *249*, 281-303.

CHAPTER 4:
CORRELATED C-C AND C-O BOND CONFORMATIONS IN SACCHARIDE
HYDROXYMETHYL GROUPS: PARAMETRIZATION AND APPLICATION OF
REDUNDANT ^1H - ^1H , ^{13}C - ^1H , AND ^{13}C - ^{13}C NMR J -COUPLINGS³

“It is a profoundly erroneous truism... that we should cultivate the habit of thinking of what we are doing. The precise opposite is the case. Civilization advances by extending the number of important operations which we can perform without thinking about them.”

– Alfred North Whitehead

4.1. Abstract

Methyl α - and β -pyranosides of D-glucose and D-galactose **1-4** were prepared containing single sites of ^{13}C -enrichment at C4, C5, and C6 (12 compounds), and ^1H and $^{13}\text{C}\{^1\text{H}\}$ NMR spectra were obtained to determine a complete set of J -couplings (1J , 2J , and 3J) involving the labeled carbon and nearby protons and carbons within the exocyclic hydroxymethyl group (CH_2OH) of each compound. In parallel theoretical studies, the dependencies of 1J , 2J , and 3J involving ^1H and ^{13}C on the C5-C6 (ω) and C6-O6 (θ)

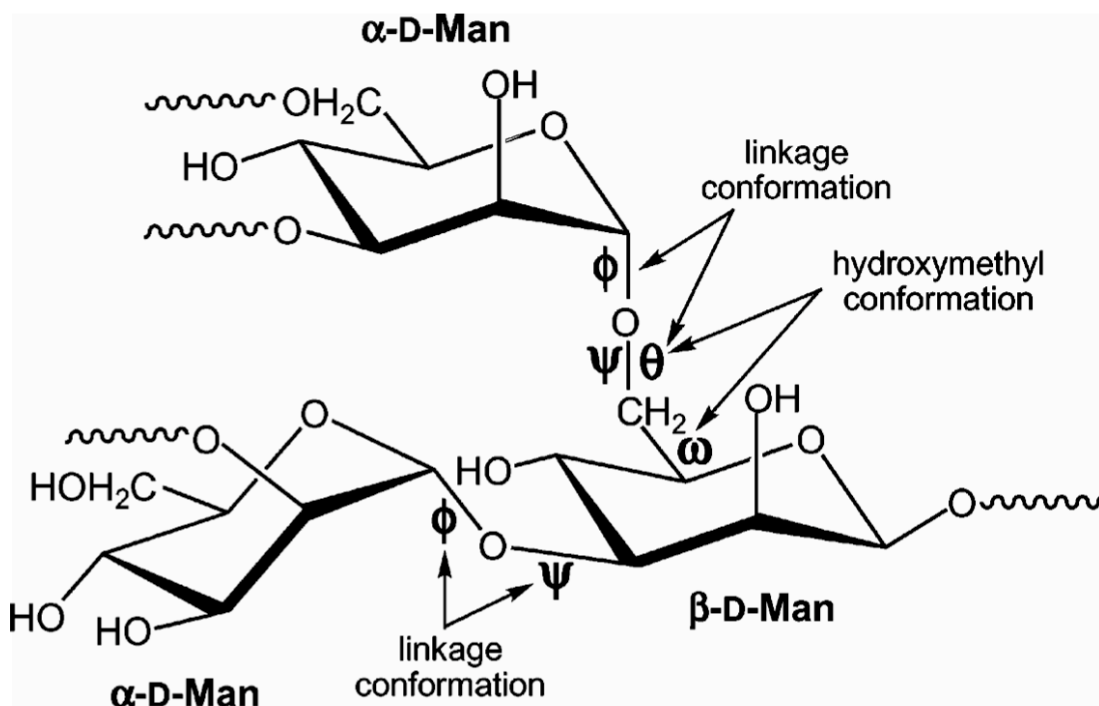
³ I gratefully acknowledge my co-authors Christophe Thibaudeau, Roland Stenutz, Brian Hertz, Shikai Zhao, Qingquan Wu, Ian Carmichael and Anthony S. Serianni for their assistance in preparing this chapter, which is submitted to the Journal of the American Chemical Society.

torsion angles in aldohexopyranoside model compounds were computed using density functional theory (DFT) and a special basis set designed to reliably recover the Fermi contact contribution to the coupling. Complete hypersurfaces for $^1J_{C5,C6}$, $^2J_{C5,H6R}$, $^2J_{C5,H6S}$, $^2J_{C6,H5}$, $^2J_{C4,C6}$, $^3J_{C4,H6R}$, $^3J_{C4,H6S}$, and $^3J_{C6,H4}$, as well as $^2J_{H6R,H6S}$, $^3J_{H5,H6R}$, and $^3J_{H5,H6S}$, were obtained and used to parametrize new equations correlating these couplings to ω and/or θ . DFT-computed couplings were also tested for accuracy by measuring J -couplings in ^{13}C -labeled 4,6-*O*-ethylidene derivatives of D-glucose and D-galactose in which values of ω and θ were constrained. Using a new computer program, *Chymesa*, designed to utilize multiple J -couplings sensitive to exocyclic CH_2OH conformation, the ensemble of experimental couplings observed in **1-4** were analyzed to yield preferred rotamer populations about ω and θ . Importantly, due to the sensitivity of some couplings, most notably $^2J_{H6R,H6S}$, $^2J_{C5,H6R}$ and $^2J_{C5,H6S}$, to both ω and θ , unique information on correlated conformation about both torsion angles was obtained. The latter treatment represents a means of evaluating *correlated* conformation in 1,6-linked oligosaccharides, since ψ and θ are redundant in these linkages. In the latter regard, multiple, redundant scalar couplings originating from both sides of the glycosidic linkage can be used collectively to evaluate conformational correlations between ψ / θ and C5-C6 bond rotamers.

4.2.Introduction

Conformational analysis of saccharides by NMR is often compromised by insufficient structural constraints on which to base firm conformational assignments^{1,2}.

This problem is particularly acute in studies of conformationally flexible domains, such as the exocyclic hydroxymethyl (CH_2OH) fragments of monosaccharides and the *O*-glycosidic linkages of oligo- and polysaccharides. In the former, the assignment of conformation is especially important when O6 is involved in the *O*-glycosidic linkage, since here three torsion angles define linkage geometry, namely, ω , ψ , and ϕ (Scheme 4.1).



Scheme 4.1. Part of the Core Structure of Glycoprotein *N*-Glycans, showing 1,3- and 1,6-Linkages and the ψ/ϕ Redundancy in the Latter

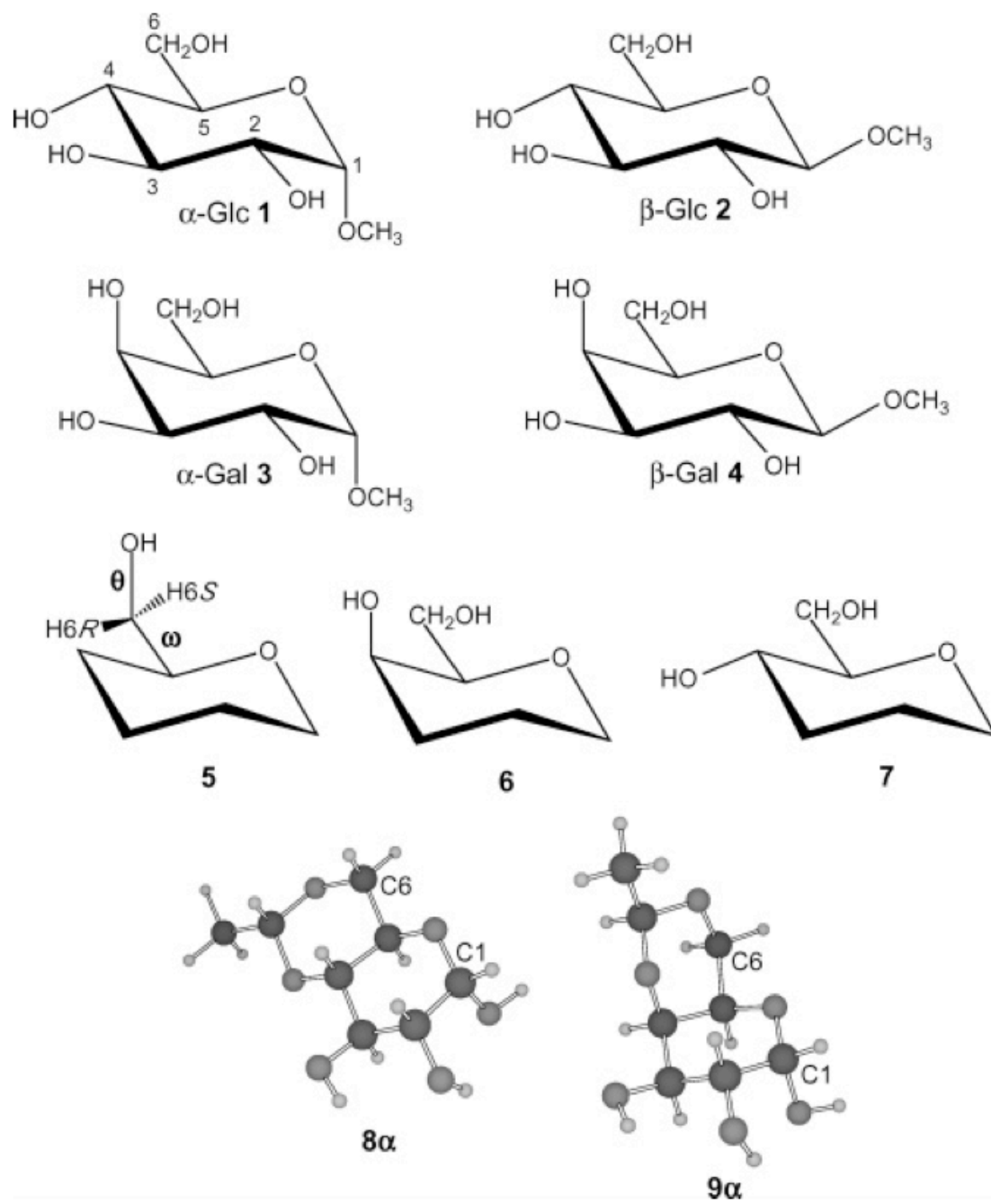
Experimental and theoretical studies of trans-*O*-glycoside couplings ($^2J_{\text{COC}}$, $^3J_{\text{COCH}}$, and $^3J_{\text{COCC}}$) were undertaken recently to determine their dependencies on oligosaccharide structure.¹⁻⁵ In addition to the expected Karplus dependence of $^3J_{\text{COCC}}$, terminal electronegative substituent effects were shown to be significant and quantifiable,

leading to more accurate interpretations of these couplings in structural terms.^{1,2} Likewise, $^3J_{\text{HCCH}}$, $^2J_{\text{HCH}}$, and $^1J_{\text{CH}}$ within saccharide exocyclic CH_2OH groups were examined, leading to new equations correlating their magnitudes to ω and ψ (Scheme 4.1).⁶ These studies demonstrated that J -couplings often display dependencies on more than one molecular parameter. These secondary dependencies are useful when direct experimental parameters are either unavailable or inaccessible to probe a specific conformational feature. For example, prior work suggests that $^3J_{\text{C1,C6}}$ in aldohexopyranosyl rings not only display the expected Karplus dependence on the C1-O5-C5-C6 torsion angle but also respond predictably to changes in the O5-C5-C6-O6 torsion, suggesting that these couplings may be valuable indirect probes of hydroxymethyl group conformation.¹ The two-parameter dependencies of J -couplings lead to the possibility of evaluating correlated conformations in saccharides. To explore this potential, the present work aimed to identify the primary structural factor(s) governing specific J -couplings and to uncover and quantify secondary (and heretofore unknown) structural dependencies that may be exploited to assess correlated behaviors. We also attempted to identify the underlying structural features (e.g., bond lengths, bond angles, stereoelectronic effects) or trends that influence specific coupling magnitudes.

The above experimental aims are more compelling when considering the likelihood of conformational flexibility about ω , ψ , and ϕ (Scheme 4.1). Arguments presented in the literature about whether oligosaccharides are rigid or flexible are largely moot; there is likely to be mobility about each of these bonds in solution. The key issues are the amplitudes and time scales of these motions, which are probably context-dependent.⁵ Given the wide range of monosaccharides and the various modes of

assembling them into oligomers, it will be challenging to establish whether these contexts can be systematically identified and categorized, thereby leading to reliable empirical rules correlating primary structure with oligosaccharide conformation and dynamics.

In this study, recent work⁶ on J -couplings sensitive to saccharide exocyclic CH₂OH conformation is extended. Previously we showed that density functional theory (DFT) calculations using a special basis set predict $^2J_{HH}$, $^3J_{HH}$, and $^1J_{CH}$ nearly quantitatively without the need for scaling, yielding new equations correlating these couplings with ω and/or θ (Scheme 4.1).⁶ Herein, $^2J_{CH}$, $^3J_{CH}$, $^1J_{CC}$, $^2J_{CC}$, and $^3J_{CC}$ are examined experimentally and theoretically; additional data on $^2J_{HH}$ and $^3J_{HH}$ are also presented. Methyl D-gluco- and D-galactopyranoside anomers **1-4** were prepared singly ¹³C -enriched at C4, C5, and C6 and used for experimental determinations of J_{CH} and J_{CC} involving the carbons and hydrogens near the CH₂OH substituent; these couplings include $^1J_{C5,C6}$, $^2J_{C5,H6R}$, $^2J_{C5,H6S}$, $^2J_{C6,H5}$, $^2J_{C4,C6}$, $^3J_{C4,H6R}$, $^3J_{C4,H6S}$, and $^3J_{C6,H4}$. Their interpretation was facilitated by DFT calculations in model structures **5-7** and by NMR measurements within conformationally constrained 4,6-*O*-ethylidene-D-gluco- and D-galactopyranoses. New parametrized equations relating J_{HH} , J_{CH} , and J_{CC} to ω and/or θ have been developed, and a concerted analysis of multiple redundant J -couplings to evaluate correlated conformation about ω and θ in aldohexopyranosyl rings is described using a new computer program, *Chymesa*. The results have important implications for future investigations of biologically relevant oligosaccharides containing 1,6-glycosidic linkages.



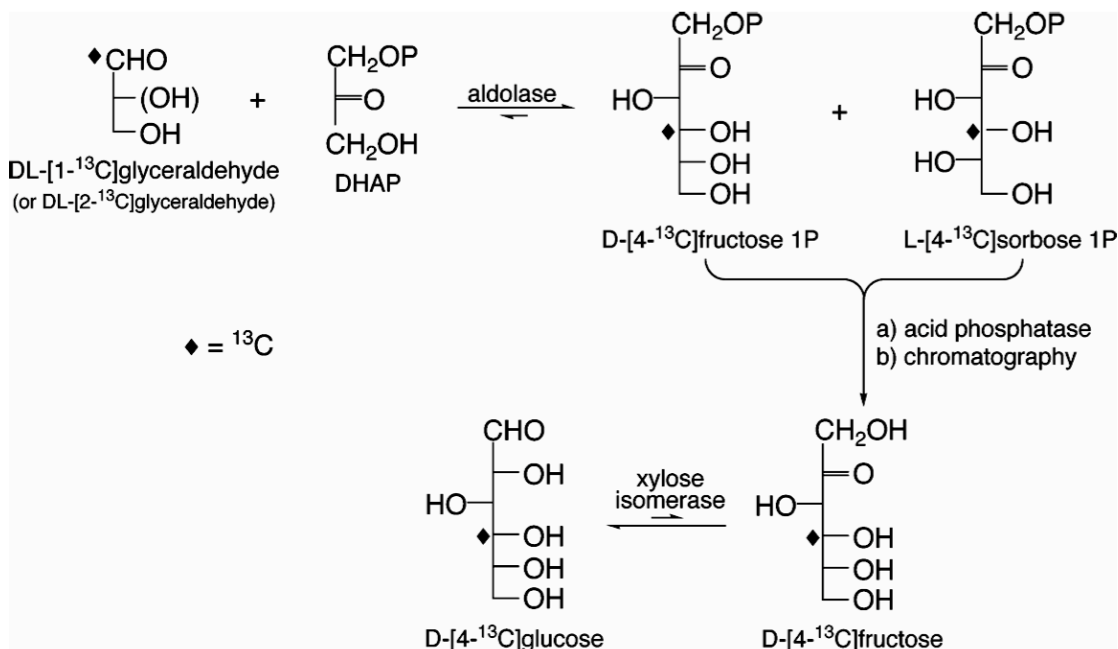
4.3.Experimental Section

4.3.1.Synthesis of Labeled Methyl Aldohexopyranosides.

Methyl α -D-[4- ^{13}C]-, [5- ^{13}C]-, and [6- ^{13}C]glucopyranosides (**1**); methyl β -D-[4- ^{13}C]-, [5- ^{13}C]-, and [6- ^{13}C]glucopyranosides (**2**); methyl α -D-[4- ^{13}C]-, [5- ^{13}C]-, and [6- ^{13}C]galactopyranosides (**3**); and methyl β -D-[4- ^{13}C]-, [5- ^{13}C]-, and [6- ^{13}C]galactopyranosides (**4**) were prepared as described previously,^{7,8} and only brief descriptions are provided here.

D-[4- ^{13}C]Glucose and D-[5- ^{13}C]glucose were prepared from DL-[1- ^{13}C]- and [2- ^{13}C]glyceraldehyde, respectively,⁹ and dihydroxyacetone phosphate (DHAP)¹⁰ using FBP aldolase (E.C. 4.1.2.13) (Scheme 4.2). The initially formed hexulose 1-phosphates were dephosphorylated with acid phosphatase (E.C. 3.1.3.2), and the neutral labeled D-fructose and L-sorbose were purified by chromatography on Dowex 50 \times 8 (200-400 mesh) in the Ca^{2+} form (fructose elutes first, followed by sorbose).¹¹ The purified labeled D-fructoses were treated with immobilized D-xylose isomerase (E.C. 5.3.1.5), and the resulting mixtures containing labeled D-glucoses and D-fructoses were purified by chromatography on Dowex 50 \times 8 (200-400 mesh) in the Ca^{2+} form (glucose elutes first, followed by fructose).

D-[6- ^{13}C]Glucose was prepared from K^{13}CN and 1,2-*O*-isopropylidene- α -D-xylo-pentodialdo-1,4-furanose as described previously.¹² D-[4- ^{13}C]-, [5- ^{13}C]-, and [6- ^{13}C]Galactoses were prepared from the corresponding labeled D-glucoses via C4-epimerization.¹³



Scheme 4.2. The Synthesis of D-[4-¹³C]Glucose.

The labeled D-glucoses and D-galactoses were converted to their methyl pyranosides by treatment with anhydrous MeOH in the presence of Dowex 50 × 8 (20-50 mesh) resin in the H⁺ form (Fischer glycosidation).¹⁴ In each case, the mixture of anomeric aldohexopyranosides was purified by chromatography on Dowex 1 × 8 (200-400 mesh) ion-exchange resin in the OH⁻ form, using water as the eluent.¹⁵ Purified glycosides (12 total) were identified by their characteristic ¹H and ¹³C chemical shifts.^{14,16}

4,6-*O*-Ethylidene-D-[4-¹³C]-, [5-¹³C]-, and [6-¹³C]glucoses, and 4,6-*O*-ethylidene-D-[6-¹³C]galactose were prepared from the corresponding labeled D-hexoses as follows.¹⁷ The labeled hexose (181 mg, 1.0 mmol) was mixed in a 10 mL round-bottom flask with acetaldehyde (60 L, 1.1 mmol) and *p*-toluenesulfonic acid

monohydrate (5 mg). The mixture was stirred at 5° C overnight and extracted with hot ethyl acetate (3 × 8 mL), and the extract was concentrated at 30° C in vacuo. The crude product was purified by chromatography on silica gel using MeOH/CH₂Cl₂ (7:1) as the solvent, and the derivatives were characterized by ¹H and ¹³C NMR. Overall yields ranged from 15 to 25%; unreacted starting aldose, which accounted for the low yield, was recovered for reuse.

4.3.2. NMR Spectroscopy.

¹H and ¹³C {¹H} NMR spectra of ¹³C-labeled methyl D-gluco- and D-galactopyranosides, and of ¹³C-labeled 4,6-*O*-ethylidene-D-gluco- and galactopyranoses, were obtained at 30° C in ²H₂O (~50 mM for ¹H; ~200 mM for ¹³C) on a Varian UnityPlus FT-NMR spectrometer operating at 599.887 MHz for ¹H and 150.854 MHz for ¹³C. 1D Spectra were processed with optimal digital resolution and resolution enhancement to extract *J*-couplings having errors of ±0.1 Hz unless otherwise noted; couplings <0.5 Hz appeared as line-broadening. Spectral simulation was required to extract accurate *J*_{HH} and *J*_{CH} couplings in all cases and to determine/confirm coupling signs; MacNUTS¹⁸ operating on Apple platforms was used to generate simulated ¹H NMR spectra.

4.3.3. Theoretical Calculations.

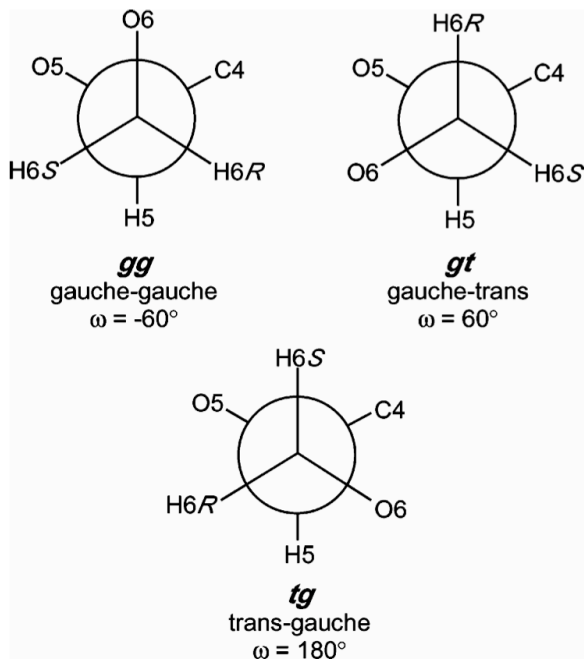
The torsion angles, ω and θ, are defined as O5-C5-C6-O6 and C5-C6-O6-O6H, respectively, in **1-7**. Density functional theory (DFT) calculations using the B3LYP functional¹⁹ and the 6-31G* basis set²⁰ were conducted within *Gaussian94*²¹ for

geometric optimization of molecular structures.^{1,2} Three model compounds (**5-7**) were used in the calculations. The most extensive data set was obtained on **5**, which lacks an OH substituent at C4, thus reducing complications caused by the arbitrary introduction of intramolecular hydrogen bonding (with concomitant undesirable changes in bond torsions) during the geometric optimizations. The ω and θ torsion angles in **5** were varied systematically from 0°-360° in 30° increments by holding both torsion angles at fixed values in the calculations, yielding 144 partially optimized geometries; all remaining molecular parameters were geometrically optimized. These data were used to generate the hypersurfaces. Nine structures were obtained containing staggered values of ω and θ wherein both torsion angles and all other degrees of freedom were optimized. A comparison of partially and fully optimized geometries gave an estimate of the extent to which holding ω and θ at fixed values affected the computed couplings.

A second series of calculations was performed on **6** and **7** that contain an axial and equatorial OH substituent at C4, respectively. In these calculations, one set of C-O torsion angles was inspected (C5-C4-O4-OH4 and C5-C6-O6-OH6 torsion angles of ~180°), and only the three staggered rotamers about ω were studied (total of six structures). All structures were fully geometrically optimized. These calculations were performed to determine the effect of OH substituents on *J*-couplings involving C4 or H4 (e.g., $^3J_{C4,H6R/S}$, $^2J_{C5,H4}$, $^2J_{C4,C6}$). Restricting these calculations to a limited set of C-O torsions avoided complications caused by intramolecular H-bonding between O4 and O6 and their attached protons, which can distort geometries and induce undesirable torsion changes in the molecules.

A third series of calculations was performed on 4,6-*O*-ethylidene- α -D-glucopyranose (**8** α) and 4,6-*O*-ethylidene- β -D-galactopyranose (**9** α). As described for **6** and **7**, one set of C-O torsions was inspected (optimized torsions were as follows: for **8** α , C2-C1-O1-H = -172.0°, C1-C2-O2-H = -46.0°, C2-C3-O3-H = -48.2°; for **9** α , C2-C1-O1-H = -171.0°, C1-C2-O2-H = -44.3°, C2-C3-O3-H = -41.2°).

Coupling constants in **5-9** were calculated² by DFT using a modified version of *Gaussian94*²¹ and an extended basis set ([5s2p1d|3s1p])⁶ designed to reliably recover the Fermi contact contribution to the coupling. Prior work has shown that, in the present cases, contributions from the non-Fermi contact terms are small and can be neglected without significantly affecting the results. All computed couplings reported are *unscaled*, and all equations correlating structure with *J*-coupling magnitudes and signs were derived using unscaled couplings.



Scheme 4.3. Idealized Staggered Rotamers (ω) about the C5-C6 Bond of Aldohexopyranosyl Rings

4.3.4. Equation Parametrization.

Equations describing the dependencies of 2J , and 3J on ω and θ were parametrized using *ProFit* 5.6.2 (Quantum Soft, Zürich, Switzerland). In the least-squares Monte Carlo fitting module integrated in *ProFit*, coefficients of the Fourier series used to formulate the equation were randomly generated, and for each set of coefficients, the deviation between J -values predicted by the equation and those from the reference dataset was calculated in the form of a χ^2 parameter. In this work, the dataset consisted of 144 (J , ω , θ) points generated from the hypersurface calculations and of 9 freely optimized (ω , θ) rotamers. For each parametrized equation, χ^2 was minimized in an iterative fashion. When no significant improvement in χ^2 was observed compared to the "best" value, the calculation was terminated and the resulting set of coefficients was used to formulate the best fit equation.

Extended equations were parametrized to better describe the dependence of J_{HH} , J_{CH} , and J_{CC} on ω and θ by systematically including ω or θ terms of increasing complexity in the Fourier series up to $\sin(2x)$ and $\cos(2x)$ and comparing the "best" χ^2 values for each extended equation to the χ^2 value generated by the simpler equations. In all cases, the number of terms was limited to 6 or 7 to avoid strongly correlated terms, which would produce an underdetermined system and an artificial improvement in χ^2 .

4.4. Results and Discussion

4.4.1. General Considerations.

Idealized staggered hydroxymethyl rotamers relevant to aldohexopyranosides are denoted *gg* ($\omega = -60^\circ$), *gt* ($\omega = 60^\circ$), and *tg* ($\omega = 180^\circ$) (Scheme 4.3). The stereochemical assignments of H6*R* and H6*S* are shown in **5**, and rotamer definitions for θ are shown in Scheme 4.4.

Systematic rotations about ω and θ in **5** (30° increments) yielded 144 (12×12 matrix) structures that define a reasonable conformational energy hypersurface (Figure 4.1). Three energy minima are observed at the three staggered ω / θ rotamers: $60^\circ / -60^\circ$ (0 kcal/mol); $300^\circ / 60^\circ$ (0.4 kcal/mol); and $180^\circ / -60^\circ$ (2.9 kcal/mol). Thus, gas-phase DFT calculations at the B3LYP/6-31G* level of theory yielded the following relative stabilities of hydroxymethyl rotamers in **5**: $gt \approx gg > tg$. It should be noted, however, that the stabilities of the *gt* and *gg* rotamers may be affected by the location of O6H (i.e., by θ); in *gg* and *gt*, O6H is oriented near one of the O5 lone pairs, and thus some stability may be conferred to both geometries due to intramolecular H-bonding. Indeed, *gg* and *gt* were higher in energy than *tg* when in the former θ was rotated to eliminate this H-bonding. Thus, *in the absence of solvent*, *tg* may be more stable than *gg* and *gt* when contributions from intramolecular H-bonding are eliminated, despite the presence of the gauche effect²² in the latter forms which has been invoked to explain the experimentally determined preference for *gg* and *gt* in aqueous solution.

Introduction of an OH group at C4 of **5**, giving **6** or **7**, affects the relative stabilities of rotamers. For **6**, tg (0.1 kcal/mol) $> gt$ (1.5 kcal/mol) $\gg gg$ (6.5 kcal/mol); for

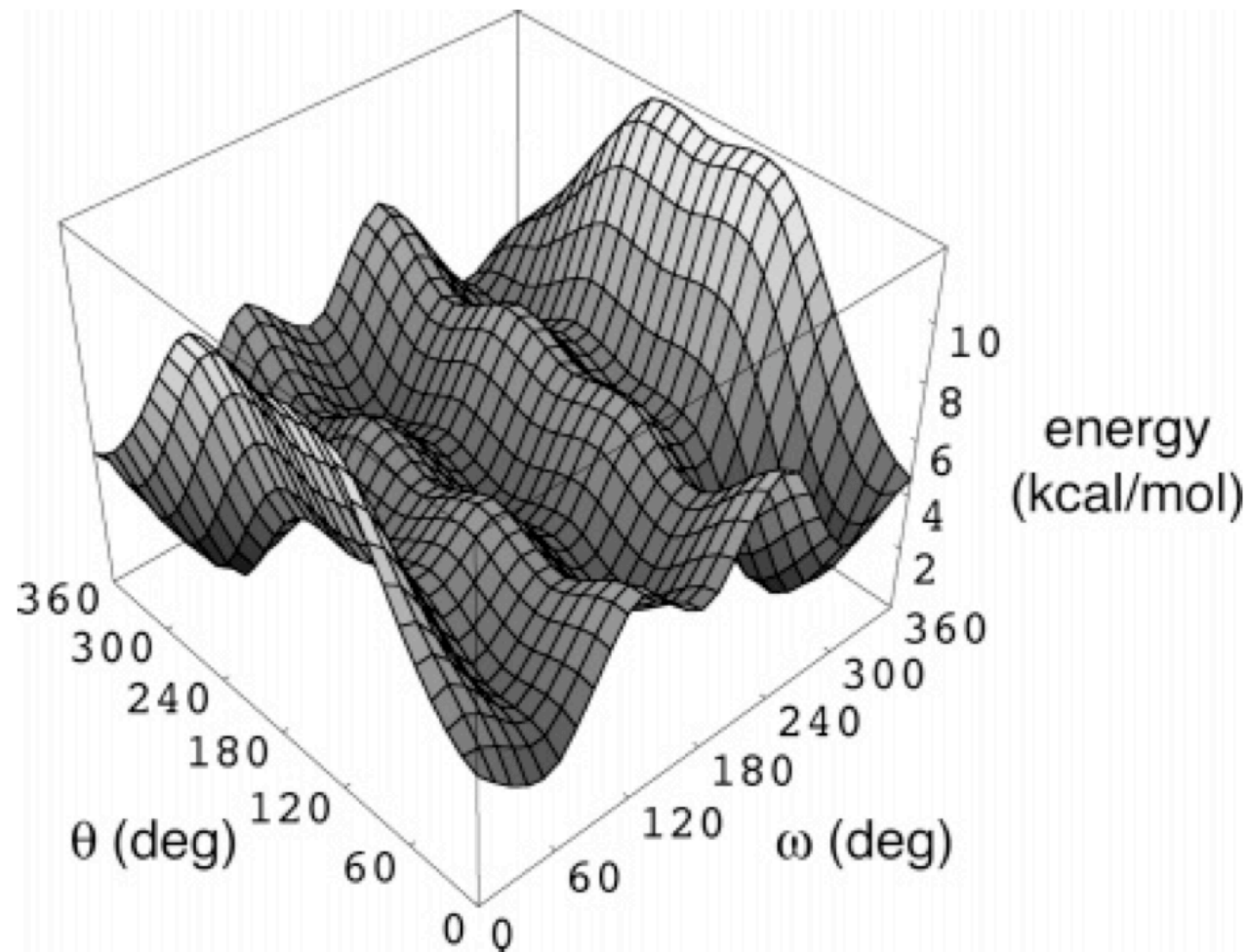
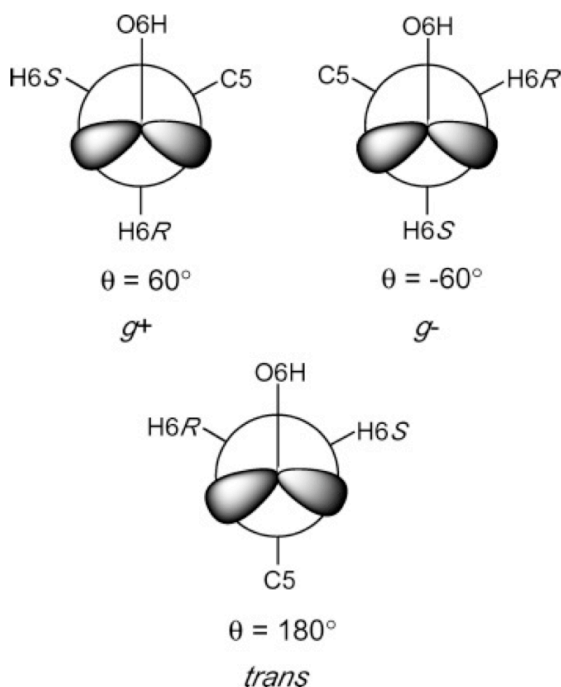


Figure 4.1. Conformational Energy Hypersurface Generated from 30° Rotations of ω and θ in **5** (144 optimized structures) determined by DFT (B3LYP/6-31G*).



Scheme 4.4. Idealized Staggered Rotamers (θ) about the C6-O6 Bond of Aldohexopyranosyl Rings.

7, gg (0 kcal/mol) \approx gt (0.4 kcal/mol) $>$ tg (2.6 kcal/mol). These trends contrast with that observed for **5**, where tg (0 kcal/mol) $>$ gt (1.4 kcal/mol) \approx gg (1.9 kcal/mol) for $\theta = 180^\circ$. The presence of an axial O4 (**6**) destabilizes gg but exerts a minimal effect on the relative energies of gt and tg . Introduction of an equatorial O4 stabilizes gg and gt significantly and destabilizes tg . However, results for **6** and **7** pertain to a small subset of C-O rotamers where intramolecular hydrogen bonding is weak or nonexistent, and relative populations derived from gas-phase calculations are expected to change significantly when the remaining C-O rotamers are taken into account, due to selective H-bonding in some forms. For these reasons, relying on conformational energy maps to predict preferences about ω can be problematic, since H-bonding and solvation forces affect torsional preferences.

4.5. Calculated NMR Scalar Coupling Constants and Parametrization.

4.5.1. Two-Bond ^{13}C - ^1H Spin-Spin Coupling Constants.

$^2J_{\text{CH}}$ Values are useful structural constraints in saccharides, nucleosides and their derivatives,^{6,14,23} and general rules have been proposed relating $^2J_{\text{CCH}}$ to specific patterns of oxygen atom substitution on the coupled carbon and on the carbon bearing the coupled hydrogen.^{23a-c} With respect to CH_2OH conformation, three $^2J_{\text{CCH}}$ are expected to be sensitive to ω : $^2J_{\text{C5,H6R}}$, $^2J_{\text{C5,H6S}}$, and $^2J_{\text{C6,H5}}$. Computed values of these couplings in **5** are given in Table 4.1. Application of the projection rule^{23a} yields two projections, 0 and 1.5, that correlate with average DFT-calculated $^2J_{\text{CCH}}$ values of -3.8 ± 1.2 Hz and $+3.2 \pm 1.8$ Hz, respectively, using data in Table 4.1. As noted previously,^{24,25} these computed couplings are shifted to more negative values than predicted by the projection rule.

The dependencies of $^2J_{\text{CCH}}$ on ω and θ are shown in Figure 4.2 for eclipsed and staggered ω rotamers. A single maximum and a single minimum are observed upon sampling ω from 0° to 360° . This behavior differs from that exhibited by $^3J_{\text{CH}}$ and $^3J_{\text{HH}}$ (see below), which display two maxima and two minima, and suggests a practical advantage of $^2J_{\text{CH}}$ in studies of CH_2OH conformation, namely, greater reliability in correlating experimental couplings to rotamer populations due to the smaller number of conformers compatible with extreme and intermediate experimental couplings. The dynamic range of $^2J_{\text{CCH}}$ is $\sim +5$ Hz to ~ -5 Hz ($\Delta \approx 10$ Hz), which is comparable to, if not slightly larger than, that observed for $^3J_{\text{CCCH}}$ ($\Delta \approx 8$ Hz) (see below). The signs of $^2J_{\text{CH}}$ depend on ω and are straightforward to determine experimentally.²⁶ Note that plots of

$^2J_{C5,H6R}$ and $^2J_{C5,H6S}$ in Figure 4.2 are complementary, which is a useful feature for stereochemical assignments of H6R and H6S and for CH₂OH conformational analysis.

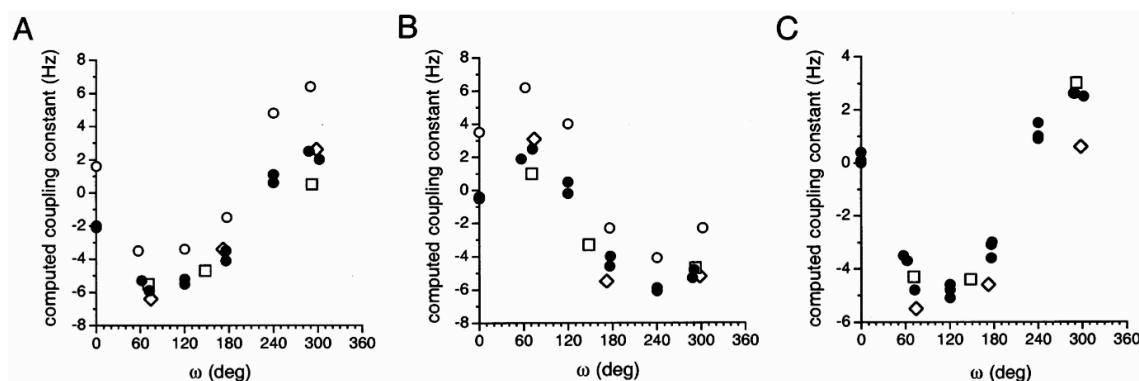


Figure 4.2. (A) Dependence of $^2J_{C5,H6R}$ on ω . (B) Dependence of $^2J_{C5,H6S}$ on ω . (C) Dependence of $^2J_{C6,H5}$ on ω . Circles, data from **5** (Table 4.1); open diamonds, data from **6** (Table S1). For **5** in plots A and B, data are divided into two groups to emphasize the enhanced coupling (open circles) observed in one θ conformation (see Scheme 4.5).

$^2J_{C5,H6R}$ and $^2J_{C5,H6S}$ exhibit a dependence on similar to that observed for $^2J_{H6R,H6S}$.⁶ Two groups of couplings are observed at a given ω for the three staggered θ rotamers (Figure 4.2A,B); two couplings are similar in magnitude and always smaller (more negative) than the third. The θ rotamer in which OH6 is gauche to both coupled nuclei consistently exhibits a more *positive* coupling than the remaining two staggered rotamers (Scheme 4.5). The effect is enhanced when the coupled proton is anti to O5 (an increase of $\sim +4$ Hz vs $\sim +2.3$ Hz). This observation is consistent with that made for $^2J_{H6R,H6S}$ where θ having OH6 gauche to H6R and H6S contributes positively to the coupling (Scheme 4.5C). The origin of this effect remains unclear, although it is noted that, in all three geometries, both coupled atoms are anti to an O6 lone pair. The expected

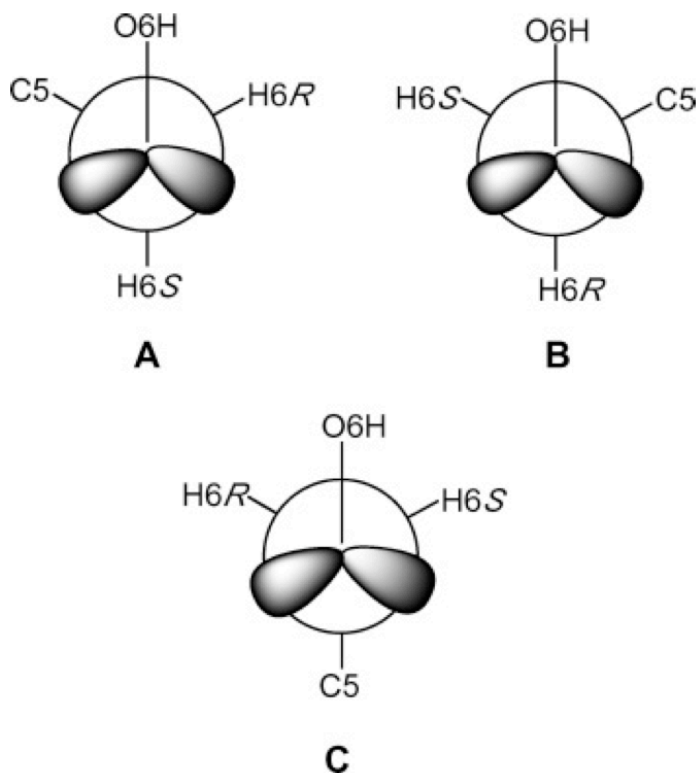
C-H and C-C bond elongation²⁷ may be partly responsible for the shift to more positive

TABLE 4.1. TORSION ANGLES^A, ω AND θ , CALCULATED $^2J_{\text{CH}}$ VALUES^B.

ω^c	θ^d	$^2J_{\text{C5,H6R}}$	$^2J_{\text{C5,H6S}}$	$^2J_{\text{C6,H5}}$	C5–C6 rotamer ^e
62	57	–5.3	+6.2	–3.7	<i>gt</i>
57	–48	–3.5	+1.9	–3.5	
72	192	–5.9	+2.5	–4.8	
–58	50	+2.0	–2.3	+2.5	<i>gg</i>
–70	–72	+6.4	–4.8	+2.6	
–72	171	+2.5	–5.3	+2.6	
176	74	–3.5	–2.3	–3.1	<i>tg</i>
177	–69	–1.5	–4.0	–3.0	
176	176	–4.1	–4.6	–3.6	
120	60	–5.5	+4.0	–4.8	
120	–60	–3.4	+0.5	–4.6	
120	180	–5.2	–0.2	–5.1	
0	60	–2.0	+3.5	+0.4	
0	–60	+1.6	–0.4	0.0	
0	180	–2.0	–0.4	+0.1	
–120	60	+1.1	–4.1	+0.9	
–120	–60	+4.8	–6.1	+1.5	
–120	180	+0.6	–5.9	+1.0	

^a In degrees. ^b In Hz. ^c Defined as O5–C5–C6–O6. ^d Defined as C5–C6–O6–HO6. ^e Defined in Scheme 3.

couplings. This effect is not observed for $^2J_{\text{C6,H5}}$ (Figure 4.2C), presumably because the C5–O5 torsion is held relatively fixed by the pyranosyl ring and cannot modulate the coupling.

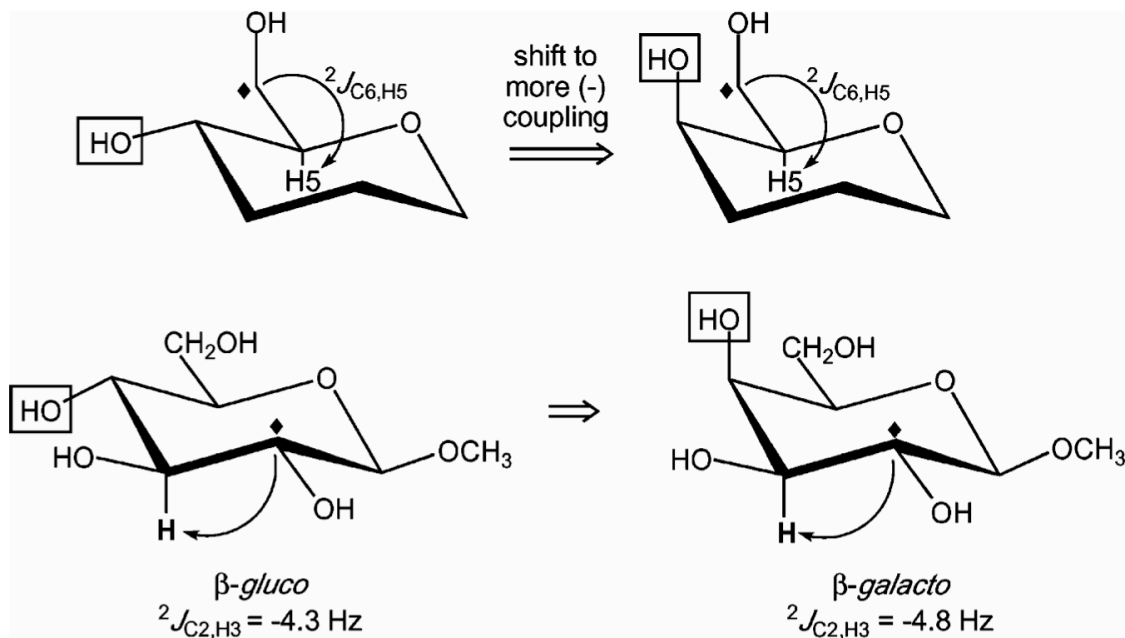


Scheme 4.5. θ Rotamers that Make a Positive Contribution to $^2J_{C5,H6R}$ (A), $^2J_{C5,H6S}$ (B), and $^2J_{H6R,H6S}$ (C)^a

Substitution of an OH group at C4 appears to affect $^2J_{C5,H6R}$ and $^2J_{C5,H6S}$ in those ring geometries in which the coupled proton experiences a 1,3-interaction with O4. In these cases, the coupling is shifted to a more negative value. For example, $^2J_{C5,H6S}$ is shifted to a more negative (less positive) value in **7** (by ~2 Hz) compared to **6** for $\omega = +60$ (Table S1); in the *gt* rotamer, H6S experiences a 1,3-interaction with the equatorial O4 in **7** which is absent in **6**. Essentially no effect of O4 is observed in the *gg* rotamer (when differences in ω are accounted for) regardless of C4 configuration, presumably because H6S is anti to C4 and thus well removed from the site of substitution. The above-noted 1,3-factor may be caused by small changes in C-H bond length induced by O4 lone pair

effects; in this case, the oxygen lone pairs are expected to reduce bond lengths slightly,²⁷ which may lead to the slightly more negative $^2J_{\text{CH}}$.

An effect of C4 hydroxylation on $^2J_{\text{C6,H5}}$ is also observed, but only when O4 is axial (Figure 4.2C). The coupling is shifted to a more *negative* value in the three staggered ω rotamers. This observation is consistent with prior reports of "remote" effects on $^2J_{\text{CCH}}$ in aldohexopyranosides;¹⁴ oxygen substituents trans to the coupled proton on adjacent carbons shift $^2J_{\text{CCH}}$ to more negative values (Scheme 4.6). The effect appears additive in that the shift observed in *gg* is ~ 2 -fold greater than that observed in *gt*, due to the presence of two anti oxygens (O4 and O6) in the former.



Scheme 4.6. C4 Configuration Dependence of $^2J_{\text{C6,H5}}$

The above discussion reveals a significant effect of C-O bond torsions on $^2J_{\text{CCH}}$ magnitudes which were anticipated earlier.⁶ To explore this effect further, a full

hypersurface was obtained for **5** wherein ω and θ were sampled in 30° increments from 0° to 360°. Two-dimensional plots for $^2J_{C5,H6R}$, $^2J_{C5,H6S}$ and $^2J_{C6,H5}$ are shown in Figure 4.3A and B. Superimposed on these plots are computed couplings determined in nine fully optimized structures (Table 4.1). The latter data agree with those obtained from partially optimized geometries, *indicating that fixing ω and θ does not significantly alter the computed couplings*. These results show that the effect of θ on $^2J_{CCH}$ is greater when the carbon bearing the oxygen *also bears the coupled proton*, as opposed to the coupled carbon; rotating θ exerts a greater effect on $^2J_{C5,H6R}$ and $^2J_{C5,H6S}$ than on $^2J_{C6,H5}$, as revealed by the narrower range of couplings observed for the latter at discrete values of ω . This effect is more clearly observed in the 3D hypersurfaces shown in Figures 4.3C-E. Presumably vicinal O6 lone pair effects²⁸ on the C6-H6R/S bond lengths (see below) perturb $^2J_{C5,H6R/S}$ more than O6 vicinal lone pair effects on the C5-C6 bond length perturb $^2J_{C6,H5}$. For this reason, $^2J_{C6,H5}$ may be more attractive than $^2J_{C5,H6R}$ and $^2J_{C5,H6S}$ for studies of CH₂OH conformation when information about θ is unavailable. In addition, the *range* of allowed couplings at each value of ω is essentially the same as that shown in Figure 4.2 when only staggered θ values were considered. The latter fact leads to simplified equations relating these couplings to ω and θ , as described below.

Valence bond angle, which has been shown to affect $^2J_{HCH}$,²⁹ might also influence $^2J_{CCH}$ values. However, in the fully optimized, staggered structures reported in Table 4.1, the C-C-H bond angle does not vary significantly; the average C5-C6-H6R, C5-C6-H6S, and C6-C5-H5 bond angles (± 1 SD) are $108.8^\circ \pm 0.5^\circ$, $108.8^\circ \pm 0.6^\circ$, and $108.1^\circ \pm 0.8^\circ$, respectively. This distribution compares favorably with that found

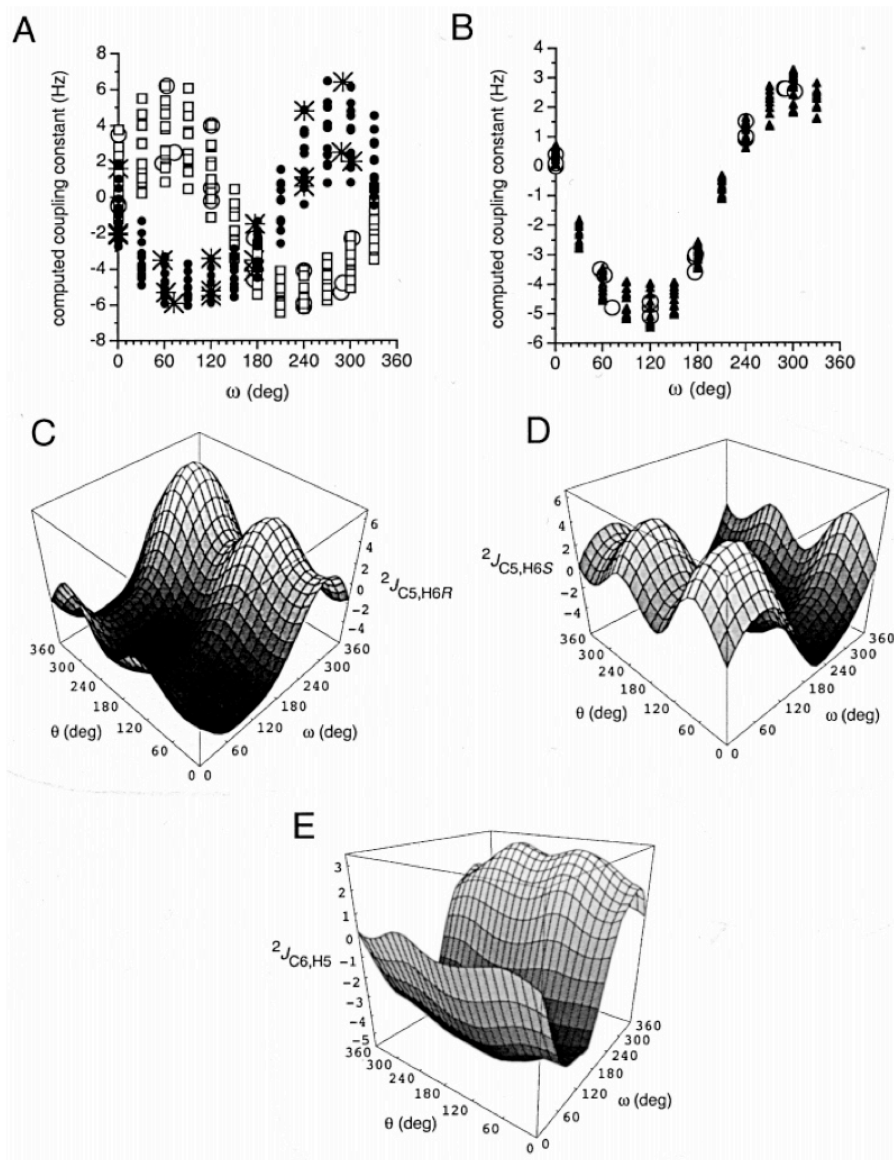


Figure 4.3. (A) The dependence of ${}^2J_{C5,H6R/S}$ on both ω and θ , determined by varying both torsion angles in **5** systematically through 360° in 30° increments. The vertical spread of points at discrete ω values demonstrates the sensitivity of these ${}^2J_{CH}$ to θ . Superimposed are coupling data computed in the fully (staggered) and partially (eclipsed) optimized structures reported in Table 4.1. Filled circles, ${}^2J_{C5,H6R}$; open squares, ${}^2J_{C5,H6S}$; stars and open circles, respective couplings taken from Table 4.1. (B) Data similar to that in part A for ${}^2J_{C6,H5}$ in **5**. Closed triangles, hypersurface data; open circles, data from Table 4.1. (C) Hypersurface (ω/θ) calculated for ${}^2J_{C5,H6R}$ in **5**. (D) Hypersurface (ω/θ) calculated for ${}^2J_{C5,H6S}$ in **5**. (E) Hypersurface (ω/θ) calculated for ${}^2J_{C6,H5}$ in **5**.

previously for the H6R-C6-H6S bond angle ($107.7^\circ \pm 0.4^\circ$),⁶ indicating that the C-C-H bond angle is probably not responsible for the observed dependence of $^2J_{\text{CCH}}$ on ω and θ , at least within the group of structures studied.

The dependencies of $^2J_{\text{C5,H6R}}$ and $^2J_{\text{C5,H6S}}$ on ω and θ were parametrized using the complete dataset of 153 datapoints (144 structures from the hypersurface; 9 staggered structures in Table 4.1), yielding eqs 4.1a and b. Equation 4.1c describes the dependence of $^2J_{\text{C6,H5}}$ on ω ; attempts to parametrize this equation by including both ω and θ terms did not improve the rms error significantly.

$$^2J_{\text{C5,H6R}} = -1.40 + 0.94 \cos(\omega) - 4.38 \sin(\omega) - 0.79 \cos(2\theta) - 1.24 \sin(2\theta) \quad (\text{rms} = 0.78 \text{ Hz}) \quad (4.1a)$$

$$^2J_{\text{C5,H6S}} = -1.32 + 2.24 \cos(\omega) + 4.12 \sin(\omega) - 0.80 \cos(2\theta) + 1.24 \sin(2\theta) \quad (\text{rms} = 0.70 \text{ Hz}) \quad (4.1b)$$

$$^2J_{\text{C6,H5}} = -1.29 + 1.53 \cos(\omega) - 3.68 \sin(\omega) \quad (\text{rms} = 0.45 \text{ Hz}) \quad (4.1c)$$

4.5.2. Three-Bond ^{13}C - ^1H Spin-Spin Coupling Constants.

$^3J_{\text{C4,H6R}}$ and $^3J_{\text{C4,H6S}}$ have been used previously to make stereochemical signal assignments of H6R and H6S in ^1H NMR spectra of aldohexopyranosyl rings, and in studies of CH_2OH conformation.^{14,30,31} A Karplus relationship has been reported³¹ and was applied recently to interpret $^3J_{\text{C4,H6R}}$ and $^3J_{\text{C4,H6S}}$ in aldohexopyranosyl rings.³²

Theoretical relationships among ${}^3J_{C4,H6R}$, ${}^3J_{C4,H6S}$, ω , and θ were examined initially in **5** using fully and partially geometrically optimized structures (Table S2). These data are plotted in Figure 4.4A, with the C-C-C-H torsion angle ϕ represented on the x-axis rather than ω . The distribution of data points at discrete values of ϕ reveals the sensitivity of ${}^3J_{CCCH}$ to θ . In comparison to ${}^2J_{CCH}$ (see above), the effect of θ on ${}^3J_{CCCH}$ is much reduced, as illustrated in the 3D hypersurfaces (Figure 4.4B and C) (note that the effect of C4-O4 bond rotation on ${}^3J_{C4,H6R/S}$ was not evaluated, but this effect is expected to be small based on observations made above on ${}^2J_{CCH}$). Both ${}^3J_{C4,H6R}$ and ${}^3J_{C4,H6S}$ display a Karplus dependence as expected, but the two curves are phase-shifted by $\sim 20^\circ$. For comparison, the previously reported theoretical curve^{31,32} is shown in Figure 4.4A. While the general features of both treatments are conserved, predicted couplings for $\pm 30^\circ$ differ significantly, with larger values predicted by the present treatment.

Concern about the applicability of Karplus curves derived from theoretical studies of **5** to the analysis of experimental couplings observed in authentic aldohexopyranosyl rings substituted with oxygen on C4 (i.e., **1-4**) was addressed by calculating ${}^3J_{CCCH}$ in **6** and **7** (Figure 4.4A). Although the data for **6** and **7** are limited, there is no indication that O4 substitution significantly alters the relationships; ~ 1 Hz deviations are observed at $\phi \approx 180^\circ$ for both couplings, whereas differences at $\phi = \sim 60$ and -60 are insignificant. The small phase shift is also evident in the limited data obtained on **6** and **7**. We conclude that two different equations are required to describe the structural dependencies of ${}^3J_{C4,H6R}$ and ${}^3J_{C4,H6S}$ and that the curves derived from **5** are applicable, to a first approximation, to rings bearing OH substituents at C4.

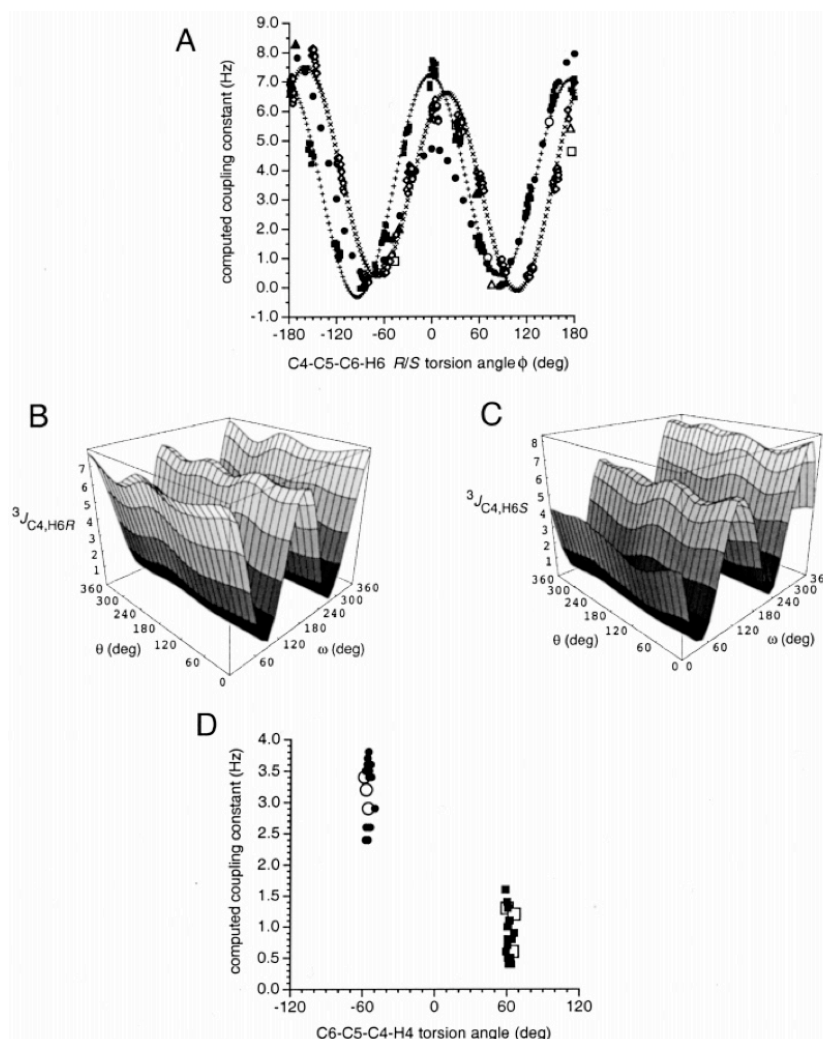


Figure 4.4. (A) Dependence of $^3J_{C4,H6R}$ and $^3J_{C4,H6S}$ on ϕ in **5**. Filled squares, $^3J_{C4,H6R}$ (hypersurface data); open diamonds, $^3J_{C4,H6S}$ (hypersurface data); filled circles, $^3J_{C4,H6R/S}$ curve reported by Tvaroska and Gadjos;³¹ open triangles, $^3J_{C4,H6R}$ in **6**; filled triangles, $^3J_{C4,H6S}$ in **6**; open circles, $^3J_{C4,H6R}$ in **7**; open squares, $^3J_{C4,H6S}$ in **7**. Small black + ($^3J_{C4,H6R}$) and \times ($^3J_{C4,H6S}$) define Karplus curves predicted from eqs 4.2 and 4.3. The vertical spread of points at discrete ϕ indicates the effect of θ . (B) Hypersurface calculated for $^3J_{C4,H6R}$ in **5**. (C) Hypersurface calculated for $^3J_{C4,H6S}$ in **5**. (D) Dependence of $^3J_{C6,H4}$ in **5** on the C6-C5-C4-H4 torsion angle (Table S2). Filled circles, $^3J_{C6,H4ax}$; filled squares, $^3J_{C6,H4eq}$. The vertical spread of points at discrete C-C-C-H torsions shows the effect of θ . Data for corresponding couplings in **6** (open squares) and **7** (open circles) are also shown.

Data in Table S2 yield additional insight into the effect of oxygen substituents on $^3J_{\text{CCCH}}$. $^3J_{\text{C4,H6R}}$ in the *gg* and *gt* rotamers is 1.1 ± 0.6 Hz and 1.2 ± 0.6 Hz for ϕ of -66.1 ± 8.8 and 64.8 ± 8.6 , respectively. $^3J_{\text{C4,H6S}}$ in *gt* and *tg* rotamers is 1.1 ± 0.7 Hz and 3.7 ± 0.2 Hz, respectively, for ϕ of -52.6 ± 9.2 and 59.8 ± 3.2 , respectively. Thus, the larger gauche coupling observed for $^3J_{\text{C4,H6S}}$ in *tg* is not caused by a significantly reduced . This behavior is attributed to anti electronegative substituent effects caused by O5 and O6. For $^3J_{\text{C4,H6S}}$ in *tg*, O5 is gauche to H6S, and O6 is gauche to C4 (i.e., there are no electronegative substituents anti to either coupled nuclei). In contrast, there is at least one electronegative substituent anti to a coupled nucleus in the remaining three cases. For example, for $^3J_{\text{C4,H6S}}$ in *gt*, H6S is anti to O5, and O6 is anti to C4, whereas for $^3J_{\text{C4,H6R}}$ in *gg* and *gt*, only one anti interaction is present. It appears that this "anti" effect, which is related to that reported for $^3J_{\text{HH}}$,⁶ is not additive; the presence of one of these interactions appears sufficient to reduce a gauche C-C-C-H coupling to its minimum value. The observed decrease in $^3J_{\text{CCCH}}$ upon introduction of one "anti" interaction is ~ 2.6 Hz.

Karplus dependencies for $^3J_{\text{C4,H6R}}$ and $^3J_{\text{C4,H6S}}$ using 18 datapoints (i.e., 9 staggered and 9 eclipsed ω conformers in Table S2) are described by eqs 4.2 and 4.3 in which is used (instead of shown in Figure 4.4A).

$$^3J_{\text{C4,H6R}} = 3.58 + 0.11 \cos(\omega) + 3.50 \cos(2\omega) + 0.35 \sin(\omega) - 0.57 \sin(2\omega) \quad (\text{rms} = 0.38 \text{ Hz}) \quad (4.2)$$

$$^3J_{\text{C4,H6S}} = 3.60 + 0.50 \cos(\omega) + 0.06 \cos(2\omega) -$$

$$0.13 \sin(\omega) - 3.46 \sin(2\omega) \quad (\text{rms} = 0.44 \text{ Hz}) \quad (4.3)$$

Inclusion of the full hypersurface data (144 data points) and/or inclusion of additional terms to describe the dependence of ${}^3J_{\text{C4,H6R/S}}$ on θ yielded virtually identical equations. ${}^3J_{\text{C4,H6R/S}}$ calculated using eqs 4.2 and 4.3 were not predicted accurately using the previous Karplus equations;^{31,32} rms deviations of 1.4 Hz were found between DFT-calculated couplings and those predicted by the previous treatments.

The effect of anti electronegative substituents on ${}^3J_{\text{CCCH}}$ is also observed in ${}^3J_{\text{C6,H4}}$ computed in **5-7** (Tables S1 and S2, Figure 4.4D). For **5**, ${}^3J_{\text{C6,H4(eq)}}$ is ~2.5 Hz smaller than ${}^3J_{\text{C6,H4(ax)}}$ (H4_{eq} is anti to O5, whereas H4_{ax} is gauche to O5), a decrease similar to that observed for ${}^3J_{\text{C4,H6R/S}}$. In addition to the "anti" effect, a small 1,3-effect appears to be present for ${}^3J_{\text{C6,H4}}$ in **5** in the *gg* rotamer (on H4_{ax}) and the *tg* rotamer (on H4_{eq}). This 1,3-effect decreases the observed ${}^3J_{\text{C6,H4}}$ by ~0.7 Hz. Similar effects were observed on ${}^3J_{\text{C6,H4}}$ in **6** and **7**, as shown in Figure 4.4D (Table S1). The introduction of an axial or equatorial O4 does not appear to influence ${}^3J_{\text{C6,H4}}$ significantly (i.e., couplings computed in **6** and **7** are similar to those computed in **5**), presumably because O4 cannot lie in the coupling plane in either orientation (i.e., a planar zigzag C6-C5-C4-O4 arrangement cannot be achieved). ${}^3J_{\text{C6,H4}}$ in **5-7** is also affected by θ (Figure 4.4D), exhibiting a range of ~1 Hz similar to that observed for ${}^3J_{\text{C4,H6R/S}}$.

4.5.3. Three- and Two-Bond ^1H - ^1H Spin-Spin Coupling Constants.

$^3J_{\text{H5,H6R}}$ and $^3J_{\text{H5,H6S}}$ were computed previously in **5** using the limited set of staggered and eclipsed geometries given in Table 4.1.⁶ Hypersurfaces were generated in the present work to more fully evaluate the effect of θ (Figure 4.5A, Figure 4.6A and B). $^3J_{\text{H5,H6R}}$ and $^3J_{\text{H5,H6S}}$ exhibit approximately the same sensitivity to θ as do $^3J_{\text{C4,H6R}}$ and $^3J_{\text{C4,H6S}}$. In addition, the curves for $^3J_{\text{H5,H6R}}$ and $^3J_{\text{H5,H6S}}$ are phase-shifted by $\sim 50^\circ$; similar behavior was observed for $^3J_{\text{C4,H6R}}$ and $^3J_{\text{C4,H6S}}$ (Figure 4.4). Importantly, corresponding curves calculated using a well-established empirically derived Karplus equation³³ are essentially superimposable on the DFT-computed curves (Figure 4.5A), thereby confirming the reliability of the DFT data.

In previous work, the dependencies of $^3J_{\text{H5,H6R}}$ and $^3J_{\text{H5,H6S}}$ on ω were described using DFT data obtained on nine completely optimized staggered and nine partially optimized eclipsed ω rotamers,⁶ yielding eqs 4.4 and 4.5.

$$^3J_{\text{H5,H6R}} = 5.08 + 0.47 \cos(\omega) - 0.12 \cos(2\omega) + 0.90 \sin(\omega) + 4.86 \sin(2\omega) \quad (4.4)$$

$$^3J_{\text{H5,H6S}} = 4.92 - 1.29 \cos(\omega) + 4.58 \cos(2\omega) + 0.05 \sin(\omega) + 0.07 \sin(2\omega) \quad (4.5)$$

The above equations were not affected (i.e., rms errors differ by <0.1 Hz) when the same nine staggered conformers and 144 additional couplings from hypersurface calculations were included in the parametrizations. Equations for $^3J_{\text{H5,H6R/S}}$ were also derived by including additional terms to account for the small effect of θ (Figure 4.5A,

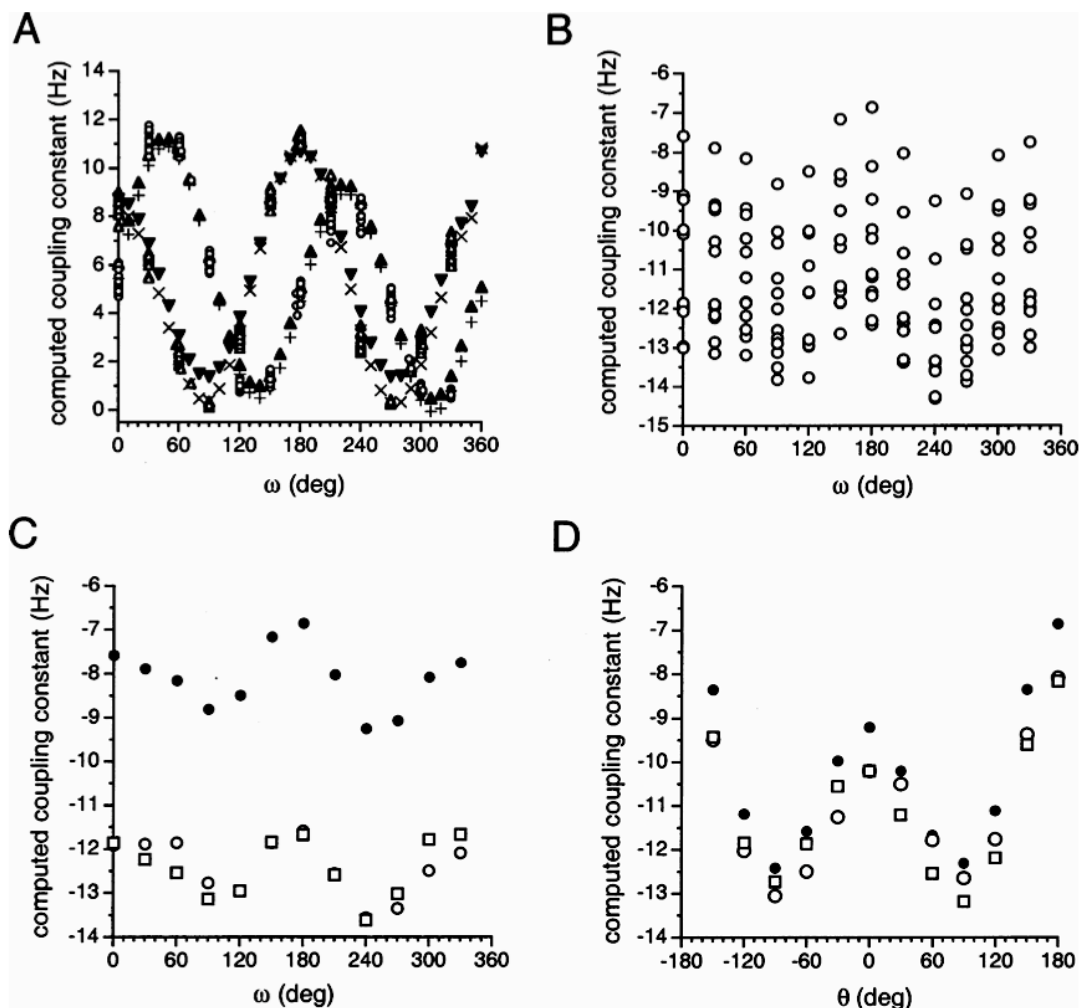


Figure 4.5. (A) Dependence of $^3J_{H5,H6R}$ and $^3J_{H5,H6S}$ on ω in **5** (open circles, $^3J_{H5,H6R}$; open triangles, $^3J_{H5,H6S}$). The vertical spread of points at discrete ω torsions indicates the effect of θ . Curves derived from eqs 4.4 and 4.5 (+ and x), and curves derived from previously reported empirically derived Karplus equations³³ (filled upright and inverted triangles) are also shown. (B) Dependence of $^2J_{H6R,H6S}$ on ω in **5**. The vertical spread of points at discrete C-C- C-H torsions indicates the effect of θ . (C) The dependence of $^2J_{H6R,H6S}$ in **5** on ω in the three perfectly staggered θ rotamers (open squares, $\theta = 60^\circ$; open circles, $\theta = -60^\circ$; filled circles, $\theta = 180^\circ$). (D) Dependence of $^2J_{H6R,H6S}$ in **5** on θ in the three perfectly staggered ω rotamers (open squares, $\omega = 60^\circ$; open circles, $\omega = -60^\circ$; filled circles, $\omega = 180^\circ$).

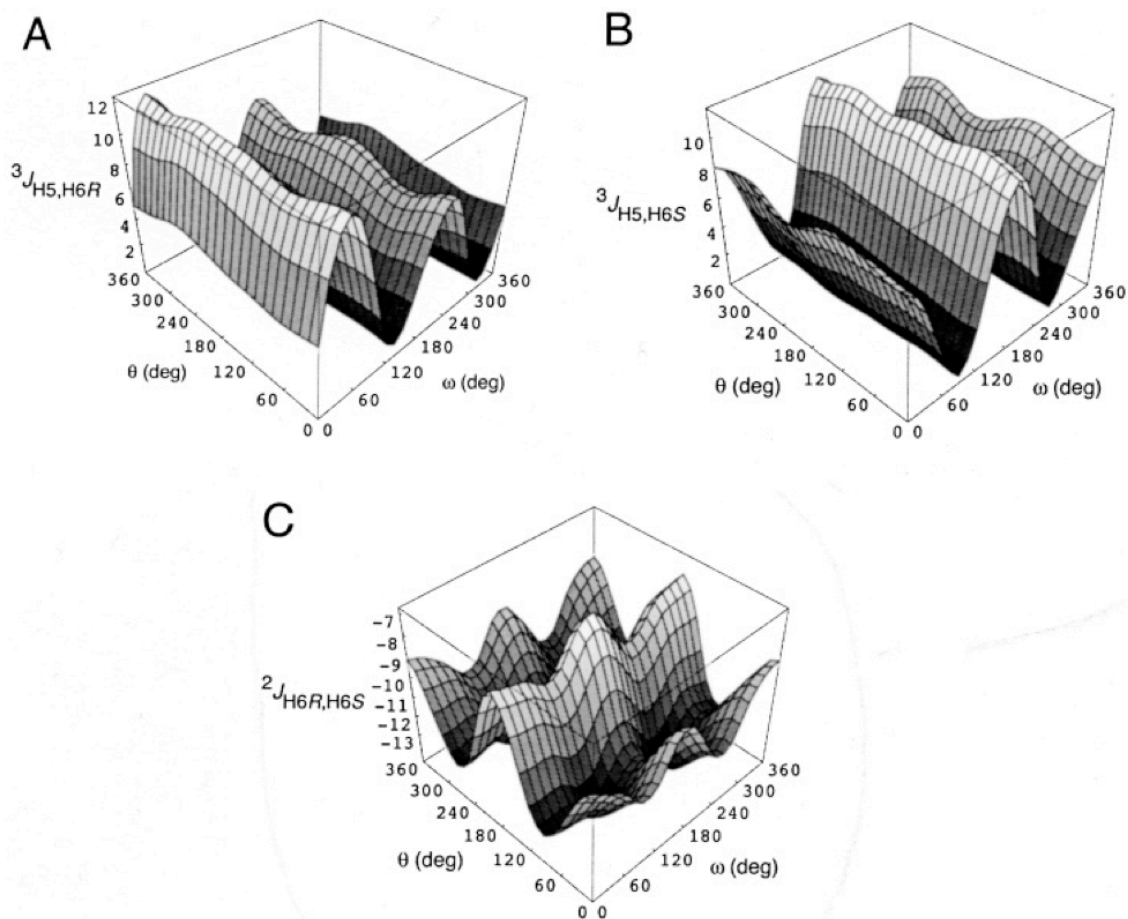


Figure 4.6. (A) Hypersurface (ω/θ) calculated for $^3J_{H5,H6R}$ in **5**. (B) Hypersurface (ω/θ) calculated for $^3J_{H5,H6S}$ in **5**. (C) Hypersurface (ω/θ) calculated for $^2J_{H6R,H6S}$ in **5**.

Figure 4.6A and B), but this refinement did not improve the quality of the parametrization significantly.

$^2J_{H6R,H6S}$ in **5** is affected by both ω and θ , but the dependence on θ is considerably greater (Figure 4.5B, Figure 4.6C). The latter conclusion is supported by data in Figure 5C and D, where computed $^2J_{HH}$ are plotted as a function of ω and θ ,

respectively. In Figure 4.5C, where data for only the three perfectly staggered θ rotamers are shown, $^2J_{\text{HH}}$ is observed to shift to *more positive* (less negative) values when $\theta = 180^\circ$ (Scheme 4.5).⁶ In contrast, Figure 4.5D shows that coupling data as a function of θ for the three perfectly staggered ω rotamers are nearly identical. The hypersurface for $^2J_{\text{H6R,H6S}}$ is shown in Figure 4.6C. A simple equation derived from a restricted dataset was proposed previously⁶ that related $^2J_{\text{H6R,H6S}}$ to ω and θ . The additional hypersurface dataset obtained in this work yielded an improved equation (eq 4.6) with substantially reduced rms error.

$$^2J_{\text{H6R,H6S}} = -11.23 + 0.13 \cos(\omega) + 0.74 \cos(2\omega) - 0.82 \sin(\theta) + 2.02 \sin(2\theta) \quad (\text{rms} = 0.51 \text{ Hz}) \quad (4.6)$$

4.5.4. Two-Bond ^{13}C - ^{13}C Spin-Spin Coupling Constants.

$^2J_{\text{CCC}}$ and $^2J_{\text{COC}}$ in saccharides have been studied previously, leading to an empirical projection resultant (PR) method that correlates the observed coupling to a projection resultant whose value depends on relative orientation of oxygen substituents on the coupled carbons.³ In the present study, $^2J_{\text{C4,C6}}$ was studied to determine its sensitivity to ω and θ .

Projection resultants determined for $^2J_{\text{C4,C6}}$ for the *gt*, *gg* and *tg* rotamers in **5** are +2.0, +0.5, and +0.5, respectively, yielding predicted couplings of +2–3 Hz, ~ -1 Hz, and ~ -1 Hz, respectively. These results are in qualitative agreement with the DFT-calculated

couplings as a function of ${}^2J_{C4,C6}$ and θ (Table S3, Figure 4.7). Like ${}^2J_{CCH}$, a plot of ${}^2J_{CCC}$ vs ω contains a single maximum and a single minimum, and couplings of positive or negative sign. The dynamic range of ~ 4.5 Hz is smaller than that observed for ${}^2J_{CCH}$.

Introduction of O4 generally shifts ${}^2J_{C4,C6}$ to more negative values (Table S1), a result consistent with PR predictions; projection resultants are shifted to more negative values by 0.5 unit, leading to the prediction of more negative couplings by ~ 1.5 Hz. The orientation of O4 appears to affect the magnitude of the negative shift for the *gt* and *tg* rotamers.

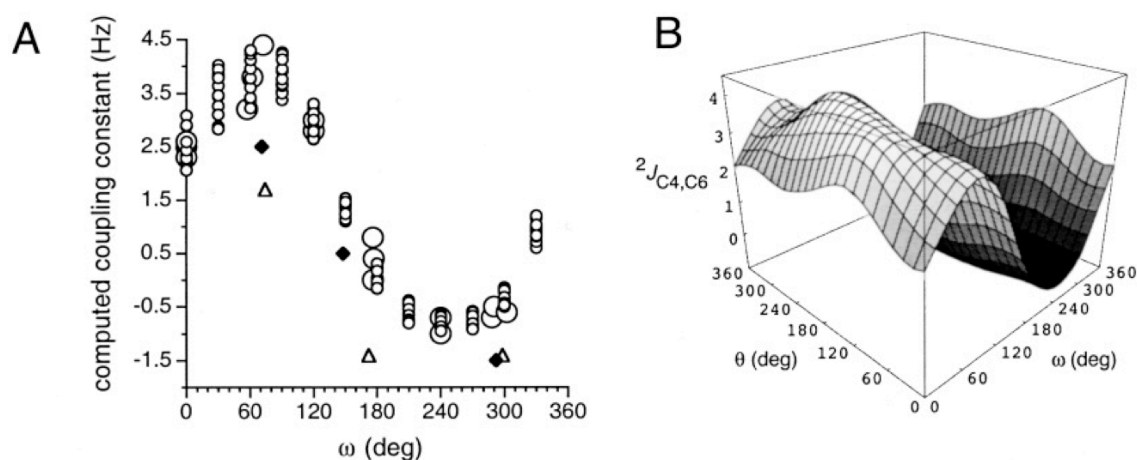


Figure 4.7. (A) Dependence of ${}^2J_{C4,C6}$ in **5** on ω . The vertical spread of points at discrete ω torsions (smaller open circles) indicates the effect of θ . Larger open circles are data taken from Table S3 for staggered and eclipsed conformations about ω . Data in triangles and diamonds were obtained from **6** and **7**, respectively (Table S1). (B) Hypersurface (ω/θ) calculated for ${}^2J_{C4,C6}$ in **5**.

${}^2J_{C4,C6}$ data calculated for **5** were fit to yield eq 4.7a, which reflects its dependence on ω .

$${}^2J_{C4,C6} = 1.36 + 1.03 \cos(\omega) + 2.26 \sin(\omega)$$

(rms = 0.3 Hz) (4.7a)

This equation was modified to account for the influence of O4 using data obtained on **6** and **7**, giving eq 4.7b.

$${}^2J_{C4,C6} = 0.20 + 0.16 \cos(\omega) + 1.34 \sin(\omega)$$

(rms = 1.5 Hz) (4.7b)

The rms error for eq 4.7b is much larger than that for eq 4.7a due to the limited data presently available to define the O4 effect.

4.5.5. One-Bond ¹³C-¹³C Spin-Spin Coupling Constants and Bond-Length Considerations.

Previous work has shown³⁴ that ¹J_{CC} values in vicinal diol fragments (HO-C-C-OH) depend on the C-C and C-O torsion angles. Coupling is minimal and maximal for O-C-C-O torsion angles of ~0° and ~180°, respectively. Superimposed on this dependence are effects due to the C-O torsions; coupling is minimal and maximal when the H-O-C-C torsion angle is ~60° and ~180°, respectively.

The above relationships derived for a simple diol were tested in the CH₂OH fragment where the C5-C6 and C6-O6 torsions are expected to modulate ¹J_{C5,C6}. Data in Table S3 show that, within each C5-C6 rotamer (three staggered and three eclipsed), ¹J_{C5,C6} is larger when θ is ~180° (e.g., for *gt*, ¹J_{C5,C6} = 43.5, 42.0, and 48.0 Hz for = 57°, -48°, and 192°, respectively). The presence of one O6 lone pair anti to the C5-C6

bond reduces $^1J_{C5,C6}$ by ~ 5 Hz (Figure 4.8A). Data obtained from the full hypersurface are shown in Figure 4.8B (in which rotamers containing perfectly staggered θ are highlighted) and Figure 4.8C.

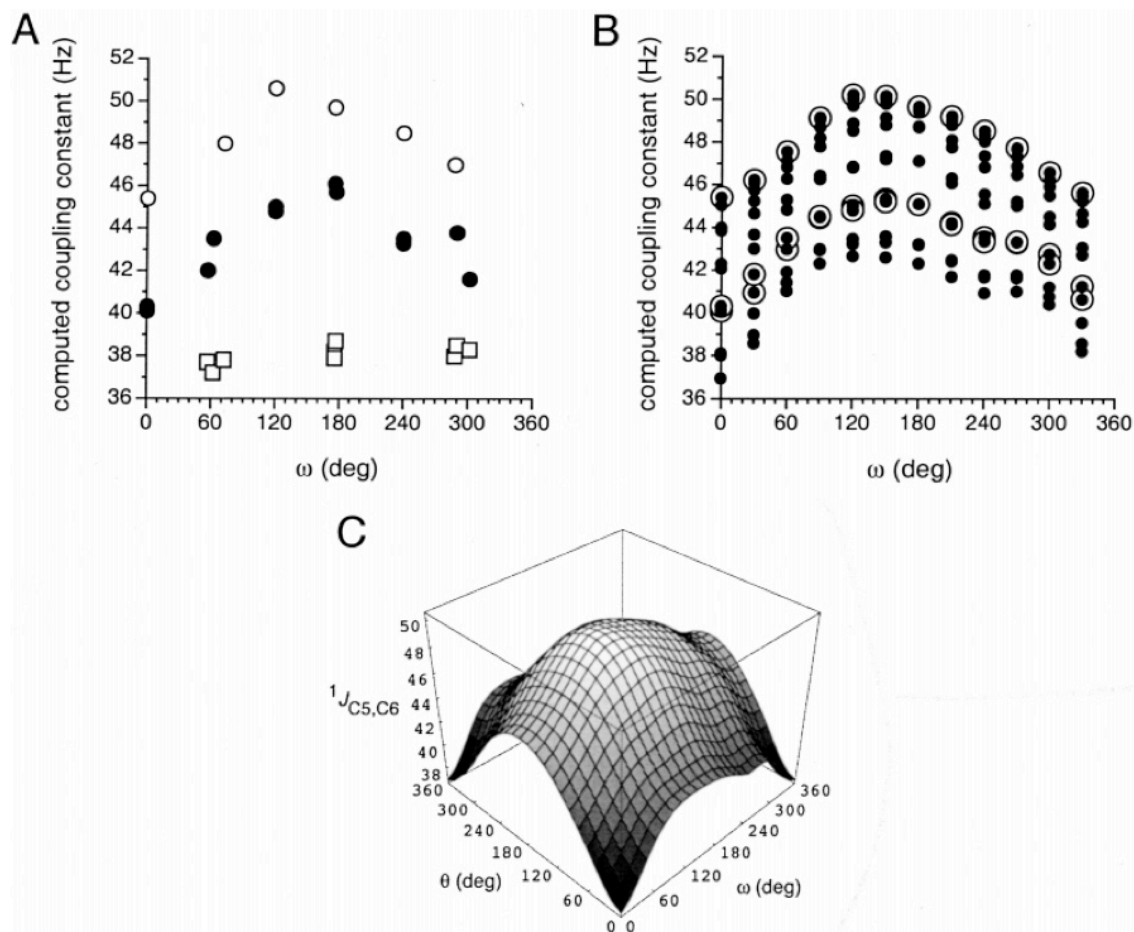


Figure 4.8. (A) Dependencies of $^1J_{C5,C6}$ and $^1J_{C4,C5}$ in **5** on ω (data taken from Table S3). Filled circles, $^1J_{C5,C6}$ when $\theta = 60^\circ$ and -60° ; open circles, $^1J_{C5,C6}$ when $\theta = 180^\circ$; open squares, $^1J_{C4,C5}$ (staggered ω rotamers only). (B) Similar plot as in part A but using data obtained from the full hypersurface. The vertical spread of points at discrete ω torsions (filled circles) indicates the effect of θ . Open circles identify perfectly staggered θ rotamers. (C) Hypersurface (ω/θ) calculated for $^1J_{C5,C6}$ in **5**.

$^1J_{C5,C6}$ also depends on ω , with smaller couplings observed for $\omega \approx 0^\circ$ than for $\omega \approx 180^\circ$. Based on data in Table S3, $^1J_{C5,C6}$ differs by ~ 5 Hz in these limiting conformations (Figure 4.8). These trends are similar to those reported in ethylene glycol.³⁴ Note that this behavior is different from that found for $^1J_{C4,C5}$, which shows essentially no dependence on ω , as expected (Figure 4.8A). A brief discussion of the effect of ω on C5-C6, C6-H6R/S, C5-O5, and C6-O6 bond lengths and $^1J_{C5,C6}$ in **5** is found in the Supporting Information (Figures S1 and S2).

The $^1J_{C5,C6}$ data in Table S3 and the hypersurface results (Figures 4.8B and C) yielded eq 4.8, which correlates this coupling to ω and θ .

$$^1J_{C5,C6} = 44.81 - 2.13 \cos(\omega) - 0.59 \cos(2\omega) - 3.57 \cos(\theta) - 0.43 \cos(2\theta) \quad (\text{rms} = 1.5 \text{ Hz}) \quad (4.8)$$

4.5.6. Three-Bond ^{13}C - ^{13}C Spin-Spin Coupling Constants.

$^3J_{C1,C6}$ and $^3J_{C3,C6}$ values depend largely on the C1-O5-C5-C6 and C3-C4-C5-C6 torsion angles (Karplus curves), respectively, but a second-order dependence on the O5-C5-C6-O6 and C4-C5-C6-O6 torsion angles, respectively, is expected.^{1,2} The latter dependencies arise from the effect of "in-plane" electronegative substituents, in the present case provided by O6 for specific values of ω . Calculated couplings in **5** (153 datapoints) show a systematic change in both $^3J_{C1,C6}$ and $^3J_{C3,C6}$ as a function of ω (Figure S3); in these calculations the torsion angle between the coupled nuclei is essentially unchanged ($\sim 180^\circ$) due to constraints imposed by the pyranosyl ring. $^3J_{C1,C6}$ is maximal when $\omega = \sim 180^\circ$ (*tg* rotamer), and $^3J_{C3,C6}$ is maximal when $\omega = \sim +60^\circ$ (*gt* rotamer); the

two curves are complementary. Both couplings exhibit a small dependence on θ . However, since **5** lacks OH substituents at C1, C3, and C4, trends observed in Figure S3 cannot be used quantitatively to assess ω in **1-4**. The potential for this application remains to be explored.

4.5.7. Experimental Validation of Computed Couplings and Proposed Equations.

^1H and ^{13}C NMR spectra of 4,6-*O*-ethylidene- α - and β -D-[4- ^{13}C]-, [5- ^{13}C]-, and [6- ^{13}C]glucopyranoses (**8 α,β**) and 4,6-*O*-ethylidene- α - and β -D-[6- ^{13}C]galactopyranoses (**9 α,β**) contain experimental couplings that can be correlated with defined hydroxymethyl conformations (*tg* in *gluco*, *gg* in *galacto*). These couplings were compared to those predicted by the above equations and to those calculated in geometrically optimized conformers of 4,6-*O*-ethylidene- α -D-glucopyranose and 4,6-*O*-ethylidene- α -D-galactopyranose. These data (Table 4.2) show that corresponding experimental and calculated *J*-values differ by <1 Hz, suggesting that the equations can be applied quantitatively in analyses of CH_2OH conformation in **1-4**. Several trends emerged from the analysis of *J*-couplings in **8** and **9**.

In **8**, $^2J_{\text{H6R,H6S}}$ is -10.4 Hz for both anomers, in excellent agreement with the computed value of -10.4 Hz in **8 α** (Table 4.2). The computed H-C-H bond angle in **8 α** is 108.5° . The corresponding bond angle computed in **5** is $107.7^\circ \pm 0.4$.

Observed $^1J_{\text{C6,H6R/S}}$ in **8** depend significantly on C-H bond orientation, with the equatorial C6-H6R bond yielding a coupling ~ 9 Hz larger than the axial C6-H6S bond. This difference suggests that the C6-H6R bond length is shorter than the C6-H6S bond length, a prediction consistent with expectations based on prior studies. Indeed, DFT

TABLE 4.2. EXPERIMENTAL J -COUPLINGS IN C-LABELED 4,6-*O*-ETHYLIDENE- α AND β -D-GLUCO- (8) AND GALACTOPYRANOSES (9) AND COMPARISON WITH CALCULATED COUPLINGS

coupling	$J_{\alpha} (\alpha)^b$	$J_{\beta} (\beta)^b$	J_{eq}^c	$J_{calc} (\alpha)^d$
$^2J_{H6R,H6S}$	-10.4	-10.4	-12.0/-11.8	-10.4/-12.1
$^3J_{H5,H6eq}$	4.9	~ 4.6	4.5/4.9	4.9(-55.7°)/1.7 (-71°)
$^3J_{H5,H6ax}$			10.8/10.8	11.1(-176.2°)/1.7 (48.2°)
$^3J_{C4,H6eq}$	5.9	6.3	7.0/6.9	6.0 (-173.6°)/5.1 (169°)
$^3J_{C4,H6ax}$			3.2/2.8	3.3 (65.9°)/0.9 (-71.8°)
$^2J_{C5,H6eq}$	-4.1	-4.4	-3.0/-3.0	-3.6 (111.8°)/-4.8 (110.5°)
$^2J_{C5,H6ax}$			-2.1/-2.3	-3.0(109.7°)/6.3 (108.7°)
$^1J_{C6,H6eq}$	151.6	152.1		153.0/154.5
$^1J_{C6,H6ax}$	143.1	142.9		141.7/137.5
$^2J_{C6,H5}$	-3.3		-2.8/-2.6	-2.7 (108.9°)/2.4 (109.8°)
$^1J_{C5,C6}$	43.2 [40.3] ^e	43.1 [40.4]	44.8/44.5	44.8/42.8
$^2J_{C4,C6}$	-1.6 [-2.2]	-1.5 [-2.1]	0.04/-0.02	-1.1 (108.4°)/-1.7 (109°)
$^3J_{C6,C1}$	3.8 [3.3]	4.9 [4.3]		4.7/4.1
$^3J_{C6,C3}$	3.2 [2.7]	3.5 [3.1]		3.2/2.7
$^3J_{C4,H2}$	1.0			
$^2J_{C4,H3}$	(-)/4.6			
$^1J_{C4,H4}$	143.6	144.7		
$^2J_{C4,H5}$	(-)/1.6	(-)/2.2		
$^3J_{C4,CH}$	~ 1.4	~ 1.4		
$^3J_{C5,H1}$	6.4	0.9		
$^3J_{C5,H3}$	1.3			
$^2J_{C5,H4}$	(-)/2.8	(-)/3.5		
$^1J_{C5,H5}$	148.8	146.2		
$^{4+4}J_{C5,CH}$	0.9			
$^3J_{C6,H4}$	~ 3.2	~ 2.6		
$^3J_{C6,CH}$	~ 1.2	~ 1.2		
$^{3+3}J_{C4,C1}$	0	0		
$^2J_{C4,C2}$	(+)/3.7	(+)/3.4		
$^1J_{C4,C3}$	40.4	41.1		
$^1J_{C4,C5}$	37.5	38.1		
$^3J_{C4,CH}$	br	br		
$^3J_{C4,CH3}$	3.1	3.1		
$^2J_{C5,C1}$	(-)/1.8	0		
$^{3+3}J_{C5,C2}$	0	0		
$^{3+3}J_{C5,CH}$	2.4	2.5		
$^2J_{C6,CH}^f$	2.1 [1.9]	2.1 [1.8]		
$^3J_{C6,CH3}$	3.2 [2.9]	3.2 [2.9]		

^a In Hz. ^b Experimental couplings in aqueous solution at 298 K obtained from first-order analysis. ^c J -couplings predicted by equations that account for the effect of either ω alone or of ω and θ (see text). Two values are listed. Left entry: $\omega = 180^\circ$ and $\theta = 60^\circ$. Right entry: $\omega = 182.7^\circ$ and $\theta = 56.6^\circ$ (torsions observed in the DFT-optimized structure of 4,6-*O*-ethylidene- α -D-glucopyranose **8a**). The following Karplus equations were used: eq 4 for $^3J_{H5,H6eq}$, eq 5 for $^3J_{H5,H6ax}$, eq 2 for $^3J_{C4,H6eq}$, eq 3 for $^3J_{C4,H6ax}$, eq 1a for $^2J_{C5,H6eq}$, eq 1b for $^2J_{C5,H6ax}$, eq 1c for $^2J_{C6,H5}$, eq 7b for $^2J_{C4,C6}$; eq 6 for $^2J_{H6R,H6S}$ and eq 8 for $^1J_{C5,C6}$. ^d DFT-calculated J -values in DFT-optimized 4,6-*O*-ethylidene- α -D-glucopyranose **8a** (first entry) and 4,6-*O*-ethylidene- α -D-galactopyranose **9a** (second entry). Relevant bond and torsion angles are given in parentheses. ^e Couplings in brackets are those observed in 4,6-*O*-ethylidene- α - and β -D-[6-¹³C]galactopyranoses. ^f Signs shown in parentheses were predicted by the projection rule ($^2J_{CH}$, ref 23a) and the projection resultant method ($^2J_{CC}$, ref 3). ^g Signs for these couplings are unknown.

calculations conducted on **8** α revealed $r_{\text{C6,H6R}}(\text{eq}) = 1.0932 \text{ \AA}$ and $r_{\text{C6,H6S}}(\text{ax}) = 1.1025 \text{ \AA}$ (in **9**; $r_{\text{C6,H6R}}(\text{ax}) = 1.1037 \text{ \AA}$ and $r_{\text{C6,H6S}}(\text{eq}) = 1.0928 \text{ \AA}$). In addition, $^1J_{\text{C5,H5}}$ is slightly larger in **8** α than in **8** β , again consistent with observations in D-glucopyranoses; this effect is attributed to the shorter C5-H5 bond in the α -pyranose caused by 1,4-interactions with lone pairs on the axial O1.²⁷

$^1J_{\text{C5,C6}}$ is smaller in **9** than in **8** by ~ 3 Hz. This difference is attributed to the change in the O5-C5-C6-O6 torsion angle from ~ 180 in the latter to ~ 60 in the former, which is expected to reduce the coupling (see $^1J_{\text{CC}}$ discussion below).³⁴

$^3J_{\text{C1,C6}}$ and $^3J_{\text{C3,C6}}$ are consistently smaller in corresponding anomers of **9** than in **8**. For $^3J_{\text{C1,C6}}$, the difference is attributed to the presence of the "in-plane " O6 in *gluco* isomers, which enhances the coupling by ~ 0.6 Hz.¹ For $^3J_{\text{C3,C6}}$, the effect is attributed mainly to the different configuration at C4, with an axial O4 reducing the coupling.^{35a} Within anomeric pairs, the β -pyranose exhibits the larger $^3J_{\text{C1,C6}}$, as expected based on the orientational effects of O1.^{35a,b}

4.5.8. Average Computed J-Couplings in Staggered Hydroxymethyl Rotamers.

Average J_{HH} , J_{CH} , and J_{CC} computed from hypersurface data by averaging the three staggered θ rotamers ($\theta = -60^\circ$, 60° , and 180°) at each staggered value of ω are given in Table 4.3. $^2J_{\text{CCH}}$ sign predictions are also reported based on the projection rule;^{23a} these predictions are in good agreement with the computed data, but the calculated coupling magnitudes are shifted to more negative values. This result is consistent with recent observations^{24,25} and probably arises from limitations of the

projection rule for predicting ${}^2J_{\text{CH}}$ not involving anomeric carbons or protons. The data in Table 4.3 provide an *average* dynamic range for each coupling, which is smaller than the actual dynamic range due to the averaging of θ effects.

TABLE 4.3. AVERAGED CALCULATED J -COUPLINGS IN HYDROXYMETHYL GROUP FRAGMENTS FOR STAGGERED ROTAMERS ABOUT Ω AND Θ^{A}

coupling	$gg (\omega = -60^\circ)$	$gt (\omega = 60^\circ)$	$tg (\omega = 180^\circ)$
${}^2J_{\text{H6R,H6S}}$	-10.8	-10.9	-10.0
${}^2J_{\text{C5,H6R}}$	+3.4 (+) ^b	-4.7 (-)	-3.0 (-)
${}^2J_{\text{C5,H6S}}$	-3.8 (-)	+3.4 (+)	-4.0 (-)
${}^2J_{\text{C6,H5}}$	+2.6 (+)	-4.0 (-)	-3.0 (-)
${}^2J_{\text{C4,C6}}$	-0.2	+3.8	0.1
${}^3J_{\text{H5,H6R}}$	0.9	10.8	4.7
${}^3J_{\text{H5,H6S}}$	2.8	2.2	11.1
${}^3J_{\text{C4,H6R}}$	1.7	1.4	6.7
${}^3J_{\text{C4,H6S}}$	6.7	0.8	3.4

^a Couplings were computed from hypersurface data by averaging the three staggered θ rotamers ($\theta = -60^\circ$, 60° , and 180°) at each staggered value of ω . Since some couplings exhibit a specific dependence on θ (see text), use of these average couplings to fit experimental data is valid only when perfectly staggered ω rotamers, and equal populations of perfectly staggered θ rotamers, are present in solution. ^b Values in parentheses are signs predicted by the projection rule.^{23a}

4.6. Experimental J -Couplings in **1-4** and Conformational Analysis

4.6.1. Qualitative Treatment and Comparison to Theory

Characteristic features of the ^1H and $^{13}\text{C}\{^1\text{H}\}$ NMR spectra of ^{13}C -labeled methyl pyranosides are shown in Figures S4 and S5. The ^1H spectrum of methyl β -D-[4- ^{13}C]galactopyranoside **4** (Figure S4) showed nonfirst-order behavior; the good agreement between the experimental and simulated spectra allowed extraction of accurate J_{HH} and J_{CH} values. The $^{13}\text{C}\{^1\text{H}\}$ spectrum of methyl α -D-[6- ^{13}C]galactopyranoside **3** (Figure S5) shows long-range coupling to both C1 and C3, one-bond coupling to C5, and no coupling to C2, C4, and the aglycone CH_3 .

Experimental J_{HH} values in **1-4** (Table 4.4) agree well with those reported previously¹⁴ except for $^3J_{\text{H5,H6R}}$ and $^3J_{\text{H5,H6S}}$ in **3**. The latter couplings were confirmed via spectral simulation (Figure S4) and are in agreement with those reported by Tvaroska et al.³² Stereochemical assignments of the H6R and H6S signals in **1-4** were made according to Ohrui et al.³⁶ (i.e., H6S downfield of H6R in *gluco*, H6R downfield of H6S in *galacto*).

Experimental J_{CH} values in **1-4** are given in Table 4.5. $^1J_{\text{C4,H4}}$ is larger in **3/4** than in **1/2**. This enhancement may be attributed to C-H bond orientation (axial vs equatorial) and/or C4-O4 bond conformation. The equatorial C4-H4 bond in **3/4** is expected to be shorter than the axial C4-H4 bond in **1/2**, possibly leading to larger $^1J_{\text{CH}}$ in the former. However, an axial O4 may disrupt directional intramolecular H-bonding between the adjacent equatorial OH groups of **1/2**, resulting in an increased population

TABLE 4.4. EXPERIMENTAL ^1H - ^1H SPIN-SPIN COUPLING CONSTANTS IN **1-4**

coupling	α -D-Glc 1	β -D-Glc 2	α -D-Gal 3	β -D-Gal 4
$^3J_{\text{H1,H2}}$	3.8 (3.8) ^b	8.0 (8.0)	3.9 (4.0)	8.0 (7.9)
$^3J_{\text{H2,H3}}$	9.8 (9.8)	9.5 (9.4)	10.3 (10.3)	9.9 (9.9)
$^3J_{\text{H3,H4}}$	9.2 (9.1)	9.2 (9.2)	3.4 (3.4)	3.5 (3.4)
$^3J_{\text{H4,H5}}$	10.0 (10.1)	10.0 (9.7)	1.2 (1.0)	1.1 (1.1)
$^3J_{\text{H5,H6R}}$	5.6 (5.5) [5.4] ^c	6.2 (6.0) [5.9]	8.2 (7.2) [8.3]	7.9 (7.9) [7.6]
$^3J_{\text{H5,H6S}}$	2.3 (2.3) [2.2]	2.3 (2.3) [2.0]	4.2 (5.2) [4.0]	4.4 (4.4) [4.4]
$^2J_{\text{H6R,H6S}}$	-12.3 (-12.3)	-12.4 (-12.3)	-11.7 (-11.7)	-11.8 (-11.7)

^a In Hz ± 0.1 Hz, $^2\text{H}_2\text{O}$ solvent, 30 °C. ^b Data in parentheses were taken from Podlasek et al..¹⁴ ^c Data in brackets were taken from Tvaroska et al..³²

TABLE 4.5. EXPERIMENTAL ^{13}C - ^1H SPIN-SPIN COUPLING CONSTANT^A IN **1-4**

coupling	α -D-Glc 1	β -D-Glc 2	α -D-Gal 3	β -D-Gal 4
$^1J_{\text{C4,H4}}$	144.4	144.8	146.4	146.3
$^1J_{\text{C5,H5}}$	144.3	141.8	143.4	140.7
$^1J_{\text{C6,H6R}}$	143.3	143.2	145.2	145.5
$^1J_{\text{C6,H6S}}$	144.2	144.4	142.5	142.9
$^2J_{\text{C4,H3}}$	-4.7	-4.8	+1.7	+1.6
$^2J_{\text{C4,H5}}$	-2.9	-2.9	+3.1	+3.3
$^2J_{\text{C5,H4}}$	-3.9	-4.0	± 1.1	± 1.0
$^2J_{\text{C5,H6R}}$	-1.9	-2.5	-5.0	-5.0
$^2J_{\text{C5,H6S}}$	-1.4	-1.1	$\pm 0.8^e$	$\pm 0.2^e$
$^2J_{\text{C6,H5}}$	-1.4	-2.2	-5.2	-5.5
$^3J_{\text{C4,H2}}$	1.0	1.1	0.8	0.6
$^3J_{\text{C4,H6R}}$	1.1 (1.1) ^d	1.2 (1.0)	1.9 (0.9)	1.9 (1.5)
$^3J_{\text{C4,H6S}}$	2.8 (2.9)	2.4 (2.4)	1.7 (3.7)	1.8 (4.0)
$^3J_{\text{C5,H1}}$	obsc ^b	1.1	6.3	0.9
$^3J_{\text{C5,H3}}$	0.9	1.1	0.4	nc ^c
$^3J_{\text{C6,H4}}$	3.6	3.6	1.0	1.0

^a In Hz ± 0.1 Hz, $^2\text{H}_2\text{O}$ solvent, 30 °C. Signs determined via the projection rule^{23a} and/or spin simulation. ^b obsc = signal obscured by the HOD signal. ^c nc = no coupling observed, $|J| \leq 0.5$ Hz. ^d Values in parentheses were reported by Tvaroska et al..³² ^e Signs were taken as (+) in calculations of ω/θ rotamer populations (see text).

(relative to **1/2**) of the C4-O4 rotamer having OH4 anti to H4 in **3/4**. In the latter rotamer, no O4 lone pairs are anti to the C4-H4 bond, and no C4-H4 bond elongation occurs.

$^1J_{\text{C5,H5}}$ exhibits a dependence on anomeric configuration, with α -anomers yielding slightly larger couplings than β -anomers. This result is consistent with prior studies of oxygen lone pair effects on saccharide C-H bond lengths.²⁷ The axial C1-O1

bond in β -anomers provides O1 lone pairs in a 1,4-orientation to the C5-H5 bond. The resulting bond shortening, which is absent in α -anomers, presumably enhances $^1J_{C5,H5}$. A similar argument was made recently in studies of 2H nuclear quadrupolar coupling constants in aldopyranosyl rings.³⁷

$^2J_{C4,H3}$, $^2J_{C4,H5}$, and $^2J_{C5,H4}$ have negative signs in **1/2** and positive signs (when detected) in **3/4**. These results are consistent with sign predictions based on the projection rule;^{23a} for **1/2** and **3/4**, projections of 0 and +1.5 are obtained, respectively, for each of these couplings, leading to predicted (-) and (+) signs, respectively. However, despite similar projections, $^2J_{C4,H3}$, $^2J_{C4,H5}$, and $^2J_{C5,H4}$ vary considerably, indicating that a general empirical method to predict coupling magnitudes is error-prone due to differences in coupling pathway structure and C-O bond conformations.

Experimental $^2J_{C5,H6R}$ and $^2J_{C5,H6S}$ range from -1.9 Hz to -5.0 Hz and ± 0.2 Hz to -1.4 Hz, respectively, whereas $^2J_{C6,H5}$ ranges from -1.5 Hz to -5.5 Hz. These couplings lie within the range predicted from the calculations (Figures 4.2 and 4.3). Large shifts to more negative couplings are observed for $^2J_{C5,H6R}$ and $^2J_{C6,H5}$ upon converting **1/2** to **3/4**. This shift is consistent qualitatively with a more populated *tg* rotamer in Gal, at the expense of the *gg* rotamer population. The *positive* contribution made to the experimental couplings by the *gg* rotamer is replaced by a *negative* contribution made by the *tg* rotamer. This shift in populations exerts a much smaller effect on $^2J_{C5,H6S}$, since both *gg* and *tg* rotamers are associated with negative couplings (Figures 4.2 and 4.3).

$^3J_{C4,H2}$ Values are slightly larger in **1/2** than in **3/4**, possibly due to a small in-plane effect from the equatorial O4.¹⁴ $^3J_{C4,H6R}$ and $^3J_{C4,H6S}$ in **1-4** differ considerably

from those reported recently.³² The couplings in Table 4.5 were confirmed through spectral simulation. Previously reported couplings³² were measured from selective excitation experiments, but the resonance frequencies for the H6 protons differ by ~7 Hz in **3** and ~23 Hz in **4** at 600 MHz, which precludes determinations of accurate $^3J_{CH}$ using first-order approaches. Presumably this complication is responsible for the observed differences.

$^3J_{C5,H1}$ in **1-4** shows the expected dependence on anomeric configuration, with larger couplings observed in α -anomers (C5 anti to H1).^{35a} $^3J_{C6,H4}$ is considerably larger in **1/2** (~3.5 Hz) than in **3/4** (~1.1 Hz) despite the gauche arrangement between C6 and H4 in all compounds. The smaller coupling in **3/4** is consistent with our theoretical findings (Figure 4.4D).

Experimental J_{CC} values in **1-4** are given in Table 4.6. $^1J_{C4,C5}$ is smaller in **3/4** compared to **1/2**, whereas the opposite is observed for $^1J_{C5,C6}$. The O4-C4-C5-O5 torsion angle changes from ~180° in **1/2** to ~60° in **3/4**, and $^1J_{CC}$ is expected to decrease;³⁴ the effect of the C4-O4 torsion on $^1J_{C4,C5}$, which can be substantial, is assumed to be negligible in this case. Similar arguments explain the $^1J_{C5,C6}$ data; the slightly larger values in **3/4** reflect a greater contribution by the tg rotamer in which O5 and O6 are anti, thus increasing the coupling. Again, C6-O6 torsion effects are assumed to be minimal.

$^2J_{C1,C5}$ depends on anomeric configuration:^{35b} ~ -2 Hz for α -anomers and ~0 Hz for β -anomers. $^2J_{C2,C4}$ is large and positive in **1/2** and ~0 Hz in **3/4**, as expected based on the projection resultant method.³ $^2J_{C4,C6}$ is ~0 Hz in **1-4**; conformational averaging of the

gg and *gt* forms for **1/2**, and the *gt* and *tg* forms for **3/4**, is expected to yield small $^2J_{C4,C6}$ (Figure 4.7).

TABLE 4.6. EXPERIMENTAL ^{13}C - ^{13}C SPIN-SPIN COUPLING CONSTANTS IN **1-4**

coupling	α -D-Glc 1	β -D-Glc 2	α -D-Gal 3	β -D-Gal 4
$^1J_{C3,C4}$	38.5	39.3	obsc ^b	38.6
$^1J_{C4,C5}$	40.4	41.0	38.2	38.5
$^1J_{C5,C6}$	43.3	43.3	44.7	44.8
$^2J_{C1,C5}$	-2.0 ^d	nc ^c	-2.0 ^d	nc
$^2J_{C2,C4}$	+3.1 ^e	+2.7 ^e	nc	nc
$^2J_{C3,C5}$	+1.8 ^e	obsc	nc	+1.6 ^e
$^2J_{C4,C6}$	nc	nc	nc	nc
$^3J_{C1,C6}$	3.3	4.2	3.5	4.4
$^3J_{C2,C5}$	obsc	nc	1.3	nc
$^3J_{C3,C6}$	3.7	~4.3	3.8	4.2

In Hz ± 0.1 Hz, $^2\text{H}_2\text{O}$ solvent, 30 °C. ^b obsc = signal obscured. ^c nc = no coupling observed, $|J| \leq 0.5$ Hz. ^d Sign based on ^{13}C - ^{13}C COSY-45 data.⁴⁴ ^e Sign predicted by the projection resultant method.³

$^3J_{C1,C6}$ and $^3J_{C3,C6}$ depend on the C1-O5-C5-C6 and C3-C4-C5-C6 torsion angles;^{35a,b} in both cases, this torsion angle in **1-4** is $\sim 180^\circ$. Small deviations in the observed coupling are probably due to small changes in the torsion angle between anomers and/or to in-plane electronegativity effects; $^3J_{C1,C6}$ is enhanced in β -anomers relative to α -anomers due to an in-plane equatorial O1.^{1,35b} In addition, the *tg* rotamer will enhance $^3J_{C1,C6}$ due to an in-plane O6; the small difference between **1** and **3**, and between **2** and **4**, may be due to the expected larger population of *tg* rotamer in Gal,

which will enhance the observed coupling. For ${}^3J_{C3,C6}$, the *gt* rotamer is expected to enhance the coupling, due to an in-plane O6. Both Glc and Gal isomers show an enhancement in ${}^3J_{C3,C6}$ in the β -anomer; this result may reflect, at least partly, an increase in the *gt* rotamer in β -anomers (see below).

4.6.2. Hydroxymethyl Rotamer (ω) Analysis in **1-4**

All regressions and multilinear fits were conducted using a Fortran 77 program, Chymesa, written in our laboratory (a copy of this program can be obtained by contacting the authors). This program allows for selection of the protocol to be used for the regression or fit, i.e., the set of experimental *J*s used in the calculation, the source of limiting *J* values for the *gt*, *gg*, and *tg* rotamers, and the weight attributed to each *J* in the fit. The latter weight is used in the determination of the overall root-mean-square (rms) error between the experimental and calculated *J*s. The use of weighting factors accounts for differences in the quality of the equations available for each coupling pathway. The program also allows the selection of ranges for each rotamer population in order to partially constrain the calculation if judged appropriate on the basis of additional experimental or theoretical data. However, in the present work, this feature was not applied. Instead, mole fractions of all conformers were allowed to vary from 0 to 1 during the fit. In addition, an equal weighting factor of 1 was applied to all *J*s used to calculate equilibrium populations.

Three analyses were performed on **1-4**, denoted as A_x , B_x , and C_x . The results of these calculations are shown in detail in Tables S4-S7 and are summarized in Table 4.7. In these calculations, the experimental *J*-couplings were analyzed in the conventional

TABLE 4.7. SUMMARY OF Ω AND Θ ROTAMER POPULATIONS DETERMINED BY SINGLE Ω ANALYSIS AND CORRELATED Ω/Θ ANALYSIS^A IN **1-4**

compound	rotamer populations (%)					
	<i>gt</i>	<i>gg</i>	<i>tg</i>	<i>g+</i>	<i>g-</i>	trans
1	53 (2)	40 (2)	7 (2)			
	51	41	8	25	55	20
2	61 (2)	31 (2)	8 (2)			
	59	32	9	21	59	20
3	74 (4)	3 (2)	23 (4)			
	74	0	26	27	36	37
4	72 (4)	3 (2)	25 (4)			
	71	0	29	23	39	38

^a Single ω analysis (first entry); data obtained by the C₃ fitting method. Correlated ω/θ analysis (second entry); data obtained by the A₃ fitting method. See text and Tables S4–S11 in Supporting Information. Values in parentheses are the respective standard deviations in the population.

manner, namely, as probes of ω ; the θ dependencies will be considered below. In A₁-A₃, ω populations were obtained using only $^3J_{H5,H6R/S}$. In B₁-B₃, ω populations were obtained using only $^3J_{C4,H6R/S}$. In C₁-C₄, multilinear fits were made using six experimental *J*s ($^3J_{H5,H6R/S}$, $^3J_{C4,H6R/S}$, $^2J_{C6,H5}$, $^2J_{C4,C6}$). Two results were obtained for the C₁-C₃ analyses: (1) the "best" fit (i.e., that which gave the lowest overall rms error between the experimental and calculated *J*s) and (2) a statistical analysis consisting of average values and standard deviations for the *gt*, *gg*, and *tg* populations derived from an ensemble of acceptable fits. The latter included calculations characterized by an overall rms error within 10% of the lowest rms error found among all analyses. This range

corresponds to an ~ 0.1 Hz uncertainty in the rms error, which is equal to the precision of the experimental J s.

The subscripts in the A_x , B_x , and C_x series of calculations designate how the limiting J -values were chosen. In A_1 , B_1 , and C_1 , an equilibrium between the *three perfectly staggered* ω rotamers ($\omega = 60^\circ$, -60° , and 180°) was considered. Limiting J -values were calculated from the *average* of hypersurface data over the three perfectly staggered θ rotamers at a specific ω ; these values are reported in Table 4.3. This approach assumes that only perfectly staggered ω rotamers are present in solution and that the populations of the three θ rotamers are equal.

For A_2 , B_2 , and C_2 , DFT-calculated J -values for nine freely optimized (ω , θ) rotamers (Tables 4.1, S2 and S3 for $^2J_{C6,H5}$, $^3J_{C4,H6R/S}$, and $^2J_{C4,C6}$, and Table 4.2 in ref 6 for $^3J_{H5,H6R/S}$) were used to calculate limiting J s for the ω rotamer from the average over the three corresponding conformations. For example, $^3J_{C4,H6R}$ for *gt* is $(1.2 + 1.7 + 0.6)/3 = 1.16$ Hz. Like A_1 , B_1 , and C_1 , no preference for a specific θ orientation is assumed.

For A_3 , B_3 , and C_3 , calculations were conducted assuming a three-state equilibrium, but limiting J -values were calculated using parametrized equations. Average torsion angles for *gt*, *gg*, and *tg* in the *gluco* (65° , -66.5° , and 175°) and *galacto* (63.8° , -52° and 178.4°) configurations were taken from statistical studies of X-ray structures^{38a} and assumed to be reasonable first-order approximations of the torsions in **1-4**.

Equations 4.4 and 4.5 were used to treat $^3J_{H5,H6R}$ and $^3J_{H5,H6S}$, and eqs 4.2 and 4.3 were used to treat $^3J_{C4,H6R/S}$ for the regression and multilinear fits. Limiting values

of ${}^2J_{\text{C6,H5}}$ were derived from eq 4.1c, and limiting values of ${}^2J_{\text{C4,C6}}$ were estimated from eq 4.7b. Contributions by θ were assumed to be uniform.

The analyses (Table 4.7) show that *gt* and *gg* predominate, and *tg* is almost absent, in **1/2**. In contrast, the *gg* population is much reduced compared to *tg* and *gt* in **3/4**. These results are consistent with the strong influence of C4 configuration on the distribution of ω rotamers in saccharides.^{38,39} However, we find that *gt* predominates over *gg* in **1/2**, contrary to prior reports.³⁹ Furthermore, for **3/4**, very little *gg* rotamer was found, whereas *gg* populations as large as 20% were reported previously.³⁹ We attribute these differences to the use of multiple *J*-couplings in the determinations; if the analyses are restricted to ${}^3J_{\text{HH}}$ only, populations similar to those reported previously are obtained. In **1/2**, however, analyses based solely on ${}^3J_{\text{HH}}$ frequently lead to negative *tg* populations. In contrast, the multiple *J* analysis yields positive populations for all three rotamers, thereby lending greater confidence to the results.

For analyses based only on two *J* values (i.e., A_x or B_x), significant negative *tg* rotamer populations in **1/2** are observed in only a few cases, suggesting that the selected limiting *J*s in the three ω rotamers are reasonable approximations (see Supporting Information). Importantly, for each compound, and for each of the A_x and B_x series, relatively small differences (less than $\pm 5\%$ from the average values) in rotamer populations are observed as the source of limiting *J*s was varied. Limiting values derived from the parametrized equations or from DFT data yielded nearly the same results. However, discrepancies (ca. $\pm 10\text{--}15\%$) were observed between populations estimated solely from ${}^3J_{\text{H5,H6R/S}}$ or solely from ${}^3J_{\text{C4,H6R/S}}$.

These findings stimulated the C_x series of analyses in which all available couplings were incorporated in the multilinear fit. For **1-4**, the C3 fits yielded the most accurate solutions to the equations. These analyses suggest that ω rotamers are not perfectly staggered in solution and that estimates of populations based on torsion angles observed in crystal structures are more accurate.

A comparison of ω populations determined by regression analysis or through multilinear fit for **1/2** reveals a small increase and decrease ($\sim 10\%$), respectively, in the populations of *gt* and *gg* in the β -pyranose relative to the α -pyranose, suggesting an effect of anomeric configuration on ω populations (Table 4.7). This effect appears absent in **3/4**.

4.6.3. Distribution of Nine (ω, θ) Rotamers in **1-4** Through Multilinear Fit

In previous work,⁶ rotamer populations having $\theta = 180^\circ$ (trans) in mono-, di-, and trisaccharides were estimated from $^2J_{H6R,H6S}$, assuming perfectly staggered ω and θ rotamers and a similar distribution of θ rotamers in each of the three ω rotamers. Four limiting *J*-values were used, and no distinction was made between *gt* and *gg* and between *g+* and *g-* rotamers. This analysis suggested that gauche C5-C6-O6-O6H rotamers are preferred in most saccharides and that as bulkier substituents at O6 are introduced, the population of trans rotamer increases. The percentage of trans rotamers for methyl β -D-gluco- and galactopyranosides was in agreement with that estimated from $^3J_{HCOH}$ (H6R/S-C6-O6-H pathway).⁴⁰

The preceding discussion showed that ω rotamer populations can be determined using five *J*-values through multilinear regression. This approach was extended to

evaluate both ω and θ using twelve J -values sensitive either to ω alone or to both ω and θ . ${}^2J_{C5,H6R/S}$ are sensitive to ω and θ (Figures 4.2 and 4.3); ${}^2J_{C6,H5}$ also exhibits a dependence on θ , albeit to a lesser extent. The effect of θ on ${}^3J_{H5,H6R/S}$ and ${}^3J_{C4,H6R/S}$ is small (~ 1.0 Hz) and less easily parametrized. Present and previous⁶ work has shown that ${}^2J_{H6R,H6S}$ is more sensitive to θ than to ω . ${}^2J_{C4,C6}$ provided information about ω alone, while ${}^1J_{C5,C6}$ is influenced by ω and θ . ${}^1J_{C6,H6R/S}$ values were used qualitatively to assess hydroxymethyl conformation.⁶

In the multilinear fitting procedure described below, different weights were applied to the couplings to account for (a) differences in the precision to which they are known from experiment, (b) the different quality of the equations (rms errors), and (c) possible contributions to their magnitudes from factors (e.g., lone pair effects on ${}^1J_{CH}$) which were neglected owing to a lack of sufficient data. The following weighting factors were chosen for the fits: 1.0 (${}^3J_{H5,H6R/S}$, ${}^3J_{C4,H6R/S}$, ${}^2J_{C5,H6R/S}$, ${}^2J_{C6,H5}$, ${}^2J_{H6R,H6S}$, and ${}^1J_{C5,C6}$), 0.1 (${}^2J_{C4,C6}$), and 0.01 (${}^1J_{C6,H6R/S}$).

Nine ω / θ conformers were considered: $\omega \approx 60^\circ$, -60° , or 180° , in each case with $\theta \approx 60^\circ$, -60° , or 180° . This model assumes that no intermediate states exist in solution with detectable lifetimes and that all states are independent. Rotamer populations were varied from 0 to 100% in 2% increments, and the best analyses were defined as those resulting in the smallest rms errors between the calculated and experimental couplings.

Three multilinear fits (A₁-A₃ in Tables S8-S11) were performed. In A₁, limiting J -values and ω and θ torsion angles were taken from DFT calculations of the nine completely optimized staggered conformers (Tables 4.1, S2, and S3). In A₂ and A₃,

parametrized equations (eqs 4.4/5 for ${}^3J_{\text{H5,H6R/S}}$, eqs 4.2/3 for ${}^3J_{\text{C4,H6R/S}}$, eqs 4.1a/b for ${}^2J_{\text{C5,H6R/S}}$, eq 4.1c for ${}^2J_{\text{C6,H5}}$, eq 4.8 for ${}^1J_{\text{C5,C6}}$, eq 4.7b for ${}^2J_{\text{C4,C6}}$, eq 4.6 for ${}^2J_{\text{H6R,H6S}}$) and elsewhere (ref 6 for ${}^1J_{\text{C6,H6R/S}}$) were used to back-calculate limiting couplings, assuming either perfectly staggered ω and θ conformers (A_2) or the torsion angles used in A_1 (A_3).

The results of these analyses are given in Tables S8-S11. The set of populations of the nine ω / θ conformers that produced the lowest weighted rms error is shown for A_1 - A_3 , followed by statistical data with average populations and standard deviations (5% tolerance from the lowest rms value), as discussed above for the regression analyses to assess alone. The sums of populations for $\omega = 60^\circ$, -60° , or 180° rotamers over the corresponding three $\theta = 60^\circ$, -60° , or 180° rotamers, and conversely, sums of populations for $\theta = 60^\circ$, -60° , or 180° rotamers over the corresponding three $\omega = 60^\circ$, -60° , or 180° rotamers, were calculated. Error analyses are provided in the form of the overall rms error of the "best" run and in the individual errors in each J , estimated from the difference between the predicted J and the corresponding experimental value. Both weighted [rms (1)] and unweighted [rms (2)] errors were determined. However, to determine the best fit among all calculations, weighted rather than unweighted rms errors were used for the reasons explained above. The results are summarized in Table 4.8.

Distribution of (ω, θ) Rotamers in 1/2: Data in Tables 4.7 and 4.8 confirm the validity of the nine-state equilibrium model. For **1/2**, the weighted rms errors of the best fits for the A_1 - A_3 multilinear regressions were consistently <0.7 Hz, while the unweighted rms errors ranged from 0.8 to 1.2 Hz. All regressions predicted time-average

TABLE 4.8. SUMMARY OF Θ ROTAMER POPULATIONS IN DIFFERENT Ω
ROTAMERS IN **1-4**

compound	rotamer populations (%)								
	$\omega = gt$			$\omega = gg$			$\omega = tg$		
	<i>g+</i>	<i>g-</i>	trans	<i>g+</i>	<i>g-</i>	trans	<i>g+</i>	<i>g-</i>	trans
1	15(9)	27(7)	9(5)	7(5)	25(6)	9(6)	3(3)	3(3)	2(2)
2	14(8)	32(7)	13(5)	4(3)	23(5)	5(4)	3(3)	4(3)	2(2)
3	19(9)	21(9)	34(4)	0(0)	0(0)	0(0)	8(7)	15(7)	3(3)
4	15(9)	21(9)	35(4)	0(1)	0(1)	0(1)	8(7)	18(7)	3(3)

^a Data obtained by the A₃ fitting method; see text and Tables S8–S11 in Supporting Information. Values in parentheses are the respective rms errors in the population.

couplings within 0.5-1.5 Hz of the experimental values except for $^1J_{C6,H6R/S}$. In all runs, $^1J_{C6,H6R}$ and $^1J_{C6,H6S}$ were not accurately predicted (errors up to ~3 Hz), which was expected since the equations were qualitative. Although the ranges of overall rms errors for A₁-A₃ were small for **1/2**, the A₃ regressions consistently produced the smallest rms errors. This finding suggests that and in solution deviate from those in perfectly staggered geometries.

The distribution of and rotamers predicted from the A1-A3 analyses are similar for **1** and **2** (Table 4.7). For **1**, the *gg* and *gt* rotamers are roughly equally populated and account for >~90% of the populations, with *tg* represented by <10%. In contrast, data for **2** suggest a preference of *gt* over *gg* (~2-fold), with *tg* still representing <10% of the

population. Thus, a small effect of anomeric configuration on ω distribution is observed in the *gluco* anomers. An analysis of θ reveals a preference for *g*- in **1/2** (Table 4.7).

More revealing is the distribution of θ rotamers within specific ω rotamers (Table 4.8). The data suggest that ω and θ are not conformationally coupled, that is, the distribution of θ rotamers is independent of the orientation about ω . For example, in *gt* of **1**, ~53% of the rotamers is *g*-, ~17% is *trans*, and ~29% is *g*+; virtually identical relative populations are found in *gg* (Table 4.8). Similar results were obtained for **2**, suggesting that anomeric configuration exerts little or no effect on correlated conformations about ω and θ in the *gluco* configuration.

The distribution of ω rotamers predicted from single (i.e., noncorrelated) analyses is in excellent agreement with that predicted from the correlated analyses (Tables 4.7 and 4.8).

Distribution of (ω, θ) Rotamers in 3/4: Overall weighted rms errors for A_1 - A_3 regression analyses performed on **3** range from 0.6 to 0.7 Hz, while slightly greater errors were found for **4** (0.7-0.9 Hz). Among all regression analyses, those performed assuming nonperfectly staggered ω and θ (i.e., A_1 and A_3) yielded smaller overall rms errors than those based on perfectly staggered rotamers.

As observed for **1/2**, the populations of ω and θ rotamers predicted from the A_1 - A_3 analyses were similar (Table 4.7). Thus, in **3/4**, *gt* predominates (~70%), followed by *tg* (~30%). Virtually no *gg* rotamer was observed. No effect of anomeric configuration on ω rotamer populations was found in **3/4**, in contrast to results obtained on **1/2**. With regard to θ , the *g*+, *g*- and *trans* rotamers are roughly equally populated (Table 4.7).

Unlike **1/2**, the *distribution* of θ rotamers in **3/4** depends on the orientation about ω . In the *gt* form of both **3/4**, *g-*, *g+* and trans θ rotamers are roughly equally populated, whereas in *tg*, *g-* predominates, followed by *g+* and trans (Table 4.8). The effect appears to be caused by a significant reduction in the trans conformation about θ in *tg* compared to *gt* in both **3/4**.

As found for **1/2**, the distribution of ω rotamers predicted from single (i.e., noncorrelated) analyses was in excellent agreement with that predicted from the correlated analyses (Tables 4.7 and 4.8).

4.7. Conclusions

Numerous experimental and theoretical determinations of hydroxymethyl group conformation and dynamics have been reported in aldohexopyranosyl rings.³⁸ An early X-ray crystallographic study^{38a} showed that ω populations change significantly when O4 changes from equatorial (in *gluco*; *gt/gg/tg* \approx 40:60:0) to axial (in *galacto*; *gt/gg/tg* \approx 58:8:34). NMR studies³⁸ have yielded estimates of the *gt* (30-55% for *gluco*, 55-78% for *galacto*), *gg* (45-70% for *gluco*, 10-25% for *galacto*), and *tg* (-25-25% for *gluco*, 2-30% for *galacto*) rotamer populations. The literature has been reviewed recently by Bock and Duus.³⁹ Despite extensive work, however, the NMR approaches to this problem have remained constant for decades. Virtually all of the available analyses rely on two $^3J_{\text{HCCH}}$, and only more recently on two $^3J_{\text{CCCH}}$. Furthermore, rotamer populations based solely on $^3J_{\text{HH}}$ are highly protocol-dependent, resulting in significant anomalies (note the broad range of reported population percentages above). In addition, $^3J_{\text{HH}}$ analyses have

frequently yielded substantial negative *tg* populations in *gluco* sugars.³⁹ The latter problem is attributed in part to the use of inaccurate torsion angles in the limiting staggered rotamers, which leads to errors in the estimates of the limiting *J*-values.

Tvaroska et al.³² recently determined the populations of *gt*, *gg*, and *tg* forms in **1-4** and related compounds in ²H₂O and methanol using either ³*J*_{H5,H6R/S} or ³*J*_{C4,H6R/S}. In this work, substantial differences were reported in the populations derived from both parameters for nearly all compounds, with a maximal uncertainty of 46% for *gg* rotamers in methyl 6-*O*-methyl- α -D-glucopyranoside.

New structural constraints to assess CH₂OH group conformation in saccharides based on multiple, redundant *J*-couplings have been described in this report. Using theoretical and experimental methods, equations were developed to correlate the magnitudes and signs of 12 scalar couplings with CH₂OH conformation. Importantly, some of these couplings display dependence not only on ω but also on θ , in some cases exhibiting a greater dependence on the latter than on the former. These second-order dependencies serve as indirect probes of C-O bond conformation in solution that do not depend on direct observation/detection of the exchangeable hydroxyl proton. More importantly, use of these equations allows assessments of correlated conformation about ω and θ .

Several key observations were made while developing these new constraints, which are summarized as follows:

(a) DFT provides a nearly quantitative tool to calculate *J*_{HH}, *J*_{CH}, and *J*_{CC} values in saccharides, judging from comparisons of calculated and experimental couplings in conformationally constrained systems. In this work, unscaled couplings were employed.

The theory appears sufficiently robust to yield accurate couplings in terms of magnitude and sign, thus obviating the need to impose empirical scaling adjustments common to studies of this type.⁴¹ The small deviations (<10%) are likely caused by neglected conformational factors, neglect of non-Fermi contact contributions, and/or solvation effects. Further work is needed to establish the relative importance of these factors in order to incorporate further corrections or refinements to the methodology.

(b) $^2J_{\text{CCH}}$ display a large sensitivity to ω if their signs are taken into account. Importantly, prior suggestions that $^2J_{\text{CH}}$ values are sensitive to C-O torsions have been confirmed and quantified. This effect appears more significant for C-O torsions involving the carbon bearing the coupled proton than for C-O torsions involving the coupled carbon.

(c) Different Karplus equations apply to the interpretation of $^3J_{\text{C4,H6R}}$ and $^3J_{\text{C4,H6S}}$, in contrast to the prior generalized treatment of these couplings.³¹ This behavior mimics that observed for $^3J_{\text{H5,H6R}}$ and $^3J_{\text{H5,H6S}}$.⁶

(d) $^1J_{\text{C5,C6}}$ depends on both ω and θ , as anticipated based on previous studies of $^1J_{\text{CC}}$ in ethylene glycol.³⁴ The present work defines a quantitative relationship between both torsions and $^1J_{\text{CC}}$ magnitude.

(e) $^3J_{\text{C1,C6}}$ and $^3J_{\text{C3,C6}}$ may be useful additional experimental constraints on ω . This sensitivity stems from the effect of terminal electronegative substituent orientation on the Karplus dependencies of $^3J_{\text{CCCC}}$ and $^3J_{\text{COCC}}$.¹

(f) Given the simplicity of the present systems compared to ethylene glycol, greater insight into the stereoelectronic effects of oxygen lone pairs on saccharide bond

lengths, and concomitant effects on J -couplings, especially $^1J_{CC}$, was obtained. In addition to their use in conformational analysis, J -couplings provide a means to indirectly evaluate saccharide electronic and stereoelectronic structure, both of which dictate their chemical and biological functions.

Nine independent ω / θ rotamers in **1-4** were assumed in the present treatment, and their populations were calculated from the multilinear regression of 12 J -couplings. The data show that θ rotamer distribution may be affected by in O6-unsubstituted molecules. However, skewing in favor of specific θ rotamers is not large, suggesting that H-bonding solvation scaffolds, if present, do not freeze C-O rotamers completely. It will be important to test these conclusions via studies of $^3J_{HCOH}$ ⁴⁰ and $^3J_{CCOH}$ ⁴² which may provide complementary information on C-O conformation in aqueous solution.

The present study focused on free CH₂OH groups in four methyl aldohexopyranosides (**1-4**) to establish new J -coupling/structure correlations in simple, well understood systems. While the application of these correlations to unsubstituted CH₂OH groups has practical benefits (e.g., in oligosaccharides where intramolecular H-bonding may influence ω and/or θ), more significant applications are expected in compounds such as 1,6-linked oligosaccharides containing substituted CH₂OH groups. These linkages are characterized by three torsions and can display significant conformational flexibility. Recent studies have addressed the concerted use of $^2J_{COC}$, $^3J_{COCH}$, and $^3J_{COCC}$ across glycosidic linkages to assess rotamer populations about ϕ and ψ .^{1,2} In 1,6-linkages, however, ψ and θ are *redundant*, and thus a significant number of redundant J -couplings can now be brought to bear on this torsion *from both sides of*

the glycosidic linkage. Furthermore, *correlated conformation* about ω and θ/ψ can be investigated, thus providing more detailed information on linkage flexibility.

Access to multiple J -couplings sensitive to CH_2OH conformation render recently described theoretical approaches to assigning CH_2OH conformation applicable to carbohydrate systems. The CUPID method⁴³ allows for calculations of a continuous rotamer distribution from NMR data provided that six conformationally sensitive parameters are available to determine a Fourier expansion of the order three. The maximum entropy method^{30d} can be applied more effectively through access to an increased number of experimental NMR constraints.

The present findings have implications not only for studies of ω and θ in exocyclic hydroxymethyl groups in oligosaccharides but also for related studies in oligonucleotides. However, the equations reported herein were derived for pyranosyl rings. Further work is needed to determine whether modifications are required to treat furanosyl rings.

Finally, it should be noted that exocyclic CH_2OH conformation cannot be assessed via $^3J_{\text{HH}}$ in some molecules. For example, $^3J_{\text{HH}}$ values are unavailable to study conformation about the C1-C2 bond in 2-ketohexoses such as D-fructose. In these cases, the additional J -coupling constraints reported herein could be advantageous.

4.8. Acknowledgment

This work was supported by a postdoctoral fellowship from the Knut och Alice Wallenberg stiftelse (Stockholm, Sweden) (to R.S.) and grants from Omicron

Biochemicals, Inc. of South Bend, IN and the National Institutes of Health (GM59239) (to A.S.). The Notre Dame Radiation Laboratory is supported by the Office of Basic Energy Sciences of the United States Department of Energy. This is Document No. NDRL-4498 from the Notre Dame Radiation Laboratory.

4.9. Supporting Information

The behavior of $^1J_{C5,C6}$ in **5** was investigated further by evaluating the relationship between $r_{C5,C6}$ and ω (Figure S1A). This bond length increases substantially in eclipsed conformations ($\omega = -120^\circ, 0^\circ$ and 120°); $r_{C5,C6} = 1.5267 \pm 0.0039$ Å and 1.5495 ± 0.0094 Å for the staggered and eclipsed conformations, respectively. Interestingly, data at each group of ω values show that $r_{C5,C6}$ is shortest in structures containing $\theta = 180^\circ$, that is, in those geometries in which both O6 lone-pairs are gauche to the C5-C6 bond. A plot of computed $^1J_{C5,C6}$ vs $r_{C5,C6}$ yields two different approximately linear correlations for staggered and eclipsed conformations about ω (Figure S1B), indicating that the relationship between $^1J_{C5,C6}$ and $r_{C5,C6}$ is not simple; apparently factors in addition to bond length modulate $^1J_{CC}$.

A plot of $r_{C6,H6R}$ and $r_{C6,H6S}$ as a function of ω shows the expected effect (Figure S2A); shorter bond lengths are found in geometries lacking O6 lone-pairs anti to the C6-H6 bond. Importantly, θ exerts a far greater effect on $r_{C6,H6R/S}$ than does ω , emphasizing the significant effect that vicinal lone-pairs exert on C-H bond lengths in saccharides.²⁸ The value of $r_{C6,O6}$ also depends on ω , with minimal values observed for

$\omega \approx 0^\circ$ (Figure S2B). Data at each group of ω values show that, in general, $r_{C6,O6}$ is enhanced when $\theta = 180^\circ$.

A plot of $r_{C5,O5}$ vs ω shows that the effect of θ is greatest (*i.e.*, largest spread of J s) for $\omega = +60^\circ$ and -60° (*gt* and *gg* rotamers, respectively) (Figure S2C). We attribute this result to the presence of 1,3-lone-pair effects on the C5-O5 bond length, which shorten the bond. A plot of $r_{C4,C5}$ vs ω (data not shown) shows a similar but somewhat reduced 1,3-lone-pair effect due to O6 lone-pairs; apparently the C5-O5 bond is more easily perturbed than the C4-C5 bond despite similar geometrical relationships to O6 lone-pairs.

TABLE 4.9. (S1) CALCULATED SCALAR COUPLINGS IN **6** AND **7**

Coupling ^b	6gg	6gt	6tg	7gg	7gt	7tg
¹ $J_{C5,H5}$	129.7	139.5	139.1	138.4	144.5	145.0
² $J_{C1,C5}$	-2.1	-2.1	-1.9	-2.2	-2.1	-1.9
² $J_{C5,H6R}$	+2.6	-6.4	-3.4	+0.5	-5.5	-4.7
² $J_{C5,H6S}$	-5.2	+3.1	-5.5	-4.7	+1.0	-3.3
² $J_{C6,H5}$	+0.6	-5.5	-4.6	+3.0	-4.3	-4.4
² $J_{C4,C6}$	-1.4	+1.7	-1.4	-1.5	+2.5	+0.5
³ $J_{C4,H6R}$	1.7	0.1	5.4	0.5	1.0	5.6
³ $J_{C4,H6S}$	8.3	2.0	3.2	4.6	0.9	5.5
³ $J_{C6,H4}$	1.3	1.2	0.6	2.9	3.2	3.4

^aOne set of C4-O4 and C6-O6 bond conformations was examined in **6** and **7**, namely, OH4 and OH6 anti to C5 (see Experimental). Coupling signs are indicated (+ or -) for ² J ; ¹ J and ³ J have + signs. ^bIn Hz.

TABLE 4.10. (S2) TORSIONS, ω AND θ , CALCULATED $^3J_{\text{CH}}$ VALUES IN 5

ω^c	θ^d	$^3J_{\text{C4,H6R}}$	$^3J_{\text{C4,H6S}}$	$^3J_{\text{C6,H4(ax)}}$	$^3J_{\text{C6,H4(eq)}}$	C5-C6 Rotamer ^e
62	57	1.2	1.1	3.5	1.1	<i>gt</i>
57	-48	1.7	0.5	3.4	0.8	
72	192	0.6	1.8	3.4	1.1	
-58	50	1.8	6.4	2.9	0.9	<i>gg</i>
-70	-72	0.8	6.0	2.6	1.0	
-72	171	0.7	5.7	2.6	1.0	
176	74	7.0	3.6	3.6	0.4	<i>tg</i>
177	-69	6.7	3.9	3.5	0.4	
176	176	6.7	3.7	3.6	0.4	
120	60	3.0	5.7	3.6	0.7	
120	-60	2.5	6.1	3.8	0.8	
120	180	2.7	6.2	3.7	0.8	
0	60	7.6	3.6	3.6	1.4	
0	-60	7.2	4.2	3.5	1.3	
0	180	7.6	4.0	3.5	1.6	
-120	60	1.2	0.6	2.4	0.6	
-120	-60	1.5	0.4	2.6	0.5	
-120	180	1.3	0.5	2.4	0.5	

^aIn degrees. ^bIn Hz. ^cDefined as O5-C5-C6-O6. ^dDefined as C5-C6-O6-HO6.^eDefined in Scheme 3.

TABLE 4.11. (S3) TORSION ANGLES, ω AND θ , AND CALCULATED $^1J_{CC}$ AND $^2J_{CC}$ VALUES IN **5**

ω^c	θ^d	$^1J_{C4,C5}$	$^1J_{C5,C6}$	$^2J_{C4,C6}$	C5-C6 Rotamer ^e
62	57	37.2	43.5	+3.8	<i>gt</i>
57	-48	37.7	42.0	+3.2	
72	192	37.8	48.0	+4.4	
-58	50	38.3	41.6	-0.6	<i>gg</i>
-70	-72	38.5	43.8	-0.5	
-72	171	38.0	47.0	-0.7	
176	74	38.2	46.1	+0.8	<i>tg</i>
177	-69	38.7	45.7	+0.4	
176	176	37.9	49.7	0.0	
120	60		44.8	+2.8	
120	-60		45.0	+2.8	
120	180		50.6	+3.0	
0	60		40.3	+2.5	
0	-60		40.1	+2.3	
0	180		45.4	+2.6	
-120	60		43.3	-0.7	
-120	-60		43.5	-0.7	
-120	180		48.5	-1.0	

^aIn degrees. ^bIn Hz. ^cDefined as O5-C5-C6-O6. ^dDefined as C5-C6-O6-HO6.^eDefined in Scheme 3.

TABLE 4.12. (S4) POPULATIONS OF ω ROTAMERS IN 1: ANALYSIS OF $^3J_{\text{H5,H6R/S}}$, $^3J_{\text{C4,H6R/S}}$, $^2J_{\text{C4,C6}}$ AND/OR $^2J_{\text{C6,H5}}$

<i>J</i> s used in the fit	method ^b	Populations of ω Rotamers (%)				Errors in Calculated <i>J</i> s (best analysis only)					
		<i>gt</i> ($\omega = 60^\circ$)	<i>gg</i> ($\omega = -60^\circ$)	<i>tg</i> ($\omega = 180^\circ$)	rms error ^a	$^3J_{\text{H5,H6R}}$	$^3J_{\text{H5,H6S}}$	$^3J_{\text{C4,H6R}}$	$^3J_{\text{C4,H6S}}$	$^2J_{\text{C4,C6}}$	$^2J_{\text{C6,H5}}$
$^3J_{\text{H5,H6R/S}}$	A ₁	48	54	-2							
	A ₂	45	51	4							
	A ₃	49	41	10							
$^3J_{\text{C4,H6R/S}}$	B ₁	71	37	-8							
	B ₂	66	35	-1							
	B ₃	68	35	-3							
$^3J_{\text{H5,H6R/S}}$	C ₁	50	49	1	0.9	0.3	0.3	0.5	0.9	1.8	0.6
		48 (4)	47 (4)	5 (3)							
$^3J_{\text{C4,H6R/S}}$	C ₂	46	48	6	0.8	0.2	0.2	0.4	0.8	1.5	0.6
		46 (4)	48 (4)	6 (4)							
$^2J_{\text{C4,C6}}$	C ₃	53	40	7	0.4	0.3	-0.3	0.6	0.5	0.4	0.1
$^2J_{\text{C6,H5}}$		53 (2)	40 (2)	7 (2)							

^aThe rms error (in Hz) between calculated and experimental *J*s was calculated according to the formula: $\text{rms} = [(\sum_i w_i (J_{\text{calc}} - J_{\text{exp}})^2)^{1/2}]/(n-1)$, where *n* = number of *J*s used in the fit, *i* = a specific coupling and *w_i* = the weighting factor used for this *J* in the calculation of the rms error. Individual errors in calculated *J*s (in Hz) are those obtained with the “best” analysis, *i.e.*, that characterized by the lowest overall rms error. ^bSee text for a description of the methods. For C₁-C₃, two sets of populations are given; the upper corresponds to the data from the analysis characterized by the lowest overall rms error, and the lower corresponds to average populations (standard deviations in parenthesis) of the *gt*, *gg* and *tg* rotamers calculated over the ensemble of “successful” fits (see text for details).

TABLE 4.13. (S5) POPULATIONS OF ω ROTAMERS IN **2** FROM AN ANALYSIS OF $^3J_{\text{H5,H6R/S}}$, $^3J_{\text{C4,H6R/S}}$, $^2J_{\text{C4,C6}}$
AND/OR $^2J_{\text{C6,H5}}$

<i>J</i> s used in the fit	method ^b	Populations of ω Rotamers (%)				Errors in Calculated <i>J</i> s (best analysis only)					
		<i>gt</i> ($\omega = 60^\circ$)	<i>gg</i> ($\omega = -60^\circ$)	<i>tg</i> ($\omega = 180^\circ$)	rms error ^a	$^3J_{\text{H5,H6R}}$	$^3J_{\text{H5,H6S}}$	$^3J_{\text{C4,H6R}}$	$^3J_{\text{C4,H6S}}$	$^3J_{\text{C4,H6S}}$	$^2J_{\text{C6,H5}}$
$^3J_{\text{H5,H6R/S}}$	A ₁	54	48	-2							
	A ₂	52	44	4							
	A ₃	56	35	10							
$^3J_{\text{C4,H6R/S}}$	B ₁	76	29	-5							
	B ₂	74	25	1							
	B ₃	75	26	-1							
$^3J_{\text{H5,H6R/S}}$ $^3J_{\text{C4,H6R/S}}$ $^2J_{\text{C4,C6}}$ $^2J_{\text{C6,H5}}$	C ₁	56	41	3	1.0	0.4	0.4	0.5	0.9	2.1	0.9
		55 (5)	39 (5)	6 (4)							
	C ₂	53	40	7	0.9	0.2	0.3	0.4	0.9	1.8	0.8
		53 (5)	39 (5)	8 (4)							
	C ₃	61	31	8	0.5	0.4	-0.2	0.5	0.5	0.6	0.4
		61 (2)	31 (2)	8 (2)							

^{a,b}See legend in Table S4.

TABLE 4.14. (S6) POPULATIONS OF ω ROTAMERS IN **3** FROM AN ANALYSIS OF $^3J_{\text{H5,H6R/S}}$, $^3J_{\text{C4,H6R/S}}$, $^2J_{\text{C4,C6}}$
AND/OR $^2J_{\text{C6,H5}}$

J s used in the fit	method ^b	Populations of ω Rotamers (%)				Errors in Calculated J s (best analysis only)					
		gt ($\omega = 60^\circ$)	gg ($\omega = -60^\circ$)	tg ($\omega = 180^\circ$)	rms error ^a	$^3J_{\text{H5,H6R}}$	$^3J_{\text{H5,H6S}}$	$^3J_{\text{C4,H6R}}$	$^3J_{\text{C4,H6S}}$	$^2J_{\text{C4,C6}}$	$^2J_{\text{C6,H5}}$
$^3J_{\text{H5,H6R/S}}$	A ₁	65	13	22							
	A ₂	68	6	26							
	A ₃	70	2	28							
$^3J_{\text{C4,H6R/S}}$	B ₁	80	11	9							
	B ₂	82	5	13							
	B ₃	84	9	7							
$^3J_{\text{H5,H6R/S}}$ $^3J_{\text{C4,H6R/S}}$ $^2J_{\text{C4,C6}}$ $^2J_{\text{C6,H5}}$	C ₁	67 66 (7)	6 9 (5)	27 26 (7)	1.4	0.3	0.5	1.0	0.2	2.5	1.9
	C ₂	68	3	29	1.3	0.1	0.3	0.9	0.3	2.7	1.7
	C ₃	66 (6)	7 (5)	27 (6)							
		75 74 (4)	0 3 (2)	25 23 (4)	0.9 ^c / 0.8 ^d	0.4	-0.3	0.9	-0.2	1.1 ^c / 0.6 ^d	1.5

^{a,b}See legend in Table S4. ^{c,d}Two analyses were performed for C₃. In the first, the experimental value for $^2J_{\text{C4,C6}}$ was set to 0.0 Hz, while in the other $^2J_{\text{C4,C6}}$ was assumed to be 0.5 Hz (*i.e.*, below the linewidth of the resonance). The higher J -value reduced the individual error between calculated and experimental $^2J_{\text{C4,C6}}$ (1.1 \rightarrow 0.6 Hz) and the overall rms of the analysis (0.9 \rightarrow 0.8 Hz).

TABLE 4.15. (S7) POPULATIONS OF ω ROTAMERS IN **4** FROM AN ANALYSIS OF ${}^3J_{\text{H5,H6R/S}}$, ${}^3J_{\text{C4,H6R/S}}$, ${}^2J_{\text{C4,C6}}$
AND/OR ${}^2J_{\text{C6,H5}}$

<i>J</i> s used in the fit	method ^b	Populations of ω Rotamers (%)				Errors in Calculated <i>J</i> s (best analysis only)					
		<i>gt</i> ($\omega = 60^\circ$)	<i>gg</i> ($\omega = -60^\circ$)	<i>tg</i> ($\omega = 180^\circ$)	rms error ^a	${}^3J_{\text{H5,H6R}}$	${}^3J_{\text{H5,H6S}}$	${}^3J_{\text{H5,H6R}}$	${}^3J_{\text{H5,H6S}}$	${}^2J_{\text{C4,C6}}$	${}^2J_{\text{C6,H5}}$
${}^3J_{\text{H5,H6R/S}}$	A ₁	62	15	24							
	A ₂	64	8	28							
	A ₃	66	4	30							
${}^3J_{\text{C4,H6R/S}}$	B ₁	78	13	9							
	B ₂	80	7	13							
	B ₃	83	11	6							
${}^3J_{\text{H5,H6R/S}}$ ${}^3J_{\text{C4,H6R/S}}$ ${}^2J_{\text{C4,C6}}$ ${}^2J_{\text{C6,H5}}$	C ₁	65 64 (7)	5 9 (5)	30 28 (7)	1.4	0.6	0.5	1.1	0.1	2.5	2.2
	C ₂	66 64 (7)	2.9 7 (5)	31 29 (7)	1.4	0.3	0.3	1.0	0.3	2.6	1.9
	C ₃	73	0	27	1.0 ^c / 0.9 ^d	0.5	-0.2	1.0	-0.2	1.1 ^c / 0.6 ^d	1.9
		72 (4)	3 (2)	25 (4)							

^{a,b}See legend in Table S4. ^{c,d}See legend in Table S6.

TABLE 4.16. (S8) MULTILINEAR FIT OF EXPERIMENTAL COUPLINGS IN α -D-GLC (1) TO ASSESS ω AND θ ROTAMER POPULATIONS

Fit	Populations of ω / θ rotamers (%)									Sums of Rotamers						
	$\omega = 60^\circ$ (<i>gt</i>)			$\omega = -60^\circ$ (<i>gg</i>)			$\omega = 180^\circ$ (<i>tg</i>)			Sums over ω			Sums over θ			
	θ	$= 60^\circ$ (<i>g+</i>)	-60° (<i>g-</i>)	180° (<i>trans</i>)	60° (<i>g+</i>)	-60° (<i>g-</i>)	180° (<i>trans</i>)	60° (<i>g+</i>)	-60° (<i>g-</i>)	180° (<i>trans</i>)	<i>gt</i>	<i>gg</i>	<i>tg</i>	<i>g+</i>	<i>g-</i>	<i>trans</i>
A₁		0	36	16	24	18	0	6	0	0	52	42	6	30	54	16
		5 (4)	35 (5)	12 (4)	23 (5)	15 (4)	4 (4)	3 (3)	3 (2)	1 (1)	52	42	7	31	53	17
A₂		2	40	14	6	28	6	2	0	2	56	40	4	10	68	22
		9 (7)	35 (10)	10 (6)	9 (7)	22 (9)	9 (6)	2 (2)	2 (2)	2 (2)	54	40	6	20	59	21
A₃		10	28	14	8	26	6	0	8	0	52	40	8	18	62	20
		15 (9)	27 (7)	9 (5)	7 (5)	25 (6)	9 (6)	3 (3)	3 (3)	2 (2)	51	41	8	25	55	20

Error analysis of *J*-couplings

Fit	rms (1) ^b	rms (2) ^b	³ <i>J</i> _{H5,H6R}	³ <i>J</i> _{H5,H6S}	³ <i>J</i> _{C4,H6R}	³ <i>J</i> _{C4,H6S}	² <i>J</i> _{C5,H6R}	² <i>J</i> _{C5,H6S}	¹ <i>J</i> _{C6,H6R}	¹ <i>J</i> _{C6,H6S}	² <i>J</i> _{C6,H5}	² <i>J</i> _{C4,C6}	¹ <i>J</i> _{C5,C6}	² <i>J</i> _{H6R,H6S}
A₁	0.63	0.91	0.56	0.44	0.60	0.50	1.12	0.93	-1.62	-0.40	0.25	1.67	0.13	1.06
A₂	0.60	1.01	0.54	0.05	0.96	0.50	1.06	1.15	-2.78	-0.42	0.27	0.46	0.30	0.32
A₃	0.50	0.79	0.44	0.00	0.77	0.44	0.87	0.95	-2.08	-0.37	0.25	0.37	0.47	0.24

^aCouplings, rms errors and individual differences between calculated and experimental coupling constants are in Hz. See text for descriptions of the A₁-A₃ protocols used to perform the multilinear regressions. ^bTwo values are tabulated for the rms error between experimental and calculated coupling constants as provided by the best fit analysis: rms (1) takes into account the weighting factors applied to the individual couplings; rms (2) is the unweighted rms error (calculated with weighting factors of 1.0).

TABLE 4.17. (S9) MULTILINEAR FIT OF EXPERIMENTAL COUPLINGS IN β -D-GLC (2) TO ASSESS ω AND θ ROTAMER POPULATIONS

Fit	Populations of ω / θ rotamers (%)									Sums of Rotamers					
	$\omega = 60^\circ$ (<i>gt</i>)			$\omega = -60^\circ$ (<i>gg</i>)			$\omega = 180^\circ$ (<i>tg</i>)			Sums over ω			Sums over θ		
	$\theta = 60^\circ$ (<i>g+</i>)	-60° (<i>g-</i>)	180° (<i>trans</i>)	60° (<i>g+</i>)	-60° (<i>g-</i>)	180° (<i>trans</i>)	60° (<i>g+</i>)	-60° (<i>g-</i>)	180° (<i>trans</i>)	<i>gt</i>	<i>gg</i>	<i>tg</i>	<i>g+</i>	<i>g-</i>	<i>trans</i>
A₁	0	44	16	20	14	0	6	0	0	60	34	6	26	58	16
	5 (4)	41 (5)	13 (4)	17 (5)	14 (5)	3 (3)	4 (3)	3 (3)	1 (1)	59	34	8	26	58	17
A₂	2	58	2	4	12	16	2	2	2	62	32	6	8	72	20
	9 (7)	42 (10)	9 (6)	8 (6)	17 (8)	8 (6)	2 (2)	3 (3)	3 (2)	60	33	8	19	62	20
A₃	6	34	20	4	28	0	0	8	0	60	32	8	10	70	20
	14 (8)	32 (7)	13 (5)	4 (3)	23 (5)	5 (4)	3 (3)	4 (3)	2 (2)	59	32	9	21	59	20

Error analysis of *J*-couplings

Fit	rms (1) ^b	rms (2) ^b	³ <i>J</i> _{H5,H6R}	³ <i>J</i> _{H5,H6S}	³ <i>J</i> _{C4,H6R}	³ <i>J</i> _{C4,H6S}	² <i>J</i> _{C5,H6R}	² <i>J</i> _{C5,H6S}	¹ <i>J</i> _{C6,H6R}	¹ <i>J</i> _{C6,H6S}	² <i>J</i> _{C6,H5}	² <i>J</i> _{C4,C6}	¹ <i>J</i> _{C5,C6}	² <i>J</i> _{H6R,H6S}
A₁	0.70	0.99	0.71	0.48	0.54	0.44	1.10	1.07	-1.24	-0.92	0.57	1.97	0.08	1.23
A₂	0.65	1.00	0.62	0.24	0.93	0.45	1.19	1.24	-2.47	-0.68	0.58	0.61	0.25	0.35
A₃	0.56	0.88	0.53	0.02	0.65	0.42	0.97	1.11	-2.27	-0.45	0.52	0.57	0.47	0.34

^aSee legend in Table S8.

TABLE 4.18. (S10) MULTILINEAR FIT OF EXPERIMENTAL COUPLINGS IN α -D-GAL (**3**) TO ASSESS ω AND θ ROTAMER POPULATIONS

Fit	Populations of ω / θ rotamers (%)									Sums of Rotamers					
	$\omega = 60^\circ$ (<i>gt</i>)			$\omega = -60^\circ$ (<i>gg</i>)			$\omega = 180^\circ$ (<i>tg</i>)			Sums over ω			Sums over θ		
	$\theta = 60^\circ$ (<i>g+</i>)	-60° (<i>g-</i>)	180° (<i>trans</i>)	60° (<i>g+</i>)	-60° (<i>g-</i>)	180° (<i>trans</i>)	60° (<i>g+</i>)	-60° (<i>g-</i>)	180° (<i>trans</i>)	<i>gt</i>	<i>gg</i>	<i>tg</i>	<i>g+</i>	<i>g-</i>	<i>trans</i>
A₁	12	32	30	0	0	0	16	10	0	64	0	26	28	42	30
	15 (7)	29 (7)	28 (4)	0 (1)	0 (1)	0 (1)	14 (8)	11 (7)	2 (2)	72	0	27	29	40	30
A₂	24	30	20	0	0	0	12	0	14	74	0	26	36	30	34
	28 (12)	20 (12)	25 (8)	1 (1)	1 (1)	1 (1)	8 (7)	7 (6)	9 (7)	73	3	24	37	28	35
A₃	22	16	36	0	0	0	0	26	0	74	0	26	22	42	36
	19 (9)	21 (9)	34 (4)	0 (0)	0 (0)	0 (0)	8 (7)	15 (7)	3 (3)	74	0	26	27	36	37

Error analysis of <i>J</i> -couplings														
Fit	rms (1) ^b	rms (2) ^b	³ <i>J</i> _{H5,H6R}	³ <i>J</i> _{H5,H6S}	³ <i>J</i> _{C4,H6R}	³ <i>J</i> _{C4,H6S}	² <i>J</i> _{C5,H6R}	² <i>J</i> _{C5,H6S}	¹ <i>J</i> _{C6,H6R}	¹ <i>J</i> _{C6,H6S}	² <i>J</i> _{C6,H5}	² <i>J</i> _{C4,C6}	¹ <i>J</i> _{C5,C6}	² <i>J</i> _{H6R,H6S}
A₁	0.67	1.18	0.52	0.07	0.76	0.10	0.76	0.53	-1.40	-1.22	1.40	2.97	0.31	0.88
A₂	0.74	1.10	0.64	0.15	1.17	-0.35	0.82	0.82	-0.98	-2.44	1.72	1.08	-0.03	0.43
A₃	0.60	0.96	0.04	-0.28	0.86	0.04	0.60	0.79	-1.99	-1.35	1.46	1.12	0.25	0.40

^aSee legend in Table S8.

TABLE 4.19. (S11) MULTILINEAR FIT OF EXPERIMENTAL COUPLINGS IN α -D-GAL (4) TO ASSESS ω AND θ ROTAMER POPULATIONS

Fit	Populations of ω / θ rotamers (%)									Sums of Rotamers						
	$\omega = 60^\circ$ (<i>gt</i>)			$\omega = -60^\circ$ (<i>gg</i>)			$\omega = 180^\circ$ (<i>tg</i>)			Sums over ω			Sums over θ			
	θ	$= 60^\circ$ (<i>g+</i>)	-60° (<i>g-</i>)	180° (<i>trans</i>)	60° (<i>g+</i>)	-60° (<i>g-</i>)	180° (<i>trans</i>)	60° (<i>g+</i>)	-60° (<i>g-</i>)	180° (<i>trans</i>)	<i>gt</i>	<i>gg</i>	<i>tg</i>	<i>g+</i>	<i>g-</i>	<i>trans</i>
A₁		6	34	32	0	0	0	14	14	0	72	0	28	20	48	32
		10 (6)	30 (7)	30 (5)	0 (1)	0 (1)	0 (1)	14 (8)	13 (8)	2 (2)	70	0	29	24	43	32
A₂		8	28	36	0	0	0	18	10	0	72	0	28	26	38	36
		23 (12)	22 (13)	24 (9)	1 (1)	1 (1)	1 (1)	9 (7)	9 (7)	10 (7)	69	3	28	33	32	35
A₃		18	14	38	0	0	0	0	30	0	70	0	30	18	44	38
		15 (9)	21 (9)	35 (4)	0 (1)	0 (1)	0 (1)	8 (7)	18 (7)	3 (3)	71	0	29	23	39	38

Error analysis of *J*-couplings

Fit	rms (1) ^b	rms (2) ^b	³ <i>J</i> _{H5,H6R}	³ <i>J</i> _{H5,H6S}	³ <i>J</i> _{C4,H6R}	³ <i>J</i> _{C4,H6S}	² <i>J</i> _{C5,H6R}	² <i>J</i> _{C5,H6S}	¹ <i>J</i> _{C6,H6R}	¹ <i>J</i> _{C6,H6S}	² <i>J</i> _{C6,H5}	² <i>J</i> _{C4,C6}	¹ <i>J</i> _{C5,C6}	² <i>J</i> _{H6R,H6S}
A₁	0.79	1.32	0.64	0.08	0.86	0.06	0.90	0.74	-2.10	-1.20	1.70	2.89	0.30	1.10
A₂	0.88	1.26	0.82	0.13	1.27	-0.40	1.04	1.07	-1.94	-2.21	2.04	1.05	0.01	0.62
A₃	0.74	1.10	0.06	-0.15	1.06	0.07	0.72	1.07	-2.24	-1.42	1.77	1.07	0.40	0.58

^aSee legend in Table S8.

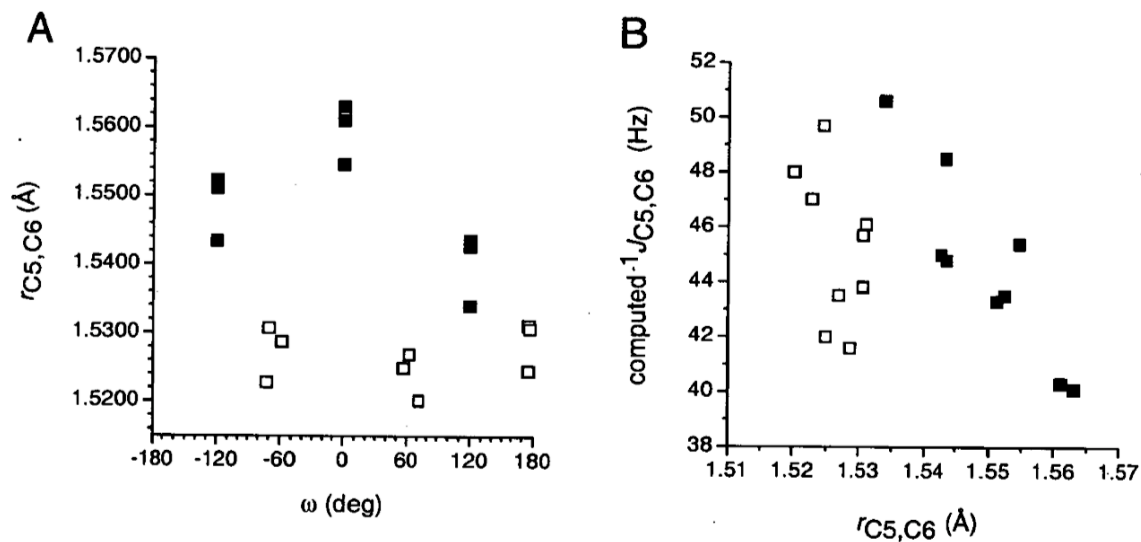


Figure 4.9. (S1) (A) The dependence of $r_{C5,C6}$ in **5** on ω . (B) Correlations between $^1J_{C5,C6}$ in **5** and $r_{C5,C6}$. The vertical spread of points at discrete ω torsions indicates the degree of sensitivity of the coupling to changes in θ . Open squares, staggered conformers; filled squares, eclipsed conformers.

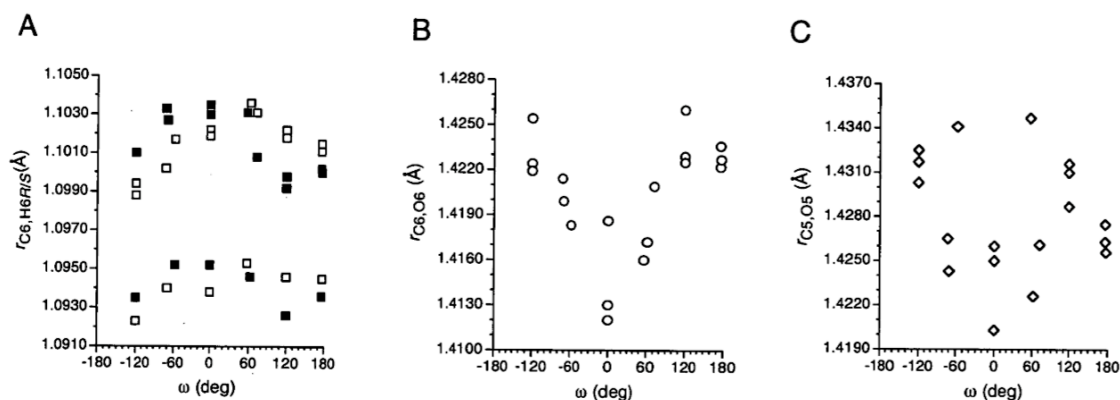


Figure 4.10. (S2) Correlation between $r_{C6,H6R/S}$ and ω in **5**. Filled squares, $r_{C6,H6R}$; open squares, $r_{C6,H6S}$. (B) Correlation between $r_{C6,O6}$ and ω in **5**. (C) Correlation between $r_{C5,O5}$ and ω in **5**. In all plots, data were taken from the 18 staggered and eclipsed structures identified in Table 1

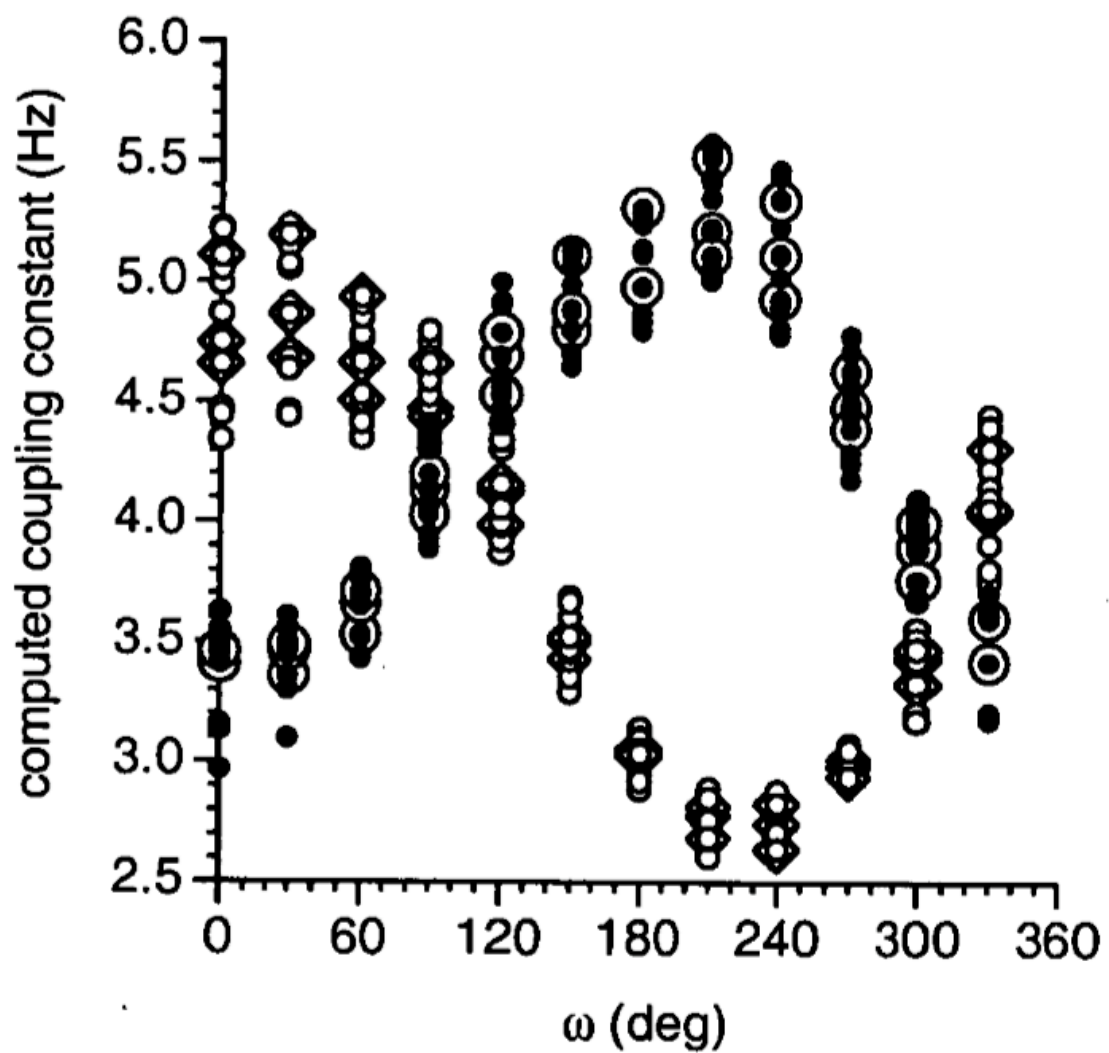


Figure 4.11. (S3) The dependencies of $^3J_{C1,C6}$ (filled circles) and $^3J_{C3,C6}$ (open circles) in **5** on ω . The vertical spread of points at discrete ω torsions indicates the effect of θ . Perfectly staggered θ rotamers at individual ω values are indicated by open circles and diamonds.

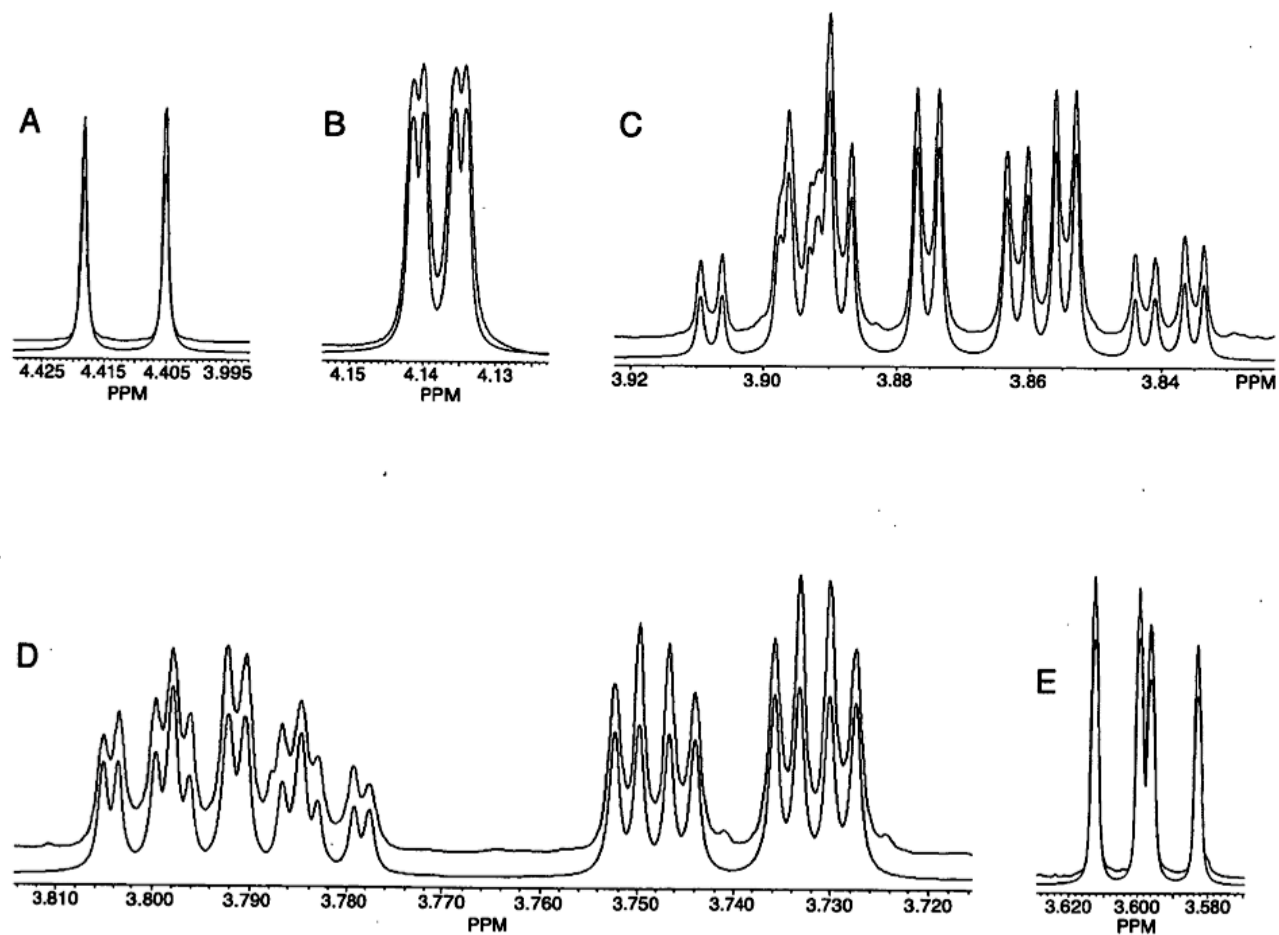


Figure 4.12. (S4) Portions of the 600-MHz ^1H NMR spectrum of methyl α -D-[4- ^{13}C]galactopyranoside **4** (upper trace) superimposed on simulated data (lower trace). (A) H1. (B) downfield half of H4. (C) H6R, upfield half of H4, and H6S. (D) H5 and H3. (E) H2.

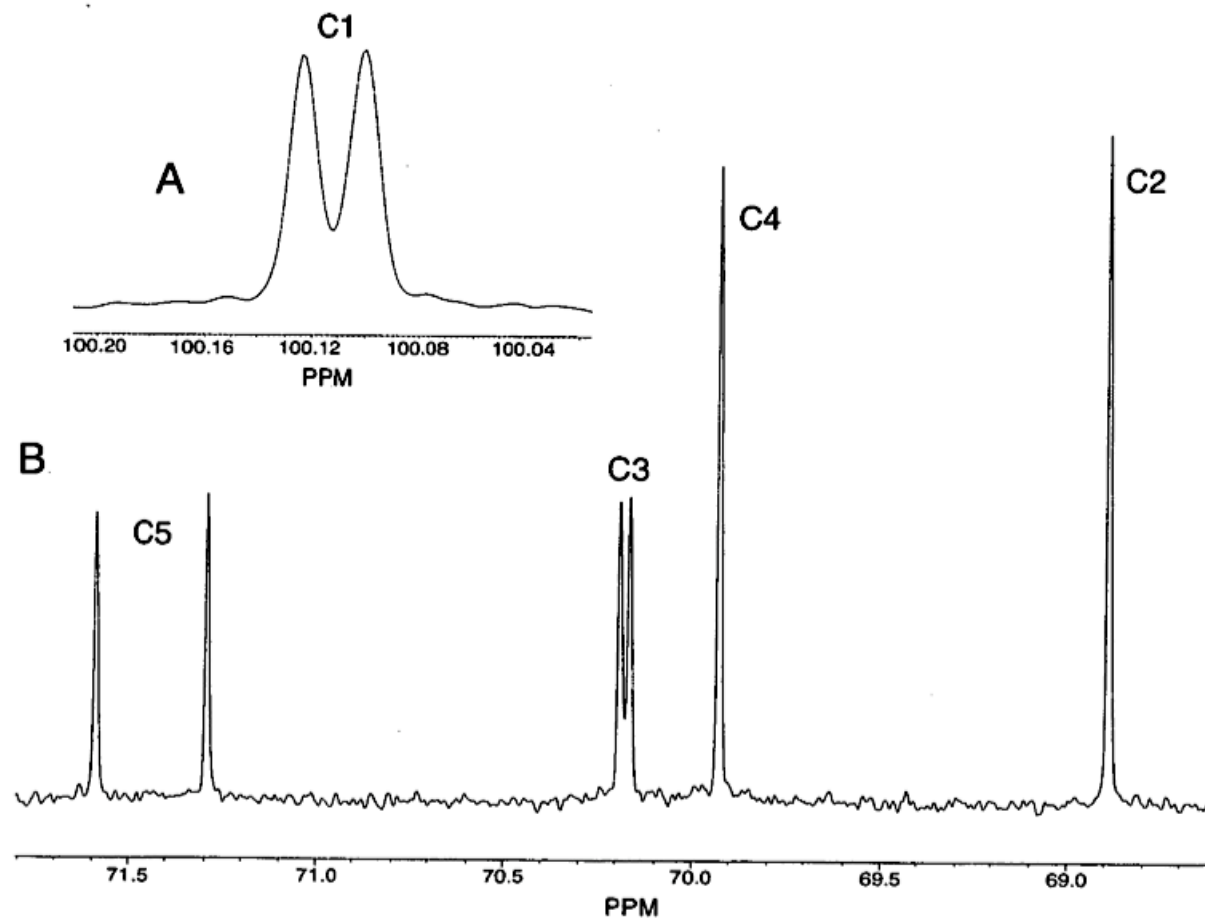


Figure 4.13. (S5) The 150-MHz $^{13}\text{C}\{^1\text{H}\}$ NMR spectrum of methyl α -D-[6- ^{13}C]galactopyranoside **3**, showing (A) $^3J_{\text{CC}}$ (to C1), $^1J_{\text{CC}}$ and $^3J_{\text{CC}}$ (B) and (to C5 and C3, respectively), and no coupling to C2 and C4. No splitting was observed in the aglycone methyl carbon signal (not shown). Only the natural abundance carbon signals are shown.

4.10. References

1. Bose, B.; Zhao, S.; Stenutz, R.; Cloran, F.; Bondo, P. B.; Bondo, G.; Hertz, B.; Carmichael, I.; Serianni, A. S. *J. Am. Chem. Soc.* **1998**, *120*, 11158-11173.
2. Cloran, F.; Carmichael, I.; Serianni, A. S. *J. Am. Chem. Soc.* **1999**, *121*, 9843-9851.
3. Church, T.; Carmichael, I.; Serianni, A. S. *Carbohydr. Res.* **1996**, *280*, 177-186.
4. Serianni, A. S.; Bondo, P. B.; Zajicek, J. *J. Magn. Reson., Ser. B* **1996**, *112*, 69-74.
5. Zhao, S.; Bondo, G.; Zajicek, J.; Serianni, A. S. *Carbohydr. Res.* **1998**, *309*, 145-152.
6. Stenutz, R.; Carmichael, I.; Widmalm, G.; Serianni, A. S. *J. Org. Chem.* **2002**, *67*, 949-958.
7. Serianni, A. S.; Cadman, E.; Pierce, J.; Hayes, M. L.; Barker, R. *Methods Enzymol.* **1982**, *89*, 83-92.
8. Serianni, A. S.; Vuorinen, T.; Bondo, P. *J. Carbohydr. Chem.* **1990**, *9*, 513-541.
9. Serianni, A. S.; Clark, E. L.; Barker, R. *Carbohydr. Res.* **1979**, *72*, 79-91.
10. Effenberger, F.; Straub, A. *Tetrahedron Lett.* **1987**, *28*, 1641-1644.
11. Angyal, S. J.; Bethell, G. S.; Beveridge, R. J. *Carbohydr. Res.* **1979**, *73*, 9-18.
12. King-Morris, M. J.; Bondo, P. B.; Mrowca, R. A.; Serianni, A. S. *Carbohydr. Res.* **1988**, *175*, 49-58.
13. Zhao, S. Personal communication.
14. Podlasek, C. A.; Wu, J.; Stripe, W. A.; Bondo, P.; Serianni, A. S. *J. Am. Chem. Soc.* **1995**, *117*, 8635-8644.
15. Austin, P. W.; Hardy, F. E.; Buchanan, J. C.; Baddiley, J. *J. Chem. Soc.* **1963**, 5350-5353.
16. Bock, K.; Pedersen, C. *Adv. Carbohydr. Chem. Biochem.* **1983**, *41*, 27-66.
17. Bonner, T. G. *Methods Carbohydr. Chem.* **1963**, *2*, 309-313.

18. *MacNUTs Pro*; Acorn NMR Inc.: Livermore, CA.
19. Becke, A. D. *J. Chem. Phys.* **1993**, *98*, 5648-5652.
20. Hehre, W. J.; Ditchfield, R.; Pople, J. A. *J. Chem. Phys.* **1972**, *56*, 2257-2261.
21. Frisch, M. J.; Trucks, G. W.; Schlegel, H. B.; Gill, P. M. W.; Johnson, B. G.; Robb, M. A.; Cheeseman, J. R.; Keith, T.; Petersson, G. A.; Montgomery, J. A.; Raghavachari, K.; AllLaham, M. A.; Zakrzewski, V. G.; Ortiz, J. V.; Foresman, J. B.; Peng, C. Y.; Ayala, P. Y.; Chen, W.; Wong, M. W.; Andres, J. L.; Replogle, E. S.; Gomperts, R.; Martin, R. L.; Fox, D. J.; Binkley, J. S.; Defrees, D. J.; Baker, J.; Stewart, J. P.; Head-Gordon, M.; Gonzalez, C.; Pople, J. A. *Gaussian94*; Gaussian, Inc.: Pittsburgh, PA, **1995**.
22. (a) Wolfe, S. *Acc. Chem. Res.* **1972**, *5*, 102-111. (b) Wiberg, K. B.; Murcko, M. A.; Laidig, K. E.; MacDougall, P. J. *J. Phys. Chem.* **1990**, *94*, 6956-6959. (c) Zefirov, N. S.; Samoshin, V. V.; Subbotin, O. A.; Baranenko, V. I.; Wolfe, S. *Tetrahedron* **1978**, *34*, 2953-2959.
23. (a) Bock, K.; Pedersen, C. *Acta Chem. Scand., Ser. B* **1977**, *B31*, 354-358. (b) Schwarcz, J. A.; Perlin, A. S. *Can. J. Chem.* **1972**, *50*, 3667-3676. (c) Schwarcz, J. A.; Cyr, N.; Perlin, A. S. *Can. J. Chem.* **1975**, *53*, 1872-1875. (d) Bandyopadhyay, T.; Wu, J.; Stripe, W. A.; Carmichael, I.; Serianni, A. S. *J. Am. Chem. Soc.* **1997**, *119*, 1737-1744. (e) Bandyopadhyay, T.; Wu, J.; Serianni, A. S. *J. Org. Chem.* **1993**, *58*, 5513-5517. (f) Church, T. J.; Carmichael, I.; Serianni, A. S. *J. Am. Chem. Soc.* **1997**, *119*, 8946-8964.
24. Cloran, F.; Carmichael, I.; Serianni, A. S. *J. Phys. Chem. A* **1999**, *103*, 3783-3795.
25. Cloran, F.; Carmichael, I.; Serianni, A. S. *J. Am. Chem. Soc.* **2001**, *123*, 4781-4791.
26. (a) Serianni, A. S.; Podlasek, C. A. *Carbohydr. Res.* **1994**, *259*, 277-282. (b) Marino, J. P.; Schwalbe, H.; Glaser, S. J.; Griesinger, C. *J. Am. Chem. Soc.* **1996**, *118*, 4388-4395.
27. Cloran, F.; Zhu, Y.; Osborn, J.; Carmichael, I.; Serianni, A. S. *J. Am. Chem. Soc.* **2000**, *122*, 6435-6448.
28. Serianni, A. S.; Wu, J.; Carmichael, I. *J. Am. Chem. Soc.* **1995**, *117*, 8645-8650.
29. Maciel, G. E.; McIver, J. W.; Ostlund, N. S.; Pople, J. A. *J. Am. Chem. Soc.* **1970**, *92*, 4151-4157.
30. (a) Hayes, M. L.; Serianni, A. S.; Barker, R. *Carbohydr. Res.* **1982**, *100*, 87-101. (b) Morat, C.; Tavel, F. R.; Vignon, M. R. *Magn. Reson. Chem.* **1988**, *26*, 264-

270. (c) Poppe, L.; Struik-Prill, R.; Meyer, B.; van Halbeek, H. *J. Biomol. NMR* **1992**, *2*, 109-136. (d) Poppe, L. *J. Am. Chem. Soc.* **1993**, *115*, 8421-8426.
31. Tvaroska, I.; Gadjos, J. *Carbohydr. Res.* **1995**, *271*, 151-162.
32. Tvaroska, I.; Taravel, F. R.; Utille, J. P.; Carver, J. P. *Carbohydr. Res.* **2002**, *337*, 353-367.
33. Donders, L. A.; de Leeuw, F. A. A. M.; Altona, C. *Magn. Reson. Chem.* **1989**, *27*, 556-563.
34. Carmichael, I.; Chipman, D. M.; Podlasek, C. A.; Serianni, A. S. *J. Am. Chem. Soc.* **1993**, *115*, 10863-10870.
35. (a) Wu, J.; Bondo, P. B.; Vuorinen, T.; Serianni, A. S. *J. Am. Chem. Soc.* **1992**, *114*, 3499-3505. (b) King-Morris, M. J.; Serianni, A. S. *J. Am. Chem. Soc.* **1987**, *109*, 3501-3508.
36. (a) Ohrui, H.; Nishida, Y.; Higuchi, H.; Hori, H.; Meguro, H. *Can. J. Chem.* **1987**, *65*, 1145-1153. (b) Ohrui, H.; Nishida, Y.; Meguro, H. *Agric. Biol. Chem.* **1984**, *48*, 1049-1053. (c) Hori, H.; Nakajima, Y.; Nishida, H.; Ohrui, H.; Meguro, H. *J. Carbohydr. Chem.* **1986**, *5*, 585-600.
37. Bose-Basu, B.; Zajicek, J.; Bondo, G.; Zhao, S.; Kubsch, M.; Carmichael, I.; Serianni, A. S. *J. Magn. Res.* **2000**, *144*, 207-216.
38. (a) Marchessault, R. H.; Perez, S. *Biopolymers* **1979**, *18*, 2369-2374. (b) Rockwell, G. D.; Grindley, T. B. *J. Am. Chem. Soc.* **1998**, *120*, 10953-10963. (c) Kuttel, M.; Brady, J. W.; Naidoo, K. J. *J. Comput. Chem.* **2002**, *23*, 1236-1243. (d) Behrends, R.; Cowman, M. K.; Eggers, F.; Eyring, E. M.; Kaatze, U.; Majewski, J.; Petrucci, S.; Richmann, K.-H.; Riech, M. *J. Am. Chem. Soc.* **1997**, *119*, 2182-2186.
39. (a) Bock, K.; Duus, J. O. *J. Carbohydr. Chem.* **1994**, *13*, 513-543. (b) Nishida, Y.; Hori, H.; Ohrui, H.; Meguro, H. *J. Carbohydr. Chem.* **1988**, *7*, 239-250.
40. Fraser, R. R.; Kaufman, M.; Morand, P.; Govil, G. *Can. J. Chem.* **1969**, *47*, 403-409.
41. (a) Houseknecht, J. B.; McCarren, P. R.; Lowary, T. L.; Hadad, C. M. *J. Am. Chem. Soc.* **2001**, *123*, 8811-8824. (b) Houseknecht, J. B.; Lowary, T. L.; Hadad, C. M. *J. Phys. Chem. A* **2003**, *107*, 372-378.
42. Dais, P.; Perlin, A. S. *Can. J. Chem.* **1982**, *60*, 1648-1656.

43. (a) Dzakula, Z.; Westler, W. M.; Edison, A. S.; Markley, J. L. *J. Am. Chem. Soc.* **1992**, *114*, 4, 6195-6199. (b) Dzakula, Z.; Edison, A. S.; Westler, W. M.; Markley, J. L. *J. Am. Chem. Soc.* **1992**, *114*, 6200-6207.
44. (a) Serianni, A. S.; Bondo, P. B.; Zajicek, J. *J. Magn. Reson.* **1996**, *112B*, 69-74. (b) Zhao, S.; Bondo, G.; Zajicek, J.; Serianni, A. S. *Carbohydr. Res.* **1998**, *309*, 145-152.

CHAPTER 5:

GEMINAL $^2J_{\text{CCH}}$ SPIN-SPIN COUPLING CONSTANTS AS PROBES OF THE ϕ
GLYCOSIDIC TORSION ANGLE IN OLIGOSACCHARIDES⁴

“Change starts when someone sees the next step..”

– William Drayton

5.1. Abstract

Two-bond ^{13}C - ^1H NMR spin-spin coupling constants ($^2J_{\text{CCH}}$) between C2 and H1 of aldopyranosyl rings have been shown to depend not only on the relative orientation of electronegative substituents on the C1-C2 fragment but also on the C-O torsions involving the same carbons. The latter dependencies were elucidated theoretically using density functional theory and appropriate model pyranosyl rings representing the four relative configurations at C1 and C2, and a 2-deoxy derivative, to probe the relationship between $^2J_{\text{C2,H1}}$ magnitude and sign and the C1-O1 (ϕ , ϕ) and C2-O2 (α) torsion angles. Related calculations were also conducted for the reverse coupling pathway, $^2J_{\text{C1,H2}}$. Computed J -couplings were validated by comparison to experimentally

⁴ I gratefully acknowledge my co-authors Ian Carmichael and Anthony S. Serianni for their assistance in preparing this chapter, which is submitted to the Journal of the American Chemical Society.

measured couplings. The results show that $^2J_{\text{CCH}}$ displays a primary dependence on the C-O torsion involving the carbon bearing the coupled proton, and a secondary dependence on the C-O torsion involving the coupled carbon. These dependencies appear to be caused mainly by the effects of oxygen lone-pairs on the C-H and C-C bond lengths along the C-C-H coupling pathway. New parameterized equations are proposed to interpret $^2J_{\text{C1,H2}}$ and $^2J_{\text{C2,H1}}$ in aldopyranosyl rings. The equation for $^2J_{\text{C2,H1}}$ has particular value as a potential NMR structure constraint for the C1-O1 torsion angle (ϕ) comprising the glycosidic linkages of oligosaccharides.

5.2. Introduction

Heteronuclear vicinal (three-bond) ^{13}C - ^1H spin-spin coupling constants ($^3J_{\text{CCCH}}$ and $^3J_{\text{COCH}}$) are finding increased use as structure constraints in the conformational analysis of saccharides in solution due to their expected Karplus-like dependencies.¹⁻⁵ In contrast, geminal (two-bond) ^{13}C - ^1H J -couplings ($^2J_{\text{CCH}}$) are less appreciated, although qualitative rules governing their dependencies on saccharide structure have been reported based on patterns of electronegative atom substitution in the C-C-H fragment.⁶⁻⁸ Two key differences distinguish the C-C torsional dependencies of $^2J_{\text{CCH}}$ and $^3J_{\text{CCCH}}$. The 2J dependencies are unimodal whereas the 3J dependencies are bimodal; one minimum and one maximum are observed in plots of $^2J_{\text{CCH}}$ vs C-C torsion compared to two minima and two maxima in plots of $^3J_{\text{CCCH}}$ vs C-C torsion. This difference confers advantages to $^2J_{\text{CCH}}$ since a reduced number of potential conformers exist that correspond to a particular coupling, thus potentially improving conformational analyses, especially in

flexible systems. In saccharides, $^2J_{\text{CCH}}$ can be positive or negative in sign, often changing sign within a given torsional regime, whereas the signs of $^3J_{\text{CCCH}}/^3J_{\text{COCH}}$ are always positive. Thus, if signs are taken into account, comparable dynamic ranges (~ 8 Hz) are observed for both types of coupling.

Recent studies of exocyclic hydroxymethyl group (CH_2OH) conformation in this laboratory have described the effect of C-C and C-O bond rotation on $^2J_{\text{CCH}}$ in saccharides.⁹ In addition to their expected unimodal dependence on ω (O5-C5-C6-O6 torsion), $^2J_{\text{C5,H6R}}$ and $^2J_{\text{C5,H6S}}$ were found to exhibit significant secondary dependencies on θ (C5-C6-O6-OH6 torsion) (Figure 5.1) (Scheme 5.1, structure **I**) (*i.e.*, rotation of the C-O bond on the carbon bearing the coupled proton influenced $^2J_{\text{CCH}}$ significantly). The latter dependence is probably caused in part by changes in C6-H6R/S bond lengths induced by specific dispositions of the O6 lone pairs (*i.e.*, rotation of the C6-O6 bond modulates the syn/anti orientation of lone pairs with respect to these C-H bonds, with anti orientations elongating the bonds).¹⁰ Other studies have shown⁹ that rotation of the C-O bond on the *coupled carbon* exerts a smaller effect on $^2J_{\text{CCH}}$. These C-O torsional effects are generalized in Scheme 5.1 (structure **II**; C-C-H coupling pathway shown in bold); $^2J_{\text{CCH}}$ displays a primary dependence on a C-O rotamer if the oxygen of that rotamer is geminal to the coupled proton (β rotation), and a secondary dependence on a C-O rotamer if the carbon of that rotamer is the coupled carbon (α rotation).

Armed with these results and arguing by analogy, we posed the question addressed in this report, namely, might $^2J_{\text{CCH}}$ serve as a probe of the phi (ϕ) glycosidic

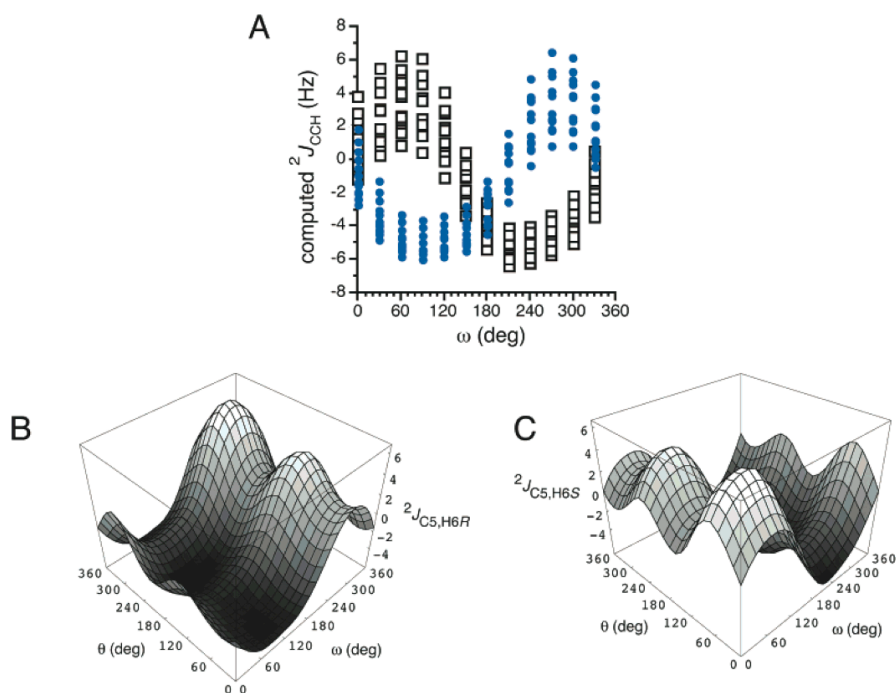
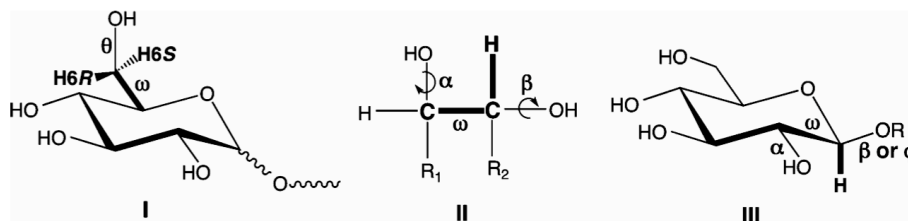
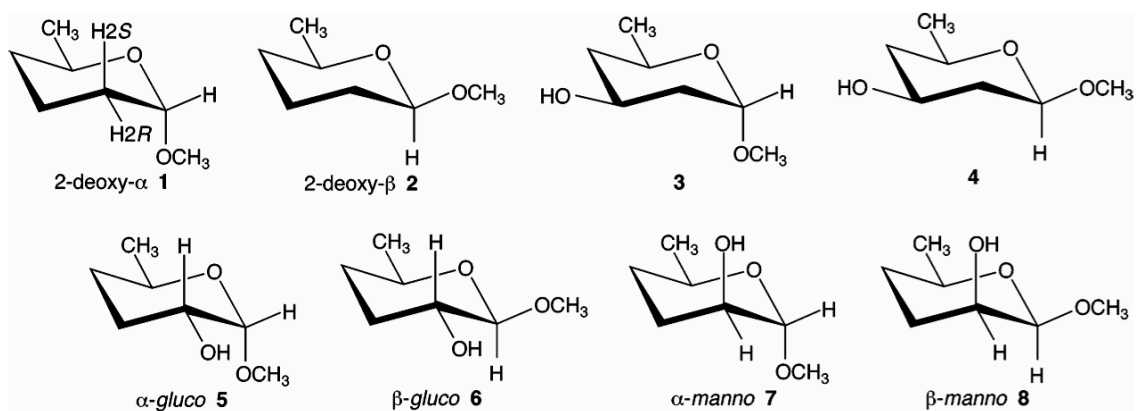


Figure 5.1. (A) Plot of computed $^2J_{\text{C5,H6R}}$ and $^2J_{\text{C5,H6S}}$ in **I** (Scheme 5.1) as a function of ω (defined as the O5-C5-C6-O6 torsion angle). The scatter of points at discrete values of ω is caused by the effect of θ (defined as the C5-C6-O6-H torsion angle). Note the unimodal behavior with respect to ω . Closed blue circles, $^2J_{\text{C5,H6R}}$; open black squares, $^2J_{\text{C5,H6S}}$. (B) Hypersurface showing the effect of ω and θ on $^2J_{\text{C5,H6R}}$ in **I**. (C) Hypersurface showing the effect of ω and θ on $^2J_{\text{C5,H6S}}$ in **I**. Data taken from ref 9.



Scheme 5.1. Rotamer Definitions

torsion angle in oligosaccharides (Scheme 5.1, structure **III**; C-C-H coupling pathway indicated in blue)? In this case, contributions from ω can be ignored because the C1-C2 bond torsion is constrained by the ring, leaving $^2J_{C2,H1}$ affected by α (C2-O2 bond torsion) and β/ϕ rotations (C1-O1 bond torsion). Note that ϕ and β are redundant. We investigated this possibility by conducting density functional theory (DFT) calculations on model structures **1-8** (Scheme 5.2) designed to capture the effect of C1 and C2 structure and configuration on $^2J_{C2,H1}$ magnitude and sign. As a control, we also studied the reverse coupling pathway, $^2J_{C1,H2}$, in the same structures. Computed couplings were validated by comparison to experimental $^2J_{C1,H2}$ and $^2J_{C2,H1}$ in aldopyranosyl rings having different structures and configurations. We show herein that $^2J_{C2,H1}$ values display a significant and systematic dependence on ϕ in glycosides regardless of the relative configuration at C1 and C2 of the aldopyranosyl ring. These findings have important implications for conformational studies of the glycosidic and non-glycosidic C-O torsion angles of saccharides in solution.



Scheme 5.2. Model Compound Structures **1-8**

5.3. Computations

Geometry optimizations were conducted as a function of varying only ϕ (defined as the O5-C1-O1-CH₃ torsion angle) in **1-4**, or both ϕ and α (defined as the C1-C2-O2-H torsion angle) in **5-8**, in 30° increments over the range 0-360°, yielding 12 structures for **1-4** and 144 structures for **5-8**. Geometry optimizations using DFT were performed using the B3LYP hybrid functional¹¹ and the 6-31G* basis set¹² within *Gaussian98*.^{13a} Coupling constants, $^2J_{\text{C1,H2}}$ and $^2J_{\text{C2,H1}}$, were computed as described previously⁵ using the standard B3LYP functional, finite-field perturbation theory implemented within *Gaussian94*^{13b}, and an extended basis set ([5s2p1d|3s1p])^{10a} designed to reliably recover the Fermi contact contribution to the coupling. Equations describing the dependencies of both J -couplings on ϕ and/or α were parameterized using the least-squares Monte Carlo fitting module within *ProFit 5.6.2* (Quantum Soft, Zürich, Switzerland).

A series of geometry optimizations and J -coupling calculations was also conducted on **5-8** in which $r_{\text{C1,H1}}$, $r_{\text{C2,H2}}$ or $r_{\text{C1,C2}}$ were varied in 0.001 Å increments about the respective average optimized bond length observed in the above ϕ/α hypersurfaces, covering an overall range of ~0.02 Å. In these calculations, ϕ and α were held constant at values observed in the lowest energy structures of the total energy hypersurface (ϕ/α for **5**, 60°/-60°; for **6**, -60°/60°; for **7**, 60°/60°; for **8**, -60°/-60°; see below). These calculations were performed to evaluate the effect of these bond lengths on $^1J_{\text{CH}}$ and $^2J_{\text{CCH}}$ values; all other molecular parameters in the structures were geometrically optimized, although the induced changes in a given bond length affected

these optimized parameters minimally (*e.g.*, changing $r_{\text{C1,H1}}$ exerted little effect on other nearby or remote bond lengths or angles).

5.4. Results and Discussion

5.4.1. Energetics

The effect of C1-O1 bond rotation (ϕ) on the total energies E of **1** and **2** is shown in Figure 5.2. For **1**, $E_{\phi\ 60^\circ} < E_{\phi\ 180^\circ} < E_{\phi\ -60^\circ}$, whereas for **2**, $E_{\phi\ -60^\circ} < E_{\phi\ 60^\circ} < E_{\phi\ 180^\circ}$. In both cases, the most stable ϕ rotamer orients the aglycone methyl carbon *anti* to C2, as predicted by the exoanomeric effect.¹⁴ The relative stabilities of the remaining two ϕ rotamers are reversed in **1** and **2**, behavior presumably caused by a combination of stereoelectronic and steric effects. In **1**, $\phi = -60^\circ$ is destabilized for steric reasons (the aglycone is oriented below the ring), while in **2**, $\phi = 180^\circ$ is destabilized by eclipsed lone-pair interactions between O1 and O5. Curve amplitude for **1** appears slightly greater than that for **2**, suggesting greater ϕ flexibility in **2**. Since **1** and **2** lack a C2 hydroxyl group, potential effects caused by C2 substitution are absent.

The effect of C2-O2 bond rotation (α) on the relative energies of ϕ rotamers in **5-8** is shown in Figure 5.3. For a specific ϕ torsion, variations in E caused by 360° α rotations vary from 3-6 kcal/mol, and the magnitude of variation depends somewhat on ϕ . Consideration of only perfectly staggered α rotamers yields a more limited variation and the emergence of a lowest energy pathway for ϕ rotation in **5-8**. In **5**, $E_{\phi\ 60^\circ} < E_{\phi\ 180^\circ} <$

$E_{\phi -60^\circ}$, whereas in **6**, $E_{\phi -60^\circ} < E_{\phi 60^\circ} < E_{\phi 180^\circ}$. These trends mimic those observed in **1** and **2**, respectively, although curve amplitude is slightly greater in **5** and **6**.

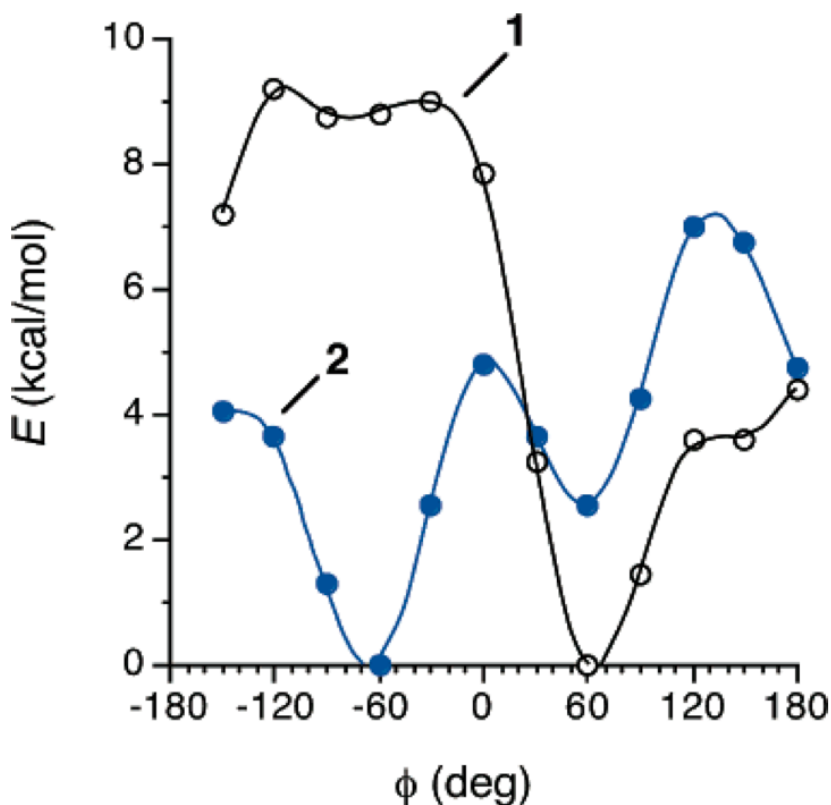


Figure 5.2. Plot showing the effect of ϕ on the calculated total energy E of **1** and **2** determined by DFT (B3LPY/6-31G*, in vacuo).

Data for **7** and **8** are similar to those for **5** and **6** (Figure 5.3C,D). Interestingly, α rotation (staggered rotamers only) in **8** appears to affect E more significantly than observed for **5-7**. As observed in **5** and **6**, the relative energies of the lowest energy pathways for **7** and **8** are similar to those observed in **1** and **2**, respectively; curve amplitudes for **2** and **8** are virtually identical. Importantly, correlations between ϕ and E in **5-8** appear similar for each of the three staggered α rotamers (the curves are y -shifted but otherwise similar in shape).

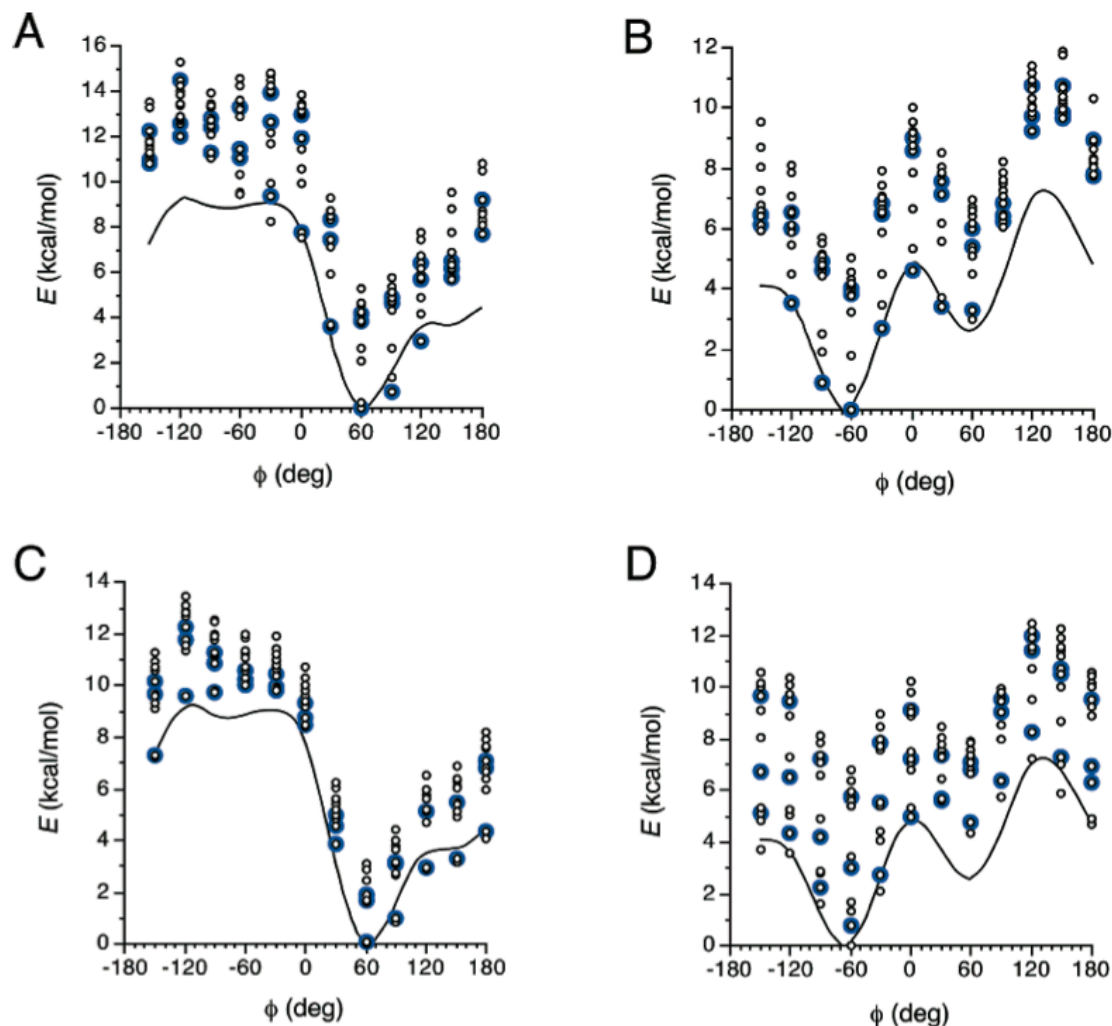


Figure 5.3. Plots showing the effect of ϕ on the calculated total energy E of **5** (A), **6** (B), **7** (C), and **8** (D) determined by DFT (B3LYP/6-31G*, in vacuo). The scatter of points at discrete values of ϕ is caused by the effect of α ; data points in blue are for perfectly staggered values of α . Superimposed on each plot is the corresponding curve derived from either **1** (A and C) or **2** (B and D).

Correlations between ϕ , α and E in **5-8** were also inspected in plots of E vs α (Figure 5.4). Scatter is greater than observed in Figure 5.3 since ϕ rotation causes a greater change in E than does α rotation. If only staggered ϕ rotamers are considered,

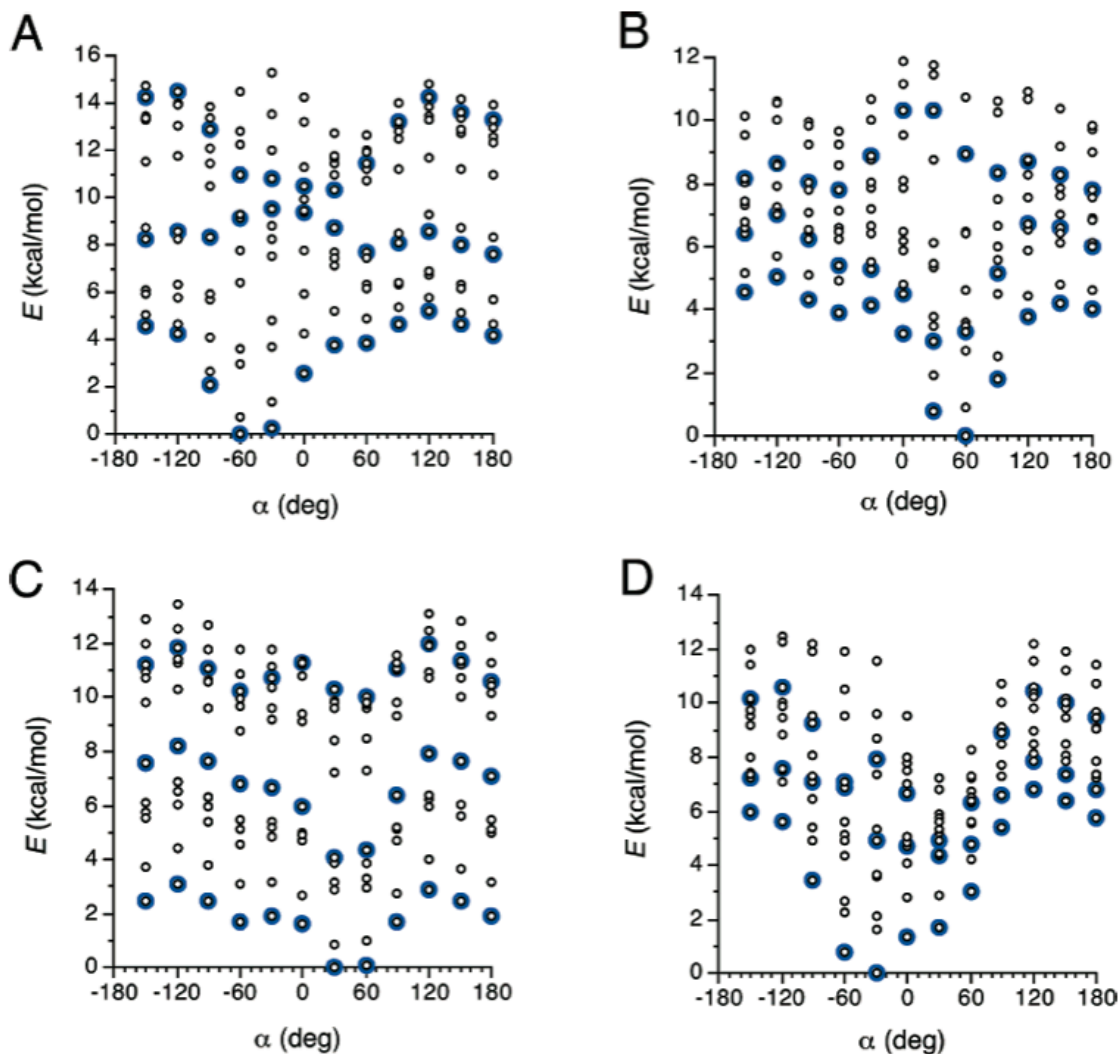


Figure 5.4. Plots showing the effect of α on the calculated total energy E of **5** (A), **6** (B), **7** (C), and **8** (D) determined by DFT (B3LYP/6-31G*, in vacuo). The scatter of points at discrete values of α is caused by the effect of ϕ ; data points in blue are for perfectly staggered values of ϕ .

minimal energy pathways emerge. Interestingly, the three curves for each structure are not only y -shifted, but also change in shape in some cases (*i.e.*, the influence of α on E depends on the value of ϕ due to H-bonding between O1H and O2H). From these data, the most stable ϕ/α combinations in **5-8** were identified as follows: **5**, 60°/-60°; **6**, -60°/60°; **7**, 60°/60°; **8**, -60°/-60°. Not unexpectedly, these conformers are characterized

by the presence of intramolecular hydrogen bonding, which in gas phase calculations confers differential stability to conformers that contain them. Whether these ϕ/α combinations are indeed the most populated states in aqueous solution is an interesting question but one of peripheral importance to the present work, provided that the presence of H-bonding in some structures does not adversely affect the parameterization of $^2J_{\text{CCH}}$ equations. The latter issue is discussed further below. Contour plots of populations computed from the data in Figures 5.3 and 5.4 are provided in Supporting Information (Figure S1). If an arbitrary 2 kcal/mol cutoff is applied, data in Figure 5.4 indicate that **7** experiences greater variability in the preferred C2-O2 torsion at the most stable C1-O1 torsion than **5**, **6** and **8** (*i.e.*, C2-O2 torsions of 60° and -60° are within 2 kcal/mol in this structure). The reduced interactions between O1 and O2 in **7** caused by their *trans* relationship apparently leads to this greater flexibility.

5.4.2. $^2J_{\text{CCH}}$ Spin-Couplings in **1-4**

$^2J_{\text{C1,H2R}}$ and $^2J_{\text{C1,H2S}}$ in **1** and **2** were calculated as a function of ϕ , and potential effects of oxygen substitution at C3 were inspected from similar calculations conducted on **3** and **4** (Figure 5.5). Adding an equatorial oxygen at C3 causes only a minor change (< 0.2 Hz) in $^2J_{\text{C1,H2R/S}}^{15}$ and $^2J_{\text{C2,H1}}$, and overall shape is conserved. Although not studied explicitly, similar results are expected for an axial O3.

Calculated $^2J_{\text{C1,H2R}}$ and $^2J_{\text{C1,H2S}}$ are similar in magnitude in **1/3** (0 - -3.5 Hz) (Fig. 5A), and change by ~ 2 Hz upon 360° rotation about ϕ . In contrast, $^2J_{\text{C1,H2R}}$ (-1.4 - -2.4 Hz) (Fig. 5B) and $^2J_{\text{C1,H2S}}$ (-6.6 - -7.6 Hz) (Fig. 5C) differ significantly in **2/4**, and change by ~ 1 Hz upon 360° rotation about ϕ . $^2J_{\text{C1,H2R/S}}/\phi$ curves for **1/2** and **2/4** appear approximately unimodal.

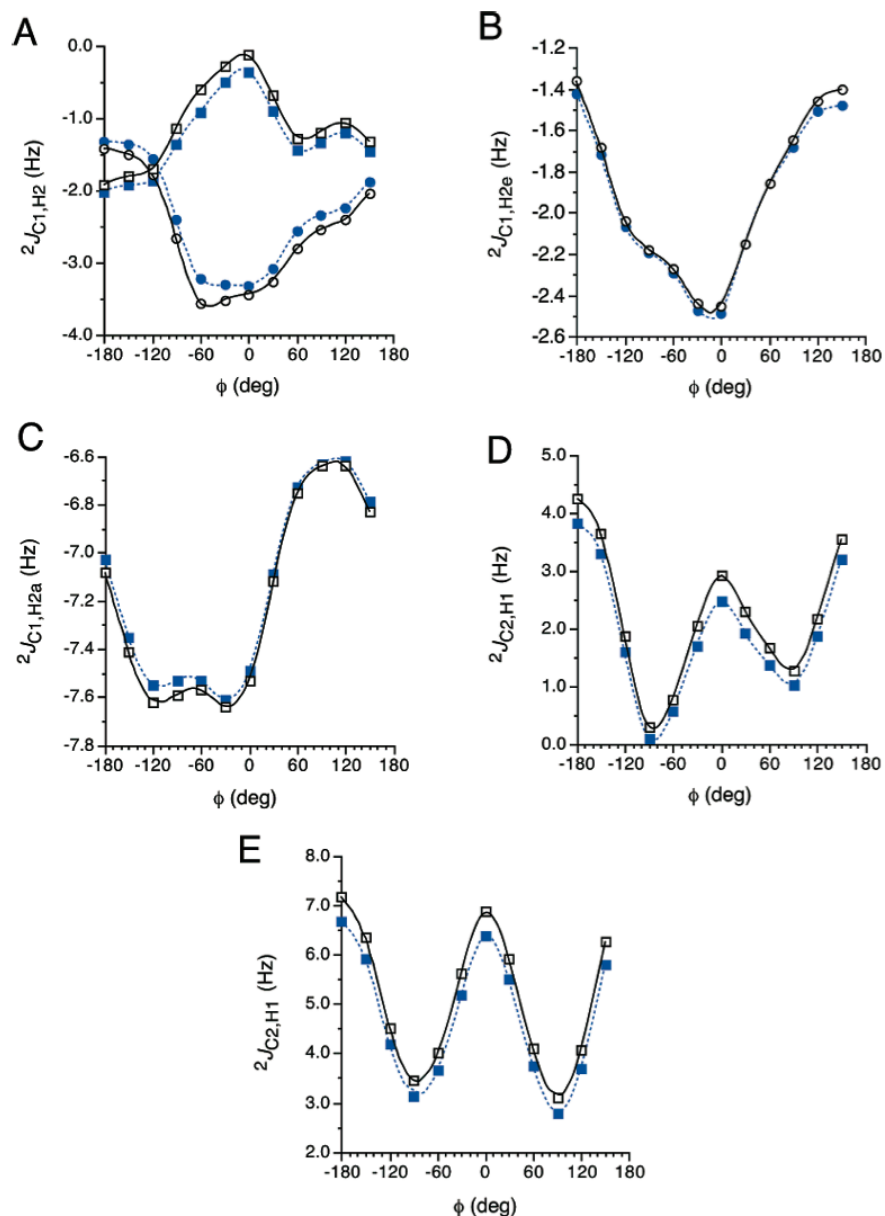


Figure 5.5. (A) Correlations between ${}^2J_{C1,H2}$ and ϕ in **1** (open symbols) and **3** (closed blue symbols). Squares, ${}^2J_{C1,H2a}$; circles, ${}^2J_{C1,H2e}$ ($H2a = H2S$; $H2e = H2R$; see Scheme 5.2). (B) Correlations between ${}^2J_{C1,H2e}$ and ϕ in **2** (open circles) and **4** (closed blue circles). (C) Correlations between ${}^2J_{C1,H2a}$ and ϕ in **2** (open squares) and **4** (closed blue squares). (D) Correlations between ${}^2J_{C2,H1}$ and ϕ in **1** (open squares) and **3** (closed blue squares). (E) Correlations between ${}^2J_{C2,H1}$ and ϕ in **2** (open squares) and **4** (closed blue squares).

Calculated ${}^2J_{C2,H1}$ in **1**/**3** and **2**/**4** change significantly upon 360° rotation about ϕ (~4 Hz) (Fig. 5D,E). In both anomeric configurations, the calculated coupling is positive in sign, with the coupling being more positive (3-7 Hz) in **2**/**4** than in **1**/**3** (0-4 Hz). In contrast to ${}^2J_{C1,H2R/S}$, ${}^2J_{C2,H1}/\phi$ curves are bimodal.

Calculated ${}^2J_{CCH}$ values were compared to experimental couplings measured in methyl 2-deoxy- α - (**9**) and 2-deoxy- β -D-*arabino*-hexopyranoses (**10**) (Scheme 5.3).¹⁶ Overall trends are maintained in the calculated and experimental couplings, but absolute magnitudes show some differences. The latter deviations are attributed to ring substitution effects, limitations in the methodology used to calculate the couplings, and/or effects of solution averaging and solvation on the experimental couplings.

Bond lengths in the vicinity of the anomeric carbons of **1** and **2** were examined as a function of ϕ . As expected from stereoelectronic considerations,¹⁷ $r_{C1,O1}$ and $r_{C1,O5}$ exhibit complementary behavior, with the former and latter showing two minima and maxima, respectively, at $\phi = \sim 60^\circ$ and $\sim -60^\circ$ (Figure 5.6). The general behavior of $r_{C1,O5}$ is very similar in **1** and **2**, whereas the global minimum for $r_{C1,O1}$ shifts from $\phi = \sim 60^\circ$ in **1** to $\phi = \sim -60^\circ$ in **2**. This shift is coincident with the shift in the global energy minimum from **1** to **2** (Figure 5.2). The exocyclic C1-O1 bond length depends on bond orientation, with the equatorial orientation in **2** exhibiting substantially shorter bond lengths. In contrast, $r_{C1,O5}$ is slightly larger in **2** than in **1**.

Bond lengths $r_{C1,H1}$ and $r_{C1,C2}$ exhibit two minima upon rotation of ϕ through 360° (Figure 5.7), as observed for $r_{C1,O1}$ and $r_{C1,O5}$. In the most stable conformers of **1** and **2**, $r_{C1,O1}$ and $r_{C1,C2}$ are minimal (or near minimal), whereas $r_{C1,H1}$ and $r_{C1,O5}$ are maximal (or near maximal). The magnitude of ${}^2J_{C2,H1}$ in **1** and **2** approximately tracks r_{C1-H1} , with shorter bonds correlating with less positive (more negative) couplings (Figure 5.8). The correlation, however, is imperfect in that the curves are slightly phase-

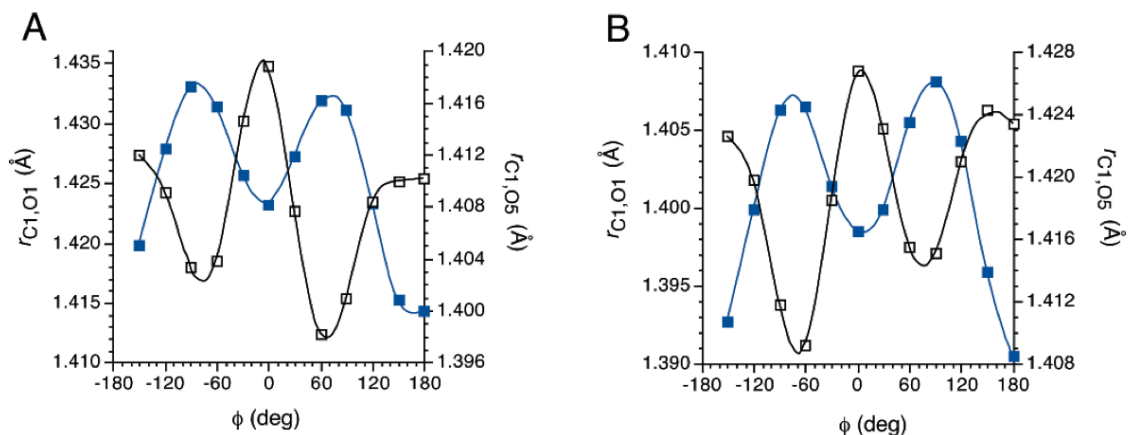


Figure 5.6. (A) Effect of ϕ on $r_{C1,O1}$ (open squares) and $r_{C1,O5}$ (closed blue squares) in **1**. (B) Effect of ϕ on $r_{C1,O1}$ (open squares) and $r_{C1,O5}$ (closed blue squares) in **2**.

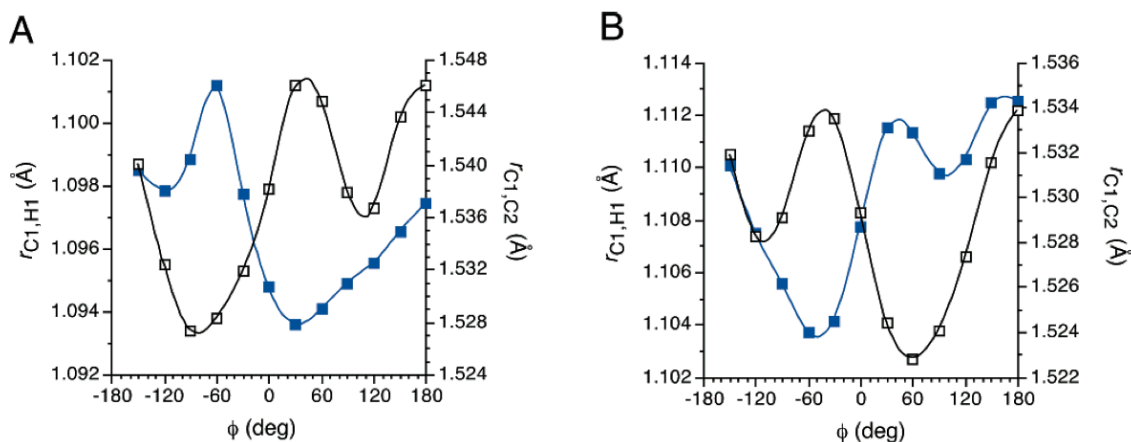
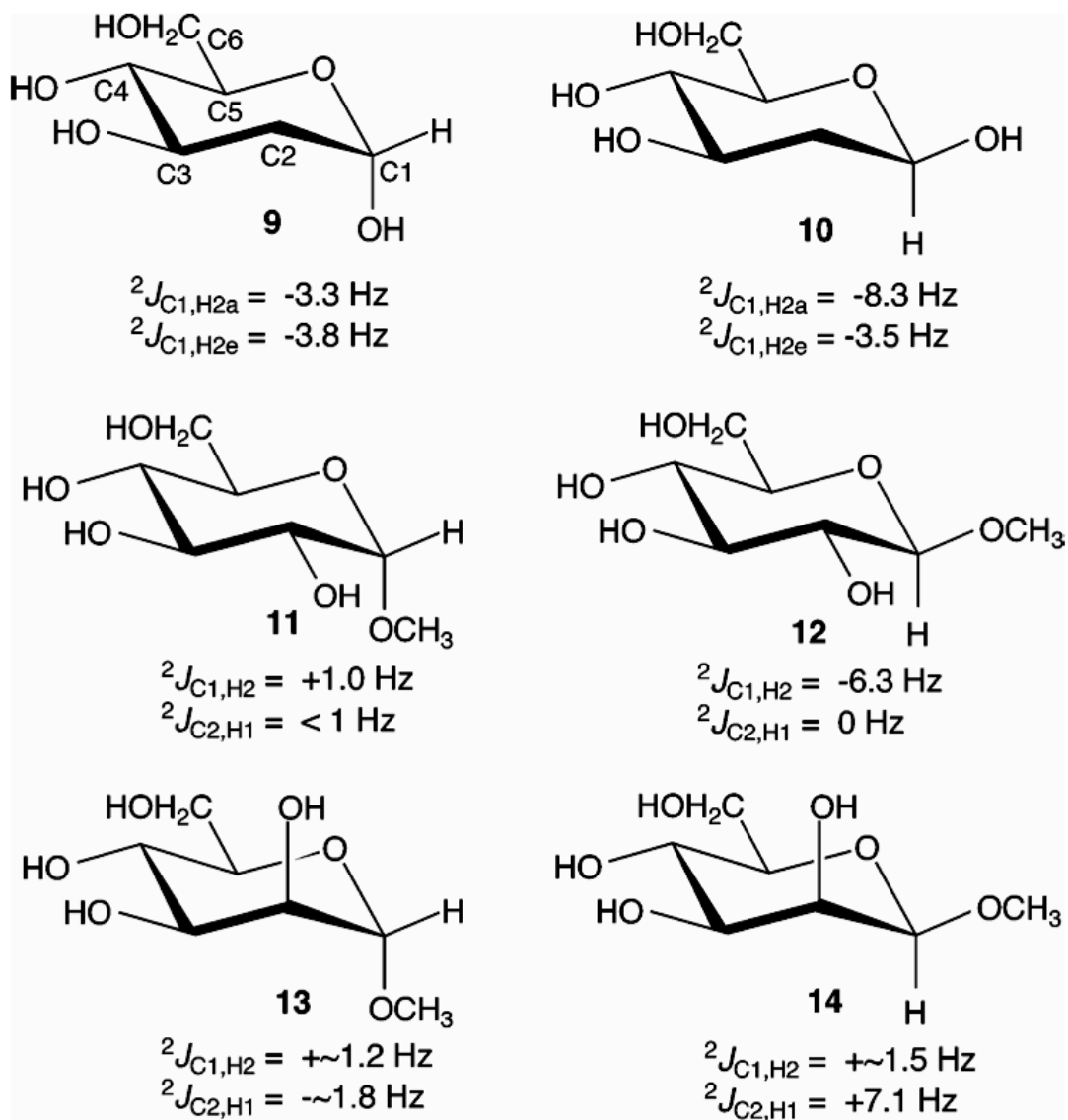


Figure 5.7. (A) Effect of ϕ on $r_{C1,H1}$ (open squares) and $r_{C1,C2}$ (closed blue squares) in **1**. (B) Effect of ϕ on $r_{C1,H1}$ (open squares) and $r_{C1,C2}$ (closed blue squares) in **2**.

shifted. This deviation apparently stems from the superimposed effects of r_{CH} and r_{CC} on ${}^2J_{CCH}$ (see below). In **2**, for example, the reduced ${}^2J_{C2,H1}$ at $\phi = -60^\circ$ is caused by a smaller $r_{C1,C2}$ in this geometry (Figure 5.7), which shifts the J -coupling to more negative (less positive) values, as does a reduction in $r_{C1,H1}$. All of these effects are observed in

the absence of an oxygen substituent at C2, which permits the isolation of energetic, structural and J -coupling effects caused solely by ϕ rotation.



Scheme 5.3. Experimental $^2J_{C1,H2}$ and $^2J_{C2,H1}$ in 9-14

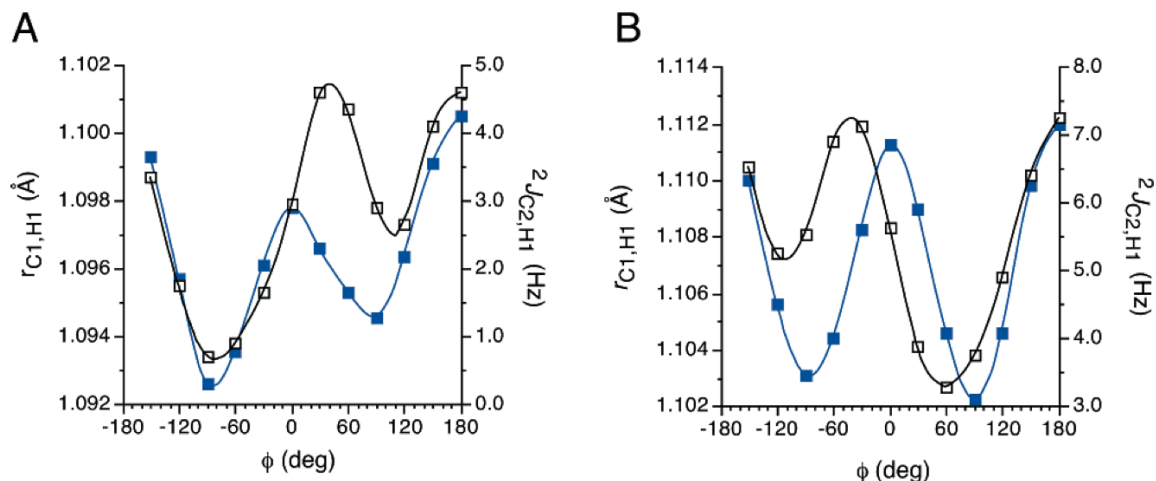


Figure 5.8. (A) Effect of ϕ on $r_{C1,H1}$ (open squares) and $^2J_{C2,H1}$ (closed squares) in **1**. (B) Effect of ϕ on $r_{C1,H1}$ (open squares) and $^2J_{C2,H1}$ (closed squares) in **2**.

5.4.3. $^2J_{CCH}$ Spin-Couplings in **5-8**

The effects of ϕ and α on computed $^2J_{C1,H2}$ and $^2J_{C2,H1}$ in **5-8** are shown in Figures 5.9-12. Computed $^2J_{C1,H2}$ display a bimodal dependence on α , with minima at $\sim 30^\circ$ and $\sim 150^\circ$, and maxima at $\sim 120^\circ$ and $\sim 60^\circ$ for **5** and **6** (Figures 5.9A and 5.10A) and with minima at $\sim 150^\circ$ and $\sim 30^\circ$, and maxima at $\sim 60^\circ$ and $\sim 120^\circ$ for **7** and **8** (Figures 5.11A and 5.12A). Absolute couplings depend on ring configuration; for **5**, -2 - 6 Hz; for **6**, -7 - -3 Hz; for **7**, -3 - 4 Hz; for **8**, -2 - 3 Hz. A comparison of computed couplings to experimental values¹⁸ in methyl glycosides **11-14** (Scheme 5.3) shows generally good agreement. Changes in ϕ do not affect the shape of the curves correlating $^2J_{C1,H2}$ to α (the curves are essentially y-shifted).

$^2J_{C1,H2}$ in **5-8** is much less affected by ϕ than by α (Figures 5.9-12, panels A and B) (Scheme 5.1; structure **III**). Consistent with this observation is that $^2J_{C2,H1}$ is

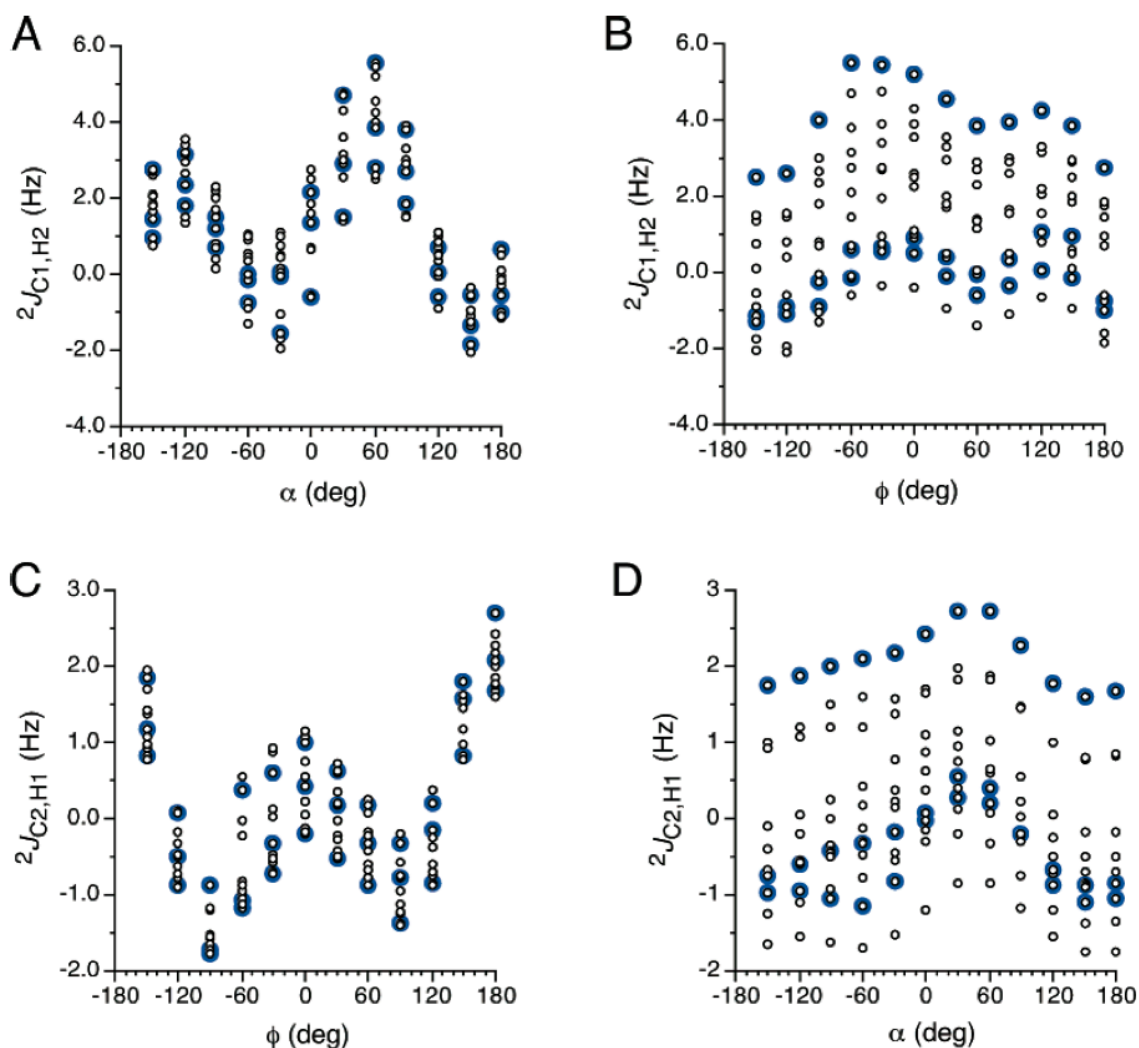


Figure 5.9. (A) Effect of α on $^2J_{C1,H2}$ in **5**. Point scatter at discrete values of α is due to the effect of ϕ ; highlighted points (open blue circles) are for perfectly staggered values of ϕ . (B) Effect of ϕ on $^2J_{C1,H2}$ in **5**. Point scatter at discrete values of ϕ is due to the effect of α ; highlighted points (open blue circles) are for perfectly staggered values of α . (C) Effect of ϕ on $^2J_{C2,H1}$ in **5**. Point scatter at discrete values of ϕ is due to the effect of α ; highlighted points (open blue circles) are for perfectly staggered values of α . (D) Effect of α on $^2J_{C2,H1}$ in **5**. Point scatter at discrete values of α is due to the effect of ϕ ; highlighted points (open blue circles) are for perfectly staggered values of ϕ .

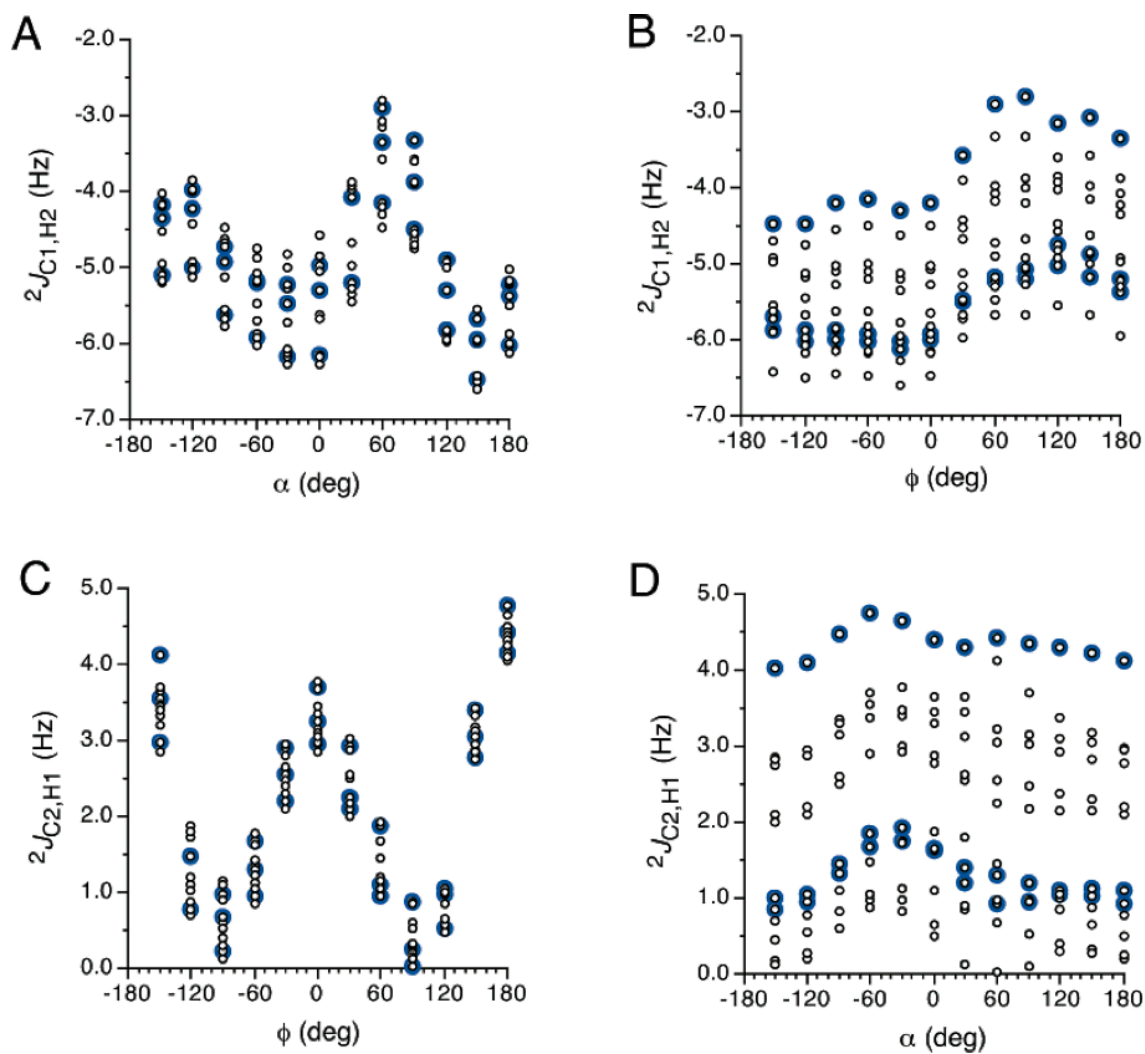


Figure 5.10. Same data as in Figure 5.9 for 6.

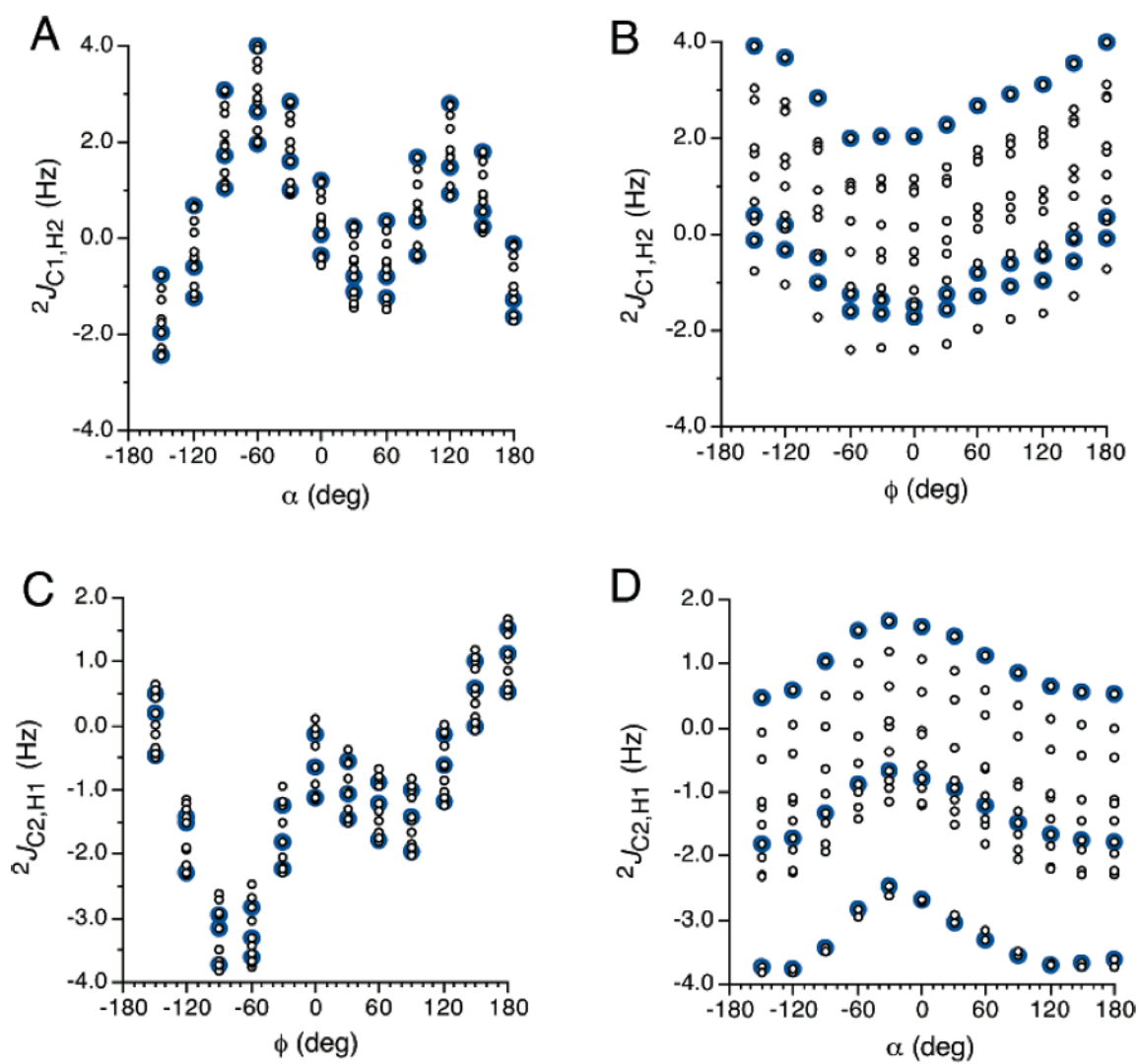


Figure 5.11. Same data as in Figure 5.9 for 7.

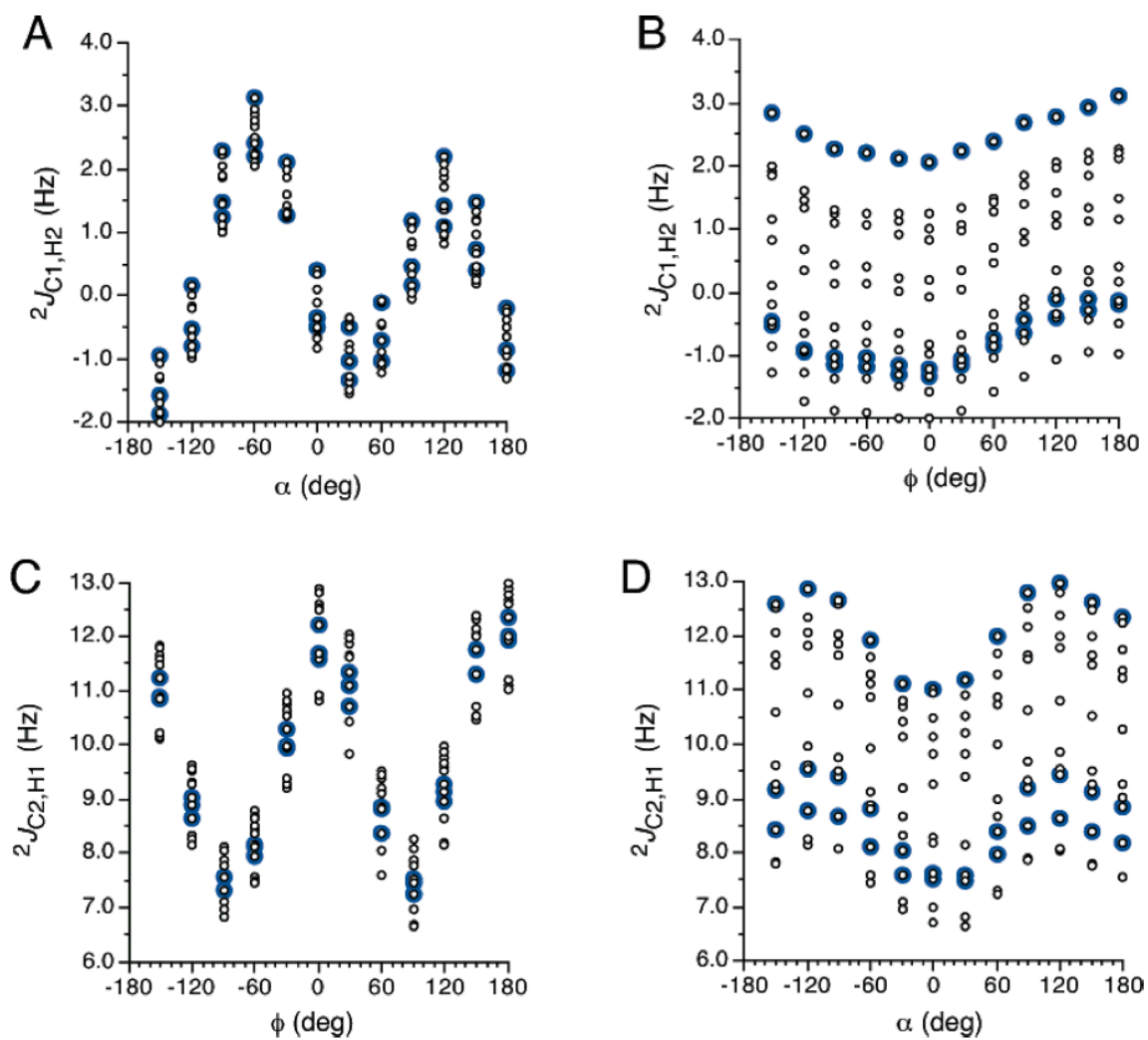


Figure 5.12. Same data as in Figure 5.9 for 8.

considerably more affected by ϕ than by α (Figures 5.9-12, panels C and D). These results support the contention that C-O bond rotations involving the carbon *bearing the coupled proton* have a more pronounced effect on $^2J_{\text{CCH}}$ magnitude than do similar rotations *involving the coupled carbon*. Importantly, the effect of α on $^2J_{\text{C2,H1}}$ is relatively small (~ 1 Hz) in **5-7**, and only slightly larger in **8**. Plots of $^2J_{\text{C2,H1}}$ vs ϕ display two minima at $\sim \pm 90^\circ$, and two maxima at $\sim 0^\circ$ and $\sim 180^\circ$; in this respect, they mirror the behavior of standard Karplus curves relating 3J to dihedral angle, although for $^2J_{\text{CCH}}$ the rotated bond is peripheral to the coupling pathway. Plots for **5**, **6** and **8** are roughly symmetric about $\phi = 0^\circ$, whereas that for **7** shows significantly different J -couplings at the minima. The dynamic range is ~ 5 -6 Hz when coupling signs are considered; for **5**, -2 - 3 Hz; for **6**, 0 - 5 Hz; for **7**, -4 - 2 Hz; for **8**, 7 - 13 Hz. *Absolute* $^2J_{\text{C2,H1}}$ values in **5-7** (2-5 Hz) are considerably smaller than observed for **8** (7-13 Hz), in agreement with experimental couplings in **11-14** (Scheme 5.3). Changes in α do not influence the shape of curves correlating $^2J_{\text{C2,H1}}$ with ϕ (the curves are essentially y -shifted); these results mirror those found for $^2J_{\text{C1,H2}}$ (see above).

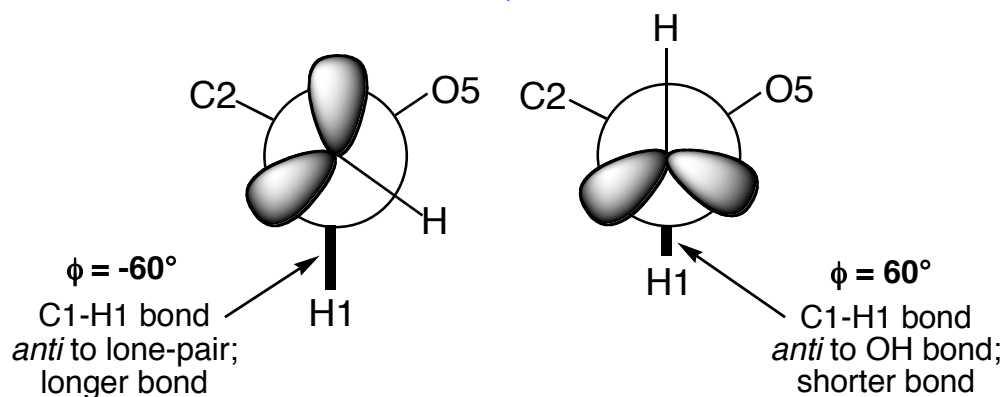
The secondary torsional dependencies of $^2J_{\text{C1,H2}}$ (ϕ) and $^2J_{\text{C2,H1}}$ (α) are small ($< \sim 2$ Hz) and essentially independent of the primary torsion (α and ϕ , respectively) (Figures 5.9-12, panels B and D).

5.4.4. Other Structural Factors Influencing $^2J_{\text{CCH}}$ in Saccharides

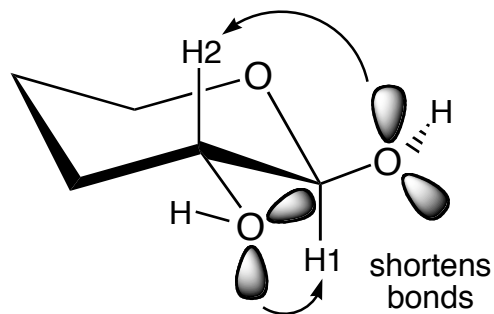
Plots of $r_{\text{C1,H1}}$ vs ϕ and $r_{\text{C2,H2}}$ vs α were evaluated in **5-8** (Figure S2) in an effort to identify structural factors responsible for the observed dependence of $^2J_{\text{C2,H1}}$ and

$^2J_{C1,H2}$ on ϕ and α , respectively. Lone-pair effects on r_{CH} can be predicted from the results of prior work;^{10b,19} vicinal oxygen lone-pairs *anti* to the C-H bond lengthen these bonds due to lone-pair donation into the σ^* antibonding orbital on carbon (Scheme 5.4). Based on this model, $r_{C1,H1}$ is expected to be smaller in α -Glc **5** and α -Man **7** for ϕ near -60° , and in β -Glc **6** and β -Man **8** for ϕ near 60° . C-H bonds should be longer and of roughly equal length in the remaining two staggered ϕ rotamers. This trend is consistently observed (Figure S3A). Lone-pair effects on $r_{C2,H2}$ are as expected, with minima near $\alpha = -60^\circ$ for α/β Glc and $\alpha = 60^\circ$ for α/β Man (Figure S2B).

vicinal lone-pair effect on $r_{C1,H1}$: β -gluco configuration



1,3-lone-pair effects on $r_{C1,H1}$ and $r_{C2,H2}$



Scheme 5.4. Lone-pair effects on r_{CH}

Superimposed on the above trends are the effects of ϕ rotation on $r_{\text{C2,H2}}$ (and presumably $r_{\text{C2,O2}}$), and of α rotation on $r_{\text{C1,H1}}$ (and presumably $r_{\text{C1,O1}}$), which were found to be consistent with prior relationships observed in furanosyl rings.¹⁹ For perfectly staggered values of the rotated C-O torsion, 1,3-lone-pair effects were observed to reduce bond length. For example, $r_{\text{C2,H2}}$ is smaller for β -Glc **6** for $\phi = -60^\circ$ and 180° than for $\phi = 60^\circ$ (Scheme 5.4).

Equipped with the above-noted bond length-lone pair relationships, the effects of the C1-C2-H2 and C2-C1-H1 bond angle on $^2J_{\text{C1,H2}}$ and $^2J_{\text{C2,H1}}$, respectively, were examined in **6** at perfectly staggered values of α and ϕ , respectively (Figure S3). A roughly linear dependence was observed for $^2J_{\text{C1,H2}}$; the coupling increases (*i.e.*, becomes less negative) by ~ 0.5 Hz per 1° increase in the bond angle regardless of the value of α (Figure S3A). This behavior is similar to that observed for $^2J_{\text{HCH}}$ ^{20a} but differs from that reported for $^2J_{\text{COC}}$.^{20b} For $\alpha = 60^\circ$, the curve is shifted by ~ 2 Hz towards less negative couplings; in this rotamer, $r_{\text{C2,H2}}$ is larger due to the presence of an O2 lone-pair *anti* to the C2-H2 bond. Interestingly, the curves for $\alpha = -60^\circ$ and 180° *coincide* despite the presence of an oxygen lone-pair *anti* to the C2-H2 bond in $\alpha = 180^\circ$. These results show that $^2J_{\text{C1,H2}}$ does not perfectly correlate with $r_{\text{C2,H2}}$. Similar observations were made for **5**, **7** and **8** (data not shown).

$^2J_{\text{C2,H1}}$ in **6** appears less affected by $\angle_{\text{C2,C1,H1}}$ (Figure S3B), although the dynamic range of the angle and the distribution of data points at each ϕ value are more limited. Couplings are similar for $\phi = 60^\circ$ and -60° (1-2 Hz), but shift to more positive values (4-5 Hz) for $\phi = 180^\circ$. For $\phi = -60^\circ$ and 180° , an O1 lone-pair is *anti* to the C1-H1

bond, yet significantly different ${}^2J_{C2,H1}$ values are observed. Thus, like ${}^2J_{C1,H2}$, ${}^2J_{C2,H1}$ magnitude does not perfectly correlate with $r_{C1,H1}$. Similar observations were made for **5**, **7** and **8** (data not shown). These data also suggest that rotating ϕ significantly influences $\angle_{C1,C2,H2}$, whereas $\angle_{C2,C1,H1}$ is much less affected by rotating α .

Further inspection of ${}^2J_{CCH}$ vs r_{CH} data provides a possible explanation for the anomalous ${}^2J_{CCH}$ values in those C-O rotamers identified above (Figure S3). In these cases (*e.g.*, $\alpha = 180^\circ$ for ${}^2J_{C1,H2}$, and $\phi = -60^\circ$ for ${}^2J_{C2,H1}$ in **6**), the C-O torsion orients the hydroxyl proton *anti* to the coupled carbon; this geometry yields a smaller r_{C1-C2} since no oxygen lone-pairs are *anti* to the bond. In these conformers, the reduced r_{C1-C2} shifts ${}^2J_{CCH}$ to a more negative value. Thus, *both the C-H and C-C bond lengths affect ${}^2J_{CCH}$, with shorter bonds leading to more negative (less positive) couplings.*

Studies of ${}^1J_{C1,H1}$ and ${}^1J_{C1,C2}$ in **5-8** as a function of r_{CH} and r_{CC} were also conducted by systematically varying bond lengths over a 0.02 Å range while optimizing the remaining parameters (only one combination of C1-O1 and C2-O2 bond torsions were inspected in each structure). ${}^1J_{CH}$ was found to vary roughly linearly with r_{CH} ,^{10b} with shorter bonds yielding larger (more positive) couplings (Figure S4A). However, in some cases, the dependence was very small (*e.g.*, ${}^1J_{C1,H1}$ vs $r_{C1,H1}$ in α -Glc and α -Man). In contrast, the effect of $r_{C1,C2}$ on ${}^1J_{C1,H1}$ was strong in all cases; moderate changes in r_{CC} influence ${}^1J_{CH}$ values more significantly than do comparable changes in r_{CH} (Figure S4A). This observation may explain why correlations between r_{CH} and ${}^1J_{CH}$ were not uniformly observed in prior work;^{10a} a critical r_{CC} factor is apparently operating and may

dominate over effects caused by r_{CH} . $^1J_{\text{CC}}$ values decrease with increasing r_{CC} , and are virtually unaffected by changes in r_{CH} on the coupled carbons (Figure S4B).

5.4.5. Quantitative Treatment of $^2J_{\text{C1,H2}}$ and $^2J_{\text{C2,H1}}$

Hypersurfaces relating $^2J_{\text{C1,H2}}$ and $^2J_{\text{C2,H1}}$ to ϕ and α in **5-8** are shown in Figures 5.13 and 5.14. These data were used to parameterize two equations relating $^2J_{\text{C1,H2}}$ and $^2J_{\text{C2,H1}}$ to ϕ and α .

$$^2J_{\text{C1,H2}} = A + B \cos \alpha + C \cos 2\alpha + D \sin \alpha + E \sin 2\alpha + F \cos \phi + G \cos 2\phi \quad (5.1)$$

$$^2J_{\text{C2,H1}} = A + B \cos \phi + C \cos 2\phi + D \sin \phi + E \sin 2\phi + F \cos \alpha + G \cos \alpha \quad (5.2)$$

Coefficients for Equations [5.1] and [5.2] are given in Table 5.1 for the four relative configurations at C1 and C2 of aldopyranosyl rings (**5-8**) and for the 2-deoxy-aldopyranosyl rings (**1,2**). The regular patterns in both torsional regimes permitted reasonable χ^2 and rms values to be obtained in the parameterizations. Single parameter equations were initially derived containing only the primary torsional variable (α for $^2J_{\text{C1,H2}}$; ϕ for $^2J_{\text{C2,H1}}$). A slightly better fit was obtained, however, with double-parameter equations containing two additional terms to treat the secondary torsional dependence (ϕ for $^2J_{\text{C1,H2}}$; α for $^2J_{\text{C2,H1}}$). The latter equations would be applicable if independent information on these secondary torsions is available (*e.g.*, via $^3J_{\text{HCOH}}$ and/or $^3J_{\text{CCOH}}$ values).

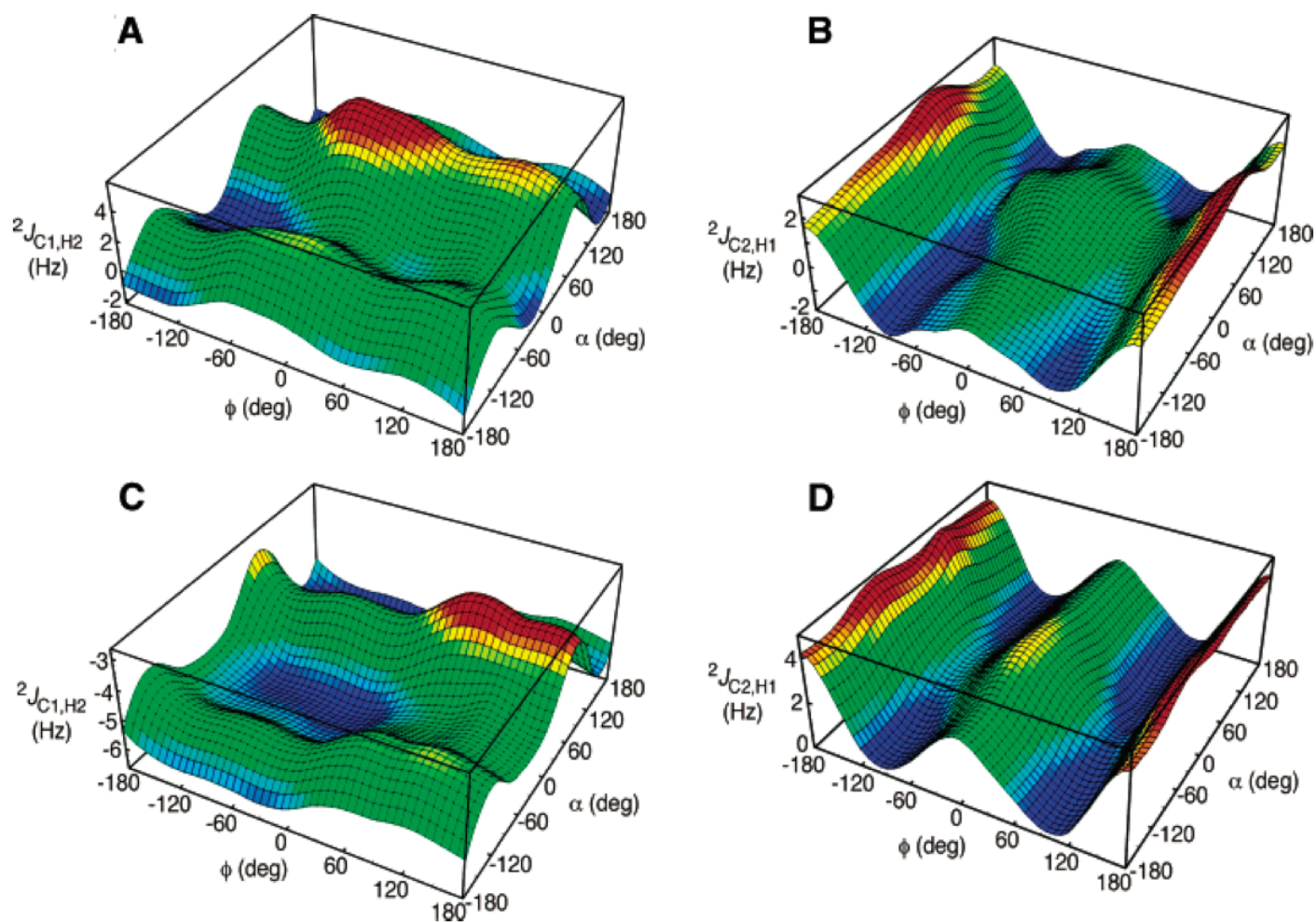


Figure 5.13. Computed hypersurfaces showing the dependencies of ${}^2J_{C1,H2}$ and ${}^2J_{C2,H1}$ on ϕ and α in **5** (A and B, respectively), and in **6** (C and D, respectively).

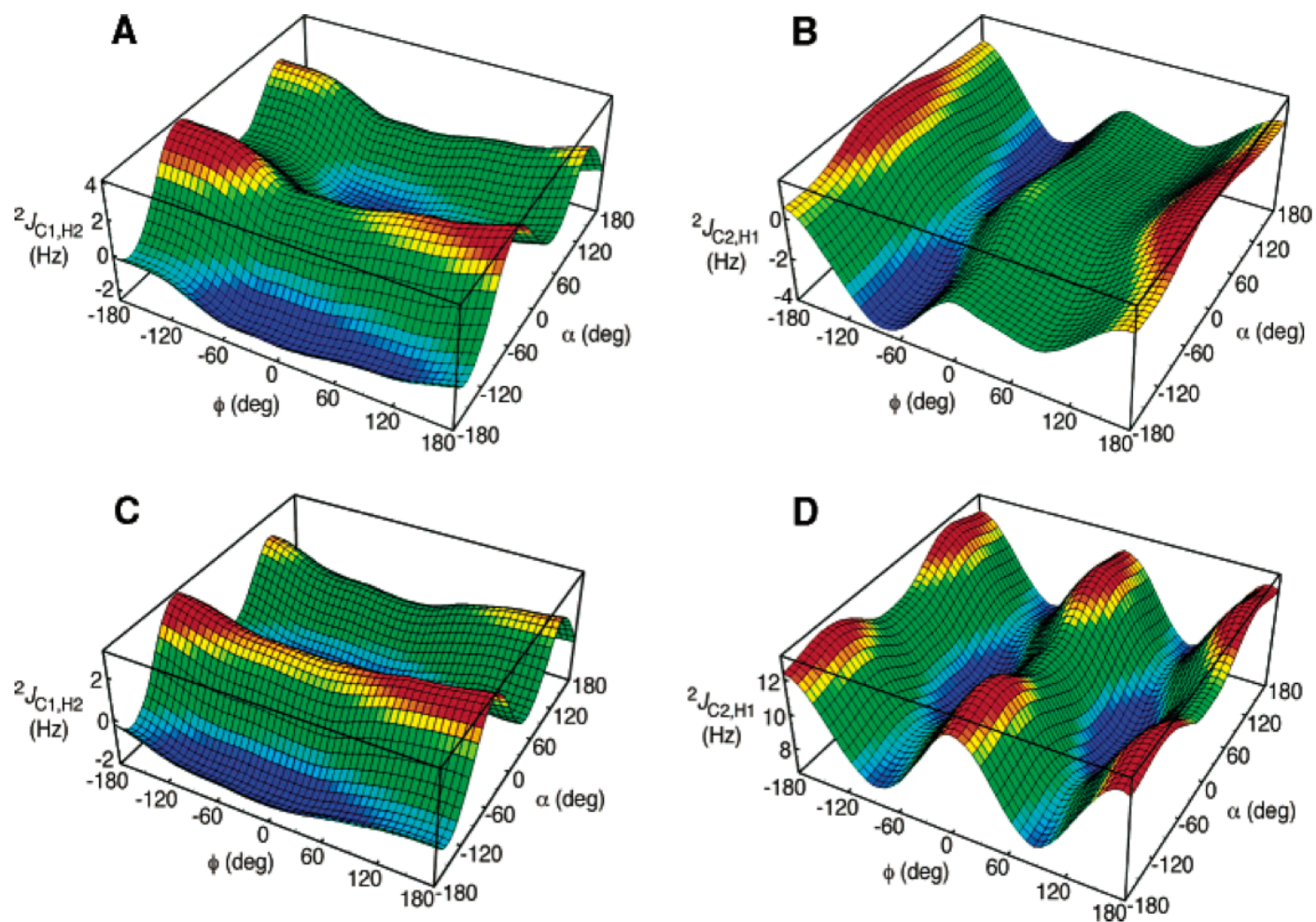


Figure 5.14. Computed hypersurfaces showing the dependencies of ${}^2J_{C1,H2}$ and ${}^2J_{C2,H1}$ on ϕ and α in **7** (A and B, respectively), and in **8** (C and D, respectively).

TABLE 5.1. COEFFICIENTS IN PARAMETERIZED EQUATIONS FOR ${}^2J_{C1,H2}$ AND ${}^2J_{C2,H1}$ IN **1**, **2**, AND **5-8**, AND χ^2 AND RMS VALUES DERIVED FROM THE FIT

	α -Glc 5 ${}^2J_{C1,H2}$	α -Glc 5 ${}^2J_{C2,H1}$	β -Glc 6 ${}^2J_{C1,H2}$	β -Glc 6 ${}^2J_{C2,H1}$	α -Man 7 ${}^2J_{C1,H2}$	α -Man 7 ${}^2J_{C2,H1}$	β -Man 8 ${}^2J_{C1,H2}$	β -Man 8 ${}^2J_{C2,H1}$	α -deoxyGlc 1 ${}^2J_{C2,H1}$	β -deoxyGlc 2 ${}^2J_{C2,H1}$
Single Parameter										
A	1.30	0.086	-5.07	2.05	0.50	-1.17	0.30	9.88	2.24	5.12
B	0.13	0.50	0.16	0.062	-0.67	1.21	-0.50	0.37	0.69	0.044
C	-1.15	-0.60	-0.41	-0.92	1.74	-0.77	1.64	-1.23	-0.79	-1.05
D	-0.81	0.50	-0.25	0.38	-0.31	0.39	-0.11	0.16	0.49	0.26
E	-1.63	0.99	-0.79	1.40	0.053	1.01	0.042	1.89	1.11	1.55
χ^2	106.1	32.6	42.0	19.9	68.3	29.0	25.8	61.6	0.19	0.09
rms (Hz)	0.74	0.23	0.29	0.14	0.48	0.20	0.18	0.43	0.02	0.01
Double Parameter										
A	1.30	0.086	-5.07	2.05	0.50	-1.17	0.30	9.88		
B	0.13	0.50	0.16	0.062	-0.67	1.21	-0.50	0.37		
C	-1.15	-0.60	-0.41	-0.92	1.73	-0.77	1.64	-1.23		
D	-0.81	0.50	-0.25	0.38	-0.31	0.39	-0.11	0.16		
E	-1.63	0.99	-0.79	1.40	0.053	1.01	0.042	1.89		
F	-0.17	-0.11	0.65	-0.21	0.40	-0.37	0.45	0.29		
G	0.56	-0.17	0.10	0.13	-0.24	0.067	0.039	0.27		
χ^2	81.7	29.7	11.0	15.4	52.6	18.9	11.0	50.6		
rms (Hz)	0.57	0.21	0.08	0.11	0.37	0.13	0.08	0.35		

5.5. Conclusions

$^2J_{\text{CCH}}$ values have received relatively little attention as conformational probes of saccharides in solution. However, recent studies of saccharide hydroxymethyl group conformation⁹ suggest a wider role for these scalar couplings stemming from their sensitivities to both C-C and C-O torsion angles. For example, the C5-C6-H6*R/S* coupling pathways in aldohexopyranosyl rings yield $^2J_{\text{CCH}}$ values that are influenced by both the C5-C6 (ω) and C6-O6 (θ) torsion angles (**I**; Scheme 5.1) (Figure 5.1). In this case, the remaining potential variable, the C5-O5 torsion angle, was fixed by the pyranosyl ring and thus played no role in modulating the couplings. In the present investigation, *the C-C torsion angle is held constant* by the pyranosyl ring, leaving both C-O torsions to potentially modulate the coupling.

The present studies show that $^2J_{\text{CCH}}$ values are influenced by C-O torsion angles at both carbons of the C-C-H coupling pathway, but the effect is greater *at the carbon bearing the coupled proton*. The observation appears valid for both $^2J_{\text{C1,H2}}$ and $^2J_{\text{C2,H1}}$, suggesting that the nature of the coupled carbon (*e.g.*, anomeric *vs* non-anomeric) is not important.

The effect of C-O bond rotation on $^2J_{\text{CCH}}$ appears to be mediated largely by oxygen lone-pair perturbations of C-H and C-C bond lengths. In general, reduction in the C-C and/or C-H bond lengths in the C-C-H coupling pathway shifts $^2J_{\text{CCH}}$ to more negative (less positive) couplings. Lone-pair effects appear mainly in two forms: vicinal effects (for the C1-H1, C2-H2 and C1-C2 bonds) and 1,3-effects (C1-H1 and C2-H2

bonds only), with the former resulting in bond length elongation and the latter causing bond length reduction. Because rotation of the C1-O1 and C2-O2 bonds induces lone-pair effects that may be reinforcing or canceling for any given bond, the dependence of $^2J_{\text{CCH}}$ on these torsions becomes a complex function of overlapping forces.

The expected vicinal lone-pair effects on $r_{\text{C1,H1}}$ and $r_{\text{C2,H2}}$ upon rotation of ϕ and α , respectively, are predicted consistently in **5-8**. This is not true for vicinal lone-pair effects on $r_{\text{C1,C2}}$; for example, rotating ϕ in **6** would be expected to increase $r_{\text{C1,C2}}$ for $\phi = 60^\circ$ and 180° (O1 lone-pair *anti* to the C1-C2 bond) relative to $\phi = -60^\circ$, and that $r_{\text{C1,C2}}$ should be similar in the former group (Figure S2B). However, these trends are not consistently observed in **5-8** (data not shown), suggesting that oxygen lone-pair effects are modulated by other structural factors that may include competing stereoelectronic effects operating at the anomeric center and/or the presence of intramolecular H-bonding. The latter complication was cause for concern about $^2J_{\text{CCH}}$ computed in systems exhibiting H-bonding between O1 and O2, since C1-C2 bond length, a determinant of $^2J_{\text{CCH}}$, was observed to be sensitive to the presence of H-bonding (the presence of H-bonding between vicinal OH groups reduces r_{CC}). However, it is believed that this effect is small, based on the smooth, continuous character of computed $^2J_{\text{CCH}}$ vs ϕ/α curves for **5-8**, and on the similarity of these curves to those found for **1** and **2**; in the latter structures, complications arising from intramolecular H-bonding are absent due to the lack of a vicinal diol fragment at C1 and C2. It is also noted that 1,3-lone-pair effects on $r_{\text{C1,H1}}$ and $r_{\text{C2,H2}}$ are consistently observed in **5-8** as suggested from prior studies in

furanosyl rings,¹⁹ although there are exceptions attributed again to the presence of H-bonding in the structure.

New equations correlating $^2J_{C1,H2}$ and $^2J_{C2,H1}$ with ϕ and/or α in aldopyranosyl rings have been derived. $^2J_{C2,H1}$ has particular relevance for studies of oligosaccharide conformation wherein assessments of preferred conformation about ϕ are important. These couplings can be measured in specific monosaccharide residues labeled with ^{13}C at C2, since signal multiplicity at the well-resolved adjacent anomeric proton can be observed readily. Alternatively, natural abundance methods for J_{CH} measurements could be applied.²¹ Recent work has suggested that trans-glycoside J -couplings yield quantitative information about C-O rotamer populations in glycosidic linkages.²² However, evaluations of ϕ appeared less firm than of ψ due to use of the less reliable (and less sensitive) trans-glycoside $^2J_{\text{COC}}$. $^2J_{C2,H1}$ may provide an additional means of evaluating ϕ . Since $^2J_{C2,H1}$ displays some sensitivity to α , however, more accurate treatments of $^2J_{C2,H1}$ in oligosaccharides may require an independent evaluation of the C2-O2 torsion angle. The latter could be obtained from measurements of $^3J_{\text{HCOH}}$ ²³ or $^3J_{\text{CCOH}}$ ²⁴ in solution. In residues lacking an hydroxyl group at C2 (*i.e.*, 2-deoxyaldopyranosyl rings), application of $^2J_{C2,H1}$ to evaluate ϕ should be more straightforward.

While this report has focused on $^2J_{\text{CCH}}$ values as constraints for ϕ in glycosides, similar couplings may also be applicable to ψ analysis. For example, in β -(1 \rightarrow 4) linkages, $^2J_{C3,H4}$ and $^2J_{C5,H4}$ may serve as additional ψ constraints, assuming that they

obey the same dependencies on C-O torsions as observed for $^2J_{C2,H1}$. This application remains to be explored.

The predicted behavior of $^2J_{C1,H2}$ and $^2J_{C2,H1}$ reported herein was deduced from studies of J -couplings in gas-phase molecules. It is thus possible that J -coupling behavior in aqueous solution may be influenced by the presence of H-bonding between saccharide hydroxyl groups and solvent water. $^1J_{CH}$ are reported to display a solvent dependence,²⁵ while $^3J_{CH}$ are expected to be considerably less affected by solvent. $^2J_{CCH}$ may display an intermediate solvent dependency, although this has not been tested computationally or experimentally. However, even if solvation affects $^2J_{CCH}$, the overall *trends* reported here are expected to be maintained, with possible changes manifested in curve amplitude shifts (*i.e.*, the absolute values of $^2J_{CCH}$ will be uniformly shifted but overall dependencies will be maintained).

Given the dual dependence of $^2J_{CCH}$ on C-O torsions on both carbons along the coupling pathway, a concerted analysis of multiple $^2J_{CCH}$ values within specific aldopyranosyl rings may lead to a more complete picture of C-O torsional preferences in solution. Thus, for example, if the eight intra-ring $^2J_{CCH}$ within **6** ($^2J_{C1,H2}$, $^2J_{C2,H1}$, $^2J_{C2,H3}$, $^2J_{C3,H2}$, $^2J_{C3,H4}$, $^2J_{C4,H3}$, $^2J_{C4,H5}$, $^2J_{C5,H4}$) were properly parameterized, and if all values were known experimentally, then the eight equations could be collectively solved to extract "best fit" C-O torsions in solution. These data could be compared or combined with other information (*e.g.*, from $^3J_{HCOH}$ and/or $^3J_{CCOH}$) to improve the reliability of the conclusions. Thus, $^2J_{CCH}$ not only reports *on relative configuration*

along the C-C-H pathway, as demonstrated by the empirical rules developed by Perlin^{7,8} and Pedersen⁶, but also holds the potential of indirectly evaluating C-O torsions in saccharides for both C-O-R and C-O-H fragments.

5.6. Acknowledgements

This work was supported by grants from Omicron Biochemicals, Inc. of South Bend, IN and the National Institutes of Health (GM) (to A.S.). The Notre Dame Radiation Laboratory is supported by the Office of Basic Energy Sciences of the United States Department of Energy. This is Document No. NDRL-4530 from the Notre Dame Radiation Laboratory.

5.7. Supporting Information

The supporting information consists of four figures showing ϕ/α population contour maps for **5-8** derived from DFT-calculated total energies (Figure S1), correlations between $r_{C1,H1}$, $2JC2,H1$, and ϕ , and between $r_{C2,H2}$, $2JC1,H2$, and R in **6** (Figure S2), correlations between C-C-H bond angle and $2JC1,H2$ and $2JC2,H1$ in **6** (Figure S3), and correlations between $r_{C1,H1}$ and $1JC1,H1$, and between $r_{C1,C2}$ and $1JC1,C2$, in **6** either in fully optimized structures or in structures containing incremented (and fixed) C1-H1 or C1-C2 bond lengths (Figure S4).

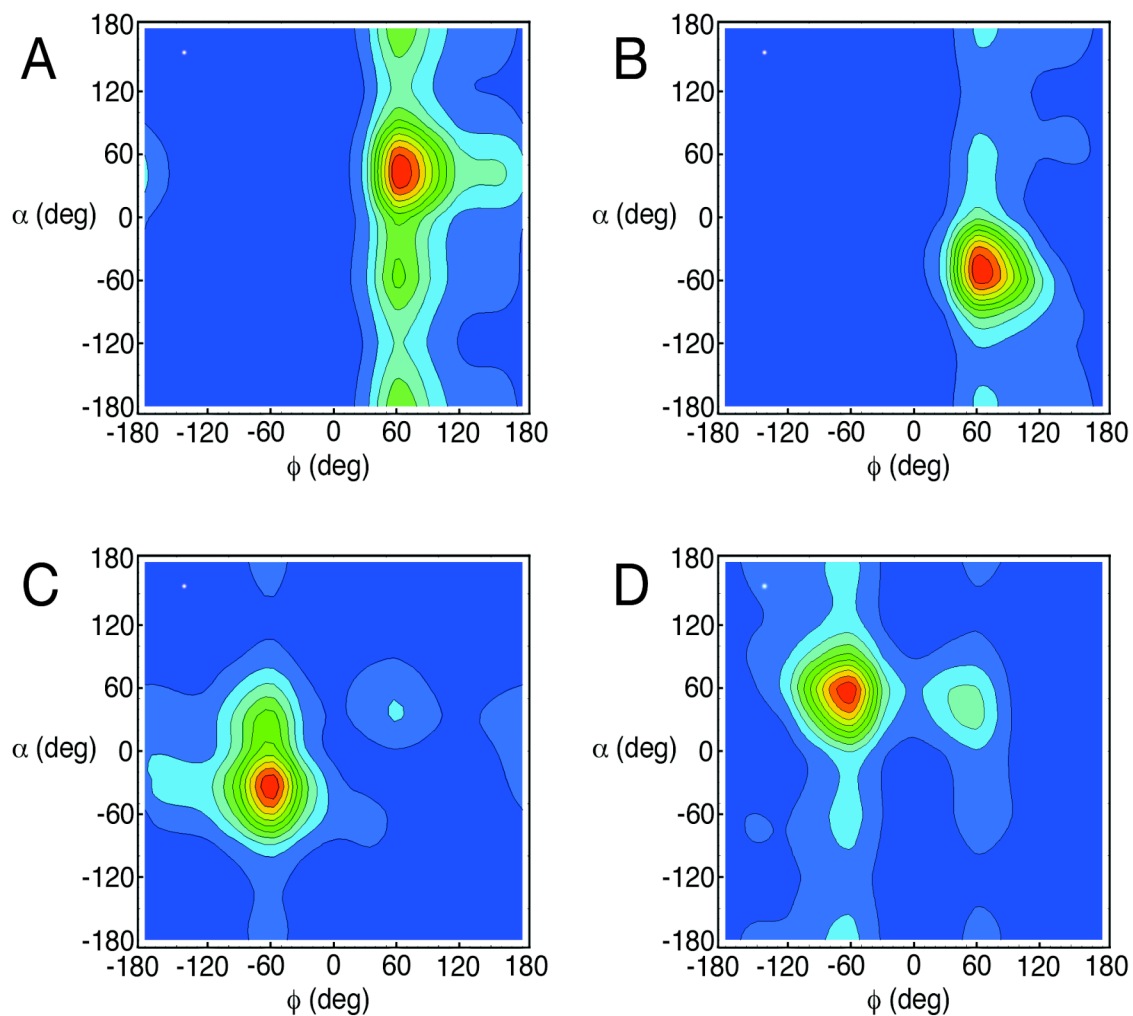


Figure 5.15. (S1) Contour maps showing preferred ϕ/α populations for **5** (A), **6** (B), **7** (C), and **8** (D) derived from total energies obtained from DFT calculations (B3LYP/6-31G*).

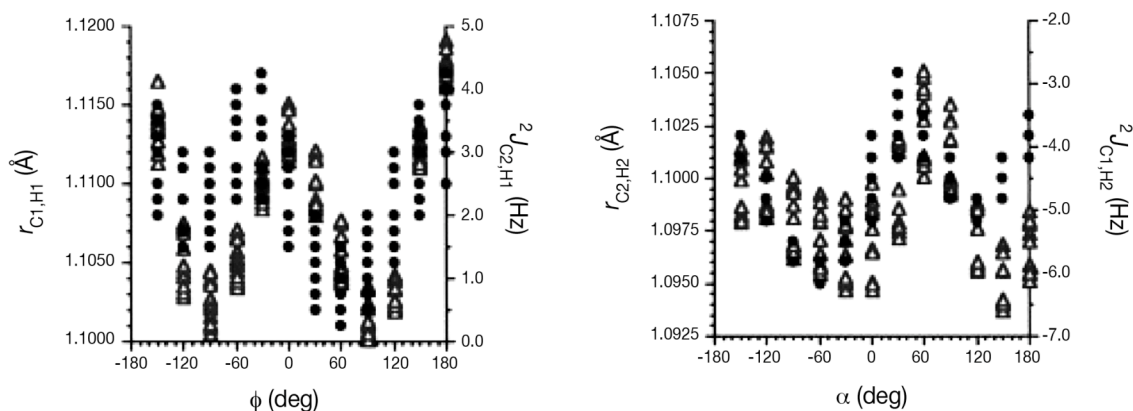


Figure 5.16. (S2) (A) Plot of $r_{C1,H1}$ (closed circles) and $^2J_{C2,H1}$ (open triangles) as a function of ϕ in **6**. Note the anomalous behavior of $^2J_{C2,H1}$ at $\phi = -60^\circ$. (B) A plot of $r_{C2,H2}$ (closed circles) and $^2J_{C1,H2}$ (open triangles) as a function of α in **6**. Note the anomalous behavior of $^2J_{C1,H2}$ at $\alpha = 180^\circ$. The shift to more negative couplings in both cases is attributed to oxygen lone-pair effects on $r_{C1,C2}$ (see text); in both cases, the lack of a vicinal lone-pair effect reduces $r_{C1,C2}$, thus shifting $^2J_{CCH}$ to more negative (less positive) values.

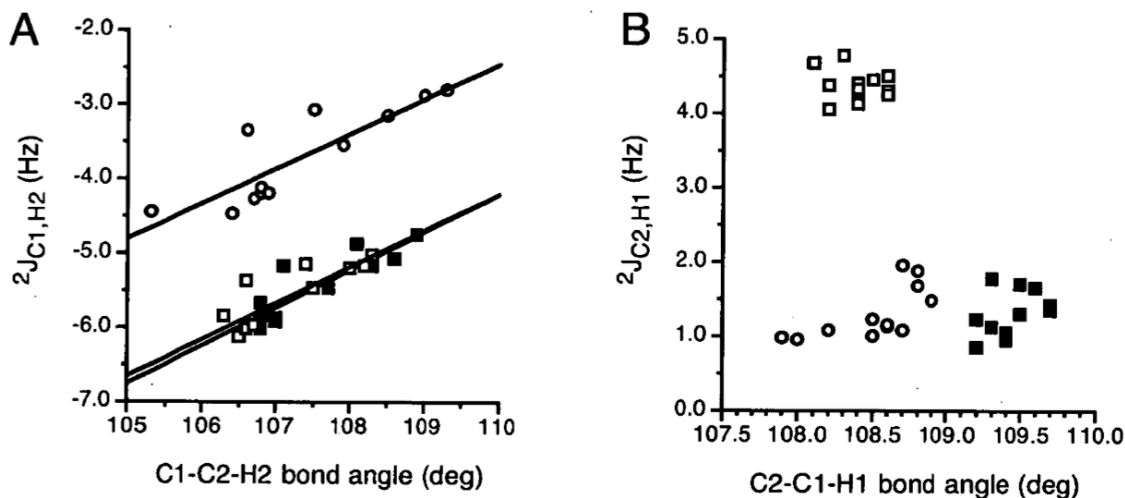


Figure 5.17. (S3) (A) Correlation between the C1-C2-H2 bond angle and $^2J_{C1,H2}$ in **6**. Open circles; $\alpha = 60^\circ$; closed squares, $\alpha = -60^\circ$; open squares, $\alpha = 180^\circ$. (B) Correlation between the C2-C1-H1 bond angle and $^2J_{C2,H1}$ in **6**. Open circles; $\phi = 60^\circ$; closed squares, $\phi = -60^\circ$; open squares, $\phi = 180^\circ$.

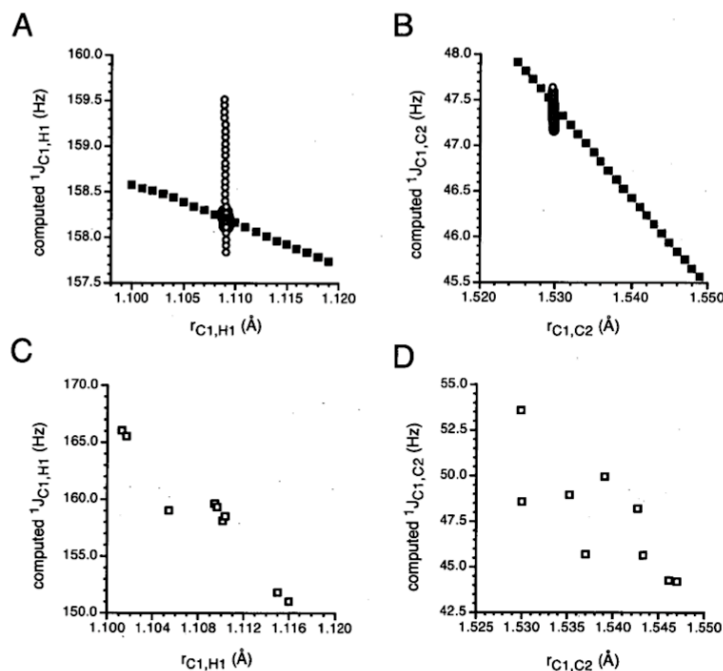


Figure 5.18. (S4) (A) Plot of $^1J_{C1,H1}$ in **6** as a function of $r_{C1,H1}$ (closed squares), showing decreasing $^1J_{CH}$ with increasing r_{CH} . The value of $r_{C1,H1}$ was systematically varied in 0.001 Å increments and held fixed; all other molecular parameters were optimized. Superimposed on this plot is the effect of varying $r_{C1,C2}$ (open circles) and $r_{C2,H2}$ (closed circles) on $^1J_{C1,H1}$; both bond lengths were varied systematically and separately in 0.001 Å increments and held fixed; all other molecular parameters were optimized. Note the small effect of $r_{C1,C2}$ and $r_{C2,H2}$, and the large influence of $r_{C1,H1}$ on $^1J_{C1,H1}$. (B) Plot of $^1J_{C1,C2}$ in **6** as a function of $r_{C1,C2}$ (closed squares), showing decreasing $^1J_{CC}$ with increasing r_{CC} . The value of $r_{C1,C2}$ was systematically varied in 0.001 Å increments and held fixed; all other molecular parameters were optimized. Superimposed on this plot is the effect of varying $r_{C1,H1}$ (open circles) and $r_{C2,H2}$ (close circles) (performed as described in A) on $^1J_{C1,C2}$. Note the modest effect of r_{CH} on $^1J_{CC}$. (C) Plot of $^1J_{C1,H1}$ as a function of $r_{C1,H1}$ in *fully optimized geometries* of **6**. Changes in r_{CH} were induced by rotating ϕ and α (only perfectly staggered rotamers are shown). Note the enhanced slope of this plot relative to that found in A. (D) Plot of $^1J_{C1,C2}$ as a function of $r_{C1,C2}$ in *fully optimized geometries* of **6**. Changes in r_{CC} were induced by rotating ϕ and α (only perfectly staggered rotamers are shown). While data scatter is significant, the average slope of this plot is greater than that found in B.

5.8. References

1. Tvaroska, I.; Hricovini, H.; Petrakova, E. *Carbohydr. Res.* **1989**, *189*, 359-362.
2. Mulloy, B.; Frenkiel, T.A.; Davies, D.B. *Carbohydr. Res.* **1988**, *184*, 39-46.
3. Tvaroska, I.; Gadjos, J. *Carbohydr. Res.* **1995**, *271*, 151-162.
4. Tvaroska, I.; Taravel, F.R.; Utille, J.P.; Carver, J.P. *Carbohydr. Res.* **2002**, *337*, 353-367.
5. Cloran, F.; Carmichael, I.; Serianni, A.S. *J. Am. Chem. Soc.* **1999**, *121*, 9843-9851.
6. Bock, K.; Pedersen, C. *Acta Chem. Scand. Ser. B* **1977**, *B31*, 354-358.
7. Schwarcz, J.A.; Perlin, A.S. *Can. J. Chem.* **1972**, *50*, 3667-3676.
8. Schwarcz, J.A.; Cyr, N.; Perlin, A.S. *Can. J. Chem.* **1975**, *53*, 1872-1875.
9. Thibaudeau, C.; Stenutz, R.; Hertz, B.; Klepach, T.; Zhao, S.; Wu, Q.; Carmichael, I.; Serianni, A.S. *J. Am. Chem. Soc.* **2004**, *126*, 15668-15685.
10. (a) Stenutz, R.; Carmichael, I.; Widmalm, G.; Serianni, A.S. *J. Org. Chem.* **2002**, *67*, 949-958. (b) Serianni, A.S.; Wu, J.; Carmichael, I. *J. Am. Chem. Soc.* **1995**, *117*, 8645-8650.
11. Becke, A.D. *J. Chem. Phys.* **1993**, *98*, 5648-5652.
12. Hehre, W.J.; Ditchfield, R.; Pople, J.A. *J. Chem. Phys.* **1972**, *56*, 2257-2261.
13. Frisch, M.J.; Trucks, G.W.; Schlegel, H.B.; Scuseria, G.E.; Robb, M.A.; Cheeseman, J.R.; Zakrzewski, V.G.; Montgomery, Jr., J.A.; Stratmann, R.E.; Burant, J.C.; Dapprich, S.; Millam, J.M.; Daniels, A.D.; Kudin, K.N.; Strain, M.C.; Farkas, O.; Tomasi, J.; Barone, V.; Cossi, M.; Cammi, R.; Mennucci, B.; Pomelli, C.; Adamo, C.; Clifford, S.; Ochterski, J.; Petersson, G.A.; Ayala, P.Y.; Cui, Q.; Morokuma, K.; Malick, D.K.; Rabuck, A.D.; Raghavachari, K.; Foresman, J.B.; Cioslowski, J.; Ortiz, J.V.; Baboul, A.G.; Stefanov, B.B.; Liu, G.; Liashenko, A.; Piskorz, P.; Komaromi, I.; Gomperts, R.; Martin, R.L.; Fox, D.J.; Keith, T.; Al-Laham, M.A.; Peng, C.Y.; Nanayakkara, A.; Challacombe, M.; Gill, P.M.W.; Johnson, B.; Chen, W.; Wong, M.W.; Andres, J.L.; Gonzalez, C.; Head-Gordon, M.; Replogle, E.S.; Pople, J.A. *Gaussian98*; Revision A.9, Gaussian, Inc.: Pittsburgh, PA, 1998. (b) Frisch, M. J.; Trucks, G. W.; Schlegel, H. B.; Gill, P. M. W.; Johnson, B. G.; Robb, M. A.; Cheeseman, J. R.; Keith, T.; Petersson, G. A.; Montgomery, J. A.; Raghavachari, K.; AlLaham, M. A.; Zakrzewski, V. G.; Ortiz, J. V.; Foresman, J. B.; Peng, C. Y.; Ayala, P. Y.; Chen, W.; Wong, M. W.; Andres, J. L.; Replogle, E. S.; Gomperts, R.; Martin, R. L.; Fox, D. J.; Binkley, J. S.;

Defrees, D. J.; Baker, J.; Stewart, J. P.; Head Gordon, M.; Gonzalez, C.; Pople, J. A. *Gaussian94*; Gaussian, Inc.: Pittsburgh, PA, 1995.

14. (a) Thøgersen, H.; Lemieux, R.U.; Bock, K.; Meyer, B. *Can. J. Chem.* **1982**, *60*, 44-57. (b) Tvaroska, I.; Bleha, T. *Adv. Carbohydr. Chem. Biochem.*, **1989**, *47*, 45-123. (c) Meyer, B. Conformational Aspects of Oligosaccharides, in *Topics in Current Chemistry 154*, (Ed.: J. Thiem) Springer-Verlag, Berlin Heidelberg, **1990**, pp.141-208. (d) Juaristi, E.; Cuevas, G. *The Anomeric Effect*, CRC Press, Boca Raton, 1995. (e) Kirby, A.J. *The Anomeric Effect and Related Stereoelectronic Effects at Oxygen*, Springer, New York, 1983. (f) Lemieux, R.U.; Koto, S. *Tetrahedron* **1974**, *30*, 1933-1944. (g) Praly, J.-P.; Lemieux, R.U. *Can. J. Chem.* **1987**, *65*, 213-223. (h) Lemieux, R.U. *Pure Appl. Chem.* **1971**, *25*, 527-548.
15. Note that the axial H2 (H2a) is H2S and the equatorial H2 (H2e) is H2R in **1-4** (see Scheme 5.2).
16. Bandyopadhyay, T.; Wu, J.; Serianni, A.S. *J. Org. Chem.* **1993**, *58*, 5513-5517.
17. Tvaroska, I.; Bleha, T. *Advances in Carbohydrate Chemistry and Biochemistry*, Tipson, R.S., Horton, D., Eds, Academic Press: San Diego, **1989**, 45.
18. Podlasek, C.A.; Wu, J.; Stripe, W.A.; Bondo, P.B.; Serianni, A.S. *J. Am. Chem. Soc.* **1995**, *117*, 8635-8644.
19. (a) Kennedy, J.; Wu, J.; Drew, K.; Carmichael, I.; Serianni, A.S. *J. Am. Chem. Soc.* **1997**, *119*, 8933-8945. (b) Cloran, F.; Zhu, Y.; Osborn, J.; Carmichael, I.; Serianni, A.S. *J. Am. Chem. Soc.* **2000**, *122*, 6435-6448.
20. (a) Maciel, G.E.; McIver, J.W.; Ostlund, N.S.; Pople, J.A. *J. Am. Chem. Soc.* **1970**, *92*, 4151. (b) Cloran, F.; Carmichael, I.; Serianni, A.S. *J. Am. Chem. Soc.* **2000**, *122*, 396-397.
21. (a) Meissner, A.; Sørensen, O.W. *Magn. Reson. Chem.* **2001**, *39*, 49-52. (b) Blechta, V.; del Rio-Portilla, F.; Freeman, R. *Magn. Reson. Chem.* **1994**, *32*, 134-137. (c) Nishida, T.; Widmalm, G.; Sandor, P. *Magn. Reson. Chem.* **1995**, *33*, 596-599.
22. (a) Cloran, F.; Carmichael, I.; Serianni, A.S. *J. Am. Chem. Soc.* **1999**, *121*, 9843-9851. (b) Thibaudeau, C.; Klepach, T.; Zhao, S.; Reed, M.; Carmichael, I.; Serianni, A.S., submitted for publication.
23. Fraser, R.R.; Kaufman, M.; Morand, P.; Govil, G. *Can. J. Chem.* **1969**, *47*, 403-409.
24. Dais, P.; Perlin, A.S. *Can. J. Chem.* **1982**, *60*, 1648.

25. Zaccari, D.G.; Snyder, J.P.; Peralta, J.E.; Taurian, O.E.; Contreras, R.H.; Barone, V. *Mol. Phys.* **2002**, *100*, 705-715.

CHAPTER 6:

^{13}C - ^{13}C NMR SPIN-COUPPLINGS IN SACCHARIDES: NEW CORRELATIONS
WITH MOLECULAR STRUCTURE⁵

“Knowledge is chimera – for beyond it lies other knowledge, and the incompleteness of what is known renders the knowing false.”

– Stephen R. Donaldson (The Thomas Covenant Chronicles)

6.1. Abstract

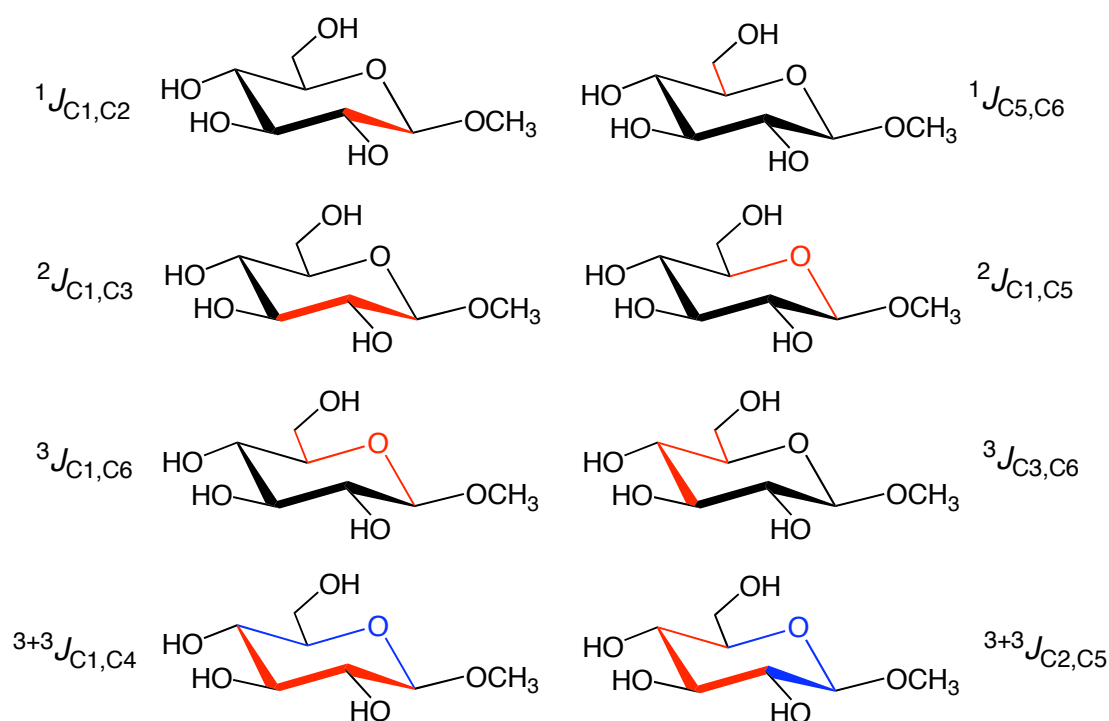
^{13}C - ^{13}C Spin-spin coupling constants (J_{CC}) have been measured in a group of aldohexopyranoses and methyl aldopyranosides singly labeled with ^{13}C at different sites to extend prior correlations between J_{CC} magnitude and sign, and saccharide structure. Using density functional theory (DFT) calculations to test empirical predictions, structural correlations for $^2J_{\text{C1,C3}}$, $^2J_{\text{C2,C4}}$, $^2J_{\text{C4,C6}}$ and $^2J_{\text{C1,C5}}$ have been confirmed. These geminal couplings depend highly on the orientation of C-O bonds appended to the terminal coupled carbons. $^3J_{\text{C1,C6}}$ and $^3J_{\text{C3,C6}}$ show expected Karplus-like dependences, but are also affected by in-plane terminal hydroxyl substituents. In both cases, rotation

⁵ I gratefully acknowledge my co-authors Bidisha Bose-Basu, Gail Bondo, Paul Bondo, Wenhui Zhang, Ian Carmichael and Anthony S. Serianni for their assistance in preparing this chapter, which is submitted to the Journal of Organic Chemistry.

about the C5-C6 bond modulates the coupling due to the alternating in-plane and out-of-plane O6. $^3J_{C3,C6}$ is also affected by C4 configuration. Both $^3J_{C1,C6}$ and $^3J_{C3,C6}$ are subject to remote effects involving structure at C3 and C1, respectively. New correlations have been determined for $^2J_{C3,C5}$, which, like $^3J_{C3,C6}$, shows a remote dependence on anomeric configuration. Investigations of dual-pathway ^{13}C - ^{13}C couplings, $^{3+3}J_{C1,C4}$ and $^{3+3}J_{C2,C5}$, revealed the importance of internal electronegative substituents on $^3J_{CC}$ in saccharides, a factor heretofore unappreciated and one of importance to the interpretation of trans-glycoside $^3J_{COCC}$ in oligosaccharides.

6.2. Introduction

With increasing applications of ^{13}C -labeled saccharides in studies of their molecular structures and dynamics, ^{13}C - ^1H and ^{13}C - ^{13}C spin-spin coupling constants (J -couplings; J_{CH} , J_{CC}) are expected to increase in importance as tools to confirm and/or extend structural conclusions based on ^1H - ^1H spin-couplings, nuclear spin relaxation, ^1H - ^1H NOE, and other data. In contrast to some of the latter NMR parameters, however, present understanding of J_{CH} and J_{CC} in saccharides is incomplete, thereby limiting more routine use. This deficiency is more pronounced for J_{CC} than for J_{CH} primarily because measurement of the former generally requires isotopic labeling, while the latter can be obtained on samples at natural abundance, although often less conveniently and with reduced accuracy.¹



Scheme 6.1. Representative $^1J_{CC}$, $^2J_{CC}$, $^3J_{CC}$ and $^{3+3}J_{CC}$ in methyl β-D-glucopyranoside. Coupling pathways are highlighted in red and blue.

J_{CC} values in carbohydrates across one ($^1J_{CC}$), two ($^2J_{CCC}$, $^2J_{COC}$) and three ($^3J_{CCCC}$, $^3J_{COCC}$) bonds (Scheme 6.1) have been reported in aldohexopyranoses singly ^{13}C -labeled at the anomeric² (C1) and hydroxymethyl³ (C6) carbons. These studies have provided a limited data set with which to develop generalized structure/ J -coupling correlations. Bossennec *et al.*⁴ have reported complete sets of J_{CC} values in α-D-glucopyranose, β-D-glucopyranose, 1,2;5,6-di-*O*-isopropylidene-α-D-glucofuranose and 1,2;5,6-di-*O*-isopropylidene-3-*O*-benzyl-α-D-glucofuranose using uniformly ^{13}C -labeled compounds, and Krivden and Kalabin⁵ have reported some general correlations between $^1J_{CC}$ and carbohydrate structure. Church *et al.*⁶ have proposed an empirical (projection resultant; PR) method to predict $^2J_{CCC}$ and $^2J_{COC}$, Bose *et al.*⁷ and Cloran *et al.*⁸ have

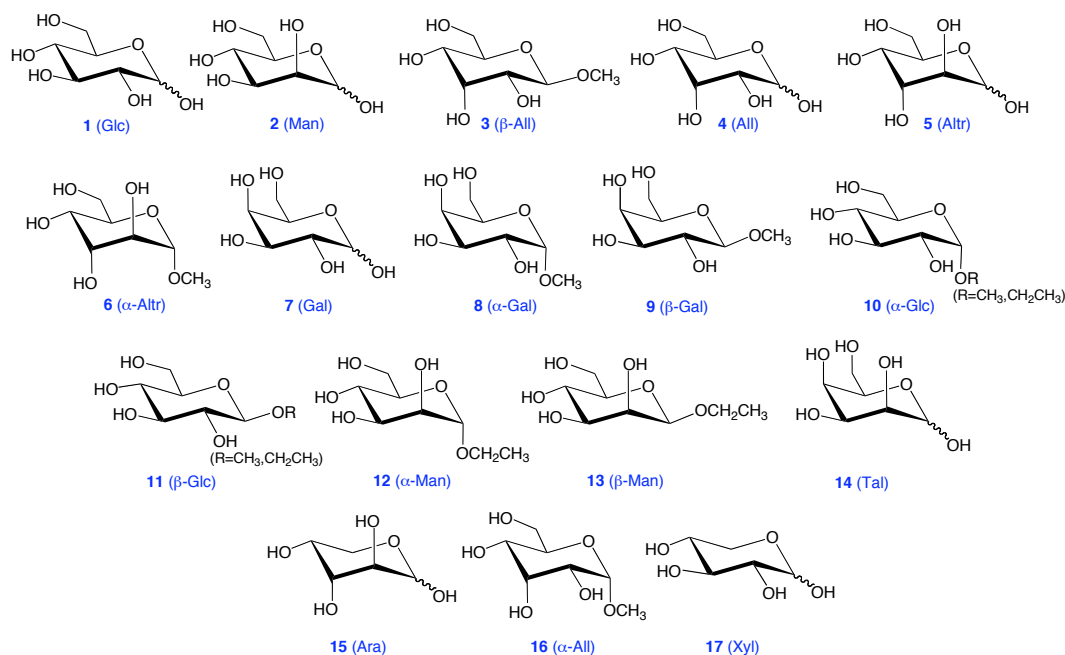
derived Karplus relationships for $^3J_{\text{COCC}}$, and experimental sign determinations for $^2J_{\text{CCC}}$ and $^2J_{\text{COC}}$ have been reported.^{9,10} A C-O-C bond-angle dependence has been identified for $^2J_{\text{COC}}$ in saccharides.¹¹ These earlier studies demonstrate the potential of J_{CC} as structural and conformational probes, especially in conformationally flexible systems (*e.g.*, α -idopyranosyl and aldofuranosyl rings), but more systematic investigations are needed to test the general applicability of these relationships and to develop new ones.

In this report, prior studies of ^{13}C - ^{13}C spin-couplings in saccharides are extended to a broader range of aldopyranosyl rings that were ^{13}C -labeled at sites other than the anomeric and exocyclic hydroxymethyl carbons. Correlations are derived between J_{CC} magnitude and sign and molecular structure, and new explanations for the structural dependencies of some of these couplings, notably $^2J_{\text{C3,C5}}$, $^3J_{\text{C1,C6}}$, $^3J_{\text{C3,C6}}$, $^{3+3}J_{\text{C1,C4}}$ and $^{3+3}J_{\text{C2,C5}}$, are proposed. Experimental observations are confirmed and/or extended by theoretical J_{CC} calculations using density functional theory (DFT). The results reported herein contribute to the long-range goal of providing complete interpretations of J_{CC} in saccharides in terms of structure and reactivity.

6.3. Experimental

6.3.1. Synthesis of ^{13}C -Labeled D-Aldoses and Methyl D-Aldopyranosides

Singly ^{13}C -labeled monosaccharides were prepared by chemical or chemo-enzymic methods. Each compound is identified in the following paragraph with the



pertinent literature reference for its synthesis. Throughout this manuscript, ^{13}C -isotopomers are identified by a compound number and a superscript denoting the location of the labeled carbon (*e.g.*, D-[1- ^{13}C]glucose is **1**¹).

D-[1- ^{13}C]Glucose (**1**¹);¹² D-[2- ^{13}C]glucose (**1**²);^{12,13} D-[3- ^{13}C]glucose (**1**³);¹²⁻¹⁴ D-[4- ^{13}C]glucose (**1**⁴);¹⁴ D-[5- ^{13}C]glucose (**1**⁵);¹⁴ D-[6- ^{13}C]glucose (**1**⁶);¹⁵ D-[1- ^{13}C]mannose (**2**¹);¹² D-[2- ^{13}C]mannose (**2**²);^{12,13} D-[3- ^{13}C]mannose (**2**³);¹²⁻¹⁴ D-[4- ^{13}C]mannose (**2**⁴);^{13,14} D-[5- ^{13}C]mannose (**2**⁵);^{13,14} D-[6- ^{13}C]mannose (**2**⁶);^{13,15} methyl β-D-[1- ^{13}C]allopypyranoside (**3**¹);^{12,16} methyl β-D-[2- ^{13}C]allopypyranoside (**3**²);^{12,13,16} methyl β-D-[3- ^{13}C]allopypyranoside (**3**³);^{12,13} D-[2- ^{13}C]allose (**4**²);^{12,13} D-[3- ^{13}C]allose (**4**³);^{12,13} D-[2- ^{13}C]altrose (**5**²);^{12,13} methyl α-D-[2- ^{13}C]altropyranoside (**6**²);^{12,13,16} D-[2- ^{13}C]galactose (**7**²);^{12,13} methyl α-D-[2- ^{13}C]galactopyranoside (**8**²);^{12,13,16} methyl α-D-[3- ^{13}C]galactopyranoside (**8**³);^{12,13,16} methyl β-D-[2- ^{13}C]galactopyranoside (**9**²);^{12,13,16} methyl β-D-[3- ^{13}C]galactopyranoside (**9**³);^{12,13,16} methyl/ethyl α-D-[2-

^{13}C]glucopyranoside (**10**²);^{12,13,16} methyl α -D-[3- ^{13}C]glucopyranoside (**10**³);^{12,13,16} methyl/ethyl β -D-[2- ^{13}C]glucopyranoside (**11**²);^{12,13,16} methyl β -D-[3- ^{13}C]glucopyranoside (**11**³);^{12,13,16} ethyl α -D-[2- ^{13}C]mannopyranoside (**12**²);^{12,13,16} ethyl β -D-[2- ^{13}C]mannopyranoside (**13**²);^{12,13,16} D-[2- ^{13}C]talose (**14**²);^{12,13} D-[3- ^{13}C]arabinose (**15**³);^{13,17} methyl α -D-[3- ^{13}C]allopyranoside (**16**³);^{12,13,16} and D-[3- ^{13}C]xylose (**17**³).^{13,17}

6.3.2. Measurement of ^{13}C - ^{13}C Spin-Coupling Constants

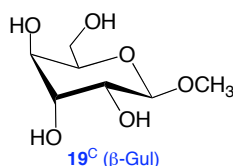
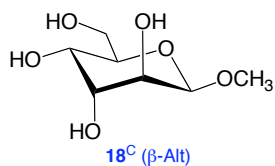
Solutions (~ 1 mL, ~ 0.1 M) of ^{13}C -labeled compounds in $^2\text{H}_2\text{O}$ (98 atom-%) were prepared and transferred to 3-mm NMR tubes. 1D $^{13}\text{C}\{^1\text{H}\}$ NMR spectra were obtained at 30 °C on a Varian Unity*Plus* 600 MHz FT-NMR spectrometer operating at 150.854 MHz for ^{13}C and equipped with a 3-mm $^{13}\text{C}/^1\text{H}$ microprobe (Nalorac). Spectra were collected with an ~ 10800 Hz spectral window and ~ 5 s recycle time (^{13}C T_1 s were estimated to be ~ 1 s¹⁸ under the experimental solution conditions). FIDs were zero-filled once or twice to give final digital resolutions of < 0.05 Hz/pt, and FIDs were processed with resolution enhancement (Gaussian or sine-bell functions) to improve resolution and facilitate the measurement of small J -couplings (Figure S1). The degree of enhancement was chosen empirically based on the observed spectral S/N and resolution. Line splittings > 0.8 Hz were typically resolved sufficiently to permit direct measurement of the J -coupling ± 0.1 Hz, but for smaller couplings, line widths (~ 1 Hz) similar in magnitude to the splitting gave larger errors (± 0.2 Hz). When possible, J -couplings were measured from different directions (*e.g.*, $^1J_{\text{C}2,\text{C}3}$ determined from [2- ^{13}C] and [3- ^{13}C]

isotopomers) and are reported independently to quantify internal consistency, accuracy, and reproducibility. Coupling signs were assigned based on the PR rule⁶ and/or on those predicted by DFT calculations (see below).

6.4. Computational

6.4.1. Selection and Geometric Optimization of Model Compounds

Theoretical calculations of J_{CC} were conducted on eleven fully substituted methyl D-aldohexopyranosides: β -All (**3^C**), α -Alt (**6^C**), α -Gal (**8^C**), β -Gal (**9^C**), α -Glc (**10^C**), β -

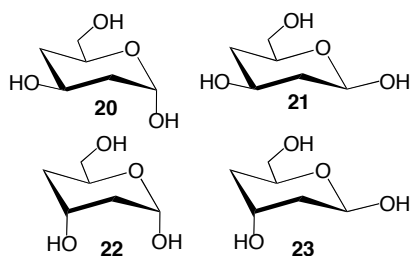


Glc (**11^C**), α -Man (**12^C**), β -Man (**13^C**), α -All (**16^C**), β -Alt (**18^C**) and β -Gul (**19^C**) (Scheme S1). The superscript “C” denotes structures

generated *in silico* to distinguish them from those studied experimentally. DFT calculations were conducted within *Gaussian03*¹⁹ using the B3LYP functional²⁰ and 6-31G* basis set²¹ for geometric optimization, as described previously.^{22,23} Initial geometric constraints were as follows: (a) all ring conformations were ⁴C₁, except for **6^C**, which was studied in the ¹C₄ ring form; (b) exocyclic hydroxymethyl (CH₂OH) groups were set in the *gt* conformation (C4-C5-C6-O6 torsion angle of 180°) in ⁴C₁ structures; in **6^C**, the O5-C5-C6-O6 torsion angle was set at 180° (*tg* conformation); (c) C2-C1-O1-CH₃ torsion angles were set at 180° (most favored geometry based on stereoelectronic considerations²⁴⁻²⁶); (d) C5-C6-O6-H torsion angles were set at 180°; and (e) the remaining H2-C2-O2-H, H3-C3-O3-H and H4-C4-O4-H torsion angles were

set arbitrarily at 180° to minimize intramolecular H-bonding. Since J_{CC} values involving internal ring carbons were a focus of attention, fully substituted model structures were chosen for study despite potential complications in the analysis of computed couplings caused by the arbitrary choice of exocyclic C-O torsions. To address effects caused by the latter, two sets of geometry optimizations were performed on each structure, denoted FIXED and FLOAT (see below). In the FIXED series, all initial molecular parameters were optimized except for the exocyclic C-O torsions, which were fixed at their initial values. In the FLOAT series, all molecular parameters, including the exocyclic C-O torsions, were optimized. This approach produced the 22 optimized structures shown in Schemes S1 and S2.

An additional series of calculations was conducted on aldohexopyranosyl rings lacking hydroxyl groups at C2 and C4. These structures mimic α -*gluco* (**20**), β -*gluco*



(**21**), α -*allo* (**22**) and β -*allo* (**23**) ring configurations.

In these calculations, the O5-C5-C6-O6 torsion angle was rotated in 30° increments through 360° and held constant, and all remaining molecular parameters were optimized. Initial C4-C3-O3-H and C5-C6-O6-H torsions angles were set at 180°.

6.4.2. Theoretical Calculations of ^{13}C - ^{13}C Spin-Coupling Constants

J -Coupling constants were calculated in 3^{C} , 6^{C} , 8^{C} , 9^{C} , 10^{C} , 11^{C} , 12^{C} , 13^{C} , 16^{C} , 18^{C} and 19^{C} (Schemes S1 and S2), and in **20-23** using *Gaussian03*.¹⁹ Both the Fermi and non-Fermi contact terms were recovered, and the reported values contain both contributions and are unscaled.

6.5. Results and Discussion

6.5.1. General Observations in **1** and **2**

J_{CC} values in α - and β -gluco- (**1** α , **1** β) and manno- (**2** α , **2** β) pyranoses singly ^{13}C -labeled at C1-C6 are listed in Table 6.1. General trends observed in these data are summarized as follows.

$^1J_{CC}$ ranges from 37.7 - 46.7 Hz, with $^1J_{\text{C1,C2}} > ^1J_{\text{C5,C6}} > ^1J_{\text{C2,C3}} \approx ^1J_{\text{C3,C4}} \approx ^1J_{\text{C4,C5}}$. Conversion of reducing sugars to methyl glycosides increases $^1J_{\text{C1,C2}}$ by 0.5 - 1 Hz, with negligible effects on the remaining couplings.

$^2J_{\text{C1,C5}}$ is either small or negative (~ -2 Hz) and depends on anomeric configuration (more negative in α -anomers). $^2J_{\text{CCC}}$ ranges from +4.5 Hz ($^2J_{\text{C1,C3}}$) to small or zero values ($^2J_{\text{C4,C6}}$), and is sensitive to configuration at the coupled carbon(s) (*e.g.*, $^2J_{\text{C1,C3}}$ and $^2J_{\text{C2,C4}}$) and configuration at remote carbons. For example, $^2J_{\text{C3,C5}}$ is ~ 0.8 Hz larger in β -anomers than in α -anomers even though C1 is not present in the coupling pathway.

$^3J_{\text{C1,C6}}$ depends on anomeric configuration, with α -pyranoses giving couplings ~ 1 Hz smaller (~ 3.3 Hz) than β -pyranoses (~ 4.2 Hz). $^3J_{\text{C3,C6}}$ has magnitudes similar to $^3J_{\text{C1,C6}}$ and shows a small dependence on anomeric configuration (α couplings are smaller than β couplings by ~ 0.5 Hz). The dual-pathway couplings, $^{3+3}J_{\text{C1,C4}}$ and $^{3+3}J_{\text{C2,C5}}$, are small, and are observed only in some ring configurations (*e.g.*, $^{3+3}J_{\text{C1,C4}}$ in **2** α).

TABLE 6.1. ^{13}C - ^{13}C SPIN-COUPPLINGS IN SELECTIVELY ^{13}C -LABELED D-GLUCO- (1α , 1β) AND D-MANNOPYRANOSIDES (2α , 2β) AND METHYL β -D-ALLOPYRANOSIDE 3^1

Coupling	α -Glc p (1α)	β -Glc p (1β)	α -Man p (2α)	β -Man p (2β)	Me β -Allo p (3^1)
$^1J_{\text{C}1,\text{C}2}$	46.2 / 46.2 ^b 46.7 ^e	46.0 / 46.0 46.9	46.7 / 46.7 47.2	42.7 / 42.7 43.8	48.1
$^2J_{\text{C}1,\text{C}3}$	<i>nc</i> / <i>nc</i> <i>nc</i>	(+) 4.5 / (+) 4.5 (+) 4.5	<i>nc</i> / <i>nc</i> <i>nc</i>	(+) 4.0 / (+) 4.0 +3.9	<i>nc</i>
$^2J_{\text{C}1,\text{C}5}$	(-) 1.8 (-) 2.0	<i>nc</i> <i>nc</i>	(-) 2.0 (-) 2.0	<i>nc</i> <i>nc</i>	(\pm) 0.7
$^3+^3J_{\text{C}1,\text{C}4}$	<i>nc</i> <i>nc</i>	<i>nc</i> <i>nc</i>	0.9 0.7	<i>nc</i> <i>nc</i>	<i>nc</i>
$^3J_{\text{C}1,\text{C}6}$	3.3 3.3	4.1 4.1	3.3 3.2	3.9 4.0	3.5
$^1J_{\text{C}2,\text{C}3}$	38.2 / 38.2 ^c 38.2	38.8 / 38.8 ^c 38.9	37.7 / 37.7 ^c 37.8	38.2 / 38.8 ^c 38.2	
$^2J_{\text{C}2,\text{C}4}$	(+) 3.1 / (+) 3.1 (+) 3.0	(+) 2.8 / (+) 2.8 (+) 2.7	<i>nc</i> / <i>nc</i> <i>nc</i>	<i>br</i> / <i>nc</i> (\pm) 0.3	
$^3+^3J_{\text{C}2,\text{C}5}$	<i>nc</i> <i>nc</i>	<i>nc</i> <i>nc</i>	<i>br</i> <i>nc</i>	<i>nc</i> <i>nc</i>	
$^1J_{\text{C}3,\text{C}4}$	38.6 / 38.6 ^d 38.5 ^f	39.4 / 39.3 ^d 39.3	39.9 / 39.9 ^d	40.3 / 40.4 ^d	
$^2J_{\text{C}3,\text{C}5}$	(+) 1.7 (+) 1.8	(+) 2.5 (+) 2.4	(+) 1.7	(+) 2.7	
$^3J_{\text{C}3,\text{C}6}$	3.8 3.7	4.3 4.2	3.7	4.2	
$^1J_{\text{C}4,\text{C}5}$	40.4 40.4	40.9 41.0	40.2	40.9	
$^2J_{\text{C}4,\text{C}6}$	<i>nc</i> <i>nc</i>	<i>nc</i> <i>nc</i>	<i>nc</i>	<i>nc</i>	
$^1J_{\text{C}5,\text{C}6}$	43.6 43.3	43.0 43.3	43.3	43.3	

^aIn Hz \pm 0.1 Hz determined in D-glucose and D-mannose selectively ^{13}C -labeled at C1-C6; in $^2\text{H}_2\text{O}$ at $\sim 25^\circ\text{C}$. An entry of *nc* implies that $J < 0.6$ Hz; *br* denotes a broadened signal containing an unresolved coupling. Signs of $^2J_{\text{CC}}$ are given in parenthesis. ^bCouplings in blue were reported previously (refs. 2, 3). ^cMeasured in the [$3\text{-}^{13}\text{C}$]isotopomer. ^dMeasured in the [$4\text{-}^{13}\text{C}$]isotopomer. ^eCouplings in brown are for the corresponding ethyl glycoside (ref. 7). ^fCouplings in green are for the corresponding methyl glycoside (ref. 28).

While studies of *gluco* and *manno* configurations provide insight into the dependencies of J_{CC} on saccharide structure, studies limited to these configurations provide incomplete data on which to develop general structural arguments. Furthermore, since not all structural effects can be studied experimentally, critical complementary

information can be obtained from theoretical calculations of J_{CC} using DFT methods.^{22,23} In the following discussion, experimental and theoretical analyses of J_{CC} are more fully developed and integrated in a broader range of structures, with emphasis on ${}^2J_{CC}$, ${}^3J_{CC}$ and ${}^{3+3}J_{CC}$.

6.5.2. ${}^2J_{CC}$ Coupling Constants

${}^2J_{C1,C3}$ and ${}^2J_{C2,C4}$ in aldopyranosyl rings are influenced mainly by the *orientation* of electronegative substituents attached to the coupled carbons.^{6,15} Ring configurations having equatorial substituents (*e.g.*, β -D-*gluco*) give strongly positive ${}^2J_{C1,C3}$ and ${}^2J_{C2,C4}$ ($\sim +2$ -4 Hz) (Tables 6.1 and 6.2).^{6,9} Conversion of one or both substituents (see **1 α** , **2 α** and **3¹** in Table 6.1) to axial orientations reduces the coupling, with di-axial arrangement eliciting negative couplings⁶ (*e.g.*, ${}^2J_{C1,C3} = -2.4$ Hz in **4 α^3** , ${}^2J_{C2,C4} = -2.1$ Hz in **14 α^2**) (Tables 6.2 and 6.4).

Computed ${}^2J_{C1,C3}$ and ${}^2J_{C2,C4}$ (Table 6.3) support the conclusions drawn from an analysis of experimental couplings based on the PR method.⁶ ${}^2J_{C1,C3}$ in **9^C**, **11^C** and **13^C** is moderately large and positive, whereas it is negative in **16^C**. Comparatively small positive (or near zero) ${}^2J_{C1,C3}$ are computed in **3^C**, **8^C**, **10^C**, **12^C**, **18^C** and **19^C**. Interestingly, ${}^2J_{C1,C3}$ in **6^C** is much larger than found experimentally, suggesting that the 4C_1 conformation, in which both the C1-O1 and C3-O3 bonds are axial, contributes to the experimental coupling; in the 4C_1 form, ${}^2J_{C1,C3}$ is probably negative (analogous to **16^C**). Computed ${}^2J_{C2,C4}$ is moderately large and positive in **10^C** and **11^C**, and much smaller (or zero) in structures bearing an axial C-O bond at either C2 or C4.

TABLE 6.2. ^{13}C - ^{13}C SPIN-COUPPLINGS INVOLVING C2 OF
ALDOHEXOPYRANOSSES AND ALKYL ALDOHEXOPYRANOSIDES

compound	$^1J_{\text{C2,C1}}$	$^1J_{\text{C2,C3}}$	$^2J_{\text{C2,C4}}$	$^{3+3}J_{\text{C2,C5}}$	$^3J_{\text{C2,Me}}$
β -D-Allop (4 β^2)	47.3 ^b				
Me β -D-Allop ^c (3 2)	48.2	38.2	(+) 2.4	~ 0	3.1
α -D-Altrop (5 α^2)	46.1	obs ^d	~ 0	1.6	
Me α -D-Altrop (6 2)	47.7		~ 0	1.5	3.5
β -D-Altrop (5 β^2)	43.8 (43.9) ^b	obs	~ 0	~ 0	
α -D-Galp (7 α^2)	46.0 (46.0) ^b	38.7	~ 0	1.5	
Me α -D-Galp (8 2)	46.4	39.5	<i>nc</i>	1.3	2.9
β -D-Galp (7 β^2)	45.9 (45.9) ^b	39.7	~ 0	~ 0	
Me β -D-Galp (9 2)	46.7	39.9	<i>nc</i>	<i>nc</i>	3.2
Et α -D-Glcp ^e (10 2)	46.7	38.2	(+) 3.1	<i>nc</i>	2.9
Et β -D-Glcp ^e (11 2)	46.9	38.9	(+) 2.7	<i>nc</i>	3.1
Et α -D-Manp ^e (12 2)	47.2	37.8	<i>nc</i>	<i>nc</i>	
Et β -D-Manp ^e (13 2)	43.8	38.2	(\pm) 0.3	<i>nc</i>	
α -D-Talop (14 α^2)	46.4 (46.5) ^b	37.8	(-) 2.1	1.5	
β -D-Talop (14 β^2)	42.3 (42.3) ^b	38.1	(-) 2.2	~ 0	

^a In Hz \pm 0.1 Hz; in $^2\text{H}_2\text{O}$ at ~ 25 °C. ^b Coupling reported in ref 2.
^c J_{CC} values indicate that the reported C2 and C3 chemical shifts of **3** (ref 39) are reversed. ^d Obs indicates that coupling could not be measured due to an obscured signal. ^e Couplings reported in ref 7. See definition of *nc* in Table 1.

TABLE 6.3. COMPUTED $^2J_{CC}$ VALUES IN MODEL ALDOPYRANOSIDES AND
COMPARISON WITH EXPERIMENTAL COUPLINGS

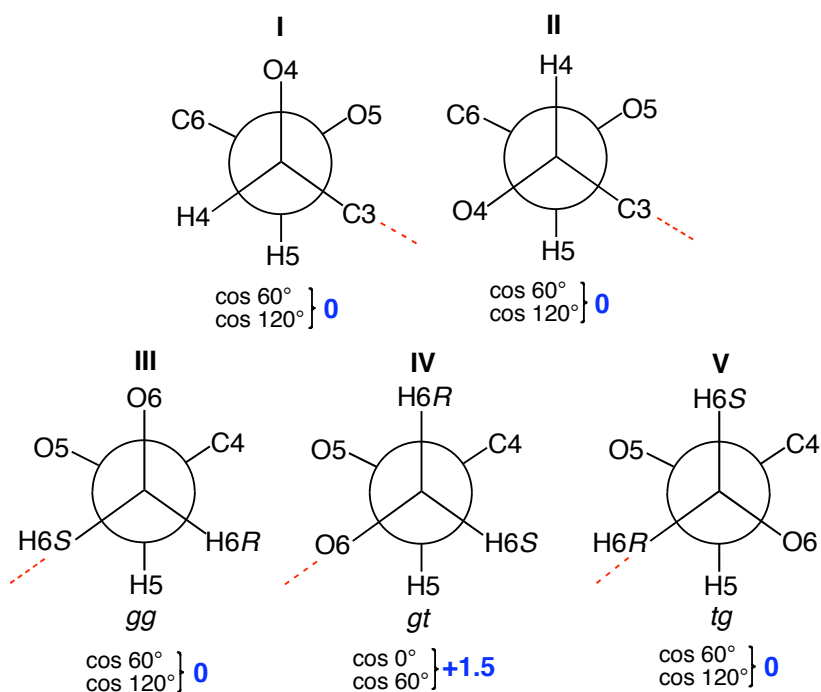
$^2J_{CC}$ (Hz)	β -All 3^C FIXED	β -All 3^C FLOAT	β -All 3	α -Alt 6^C FIXED	α -Alt 6^C FLOAT	α -Alt 6	α -Gal 8^C FIXED	α -Gal 8^C FLOAT	α -Gal 8	β -Gal 9^C FIXED	β -Gal 9^C FLOAT	β -Gal 9
$^2J_{C1,C3}$	0.9	0.9	<i>nc</i>	6.8 ^a	3.6	<i>nc</i> *	0.9	0.5	<i>nc</i> *	7.1	6.4	+4.6*
$^2J_{C1,C5}$	-0.6	-0.5	± 0.7	-1.2	-1.4	-1.6*	-2.3	-2.4	-1.9*	-0.7	-1.1	<i>nc</i> *
$^2J_{C2,C4}$	1.0	0.6	+2.4	0.2	0.0	~ 0	0.6	-0.8	<i>nc</i>	0.3	-1.0	<i>nc</i>
$^2J_{C3,C5}$	-1.2	-1.1	-1.0	0.7	1.1		0.8	0.5	<i>nc</i>	1.1	0.9	+1.6
$^2J_{C4,C6}$	3.8	3.8	<i>nc</i> *	2.5	3.6	1.7*	1.0	1.5	<i>nc</i> *	1.2	1.6	<i>nc</i> *
	α -Glc 10^C FIXED	α -Glc 10^C FLOAT	α -Glc 10	β -Glc 11^C FIXED	β -Glc 11^C FLOAT	β -Glc 11	α -Man 12^C FIXED	α -Man 12^C FLOAT	α -Man 12	β -Man 13^C FIXED	β -Man 13^C FLOAT	β -Man 13
$^2J_{C1,C3}$	0.6	0.7	<i>nc</i>	6.5	3.7	+4.5	-0.7	-0.3	<i>nc</i>	2.9	2.4	+3.9
$^2J_{C1,C5}$	-2.2	-2.3	-2.0	-0.5	-0.7	<i>nc</i>	-2.1	-2.2	-2.0	-0.3	-0.3	<i>nc</i>
$^2J_{C2,C4}$	3.8	3.0	+3.0	3.0	1.8	+2.7	0.4	0.1	<i>nc</i>	0.1	-0.2	± 0.3
$^2J_{C3,C5}$	3.1	1.0	+1.8	3.7	1.8	+2.5*	3.3	1.0	+1.7*	4.1	1.7	+2.7*
$^2J_{C4,C6}$	2.1	1.8	<i>nc</i>	2.6	2.5	<i>nc</i>	2.1	1.7	<i>nc</i> *	2.4	2.0	<i>nc</i> *
	α -All 16^C FIXED	α -All 16^C FLOAT	α -All 16	β -Alt 18^C FIXED	β -Alt 18^C FLOAT	β -Gul 19^C FIXED	β -Gul 19^C FLOAT					
$^2J_{C1,C3}$	-1.5	-2.0	-2.4	-0.1	0.1	1.6	1.7					
$^2J_{C1,C5}$	-2.1	-2.1		-0.9	-0.9	-1.1	-1.1					
$^2J_{C2,C4}$	1.0	0.4		-0.6	-0.5	-0.6	-0.4					
$^2J_{C3,C5}$	-0.5	-0.6	-1.1	0.1	0.1	-1.0	-1.0					
$^2J_{C4,C6}$	3.0	2.9	<i>nc</i> *	3.3	3.3	1.6	1.8					

^aValues in blue are couplings in FIXED and FLOAT structures (Schemes S1 and S2) that differ by > 0.5 Hz. *In the corresponding reducing sugar. See definition of *nc* in Table 1.

Computed $^2J_{C1,C5}$ (Table 6.3) generally confirm a dependence on anomeric configuration, with couplings of ~ -2 Hz observed in α -pyranoses and essentially no coupling observed in β -pyranoses (4C_1 form). $^2J_{C1,C5}$ is moderately large and negative in the 1C_4 form of **6^C**, and in **19^C**. These data, along with the experimentally observed $^2J_{C1,C5}$ of ± 0.7 Hz in **3**, suggest that $^2J_{C1,C5}$ may be observed in some ring structures bearing an equatorial C1-O1 bond. The large coupling predicted in **6^C** (1C_4 form) may

be partly caused by the larger C1-O5-C5 bond angle in this structure ($\sim 117^\circ$) compared to the other structures (114° - 115°). As shown previously,¹¹ $^2J_{\text{COC}}$ depends on the C-O-C bond angle, with increasing angles correlated with more negative couplings.

Experimental $^2J_{\text{C4,C6}}$ in most D-aldohexopyranosyl rings ($^4\text{C}_1$ forms) is small or zero (Table 6.1),³ and the PR rule⁶ provides an explanation for this observation. One-half of the PR component yields the same projection (0) for axial and equatorial OH groups at C4 (structures **I** and **II**, respectively) (Scheme 6.2). The second half of the PR

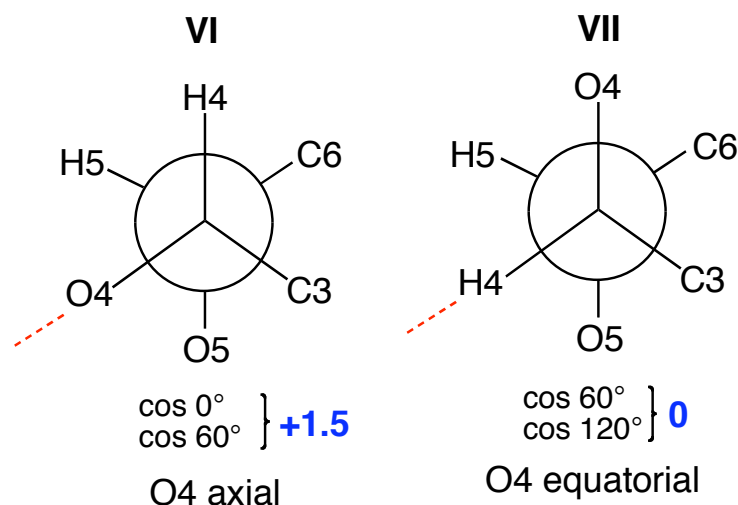


Scheme 6.2. Application of the Projection Resultant (PR) Method to $^2J_{\text{C4,C6}}$ in D-Aldohexopyranosyl Rings ($^4\text{C}_1$)

component depends on hydroxymethyl group conformation, with values of 0, +1.5 and 0 correlating with *gg*, *gt* and *tg* (structures **III-V**, respectively). Averaging of **I** (or **II**) with different populations of *gg*, *gt* and *tg* will lead to small $^2J_{\text{C4,C6}}$, since averaged projection

resultants of +0.5-+1 should yield small couplings (PR values of 0 yield \sim 2 Hz couplings, whereas PR values of +1.5 yield \sim +2 Hz couplings). This interpretation assumes that the PR correlation, which was derived mainly from $^2J_{C1,C3}$ data, can be applied to $^2J_{C4,C6}$. This uncertainty notwithstanding, the prediction appears consistent with experimental observations.

The above arguments concerning $^2J_{C4,C6}$ require modification for pyranosyl rings in the 1C_4 conformation, and relevant projections are shown in Scheme 6.3. Structures having an equatorial O4 (**VII**) should exhibit coupling behavior similar to 4C_1 structures,



Scheme 6.3. Projections for $^2J_{C4,C6}$ in D-Aldohexopyranosyl Rings (1C_4)

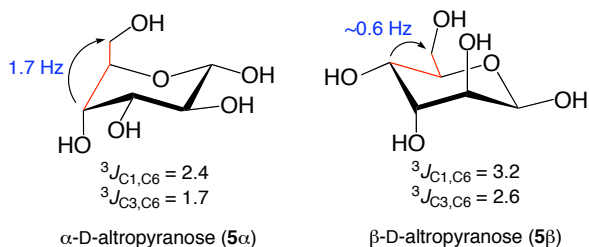
assuming similar rotameric populations about the C5-C6 bond. Indeed, $^2J_{C4,C6}$ in α -D-idopyranose is \sim 0.7 Hz.³ However, for structures bearing an axial O4 (**VI**), PR values are more positive (maximum of +3.0) than the \sim +1 observed in 4C_1 forms, especially if

the *gt* rotamer is highly preferred. This situation pertains to the α -D-altropyranosyl ring that exists partly in the 1C_4 or related

twist-boat form in solution.²⁷ ${}^2J_{C4,C6} =$

1.7 Hz in α -D-altropyranose **5 α**

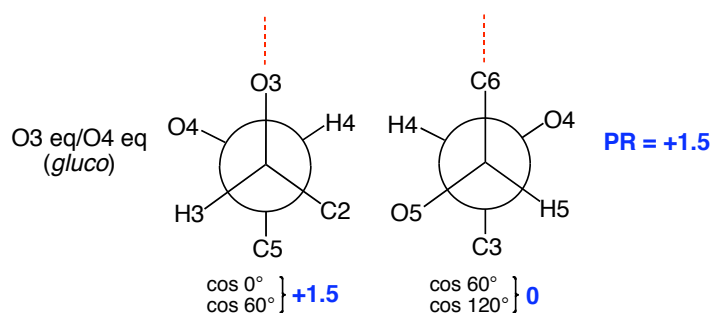
(presumably positive in sign), and ~ 0.6



Hz in β -D-altropyranose **5 β** ,³ suggesting a greater percentage of 1C_4 conformer in aqueous solutions of the former. This conclusion is supported by ${}^3J_{C1,C6}$ and ${}^3J_{C3,C6}$, which are both smaller in **5 α** than in **5 β** .

Inspection of computed ${}^2J_{C4,C6}$ (Table 6.3) reveals positive couplings ranging from 1.0 – 3.8 Hz. These couplings are pertinent to 4C_1 ring forms *with exocyclic CH₂OH conformation in the gt form in nearly all cases*. Thus, a correlation of PR +1.5 with ${}^2J_{C4,C6}$ of $\sim +2$ Hz is confirmed by the calculations. Variability in the computed couplings presumably reflects the slightly different C5-C6 torsion angles in the optimized structures, although possibly other unidentified structural factors may be at work. The large positive coupling predicted in 1C_4 conformations is also confirmed for rings bearing an axial C4-O4 bond. The computed ${}^2J_{C4,C6}$ in 6C is $\sim +3$ Hz, even for a CH₂OH conformation in the *tg* state. Presumably this coupling would be larger in the *gt* form.

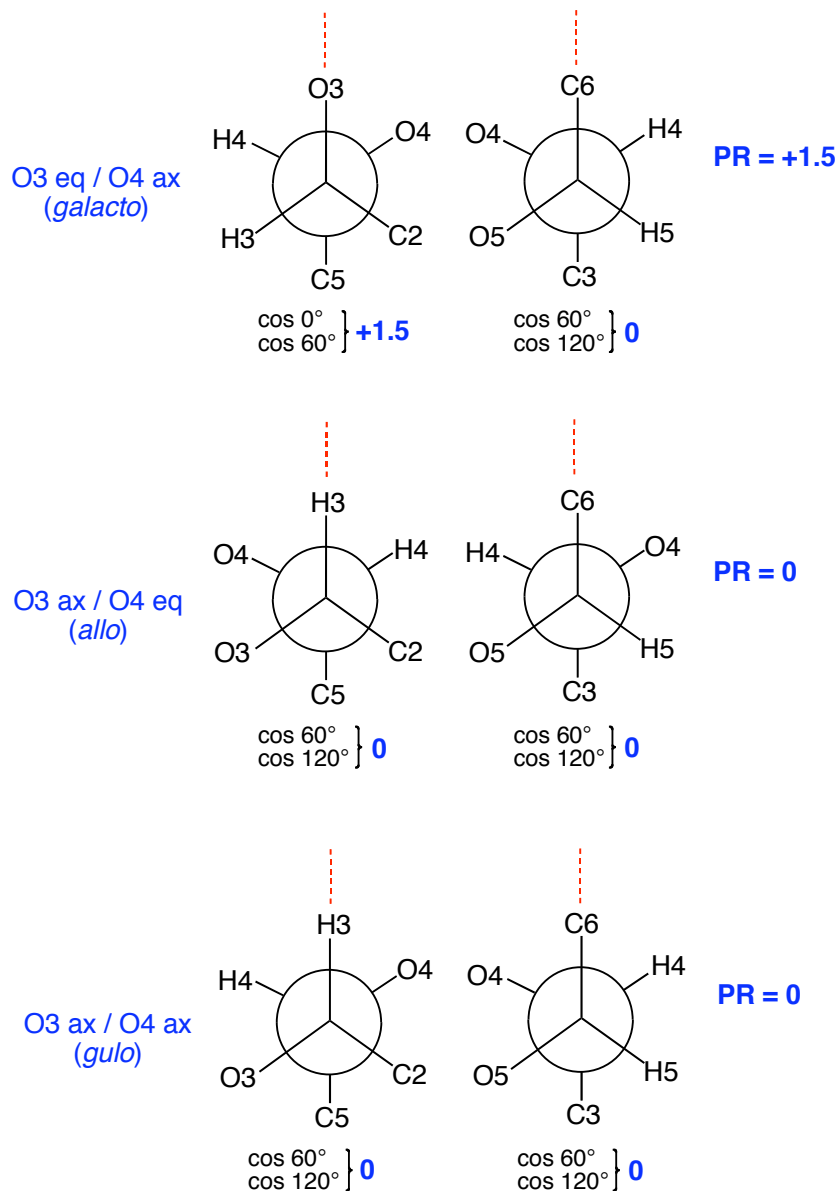
The remaining ${}^2J_{CCC}$ in aldopyranosyl rings is ${}^2J_{C3,C5}$, whose properties have not been studied previously. Application of the PR method to this coupling in rings having the D-*gluco* configuration (Scheme 6.4) gives a PR value of +1.5, which translates into a predicted ${}^2J_{C3,C5}$ of $\sim +2$ Hz. Similar treatment of the D-*galacto* configuration (O4 axial) yields the same predicted magnitude and sign (Scheme 6.5). However, rings



Scheme 6.4. Application of the Projection Resultant (PR) Method to $^2J_{C3,C5}$ in D-Glucopyranosyl Rings

having either O3 axial, or both O3 and O4 axial, yield PR values of 0, translating into $^2J_{C3,C5}$ of ~ -2 Hz. Thus, $^2J_{C3,C5}$ is expected to be negative in D-*allo* (O3 axial) and D-*gulo* (O3 and O4 axial) ring configurations. In the latter, deviation from prediction would occur if the ring assumes a conformation other than, or in addition to, 4C_1 (likely for α -D-*gulo*).

In $1\alpha/1\beta$ and $2\alpha/2\beta$, $^2J_{C3,C5}$ shows a small dependence on anomeric configuration, with α -anomers giving couplings $\sim 0.8 - 1.0$ Hz smaller than β -anomers (Table 6.1). Similar absolute couplings and trends are observed in **10/11** and **17 α /17 β** (Table 6.4). Conversion of O4 to an axial orientation reduces $^2J_{C3,C5}$ by ~ 1 Hz despite PR values identical to those for *gluco* rings (see above), but the anomeric effect is maintained (~ 0 Hz in **8**, $+1.6$ Hz in **9**) (Table 6.4). However, conversion of O3 to an axial orientation eliminates the effect, with **3**, **4 α** , **4 β** and **16** giving virtually identical couplings (~ -1.0 Hz) (Table 6.4).



Scheme 6.5. Application of the Projection Resultant (PR) Method to $^2J_{C3,C5}$ in Other D-Aldohexopyranosyl Rings

Computed $^2J_{C3,C5}$ largely confirm the predictions based on the empirical PR method (Table 6.3). Couplings are positive for rings having the *gluco*, *manno*, and *galacto* configurations, and negative for *allo* and *gulo* configurations. $^2J_{C3,C5}$ in ^{18}C is unexpectedly small, suggesting that a remote effect from an axial C2-O2 bond may exist;

TABLE 6.4. ^{13}C - ^{13}C SPIN-COUPPLINGS INVOLVING C3OF
ALDOHEXOPYRANOSSES AND METHYL ALDOHEXOPYRANOSIDES

compound	$^1J_{\text{C3,C2}}$	$^1J_{\text{C3,C4}}$	$^2J_{\text{C3,C1}}$	$^2J_{\text{C3,C5}}$	$^3J_{\text{C3,C6}}$
α -D-Arabinop ^b (15 α^3)				<i>nc</i>	
α -D-Allop (4 α^3)	37.0	37.6	(-) 2.4	(-) 1.1	2.7
Me α -D-Allop ^c (16 β^3)	37.1	37.5	(-) 2.6	(-) 1.1	2.8
β -D-Allop (4 β^3)	<i>obs</i>	38.6	<i>nc</i>	(-) 1.1	2.9
Me β -D-Allop (3 β^3)	38.4	38.5	<i>nc</i>	(-) 1.0	3.0
Me α -D-Galp ^d (8 2,3)	39.5		<i>nc</i>	<i>nc</i>	3.8
Me β -D-Galp ^d (9 2,3)	39.9	38.6	(+) 4.7	(+) 1.6	4.2
Me α -D-Glcp ^d (10 β^3)	38.3	38.5	<i>nc</i>	(+) 1.8	3.7
Me β -D-Glcp ^d (11 β^3)	39.0	39.3	(+) 4.6	(+) 2.4	4.2
α -D-Xylop ^b (17 α^3)				(+) 0.9	
β -D-Xylop ^b (17 β^3)				(+) 2.0	

^aIn Hz \pm 0.1 Hz; in $^2\text{H}_2\text{O}$ at $\sim 25^\circ\text{C}$; *nc* denotes no coupling was observed ($J < 0.6$ Hz).

^bCoupling reported in ref. 3. ^c J_{CC} values indicate that the reported C4 and C5 chemical shifts for **16** (ref. 36) are reversed. ^dCouplings reported in ref. 28.

this was not confirmed experimentally. The computed couplings also support the contention that $^2J_{\text{C3,C5}}$ depends on anomeric configuration. For α/β pairs in the *gluco* and *manno* configurations, the α -pyranose consistently gave the smaller coupling. Data for the *galacto* configuration were less conclusive.

6.5.3. $^3J_{CC}$ Coupling Constants

$^3J_{C1,C6}$ is ~ 0.7 Hz larger in **1 β** and **2 β** than in **1 α** and **2 α** (Table 6.1) despite similar C-O-C-C dihedral angles. The terminal “in-plane” O1 in β -anomers enhances this coupling. This effect also operates for $^3J_{C3,C6}$, with couplings ~ 0.9 Hz smaller in **3** and **16** than in **10** and **11**.

$^3J_{C1,C6}$ is modulated by C3 configuration. For example, $^3J_{C1,C6}$ is 3.3 and 4.1 Hz in **1 α** and **1 β** , but 2.9 and 3.3 Hz in **4 α** and **4 β** .^{3,15} $^3J_{C1,C6}$ is also small (3.2 Hz) in β -D-altropyranose,^{3,15} reinforcing the conclusion that an axial O3 truncates this coupling. While O6 orientation also affects $^3J_{C1,C6}$ (a terminal “in-plane” O6 found in the *tg* rotamer enhances the coupling; see Figure 6.1), this factor cannot be responsible for the observed differences, since CH₂OH conformation in *gluco* and *allo* structures is similar based on J_{HH} analysis ($^3J_{H5,H6}$ and $^3J_{H5,H6'}$ are 2.2 Hz and 6.0 Hz in methyl β -gluco- and β -allopysanosides¹⁶). Furthermore, since O6 is expected to be mostly out-of-plane in β -*gluco* structures (*gg* and *gt* rotamers are favored²⁸), $^3J_{C1,C6}$ cannot be reduced further in β -*allo* configurations by O6 effects.

Calculated $^3J_{CC}$ (Table 6.5) shed further light on this issue. In structures having the *gluco*, *manno*, and *galacto* configurations, $^3J_{C3,C6} > ^3J_{C1,C6}$ despite similar dihedral angles ($\sim 175^\circ$). However, all of the computed structures contain the exocyclic CH₂OH group in the *gt* conformation (see Computational), placing the terminal O6 out-of-plane for the C1-O5-C5-C6 pathway and in-plane for the C3-C4-C5-C6 pathway. The terminal “in-plane” effect contributes ~ 0.7 Hz to the coupling.⁷ When this factor is taken into account, computed $^3J_{C1,C6}$ and $^3J_{C3,C6}$ become similar in magnitude. Importantly,

TABLE 6.5. COMPUTED $^3J_{CC}$ AND $^3+^3J_{CC}$ IN MODEL ALDOHEXOPYRANOSIDES AND COMPARISON WITH EXPERIMENTAL COUPLINGS

$^3J_{CC}$ or $^3+^3J_{CC}$ (Hz)	β -All 3^C FIXED	β -All 3^C FLOAT	β -All 3	α -Alt 6^C FIXED	α -Alt 6^C FLOAT	α -Alt 6	α -Gal 8^C FIXED	α -Gal 8^C FLOAT	α -Gal 8	β -Gal 9^C FIXED	β -Gal 9^C FLOAT	β -Gal 9
$^3J_{C1,C6}$	3.6	3.8	3.5	1.1	0.8	2.4*	3.9	4.0	3.6*	4.5	4.6	4.4*
$^3J_{C3,C6}$	3.4	3.4	3.0*	0.3	0.2	1.7*	3.9	4.4	3.7*	4.0	4.7	4.1*
$^3+^3J_{C1,C4}$	-0.3	-0.2	nc*	0.2	0.7	1.0*	0.0	0.3	nc*	-0.4	-0.1	nc*
$^3+^3J_{C2,C5}$	0.0	0.1	~0	0.5	0.8	1.5	1.5 ^a	2.1	1.3	0.2	0.6	nc
	α -Glc 10^C FIXED	α -Glc 10^C FLOAT	α -Glc 10	β -Glc 11^C FIXED	β -Glc 11^C FLOAT	β -Glc 11	α -Man 12^C FIXED	α -Man 12^C FLOAT	α -Man 12	β -Man 13^C FIXED	β -Man 13^C FLOAT	β -Man 13
$^3J_{C1,C6}$	3.7	3.9	3.3	4.4	4.4	4.1	3.7	3.7	3.2	4.4	4.4	4.0
$^3J_{C3,C6}$	4.3	4.8	3.7	4.6	5.1	~4.3	4.0	4.5	3.7*	4.3	4.8	4.2*
$^3+^3J_{C1,C4}$	-0.3	-0.2	nc	-0.7	-0.4	nc	0.7	0.9	0.7	0.1	0.4	nc
$^3+^3J_{C2,C5}$	0.0	0.4	nc	-0.5	-0.3	nc	0.5	1.0	nc	-0.1	0.0	nc
	α -All 16^C FIXED	α -All 16^C FLOAT	α -All 16	β -Alt 18^C FIXED	β -Alt 18^C FLOAT	β -Alt 5	β -Gul 19^C FIXED	β -Gul 19^C FLOAT				
$^3J_{C1,C6}$	3.2	3.3	2.9*	3.6	3.8	3.2*	3.8	4.0				
$^3J_{C3,C6}$	3.2	3.2	2.8*	3.3	3.5	2.6*	2.4	2.5				
$^3+^3J_{C1,C4}$	0.4	0.8	nc*	1.6	1.7	1.3*	0.3	0.3				
$^3+^3J_{C2,C5}$	1.1	1.4	1.6*	0.1	0.2		1.0	1.1				

^aValues shown in blue are couplings in FIXED and FLOAT structures (Schemes S1 and S2) that differ by > 0.5 Hz. *In the corresponding reducing sugar. See definition of nc in Table 1.

$^3J_{C3,C6}$ is reduced substantially in the *allo* (**3**^C and **16**^C) and *gulo* (**19**^C) configurations relative to **10**^C and **11**^C, as expected since O3 is not a terminal “in-plane” substituent in the former. $^3J_{C3,C6}$ also differs between the *gulo* and *allo* configurations, with the former couplings smaller, in agreement with experimental results and with prior claims that a diaxial O3/O4 combination significantly reduces $^3J_{C3,C6}$ relative to the axial O3/equatorial O4 case for a C-C-C-C torsion angle of $\sim 180^\circ$.³

$^3J_{C3,C6}$ is smaller than $^3J_{C1,C6}$ in **6**^C despite similar torsion angles ($\sim 60^\circ$). This observation is attributed largely to the effect of internal substituents on $^3J_{CCCC}$. Specifically, in **6**^C, O4 is anti to one of the coupled carbons (C6), and *this arrangement is expected to decrease the gauche C-C-C-C coupling by ~ 1 -1.5 Hz relative to the case when O4 is out-of-plane (i.e., when O4 is equatorial)*. This effect, which has been observed for gauche $^3J_{HH}$,²⁹ has important implications for the interpretation of $^3+^3J_{CC}$, as discussed below.

Computed $^3J_{C1,C6}$ in *allo* structures appear uniformly smaller than values computed in *gluco*, *manno* and *galacto* configurations (Table 6.5), in agreement with experimental observations. The remote effect of an axial O3 on the C1-O5-C5-C6 coupling pathway is captured by the DFT calculations. A similar effect is observed in **19**^C.

The above-noted remote O3 effect on $^3J_{C1,C6}$ was investigated by DFT in model structures **20-23**. The effect of C5-C6 bond rotation on $^3J_{C1,C6}$ is shown in Figure 6.1A. The general shape of the curves is conserved in the four structures. $^3J_{C1,C6}$ is minimal at 0° and near maximal at 180° (*tg* rotamer; O6 in-plane), and curve amplitudes are ~ 2 Hz.

For each α/β pair, the α -anomer yielded smaller couplings by 0.5 - 1.0 Hz due to the effect of the terminal O1 substituent. Curves for **22** and **23** lie *below* those for **20** and **21**, respectively, despite very similar C1-O5-C5-C6 torsion angles, indicating that the “remote” axial O3 reduces $^3J_{C1,C6}$ in *allo* configurations in all CH₂OH conformations.

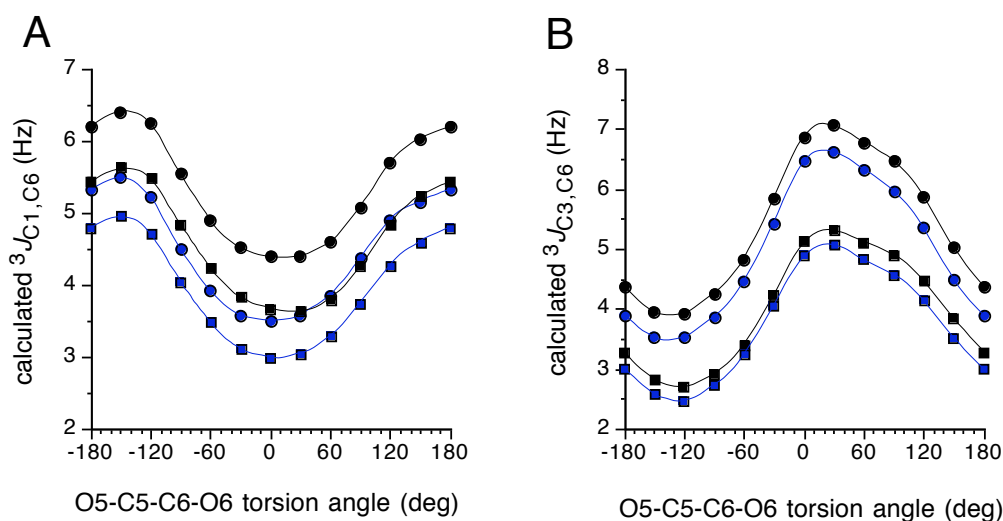


Figure 6.1. (A) Effect of hydroxymethyl group conformation on calculated $^3J_{C1,C6}$ in **20** (blue circles), **21** (black circles), **22** (blue squares), and **23** (black squares). (B) Effect of hydroxymethyl conformation on calculated $^3J_{C3,C6}$ (same symbols as in (A)).

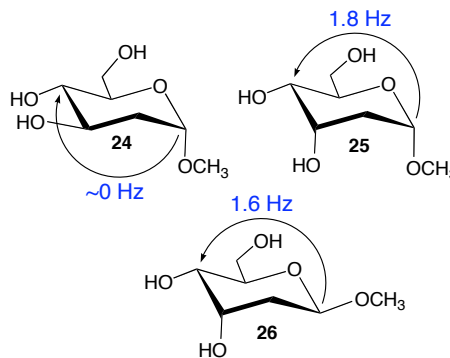
Similar data for $^3J_{C3,C6}$ (Figure 6.1B) show that this coupling is maximal at O5-C5-C6-O6 torsion angles of $\sim 60^\circ$ (*gt* rotamer; O6 in-plane) and near minimal at $\sim 120^\circ$ (C4 and O6 eclipsed). Curves for the **20/21** and **22/23** pairs nearly coincide, with the latter pair displaced to smaller couplings due to the out-of-plane (axial) O3. These data show a small dependence of $^3J_{C3,C6}$ on anomeric configuration (remote effect), with α -anomers yielding slightly smaller couplings, in agreement with the experimental findings.

Plots for ${}^2J_{C1,C3}$, ${}^2J_{C1,C5}$ and ${}^2J_{C3,C5}$ in **20-23** are shown and discussed in Supporting Information (Figures S2-S4).

6.5.4. ${}^{3+3}J_{CC}$ Coupling Constants

Two intra-ring dual-pathway ${}^{13}C$ - ${}^{13}C$ J -couplings exist in aldopyranosyl rings, namely, ${}^{3+3}J_{C1,C4}$ and ${}^{3+3}J_{C2,C5}$ (Scheme 6.1), and their magnitudes and signs are presumably determined by the algebraic sum of the couplings arising from the two constituent three-bond pathways (*e.g.*, C1-C2-C3-C4 (front pathway) and C1-O5-C5-C4 (rear pathway) for ${}^{3+3}J_{C1,C4}$).³⁰ The C-C-C-C or C-O-C-C torsion angles for both component pathways is $\sim\pm 60^\circ$ and the corresponding ${}^3J_{CC}$ values are expected to be positive in sign. Thus, ${}^{3+3}J_{CC}$ values, when observed, are expected to be positive.

${}^{3+3}J_{C1,C4}$ is very small or zero in **1 α /1 β** and **2 β** , but ~ 0.8 Hz in **2 α** (Table 6.1). ${}^{3+3}J_{C1,C4}$ in methyl 2-deoxy- α -D-glucopyranoside **24** is also small, but ${}^{3+3}J_{C1,C4}$ in methyl 2-deoxy- α -D-allopyranoside **25** and methyl 2-deoxy- β -D-allopyranoside **26** are 1.8 Hz and 1.6 Hz, respectively. *These results suggest that the conversion of OH substituents from equatorial to axial orientations along the front pathway increases ${}^{3+3}J_{C1,C4}$, and lead to the prediction that ${}^{3+3}J_{C1,C4}$ should be relatively large in β -D-altropyranose **5 β** . Indeed, a coupling of 1.3 Hz is observed in this structure.*¹⁵

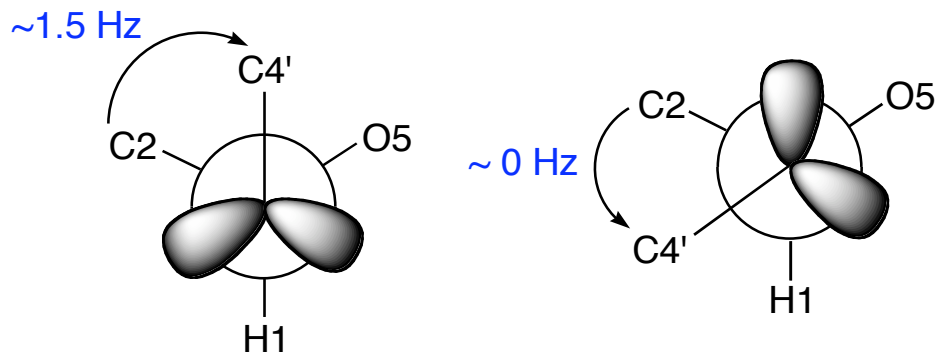


Electronegative substituents anti to coupled hydrogens for gauche H-C-C-H coupling pathways are known to reduce $^3J_{HH}$ values.²⁹ A similar effect operates for $^3J_{CCOC}$.³¹ For example, scalar coupling between C2 and the aglycone C4' in β -(1 \rightarrow 4) glycosidic linkages is not equivalent in the two gauche conformations, with one coupling ~ 0 Hz (O5 anti to C4') and the other ~ 1.5 Hz (H1 anti to C4') (Scheme 6.6). By analogy, the C1-C2-C3-C4 coupling pathway in aldopyranosyl rings should be subject to similar effects. When O2 and O3 are equatorial, they are anti to C4 and C1, respectively, and this geometry should reduce the front pathway $^3J_{CCCC}$ to ~ 0 Hz. When one (*e.g.*, in **2 α**) or both (*e.g.*, in **5 β**) of these oxygens is/are axial, the reduction is mitigated and a larger coupling obtains in the front pathway. The effect appears additive, with **5 β** yielding a coupling ~ 2 -fold greater than observed in **2 α** . Removing an equatorial substituent (deoxygenation at C2; **24-26**) elicits a similar mitigating effect.

Configuration at the *intervening* carbons of the front pathway appears to influence $^{3+3}J_{C1,C4}$ more than the orientation of terminal electronegative substituents on the coupled carbons. This conclusion presumes that the contribution made by the rear $^3J_{COCC}$ pathway to $^{3+3}J_{C1,C4}$ is constant and ~ 0 Hz, that is, this contribution is essentially unaffected by configuration at C2 and C3.

The above interpretation was tested by calculating $^{3+3}J_{C1,C4}$ in **20-23** as a function of hydroxymethyl group conformation (Figure 6.2). Calculated couplings are positive in sign, and are 0.5 - 1.0 Hz for **20/21** and ~ 2 Hz for **22/23**. The effect of terminal carbon configuration (anomeric configuration in this case) is much smaller than the effect of configuration at the internal C3 carbon. Structures containing an axial O3

(**22/23**) show enhanced couplings by ~ 1 Hz compared to those containing an equatorial O3 (**20/21**).



Scheme 6.6. Projections About the C1-O1 Bond in a β -(1 \rightarrow 4) Glycosidic Linkage Showing the Two Arrangements that Orient C2 and C4' Gauche

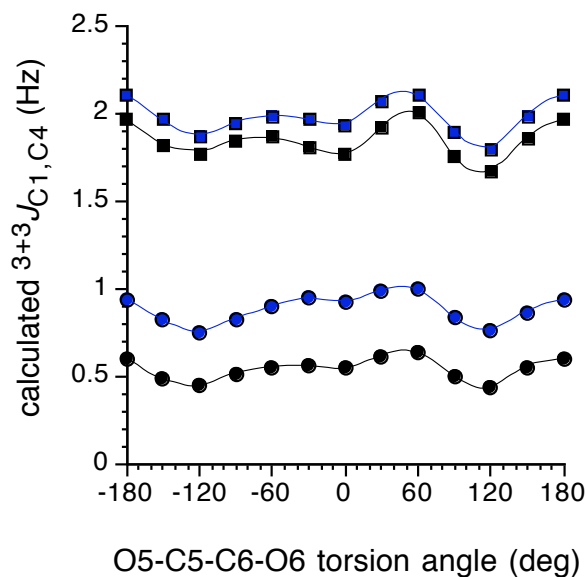


Figure 6.2. Effect of exocyclic hydroxymethyl group conformation on calculated $^3J_{C1,C4}$ in **20** (blue circles), **21** (black circles), **22** (blue squares), and **23** (black squares).

$^3J_{C2,C5}$ is small or zero in $1\alpha/1\beta$ and $2\alpha/2\beta$. By analogy to $^3J_{C1,C4}$, configuration at C3 and C4 should influence the C2-C3-C4-C5 pathway, and

configuration at C1 should influence the C2-C1-O5-C5 pathway. In the *galacto* and *talo* configurations, ${}^3J_{C2,C5}$ is ~ 1.5 Hz in α -anomers, and virtually zero in the corresponding β -anomers (Table 6.2). In these configurations, O4 is axial, and this factor presumably enhances the C2-C3-C4-C5 contribution by ~ 1.5 Hz. The “axial” enhancement is mitigated by converting O1 from an axial to an equatorial orientation. This interpretation leads to the prediction that ${}^3J_{C2,C5}$ will be non-zero in β -D-gulopyranose, since the two axial contributions within the C2-C3-C4-C5 pathway would override the single equatorial contribution from the C2-C1-O5-C5 pathway.

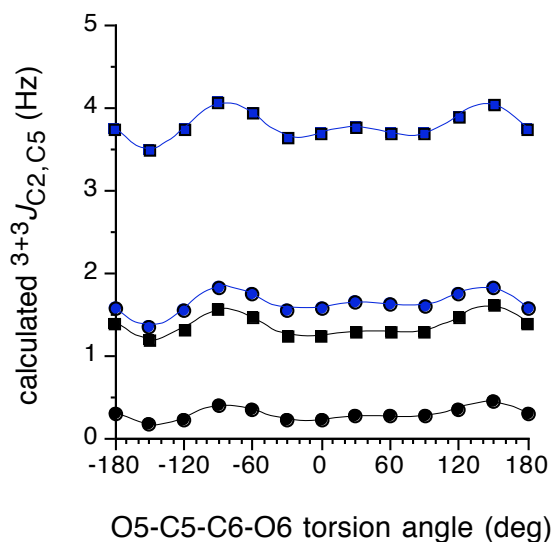


Figure 6.3. Effect of exocyclic hydroxymethyl group conformation on calculated ${}^3J_{C2,C5}$ in **20** (blue circles), **21** (black circles), **22** (blue squares), and **23** (black squares).

${}^3J_{C2,C5}$ in **20-23** was calculated as a function of hydroxymethyl group conformation to test the above interpretations and predictions (Figure 6.3). Three groups of couplings were observed: ~ 0 Hz (**21**); $\sim +1.5$ Hz (**20** and **23**); and $\sim +4$ Hz (**22**). In **21**, both component pathways yield couplings of ~ 0 Hz, which is consistent with both

pathways containing an equatorial C-O bond (O1 and O3 are anti to C5). Each component pathway presumably elicits +1.5 - 2.0 Hz couplings in **22**, given that each contains an axial C-O bond (O1 and O3 are gauche to C5). In **20** and **23**, one component pathway contains an axial and the other an equatorial C-O bond, leading to a coupling of intermediate magnitude.

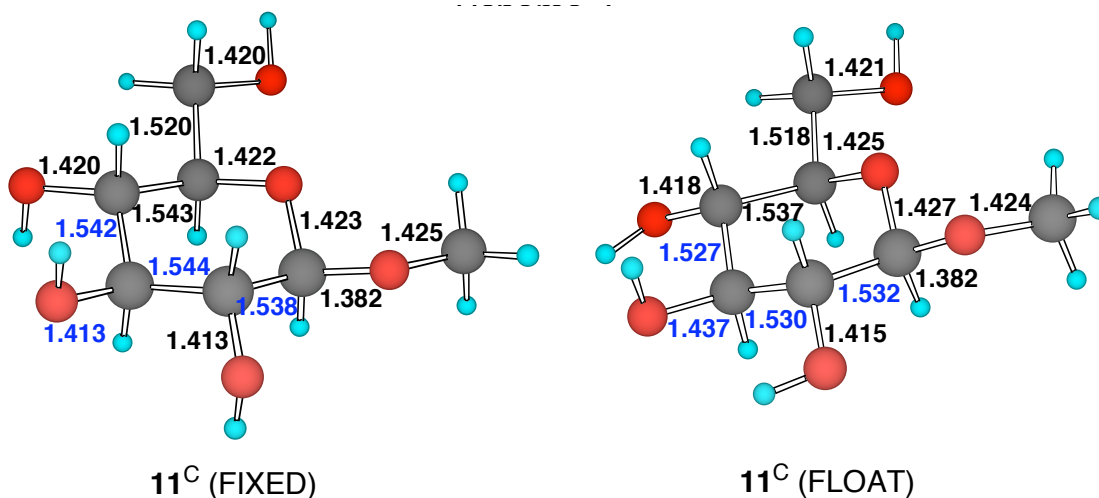
6.5.5. $^1J_{CC}$ Coupling Constants

With the exception of $^1J_{C1,C2}$, experimental endocyclic $^1J_{CC}$ values are typically larger in β -anomers than in their corresponding α -anomers (Tables 6.1, 6.2 and 6.4). For example, $^1J_{C2,C3}$, $^1J_{C3,C4}$ and $^1J_{C4,C5}$ are 38.2, 38.6 and 40.4 in **1 α** , and 38.8, 39.4 and 40.9 in **1 β** , respectively. A structural explanation for this effect remains unclear, but may arise from slightly shorter C-C bonds in the β -anomers caused by different preferred exocyclic C-O bond conformations (see below) and/or other structural and/or stereoelectronic factors.

6.5.6. General Observations on Computed J_{CC} Values

Calculated J_{CC} in Tables 6.3 and 6.5 were determined in two conformations of each model structure that differ in the orientations of some of the exocyclic hydroxyl groups. Conversion of FIXED to FLOAT structures produced changes in no (**3^C**, **16^C**, **18^C** and **19^C**), one (**6^C**, **8^C**, **9^C**, **10^C**, **12^C** and **13^C**), or two (**11^C**) C-O torsions (Schemes S1 and S2). Within each pair of structures, the FLOAT structure was consistently lower in energy by 1.3 – 8.5 kcal/mol. Data in Tables 6.3 and 6.5 show that these C-O torsion

angle changes affect ${}^2J_{CC}$ more than ${}^3J_{CC}$. Specifically, exocyclic C-O torsions along a



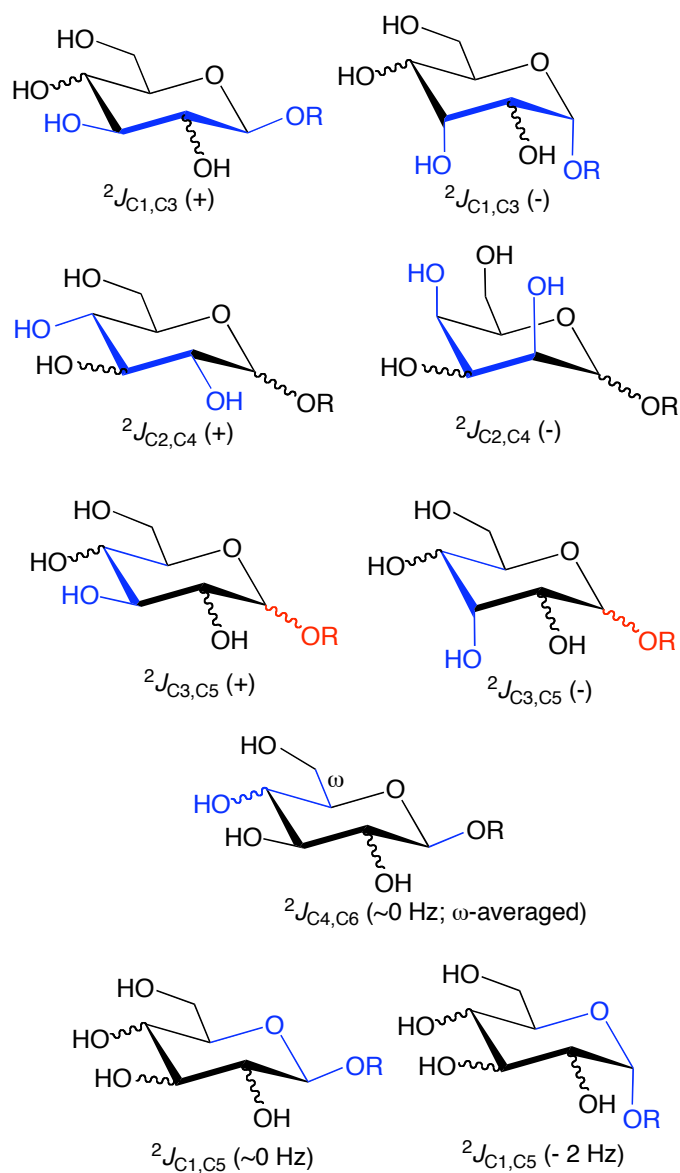
Scheme 6.7. C-C and C-O Bond Lengths (Å) in **11^C**

C-C-C coupling pathway (${}^2J_{C1,C3}$, ${}^2J_{C2,C4}$, ${}^2J_{C3,C5}$) influence coupling magnitude, although presently it is not possible to determine the underlying structural dependencies. It is clear, however, that rotation of specific C-O bonds modulates saccharide structure significantly. A comparison of C-C and C-O bond lengths in **11^C (FIXED)** and **11^C (FLOAT)** is shown in Scheme 6.7. The two structures differ in the C1-C2-O2-H and C3-C4-O4-H torsion angles. Bond length differences are significant in the region of conformational change, with $r_{C1,C2}$, $r_{C2,C3}$, $r_{C3,O3}$ and $r_{C3,C4}$ most affected (values shown in blue). Since J_{CC} are influenced highly by bond hybridization, as reflected in bond lengths, it is not surprising that exocyclic C-O torsions affect these parameters. Prior interpretations of ${}^2J_{CC}$ using the PR rule⁶ have been based solely on the inspection of the relative *orientation* of electronegative substituents on the coupled carbons. The present results suggest that further improvements in the interpretation of these couplings may require a fuller appreciation of C-O torsional contributions.

6.6. Conclusions

Empirical correlations between saccharide structure and experimental J_{CC} values have been described in this report and were subsequently tested by quantum mechanical calculations. New structural correlations have been proposed for ${}^2J_{C3,C5}$, and new insights into the behavior of dual-pathway ${}^{13}\text{C}$ - ${}^{13}\text{C}$ couplings in aldopyranosyl rings have been obtained. Remote effects on J_{CC} have been identified, namely, the effect of anomeric configuration on ${}^2J_{C3,C5}$, the effect of O3 orientation on ${}^3J_{C1,C6}$, and the effect of anti oxygen substituents on gauche ${}^3J_{CC}$. While the underlying structural origins of these remote effects remain unclear, documenting their existence is an important initial step toward achieving this understanding, which may prove essential for more quantitative interpretations of these J -couplings.

Structure-coupling correlations for ${}^2J_{CC}$ are summarized in Scheme 6.8. Maximal ${}^2J_{CCC}$ (most positive) are observed when both terminal OH substituents are equatorial, and these couplings are minimal (most negative) when both substituents are axial. Intermediate couplings are observed when one OH is axial and the other equatorial. For ${}^2J_{COC}$, orientation of O1 largely determines the coupling, with small or zero values observed when O1 is in-plane (equatorial), and negative couplings observed when O1 is out of plane (axial). For ${}^2J_{CCC}$, theoretical calculations show that C-O conformation involving terminal and/or intervening carbons modulates the coupling, probably in part due to the substantial bond length changes that accrue, but a more systematic study of these effects remains to be undertaken, similar to that reported recently for ${}^2J_{CCH}$.³² The remote effect of anomeric configuration on ${}^2J_{C3,C5}$ may be

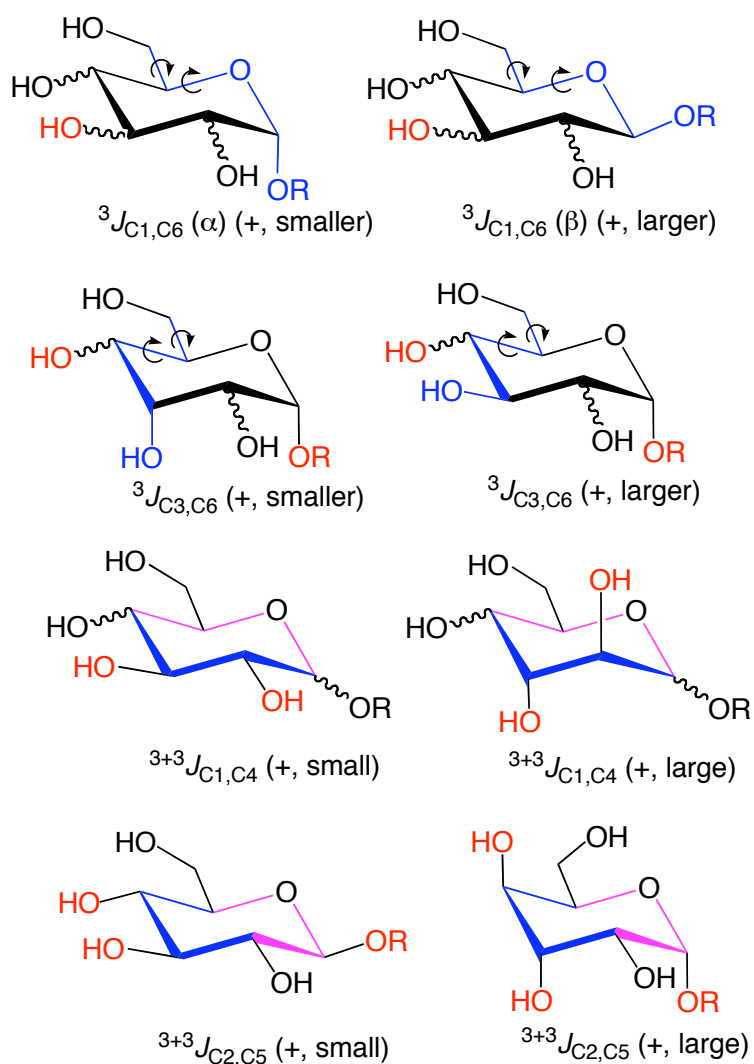


Scheme 6.8. Summary of $^2J_{CC}$ behaviour in Aldopyranosyl Rings. Coupling pathways and direct substituent effects are shown in blue, and remote substituent effects are shown in red.

due to different average conformations about the C4-O4 bond in the two anomers, possibly caused by different intra- and/or intermolecular H-bonding in solution, but this explanation will require further investigation.

Correlations involving single-pathway and dual-pathway $^3J_{CC}$ are summarized in Scheme

6.9. While single-pathway couplings depend primarily on either the C-C-C-C or



Scheme 6.9. Summary of $^3J_{CC}$ behaviour in Aldopyranosyl Rings.

Coupling pathways and direct substituent effects are shown in blue and pink, and remote substituent effects are shown in red.

C-C-O-C torsion angle, electronegative atom orientation at the terminal (coupled) carbon(s) is an important secondary determinant. For $^3J_{C1,C6}$ and $^3J_{C3,C6}$, the latter factor leads to their partial dependence on hydroxymethyl group conformation. $^3J_{C1,C6}$

and $^3J_{C3,C6}$ are also influenced by configuration at remote carbons, with C3 configuration affecting the former and C1 configuration affecting the latter. It is noteworthy that, in these cases, the remote carbon bears the same structural relationship to the affected coupling pathway.

New insights, substantiated by DFT calculations, have been obtained on the structural dependencies of dual-pathway $^3J_{CC}$ in saccharides. For aldopyranosyl rings in ideal chair forms, both constituent coupling pathways orient the coupled carbons gauche. *Internal* OH substituents modulate $^3+^3J_{CC}$ by either orienting gauche or anti to one or both of the terminal coupled carbons, with the former orientation contributing positively to the coupling. This finding has important implications for the analysis of $^3J_{CC}$ in general, since it suggests that internal electronegative substituents can exert an important effect on these couplings, superimposed on those caused by terminal substituents. For $^3+^3J_{CC}$, the orientation of terminal OH groups appears less important than the orientation of internal OH groups. The available data support the contention that the observed coupling is determined by summing the constituent couplings directly, since both are expected to be positive in sign.

The present findings add to a growing, but still incomplete, body of knowledge about the behavior of ^{13}C - ^{13}C J -couplings in saccharides. The underlying motivation for this work lies in the expectation that, in addition to their value as structural and conformational probes, these parameters may reveal or explain important functional properties. The first step in achieving this goal is to establish correlations between structure and J -coupling magnitude. The second step is to draw correlations between J -coupling and specific functions. Since J -couplings provide a convenient window into

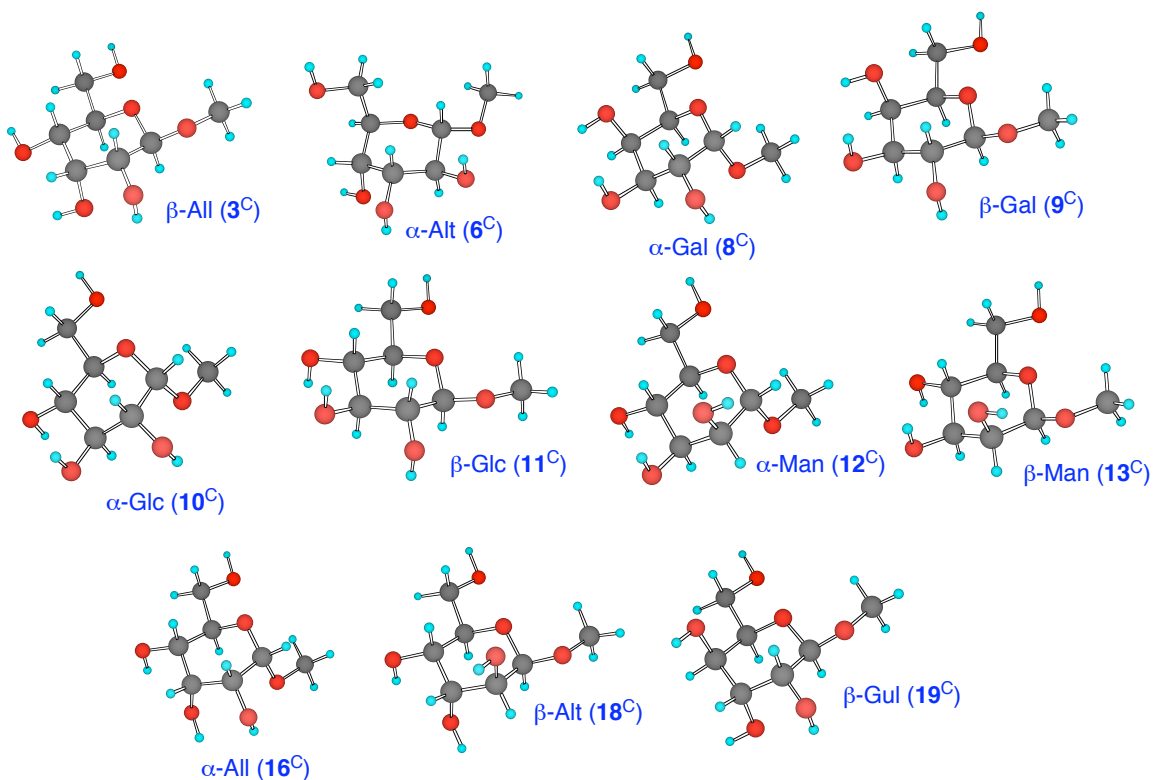
electronic structure, and since electronic structure dictates reactivity, these parameters offer an opportunity to probe and understand saccharide reactivities. Recently, this connection has been established in which $^1J_{\text{CH}}$ values in -CHOH- groups were related to the strength of H-bonds involving the OH hydrogen.³³

A complete repertoire of J -coupling/structure correlations may permit more detailed investigations of the more elusive characteristics of saccharides, an example being OH properties, or more specifically, non-glycosidic C-O torsional properties. Hydroxyl groups lie on the periphery of saccharides and are thus in intimate contact with the environment. They thus serve as important recognition sites in saccharide-protein binding and mediate the interactions of saccharides with solvent water. That C-O torsions in saccharides in solution, or potentially in the bound state, can be evaluated indirectly through $^1J_{\text{CC}}$ ³⁴ or $^1J_{\text{CH}}$ ³⁵, parameters not commonly associated with this type of information, is an intriguing proposition. Integrated studies of $^1J_{\text{CC}}$, $^1J_{\text{CH}}$, $^3J_{\text{HCOH}}$ and/or $^3J_{\text{CCOH}}$ promise to provide more complete pictures of how these C-O torsions behave in solution and how they may modulate chemical and biological reactivity in the free or bound state. This study has shown that apparently innocuous changes in C-O torsions induce major changes in saccharide covalent structure, changes that may be exploited in controlling biological function and reactivity. For example, freezing local C-O conformation(s) in the bound state could result in bond length changes that, in turn, facilitate a change in preferred global conformation and/or influence inherent chemical reactivity. We expect further developments in this regard as future studies of the behaviors of J -couplings in saccharides emerge.

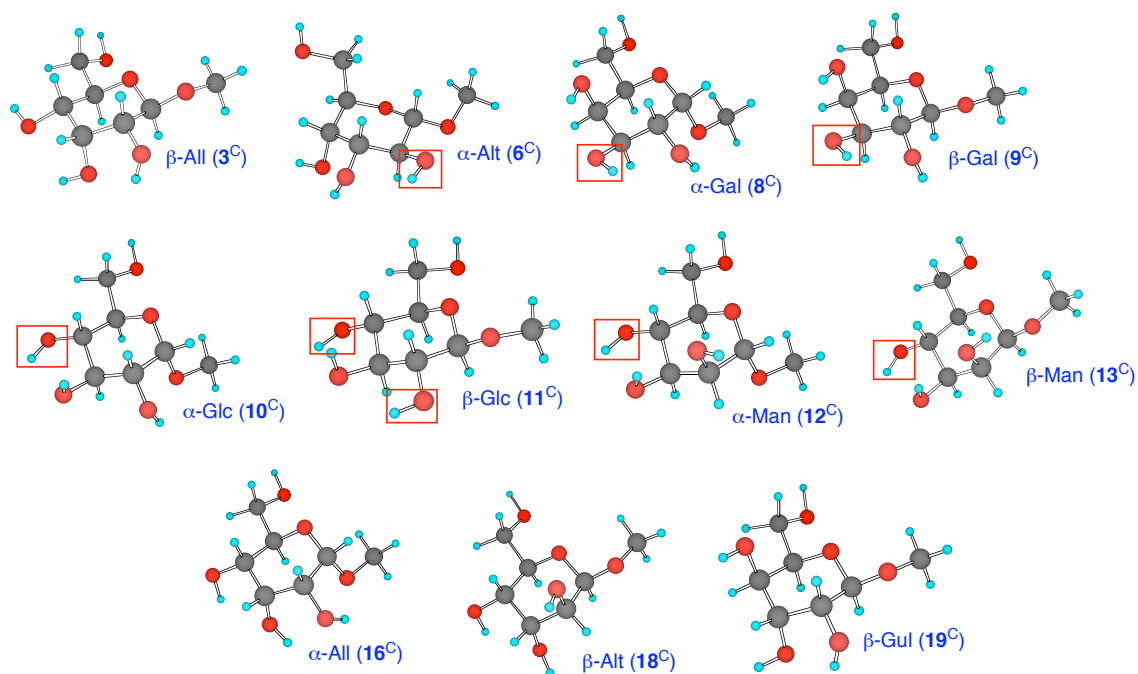
6.7. Acknowledgements

This work was supported by a grant (to A.S.) from the National Institutes of Health (GM). The Notre Dame Radiation Laboratory is supported by the Office of Basic Energy Sciences of the United States Department of Energy. This is Document No. NDRL-4545 from the Notre Dame Radiation Laboratory.

6.8. Supporting Information

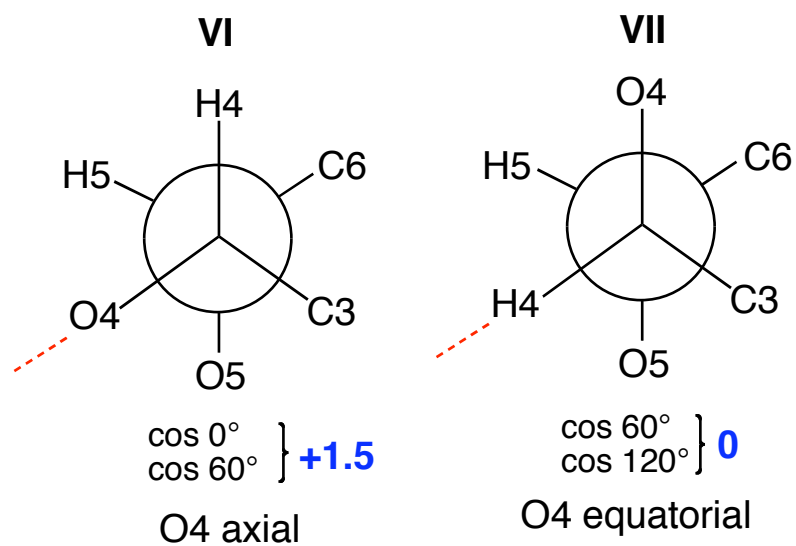


Scheme 6.10. (S1) DFT-Optimized Structures (B3LYP/6-31G*) – FIXED Series

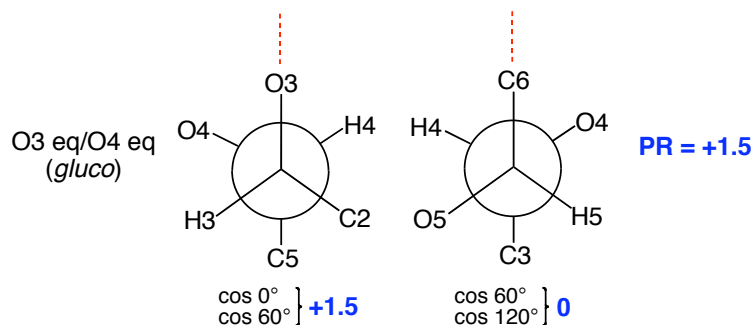


(OH groups in red boxes differ in orientation substantially between the FIXED and FLOAT series)

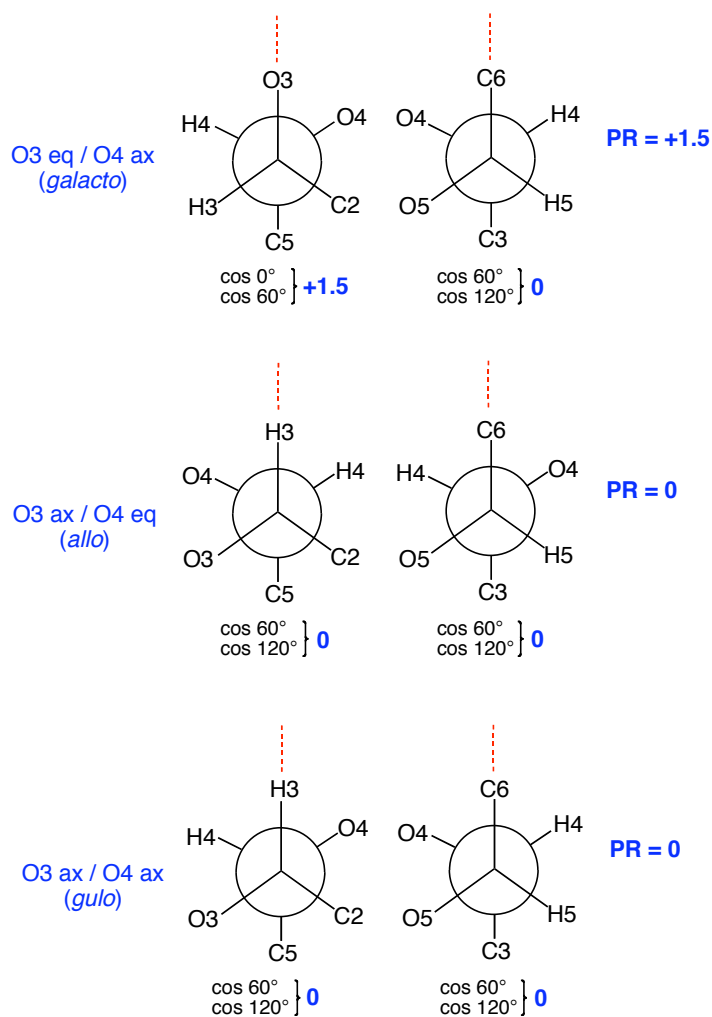
Scheme 6.11. (S2) DFT-Optimized Structures (B3LYP/6-31G*) – FLOAT Series



Scheme 6.12. (S3) Projections for ${}^2J_{C4,C6}$ in D-aldohexopyranosyl rings (1C_4)



Scheme 6.13. (S4) Application of the projection resultant (PR) method to $^2J_{C3,C5}$ in glucopyranosyl rings.



Scheme 6.14. (S5) Application of the projection resultant (PR) method to $^2J_{C3,C5}$ in other aldohexopyranosyl rings.

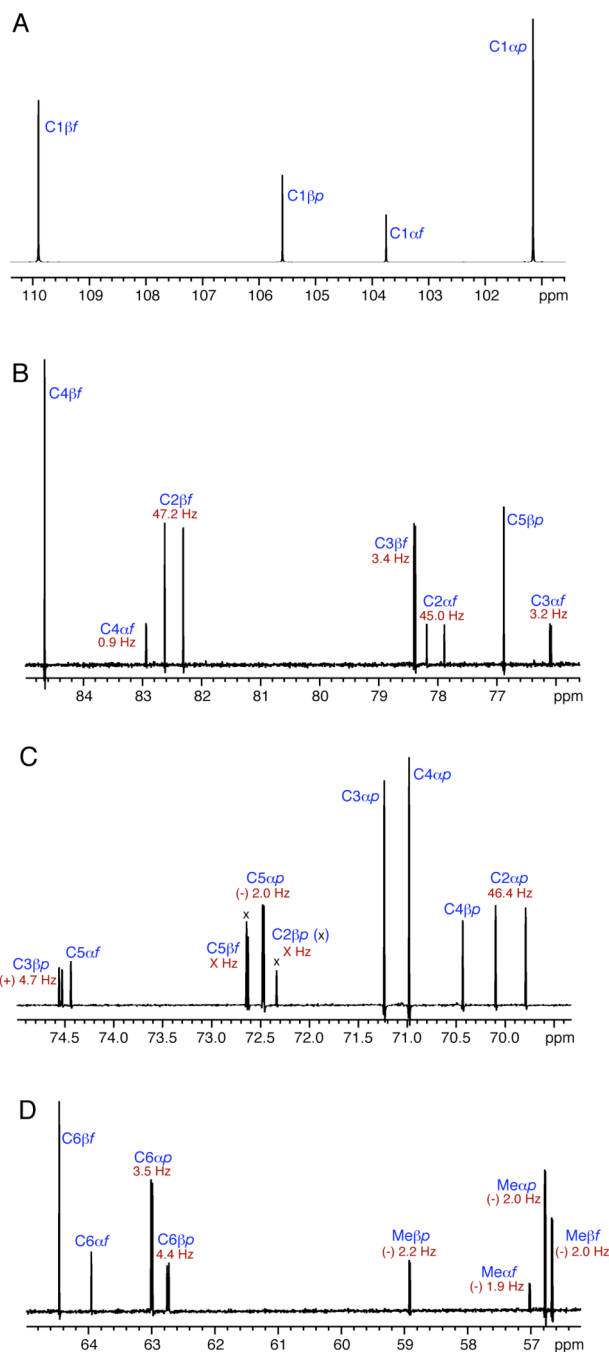


Figure 6.4. (S1) $^{13}\text{C}\{^1\text{H}\}$ NMR spectrum (150 MHz) of an aqueous solution of methyl glycosides generated from Fischer glycosidation of D-[1- ^{13}C]galactose. Four forms are present (see adjacent structures): Gal α p, Gal β p, Gal α f and Gal β f. Expanded regions of the spectrum are shown in A-D, with signal assignments shown in blue and J_{CC} values shown in red.

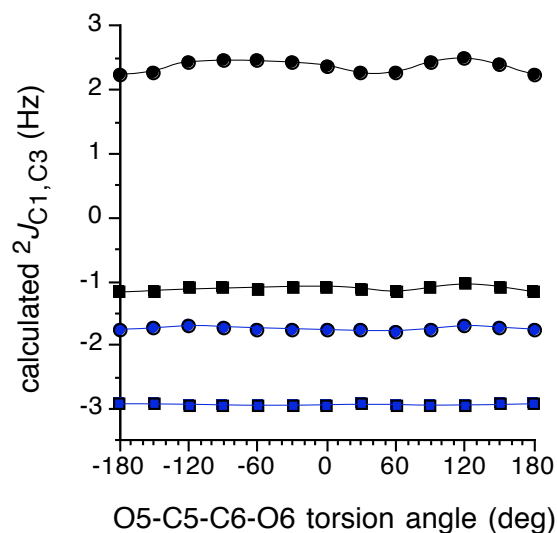


Figure 6.5. (S2) Effect of exocyclic hydroxymethyl group conformation on calculated ${}^2J_{C1,C3}$ in **20** (blue circles), **21** (black circles), **22** (blue squares), and **23** (black squares). The most negative coupling is observed in **22**, which bears two axial C-O bonds at C1 and C3. In contrast, the most positive coupling is observed in **21**, which bears two equatorial C-O bonds at C1 and C3. Intermediate couplings are observed in **20** and **23** which contain one axial and one equatorial C-O bond at C1 and C3. These findings validate the predictions based on the empirical PR rule.⁶

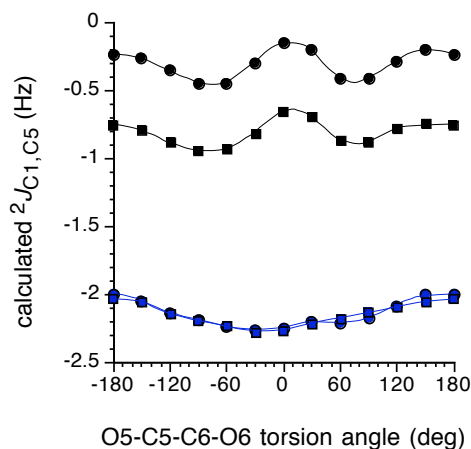


Figure 6.6. (S3) Effect of exocyclic hydroxymethyl group conformation on calculated ${}^2J_{C1,C5}$ in **20** (blue circles), **21** (black circles), **22** (blue squares), and **23** (black squares). A dependence of this coupling on anomeric configuration is observed, with α -anomers (**20**, **22**) giving couplings of ~ -2 Hz and β -anomers giving couplings of ~ -0.5 Hz. These data are consistent with experimental data (Table 1) and PR predictions.⁶

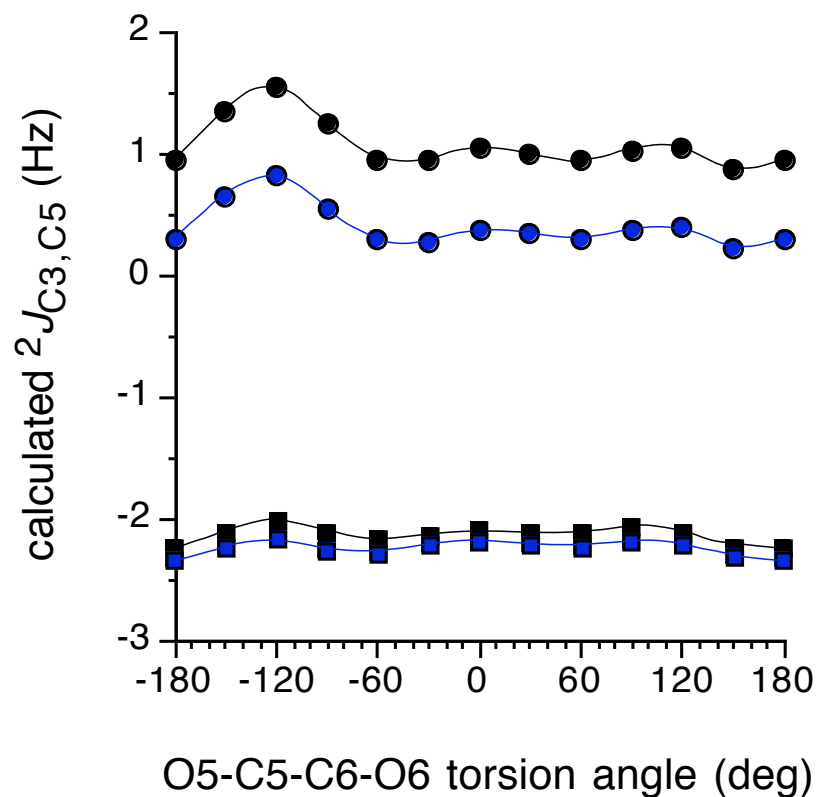


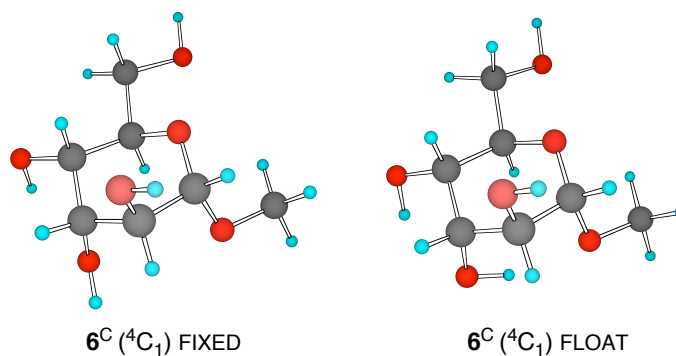
Figure 6.7. (S4) Effect of exocyclic hydroxymethyl group conformation on calculated $^2J_{C3,C5}$ in **20** (blue circles), **21** (black circles), **22** (blue squares), and **23** (black squares). Changing the orientation of O3 from equatorial to axial results in a significant shift in $^2J_{C3,C5}$ to more negative values. The remote effect of anomeric configuration on $^2J_{C3,C5}$ is also evident, with the coupling in **21** ~ 0.6 Hz larger than in **20**. However, a related remote effect in **22** and **23** is not observed. These results are consistent with experimental observations (Tables 1 and 3).

TABLE 6.6. (S1) FERMI CONTACT AND NON-FERMI CONTACT
CONTRIBUTIONS TO TOTAL CALCULATED J_{CC} VALUES IN **11**^c

J -Coupling	FC (Hz)	SD (Hz)	PSO (Hz)	DSO (Hz)	Total (Hz)	Total NFC ^b (Hz)
$^1J_{C1,C2}$	46.98	1.21	-1.13	0.41	47.47	+0.49
$^1J_{C2,C3}$	36.63	1.12	-1.28	0.38	36.85	+0.22
$^1J_{C5,C6}$	48.60	1.09	-1.30	0.34	48.73	+0.13
$^2J_{C1,C3}$	6.48	-0.05	-0.10	0.14	6.47	-0.01
$^2J_{C1,C5}$	-0.36	-0.02	-0.23	0.09	-0.52	-0.16
$^2J_{C2,C4}$	3.06	-0.06	-0.14	0.12	2.98	-0.08
$^2J_{C3,C5}$	3.73	-0.06	-0.15	0.13	3.65	-0.08
$^3J_{C1,C6}$	4.37	0.05	0.01	-0.04	4.39	0.02
$^3J_{C3,C6}$	4.61	0.03	0.02	-0.02	4.64	0.03
$^{3+3}J_{C1,C4}$	-0.75	-0.02	-0.04	0.09	-0.72	0.03
$^{3+3}J_{C2,C5}$	-0.51	-0.01	-0.03	0.08	-0.47	0.04

^aFC = Fermi contact; SD = spin-dipolar; PSO = paramagnetic spin-orbit;
DSO = diamagnetic spin-orbit. ^bEqual to SD + PSO + DSO.

The NFC contribution to calculated J_{CC} values is small, ranging from +0.13 - +0.49 Hz for $^1J_{CC}$, and from -0.16 – +0.4 Hz for $^2J_{CC}$ and $^3J_{CC}$. Although the reported couplings in the manuscript contain both FC and NFC components, ignoring the latter contributions would not adversely affect the quality of the analysis.



Scheme 6.15. (S5) Structures of **6^C (⁴C₁)** FIXED and FLOAT

TABLE 6.7. (S2) CALCULATED J_{CC} VALUES IN **6^C** IN THE ⁴C₁ CONFORMATION

<i>J</i> -coupling	6^C (⁴C₁) FIXED	6^C (⁴C₁) FLOAT
$^2J_{C1,C3}$	-1.6	-2.0
$^2J_{C1,C5}$	-2.1	-2.1
$^2J_{C2,C4}$	-0.5	0.3
$^2J_{C3,C5}$	-0.6	-0.5
$^2J_{C4,C6}$	2.8	2.6
$^3J_{C1,C6}$	3.2	3.3
$^3J_{C3,C6}$	2.9	3.2
$^{3+3}J_{C1,C4}$	1.6	1.9
$^{3+3}J_{C2,C5}$	1.7	1.7

^aIn Hz.

A comparison of calculated $^2J_{CC}$, $^3J_{CC}$ and $^{3+3}J_{CC}$ in **6^C** in the ¹C₄ (Tables 3 and 5) and ⁴C₁ (above) ring conformations shows a significantly more negative $^2J_{C1,C3}$ in the ⁴C₁ form as expected from the di-axial arrangement of O1 and O3. $^2J_{C1,C5}$ is also more negative in ⁴C₁ and assumes a value similar to those found in other ⁴C₁ structures (~2 Hz). $^3J_{C1,C6}$ and $^3J_{C3,C6}$ are larger in ⁴C₁ due to the increased C1-O5-C5-C6 and C3-C4-C5-C6 dihedral angles. Dual pathway J_{CC} values increase in ⁴C₁ due to the larger number of internal axial hydroxyl substituents present in the constituent pathways.

6.9. References

1. (a) Blechta, V.; del Rio-Portilla, F.; Freeman, R. *Magn. Res. Chem.* **1994**, *32*, 134-137. (b) Nishida, T.; Widmalm, G.; Sandor, P. *Magn. Res. Chem.* **1995**, *33*, 596-599.
2. King-Morris, M.J.; Serianni, A.S. *J. Am. Chem. Soc.* **1987**, *109*, 3501-3508.
3. Wu, J.; Bondo, P.B.; Vuorinen, T.; Serianni, A.S. *J. Am. Chem. Soc.* **1992**, *114*, 3499-3505.
4. Bossennec, V.; Firmin, P.; Perly, B.; Berthault, P. *Magn. Reson. Chem.* **1990**, *28*, 149-155.
5. Krivdin, L.B.; Kalabin, G.A. *Prog. NMR Spectrosc.* **1989**, *21*, 293-448.
6. Church, T.; Carmichael, I.; Serianni, A.S. *Carbohydr. Res.* **1996**, *280*, 177-186.
7. Bose, B.; Zhao, S.; Stenutz, R.; Cloran, F.; Bondo, P.B.; Bondo, G.; Hertz, B.; Carmichael, I.; Serianni, A.S. *J. Am. Chem. Soc.* **1998**, *120*, 11158-11173.
8. Cloran, F.; Carmichael, I.; Serianni, A.S. *J. Am. Chem. Soc.* **1999**, *121*, 9843-9851.
9. Serianni, A.S.; Bondo, P.B.; Zajicek, J. *J. Magn. Reson.* **1996**, *B112*, 69-74.
10. Zhao, S.; Bondo, G.; Zajicek, J.; Serianni, A.S. *Carbohydr. Res.* **1998**, *309*, 145-152.
11. Cloran, F.; Carmichael, I.; Serianni, A.S. *J. Am. Chem. Soc.* **2000**, *122*, 396-397.
12. Serianni, A.S.; Nunez, H.A.; Barker, R. *Carbohydr. Res.* **1979**, *72*, 71-78.
13. Hayes, M.L.; Pennings, N.J.; Serianni, A.S.; Barker, R. *J. Am. Chem. Soc.* **1982**, *104*, 6764-6769.
14. Serianni, A.S.; Vuorinen, T.; Bondo, P. *J. Carbohydr. Chem.* **1990**, *9*, 513-541.
15. King-Morris, M.J.; Bondo, P.B.; Mrowca, R.A.; Serianni, A.S. *Carbohydr. Res.* **1988**, *175*, 49-58.
16. Podlasek, C.A.; Wu, J.; Stripe, W.A.; Bondo, P.B.; Serianni, A.S. *J. Am. Chem. Soc.* **1995**, *117*, 8635-8644.

17. Serianni, A.S.; Clark, E.L.; Barker, R. *Carbohydr. Res.* **1979**, *72*, 79-91.
18. Serianni, A.S.; Barker, R. *J. Magn. Reson.* **1982**, *49*, 335-340.
19. Frisch, M.J.; Trucks, G.W.; Schlegel, H.B.; Scuseria, G.E.; Robb, M.A.; Cheeseman, J.R.; Montgomery, Jr., J.A.; Vreven, T.; Kudin, K.N.; Burant, J.C.; Millam, J.M.; Iyengar, S.S.; Tomasi, J.; Barone, V.; Mennucci, B.; Cossi, M.; Scalmani, G.; Rega, N.; Petersson, G.A.; Nakatsuji, H.; Hada, M.; Ehara, M.; Toyota, K.; Fukuda, R.; Hasegawa, J.; Ishida, M.; Nakajima, T.; Honda, Y.; Kitao, O.; Nakai, H.; Klene, M.; Li, X.; Knox, J.E.; Hratchian, H.P.; Cross, J.B.; Adamo, C.; Jaramillo, J.; Gomperts, R.; Stratmann, R.E.; Yazyev, O.; Austin, A.J.; Cammi, R.; Pomelli, C.; Ochterski, J.W.; Ayala, P.Y.; Morokuma, K.; Voth, G.A.; Salvador, P.; Dannenberg, J.J.; Zakrzewski, V.G.; Dapprich, S.; Daniels, A.D.; Strain, M.C.; Farkas, O.; Malick, D.K.; Rabuck, A.D.; Raghavachari, K.; Foresman, J.B.; Ortiz, J.V.; Cui, Q.; Baboul, A.G.; Clifford, S.; Cioslowski, J.; Stefanov, B.B.; Liu, G.; Liashenko, A.; Piskorz, P.; Komaromi, I.; Martin, R.L.; Fox, D.J.; Keith, T.; Al-Laham, M.A.; Peng, C.Y.; Nanayakkara, A.; Challacombe, M.; Gill, P.M.W.; Johnson, B.; Chen, W.; Wong, M.W.; Gonzalez, C.; Pople, J.A. *Gaussian03*, Revision A.1, Gaussian, Inc., Pittsburgh PA, 2003.
20. Becke, A.D. *J. Chem. Phys.* **1993**, *98*, 5648-5652.
21. Hehre, W.J.; Ditchfield, R.; Pople, J.A. *J. Chem. Phys.* **1972**, *56*, 2257-2261.
22. Cloran, F.; Zhu, Y.; Osborn, J.; Carmichael, I.; Serianni, A.S. *J. Am. Chem. Soc.* **2000**, *122*, 6435-6448.
23. Cloran, F.; Carmichael, I.; Serianni, A.S. *J. Am. Chem. Soc.* **2001**, *123*, 4781-4791.
24. Lemieux, R.U. *Pure Appl. Chem.* **1971**, *25*, 527-548.
25. Praly, J.-P.; Lemieux, R.U. *Can. J. Chem.* **1987**, *65*, 213-223.
26. Juaristi, E.; Cuevas, G. *The Anomeric Effect*, CRC Press, Boca Raton, 1995.
27. Angyal, S.J. *Angew. Chem. Int. Ed. Engl.* **1969**, *8*, 157.
28. Thibaudeau, C.; Stenutz, R.; Hertz, B.; Klepach, T.; Zhao, S.; Wu, Q.; Carmichael, I.; Serianni, A.S. *J. Am. Chem. Soc.* **2004**, *126*, 15668-15685.
29. (a) Günther, H. *NMR Spectroscopy*, John Wiley & Sons, 1995, pp. 119-120. (b) Pachler, K.G.R. *Tetrahedron* **1971**, *27*, 187-199.
30. Marshall, J.L. *Carbon-Carbon and Carbon-Proton NMR Couplings: Applications to Organic Stereochemistry and Conformational Analysis*, Verlag Chemie International, Deerfield Beach, 1983, pp. 186-193.

31. Zhao, H.; Serianni, A.S. unpublished results.
32. Klepach, T.; Carmichael, I.; Serianni, A.S. *J. Am. Chem. Soc.* **2005**, *127*, 9781-9793.
33. Maiti, N.C.; Zhu, Y.; Carmichael, I.; Serianni, A.S.; Anderson, V.E. *J. Org. Chem.* **2006**, *71*, 2878-2880.
34. Carmichael, I.; Chipman, D.M.; Podlasek, C.A.; Serianni, A.S. *J. Am. Chem. Soc.* **1992**, *115*, 10863-10870.
35. Serianni, A.S.; Wu, J.; Carmichael, I. *J. Am. Chem. Soc.* **1995**, *117*, 8645-8650.
36. Bock, K.; Pedersen, C. *Adv. Carbohydr. Chem. Biochem.* **1983**, *41*, 27